

**Determination of Design and Operation Parameters
for Upper Atmospheric Research Instrumentation
to Yield Optimum Resolution with Deconvolution**

*GRANT
1979-1981
2.16
P.163*

NASA Grant NAG 1-804

FINAL REPORT

1 Aug 1987 - 31 Dec 1991

N93-26034

Unclas

G3/45 0157636

**Dr. George E. Ioup, Principal Investigator
Dr. Juliette W. Ioup, Principal Investigator
Department of Physics
University of New Orleans
New Orleans, LA 70148**

(NASA-CR-192832) DETERMINATION OF
DESIGN AND OPERATION PARAMETERS FOR
UPPER ATMOSPHERIC RESEARCH
INSTRUMENTATION TO YIELD OPTIMUM
RESOLUTION WITH DECONVOLUTION Final
Report, 1 Aug. 1987 - 31 Dec. 1991
(New Orleans Univ.) 169-D

197951 1558

1

**Determination of Design and Operation Parameters
for Upper Atmospheric Research Instrumentation
to Yield Optimum Resolution with Deconvolution**

NASA Grant NAG 1-804

FINAL REPORT

1 Aug 1987 - 31 Dec 1991

Dr. George E. Ioup, Principal Investigator
Dr. Juliette W. Ioup, Principal Investigator
Department of Physics
University of New Orleans
New Orleans, LA 70148

Determination of Design and Operation Parameters for Upper Atmospheric Research Instrumentation to Yield Optimum Resolution with Deconvolution

The subject NASA grant number NAG 1-804 was instituted 1 Aug 1987, originally for a three-year period, through 31 July 1990. No-cost extensions were granted so that the grant finally terminated on 31 Dec 1991. During the period in which the Principal Investigators were partially supported by the grant, Graduate Research Assistants and a Graduate Research Associate, Mr. Abolfazl M. Amini, were also supported on an intermittent basis. A good deal of grant-related research was performed by graduate students who were not directly supported by the grant, but were employed by the University of New Orleans Department of Physics as Teaching Assistants, or otherwise employed.

In addition to the support provided by NASA Langley Research Center, two other sources of support were associated with this grant. Two funding increments through this NASA grant were provided by the U. S. Army Cold Regions Research and Engineering Laboratory (CRREL) for research performed by the Principal Investigators and an additional Investigator, Dr. Clyde Bergeron of the Department of Physics. A funding increment was also provided by NASA Marshall Space Flight Center to begin research into the analysis and prediction of the tethered satellite tether skiprope mode, which could occur in the NASA/Italy ASI TSS-1 experiment.

The research for the basic NASA Langley grant and for the additional increments of

funding has been described in journal and proceedings articles, published abstracts, student Master's theses, and reports, all of which are included in this final report document. We include both papers directly supported by NASA and the related research directed by the Principal Investigators which did not receive direct NASA support. A list of the journal and proceedings articles, research papers with published abstracts, and theses directly related to the subject of the initial grant is included in Appendix 1, along with copies of the articles and abstracts. Appendix 1 is bound in this volume.

Appendices 2, 3, and 4 contain the three student Master's theses listed in Appendix 1. Each of these is bound separately and enclosed as a volume with this report. The two reports written to describe the research supported by CRREL are included as Appendices 5 and 6, which are bound in this volume. Finally, the Engineering Notebook, Appendix 7, written for and submitted to NASA Marshall Space Flight Center, is also part of this report, and is included as an enclosed separate volume.

Among all the research results reported in the Appendices, note should be made of the specific investigation of the determination of design and operation parameters for upper atmospheric research instrumentation to yield optimum resolution with deconvolution. As reported by G. Ioup et al (1988, 1989), a methodology has been developed to determine design and operation parameters for error minimization when deconvolution is included in data analysis. An error surface is plotted versus the signal-to-noise ratio (SNR) and all parameters of interest. Instrumental characteristics will determine a curve in this space. The SNR and parameter values which give the projection from the curve to the surface, corresponding to the smallest value for the error, are the optimum values. These values are

constrained by the curve and so will not necessarily correspond to an absolute minimum in the error surface.

During the period of this grant, the Investigators and their students have maintained frequent contact with the original technical monitor, Dr. George M. Wood, and the new monitor, Dr. Billy T. Upchurch, both of NASA Langley Research Center. This interaction has been immensely rewarding for both the Investigators and their students. We are very grateful to NASA Langley Research Center, not only for the funding of the research, but also for the interaction and research opportunities which have been provided to the Department of Physics at the University of New Orleans. We anticipate with pleasure continued association with the research staff of NASA Langley Research Center.



**Determination of Design and Operation Parameters
for Upper Atmospheric Research Instrumentation
to Yield Optimum Resolution with Deconvolution**

NASA Grant NAG 1-804

FINAL REPORT

APPENDIX 1

Dr. George E. Ioup, Principal Investigator
Dr. Juliette W. Ioup, Principal Investigator
Department of Physics
University of New Orleans
New Orleans, LA 70148



**Determination of Design and Operation Parameters
for Upper Atmospheric Research Instrumentation
to Yield Optimum Resolution with Deconvolution**

PUBLICATIONS LIST AND COPIES OF ARTICLES AND ABSTRACTS

JOURNAL AND PROCEEDINGS ARTICLES

Autocorrelation estimation using constrained iterative spectral deconvolution, Murali Ramaswamy and George E. Ioup, *Geophysics* 54, 381-391, 1989

Enhanced data from analytical instrumentation by deconvolution of periodically sampled signals, George E. Ioup, Juliette W. Ioup, Abolfazl Amini, Grayson H. Rayborn, Dong Wang, and George M. Wood, paper presented at the 4th International Conference on Computational Methods and Experimental Measurements (CMEM 89) of the Computational Mechanics Institute, 23-26 May 1989, Capri, Italy, and published in *Computers and Experiments in Stress Analysis*, G. M. Carlomagno and C. A. Brebbia, eds., Springer-Verlag, Berlin, hardbound, p. 449-463, 1989

RESEARCH PAPERS WITH PUBLISHED ABSTRACTS

Determination of Instrumentation Parameters for Optimum Resolution with Deconvolution, George E. Ioup, Abolfazl M. Amini, and Juliette W. Ioup, paper presented at the March Meeting of the American Physical Society, 21- 25 Mar 1988, New Orleans, abstracted in *Bull. Am. Phys. Soc.* 33, 705, 1988

Single Filter Application of Always-Convergent Iterative Deconvolution to Physical Data, Haihong Ni, Abolfazl M. Amini, Tahar A. Bensueid, George E. Ioup, and Juliette W. Ioup, paper presented at the March Meeting of the American Physical Society, 21-25 Mar 1988, New Orleans, abstracted in *Bull. Am. Phys. Soc.* 33, 669, 1988

Optimization of Convergent Iterative Deconvolution for Physical Data, Abolfazl M. Amini, George E. Ioup, and Juliette W. Ioup, paper presented at the March Meeting of the American Physical Society, 21-25 Mar 1988, New Orleans, abstracted in *Bull. Am. Phys. Soc.* 33, 669, 1988

Statistical Optimization of Morrison's Iterative Noise Removal and van Cittert's Iterative Deconvolution, James H. Leclere, George E. Ioup, and Juliette W. Ioup, paper presented at

the March Meeting of the American Physical Society, 21-25 Mar 1988, New Orleans, abstracted in Bull. Am. Phys. Soc. 33, 669, 1988

Always-Convergent Iterative Deconvolution for Acoustic Non-Destructive Evaluation, Edward J. Murphy, Juliette W. Ioup, George E. Ioup, and Doron Kishoni, paper presented at the March Meeting of the American Physical Society, 21-25 Mar 1988, New Orleans, abstracted in Bull. Am. Phys. Soc. 33, 487, 1988

Least-squares and single-filter always-convergent iterative deconvolution of transient signals for correlation processing, James H. Leclere, George E. Ioup, Juliette W. Ioup, and Robert L. Field, paper presented at the fall meeting of the Acoustical Society of America, 14-18 Nov 1988, Honolulu, HI, and abstracted in Jour. Acous. Soc. Am. 84, S17, 1988

Deconvolution for Increased Resolution in AEM Data, Clyde J. Bergeron, Jr., George E. Ioup, Juliette W. Ioup, Long B. Trinh, and Abolfazl M. Amini, paper presented at the fall meeting of the American Geophysical Union, 3-7 Dec 1990, San Francisco, and abstracted in EOS Trans. Amer. Geophysical Union 71, 1282, 1990

THESES

Thesis (M. S. in Physics): Expanded Analysis of Combined Window Spectral Estimate Channel Clearing, James Lester Kreamer, Aug 1988

Thesis (M.S. in Physics): Optimization of Single Filter Application of Always-Convergent Iterative Deconvolution, HaiHong Ni, Aug 1989

Thesis (M. S. in Physics): Least Squares Minimization for Spectral Regions of Combined Lag Windows, Michael Kent Broadhead, Dec 1989

Autocorrelation estimation using constrained iterative spectral deconvolution

Murali Ramaswamy* and George E. Ioup‡

ABSTRACT

Computing an autocorrelation conventionally produces a biased estimate, especially for a short data sequence. Windowing the autocorrelation can remove the bias but at the expense of violating the nonnegativity of the corresponding power spectrum. Constrained iterative deconvolution provides a basis for improving an autocorrelation estimate by reducing the bias while guaranteeing nonnegative definiteness.

The length of the autocorrelation is increased in order to satisfy the nonnegativity constraints on the power spectral estimate. The constraints can also have significant effects on small, poorly determined values of the autocorrelation. The technique is applied to synthetic and real examples to show the improvements in the autocorrelation and power spectrum which are possible.

The method is reasonably stable in the presence of noise and it approximately preserves the area of the power spectrum. Comparison to the maximum entropy technique shows that the iterative method gives power spectral resolution which is sometimes better and sometimes not as good, but that there are cases for which it is the more desirable approach.

INTRODUCTION

Autocorrelation and power spectral estimation are difficult when the segment of data available is of inadequate length. To reduce the variance in the power spectral estimate, autocorrelation windows (Blackman and Tukey, 1958; Geckinli and Yavuz, 1983) or some forms of spectrum averaging are used (Daniell, 1946; Bartlett, 1948; Welch, 1967). Bias in the autocorrelation due to missing lagged products, with more products missing as the lag increases (Cooley et al., 1970), is especially acute for short data segments, since the suggestion of Blackman and Tukey (1958) to use only 10 percent to 20

percent of available lags is no longer practical. Short data sequences are commonly selected in designing filters for non-stationary or shift-variant data so that there will be approximate stationarity or shift invariance within the window. This approach is often taken in processing seismic data.

Maximum entropy (MEM) spectral estimation (Burg, 1975; Kanasewich, 1973) is the technique generally used for obtaining an improved autocorrelation and power spectrum for short data sequences (Jurkevics and Wiggins, 1984). Maximum entropy spectral estimation assumes an autoregressive model for the data. When the method works, it works very well. However, it is sensitive to noise and is unstable for some data types (Lacoss, 1971; Chen and Stegan, 1974). It also does not return a true magnitude for the power spectrum (Lacoss, 1971; Johnson and Anderson, 1978).

In this paper we suggest for improving estimates of autocorrelations and power spectra an alternative approach, which is not very sensitive to noise and assumes only that the data sequence is a truncated portion of a larger data set.

The method begins with a biased estimate. It removes the bias using constrained iterative deconvolution of the power spectrum. If run to convergence, the technique removes almost all the bias. For difficult data however, the iterations may be terminated before all bias is removed. The constraint guarantees the nonnegative definite property of the autocorrelation by keeping the power spectrum nonnegative. The principal effect of the constraint is to extend the autocorrelation beyond the number of lags originally possible, but it can also improve the estimate in the original lag domain and reduce the effects of variance in estimating small autocorrelation values (Yoerger, 1978; Yoerger and Ioup, 1983). The constraints will most affect power spectra which have peaks with valleys near the zero baseline and least affect flat power spectra which rarely approach the zero baseline. For all data, however, the proposed approach (Ramaswamy, 1985) removes the bias in the autocorrelation estimate and sharpens the power spectral estimate; i.e., the bias in the autocorrelation results from deemphasizing the larger autocorrelation lag values, which in turn smooths the spectral estimate.

Manuscript received by the Editor April 7, 1986; revised manuscript received August 15, 1988.

*Shell Western E&P Inc., P.O. Box 4252, Houston, TX 77210-4252 and Department of Physics, University of New Orleans, New Orleans, LA 70148.

‡Department of Physics and Geophysical Research Laboratory, University of New Orleans, New Orleans, LA 70148.

© 1989 Society of Exploration Geophysicists. All rights reserved.

We briefly discuss basic methods for autocorrelation and power spectrum calculations for truncated data sequences to show the bias which is inherent in the resulting estimate (Cooley et al., 1970). We then summarize iterative deconvolution as it is currently practiced in the function domain, show how the technique is applied in the transform domain to improve the autocorrelation estimate, discuss practical considerations, and give some examples.

AUTOCORRELATION ESTIMATION

The autocorrelation of a time sequence $x(t)$ that is N samples long is often defined as (Cooley et al., 1970)

$$b(t) = 1/N \sum_{t'=0}^{N-1} x(t')x(t' - t). \quad (1)$$

The above formulation leads to a biased estimate of the autocorrelation because the number of lagged products going into the estimate of $b(t)$ is a function of t . To correct this effect, the equation is rewritten for an unbiased estimate $u(t)$,

$$u(t) = 1/(N - |t|) \sum_{t'=0}^{N-1} x(t')x(t' - t). \quad (2)$$

Although the above equation results in reduced bias, this form can lead to a violation of the nonnegative definite property of autocorrelations of real sequences, corresponding to the nonnegativity of the power spectrum.

The biased estimate $b(t)$ is related to the unbiased sequence $u(t)$ by the relation

$$b(t) = u(t)w(t), \quad (3)$$

where $w(t)$ is a triangular or Bartlett window of unit peak amplitude at the origin (Cooley et al., 1970). The window can be expressed as

$$w(t) = (N - |t|)/N, \quad -N \leq t \leq N. \quad (4)$$

Uppercase notation is used to represent the transform variables as follows:

$$\begin{aligned} b(t) &\leftrightarrow B(f), \\ u(t) &\leftrightarrow U(f), \end{aligned} \quad (5)$$

and

$$w(t) \leftrightarrow W(f).$$

Applying the convolution theorem (Bracewell, 1978),

$$B(f) = U(f) * W(f), \quad (6)$$

where the asterisk denotes convolution. In performing a straightforward autocorrelation estimation, one chooses between the biased estimate in equation (1) and the unbiased estimate of equation (2). The advantages of the former are that the estimate satisfies the nonnegative definite property and that it deemphasizes the presumably less reliable values at larger lags. Its disadvantage is the same deemphasis, i.e., the bias in the estimate. The unbiased estimate eliminates this bias but sacrifices the nonnegative definite property. The method proposed in this paper eliminates the need to choose between these estimates by removing the bias, subject to satisfaction of the nonnegative definite property; it simultaneously offers estimation capability beyond either of the above approaches.

The problem is to get an estimate of $U(f)$ when $B(f)$ and $W(f)$ are known. $W(f)$ is the function

$$W(f) = 1/N[\sin^2 \pi Nf / \sin^2 \pi f],$$

which for large N becomes

$$W(f) \approx \sin^2 \pi Nf / N\pi^2 f^2 = N \operatorname{sinc}^2 Nf.$$

Therefore, from equation (6), $B(f)$ is a smoothed version of $U(f)$. One way to remove this smoothing effect is to deconvolve $B(f)$. However, deconvolution is not straightforward if we wish to include the nonnegative definite constraint imposed on autocorrelations, which corresponds to a nonnegativity constraint on $U(f)$ (Papoulis, 1962; Robinson, 1980). Also note that deconvolving in the frequency domain produces $u(t)$, which could be computed directly if the nonnegative definite property is ignored.

In this paper a method to mitigate the effect of $W(f)$ on the spectral estimate is proposed through a constrained iterative deconvolution process carried out in the spectral domain.

ITERATIVE DECONVOLUTION

The method of deconvolution using successive substitution (Bracewell and Roberts, 1954; Ioup, 1968; Lacoste, 1982; Ioup and Ioup, 1983; Jansson, 1984) was originally described in the *time domain*. For a function $f(t)$, input to a linear shift invariant system with impulse response $h(t)$, the output $x(t)$ is

$$x(t) = \int f(t')h(t - t') dt' = f(t) * h(t), \quad (7)$$

where the asterisk denotes the convolution operation. Alternatively,

$$X(f) = F(f)H(f), \quad (8)$$

where $X(f)$, $F(f)$, and $H(f)$ are the Fourier transforms of $x(t)$, $f(t)$, and $h(t)$, respectively. The problem of deconvolution is to find $f(t)$, given $x(t)$ and $h(t)$. The principal solution (Bracewell and Roberts, 1954) for $F(f)$ is

$$F(f) = \begin{cases} X(f)/H(f) & \text{for } f: H(f) \neq 0 \\ 0 & \text{for } f: H(f) = 0. \end{cases} \quad (9)$$

Ioup and Ioup (1983) discuss the case when $H(f) = 0$. The van Cittert solution to the problem is stated in the time domain by the following equations:

$$\begin{aligned} f_0(t) &= x(t), \\ f_1(t) &= f_0(t) + \left[x(t) - f_0(t) * h(t) \right], \\ &\vdots \\ f_n(t) &= f_{n-1}(t) + \left[x(t) - f_{n-1}(t) * h(t) \right], \end{aligned} \quad (10)$$

where $f_n(t)$ is an approximation to $f(t)$ which converges to the principal solution in a finite number of iterations. Time-domain constraints can be enforced after each iteration. Ioup and Ioup (1983) and the references cited therein discuss this method in greater detail, and Jansson (1984) gives a very complete development.

APPLICATION TO AUTOCORRELATION ESTIMATION

The van Cittert solution is given in the time domain, whereas spectral estimation requires deconvolution in the frequency domain. In equation (6), $B(f)$ and $W(f)$ are known, and an estimate of $U(f)$ must be computed that is positive at all frequencies. From equation (3),

$$u(t) = b(t)/w(t) \quad (11)$$

The iterative method yields a solution for $U(f)$ given by

$$\begin{aligned} U_0(f) &= B(f) \\ U_1(f) &= U_0(f) + \left[B(f) - U_0(f) * W(f) \right], \\ &\vdots \\ U_n(f) &= U_{n-1}(f) + \left[B(f) - U_{n-1}(f) * W(f) \right]. \end{aligned} \quad (12)$$

To understand these equations and to determine whether they satisfy conditions for convergence, we examine the time-domain equivalents:

$$\begin{aligned} u_0(t) &= b(t) \\ u_1(t) &= u_0(t) + \left[b(t) - u_0(t)w(t) \right], \\ &\vdots \\ u_n(t) &= u_{n-1}(t) + \left[b(t) - u_{n-1}(t)w(t) \right]. \end{aligned} \quad (13)$$

Upon substituting successively, one obtains

$$u_n(t) = b(t) \{ 1 + [1 - w(t)] + [1 - w(t)]^2 + \dots + [1 - w(t)]^n \}. \quad (14)$$

This simple geometric series, which may be summed to give

$$u_n(t) = \{ 1 - [1 - w(t)]^{n+1} \} b(t)/w(t), \quad (15)$$

converges for $|1 - w(t)| < 1$. The definition of $w(t)$ guarantees convergence for all real input sequences except at $t \geq N$, where $w(N) = 0$; and the discussion for zeros in the transfer function applies (Ioup and Ioup, 1983). In the limit as n tends to infinity, the convergent geometric series sums to

$$u(t) = b(t)/w(t). \quad (16)$$

This is precisely the result of the deconvolution [equation (11)]. However, note that for finite n the deconvolution is not perfect but is modified by the van Cittert window [equation (15)].

This general form of iterative deconvolution is what is used for improved autocorrelation and power spectral estimation. One key additional aspect, however, is the application of constraints to equation (12). This is accomplished in an *ad hoc* fashion in that the nonnegativity is simply enforced on each $U_n(f)$ by setting all negative values to zero before beginning the $(n + 1)$ th iteration. The nonnegativity of the spectral estimate is thus ensured.

In addition to the guaranteed nonnegativity, the iterations proceed gradually and can be terminated before too much bias is removed if the large-lag autocorrelation values are unreliable. The constraints mainly affect those values of $u_n(t)$ at

for which $w(t)$ is small or zero. These are the values of the unbiased estimate $u(t)$ which are least reliable.

Also, since $u(0)$ and $b(0)$ represent the area of the power spectral estimates of $U(f)$ and $B(f)$ and since $w(0) = 1$, equation (15) implies that the method preserves area. It is not preserved exactly due to the effects of constraints, truncation, etc.

PRACTICAL CONSIDERATIONS

An important consideration in iterative deconvolution is the growth of the length of the solution with each iteration, since the length of u_n is longer than u_{n-1} by $m - 1$ when there are m samples in $w(t)$. In practice it is necessary to truncate or limit the maximum length of u . For many response functions, only one expansion by convolution is necessary, and the effect of ignoring length expansion in further iterations is negligible (Ioup 1968; Hill, 1973). In some cases it may be necessary to use the neighboring replications of the power spectrum and the window transform natural to the discrete Fourier transform representation. A program to implement this scheme was written and sample functions were tested.

The power spectral estimate is sometimes calculated directly from the square modulus of the discrete Fourier transform (DFT) of the data. Our method may still be applied to deconvolve the power spectrum, but only if the data are extended by at least $(N - 1)$ zeros before calculating the DFT to avoid wraparound in the autocorrelation calculation.

EXAMPLES

The following examples are included to demonstrate the technique. The input sequence was extended by 32 zeros to allow for autocorrelation extension. A 64 point FFT was used in all examples. Half the points in the autocorrelation and FFT represent negative times or frequencies and are not displayed. The sampling rate may be considered to be unity, making the Nyquist frequency 0.5 Hz, and the plots are normalized so that the peak amplitude shown is the maximum ordinate value. The actual peak amplitude observed in the data is indicated on the ordinate of each plot. The increase in peak height which accompanies increased spectral resolution is therefore not readily apparent on the displays although it is indicated numerically on the vertical axes.

Ten iterations were done in each example using the proposed algorithm. The number of iterations needed was not optimized in any way. The noise sequence added to the signal was *approximately white*. It was generated by transforming to time a spectrum of constant amplitude with random phase. Since only a part of this sequence was used, it is not strictly white. The signal-to-noise ratio was set to approximately unity in the examples with noise.

The maximum entropy spectrum was obtained using the method described by Press et al. (1986). The order of the maximum entropy estimate was set to 5, with no attempt made to optimize the order.

The first example is the 20 sample input of Figure 1;

$$\text{Input} = \sin(8\pi t/32) + \text{noise}.$$

The signal-to-noise ratio (S/N) was approximately unity. The steep triangular weighting on the autocorrelation due to the

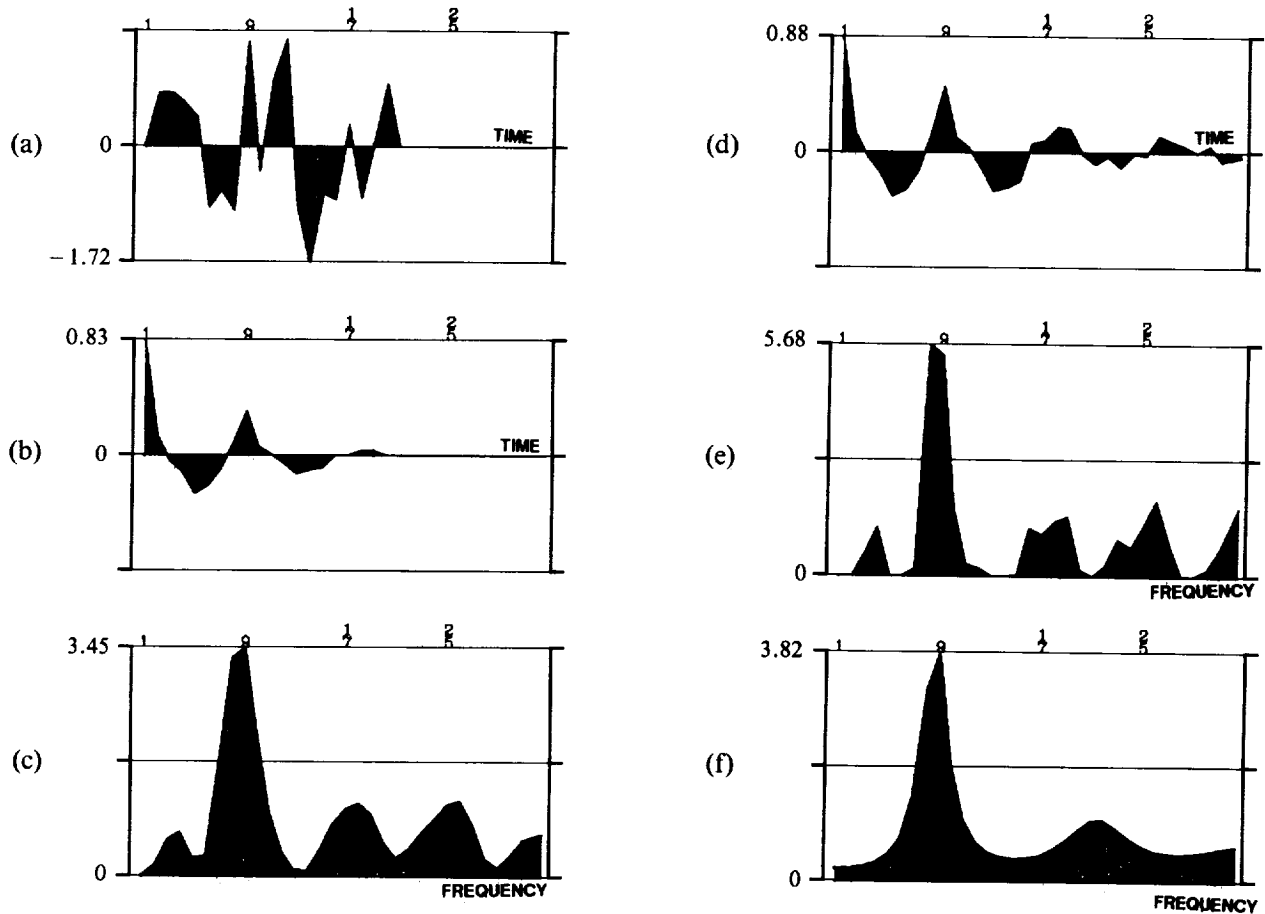


FIG. 1. Single sinusoid with noise. (a) Original data. (b) Conventional autocorrelation. (c) Power spectrum [FT of (b)]. (d) Autocorrelation estimate [inverse FT of (e)]. (e) Spectrum calculated by iterative deconvolution from (c). (f) Maximum entropy power spectrum of (a).

decreased number of terms at higher lag values is apparent. The autocorrelation obtained by iterative deconvolution decays more slowly. The extended part of the autocorrelation seems reasonable in that there is no dramatic change in its characteristics at long lags.

Since the first sample in the spectrum represents $f = 0$, the spectrum should peak at the ninth sample, as occurs in Figure 1c, the conventional spectrum. The iterative method places the peak at the eighth sample but the ninth sample amplitude is very close to the peak amplitude. The MEM spectrum places the peak at the correct sample. The peak amplitude in the MEM spectrum is smaller than that obtained by the iterative method. Side-lobe suppression is better in the MEM spectrum.

As a severe test of the proposed method, a nine-sample sequence was input in Figure 2. The input is $\sin(8\pi t/32)$, a single period of a sinusoid with no noise. Due to the frequency and sampling rate, of the nine sample values, three are exactly zero. The autocorrelation is extended in a reasonable manner to four times its original length, and the spectrum is sharpened by the iterative method. The method gives reasonable results to lags of more than one and one-half times the original autocorrelation length. At subsequent lags, autocorrelation values are small.

Again, one would expect the spectrum to peak at the ninth sample. However both the conventional spectrum and the iter-

ative method peak at the eighth sample. The MEM estimate peaks at the seventh sample. This example was very sensitive to the order of the MEM estimate. Increasing the order from 5 to 7 yielded totally erroneous results.

In Figure 3 the 20 samples comprising the input are obtained from

$$\text{Input} = \sin(0.7 + 7\pi t/32) + \sin(0.9 + 9\pi t/32).$$

In Figures 4a-4f, the same data and calculations are shown for the noise-added case. S/N was once again set to unity. Due to the presence of noise, the expected beating is not very evident in the noisy input Figure 4a, compared to the noise-free input of Figure 3a. Comparison of the noisy autocorrelation Figure 4b to the noise-free autocorrelation Figure 3b, for 20 points of this input, shows that the noise produces mainly modest changes in the autocorrelation amplitudes, except that the first negative lobe is less than half as large as it should be. In addition, noise causes the fourth (at a half-period), fifth, and sixth zero crossings to be delayed. The autocorrelations obtained by iterative deconvolution, Figures 3d and 4d, on the other hand, resemble much more the autocorrelation of 34 samples of the original function, shown in Figure 3h, with a reduction in amplitudes at larger lags. The noise-free iterative deconvolution result in Figure 3e has all zero crossings in agreement with Figure 3h out to the 28th lag, except for the

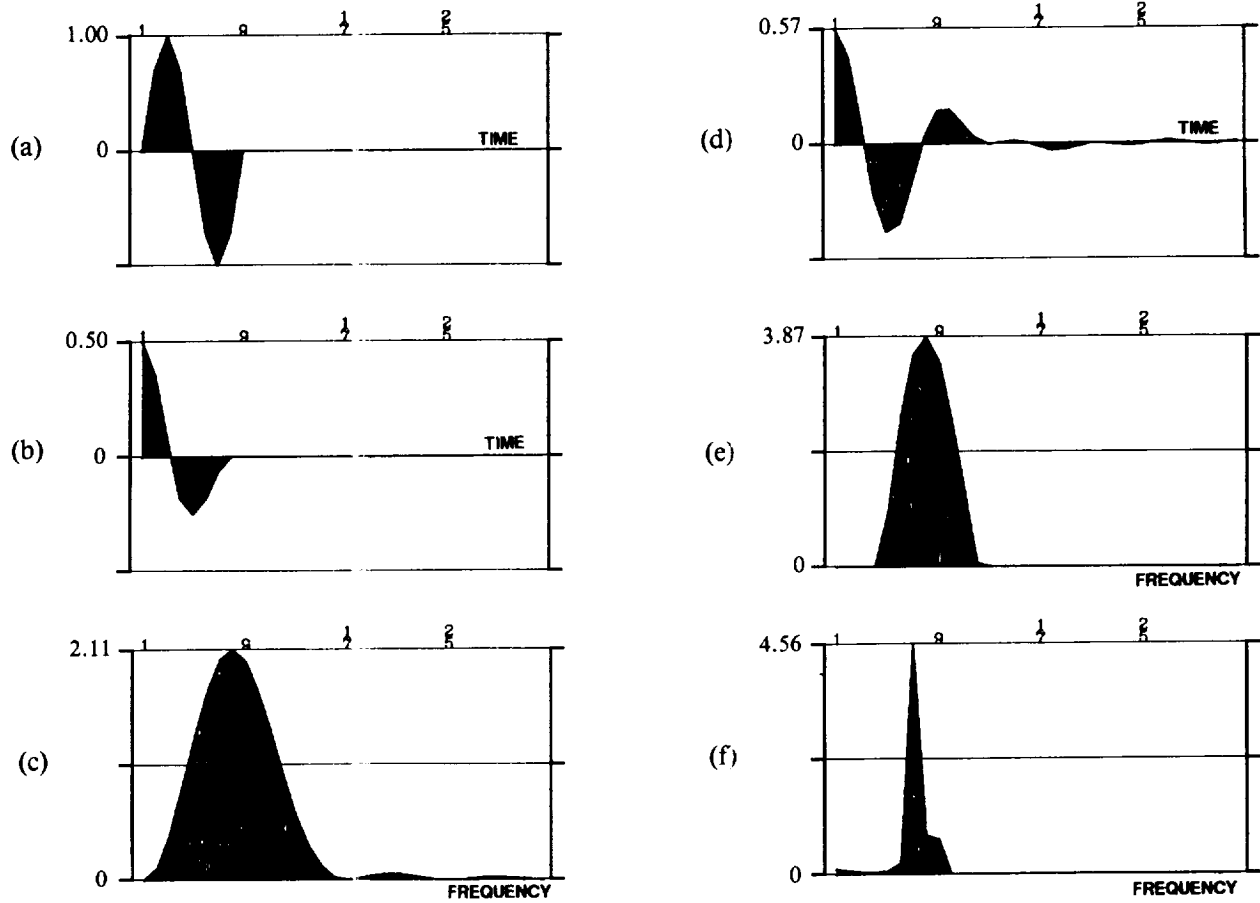


FIG. 2. Single sinusoidal wavelet. (a) Original data. (b) Conventional autocorrelation. (c) Power spectrum [FT of (b)]. (d) Autocorrelation estimate [inverse FT of (e)]. (e) Spectrum calculated by iterative deconvolution from (c). (f) Maximum entropy power spectrum of (a).

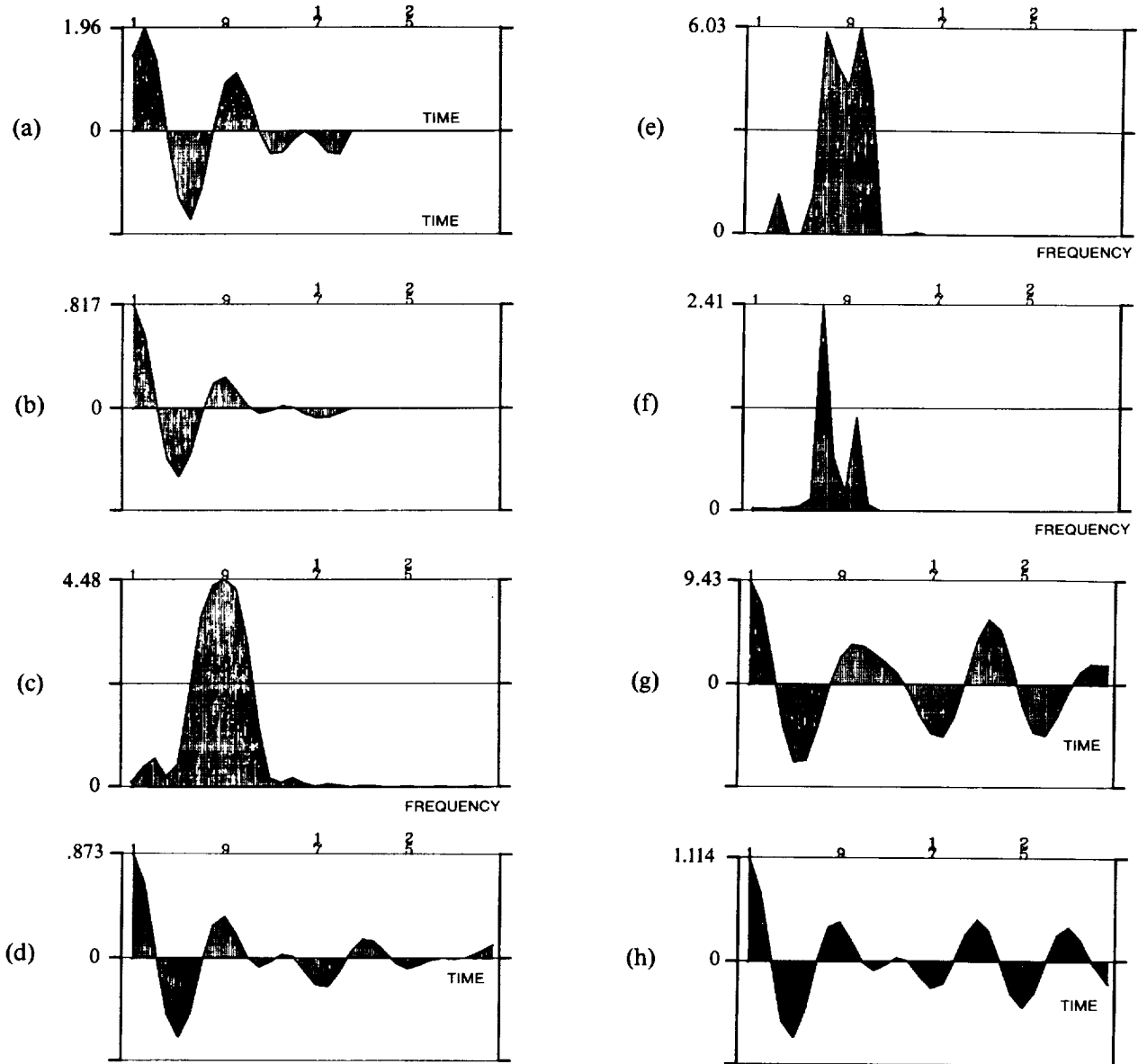


FIG. 3. Two sinusoids. (a) Original data. (b) Conventional autocorrelation. (c) Power spectrum [FT of (b)]. (d) Autocorrelation estimate [inverse FT of (e)]. (e) Spectrum calculated by iterative deconvolution from (c). (f) Maximum entropy power spectrum of (a). (g) Autocorrelation calculated from (f). (h) First 32 autocorrelation lags using 34 samples of the two sinusoids.

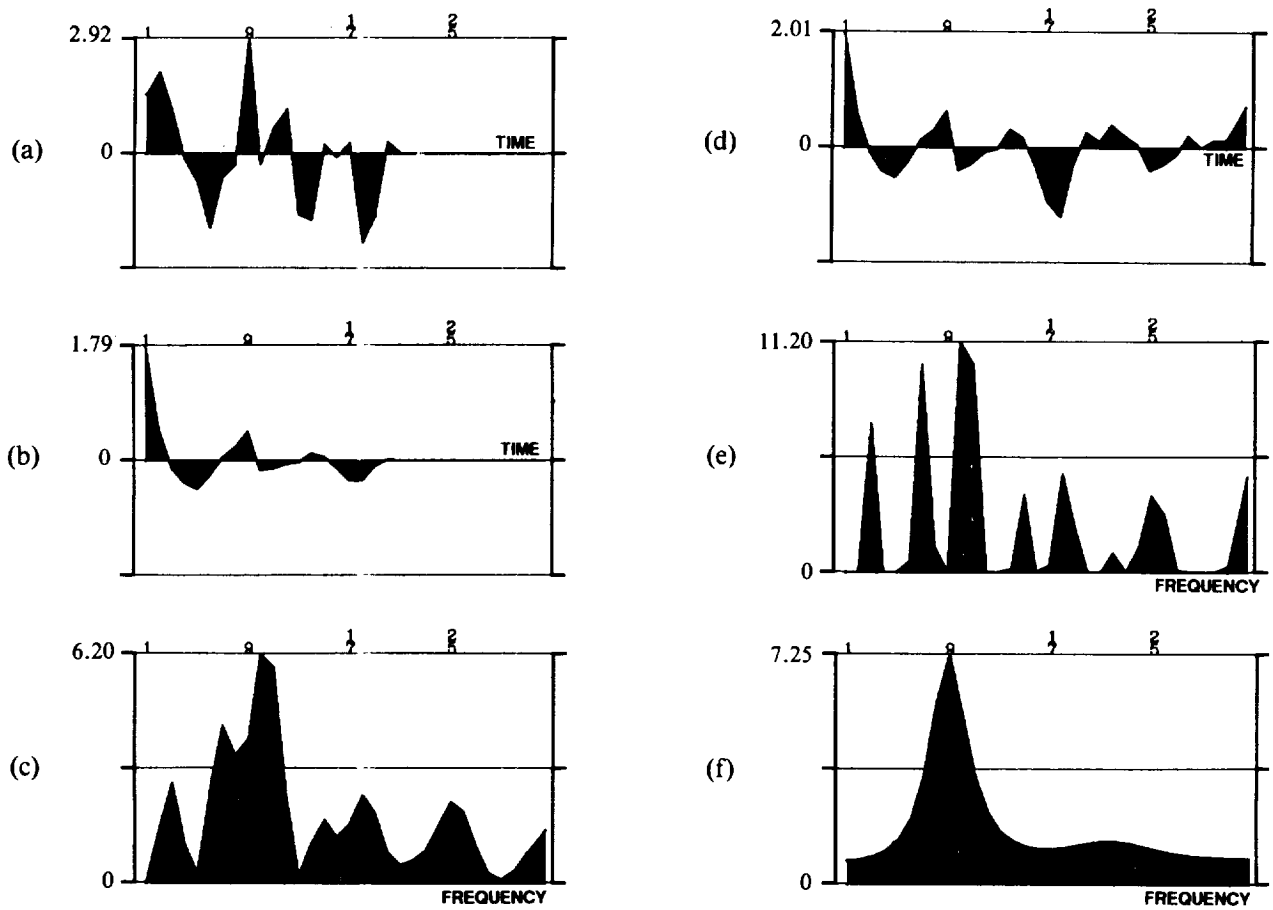


FIG. 4. Two sinusoids with noise. (a) Original data. (b) Conventional autocorrelation. (c) Power spectrum [FT of (b)]. (d) Autocorrelation estimate [inverse FT of (e)]. (e) Spectrum calculated by iterative deconvolution from (c). (f) Maximum entropy power spectrum of (a).

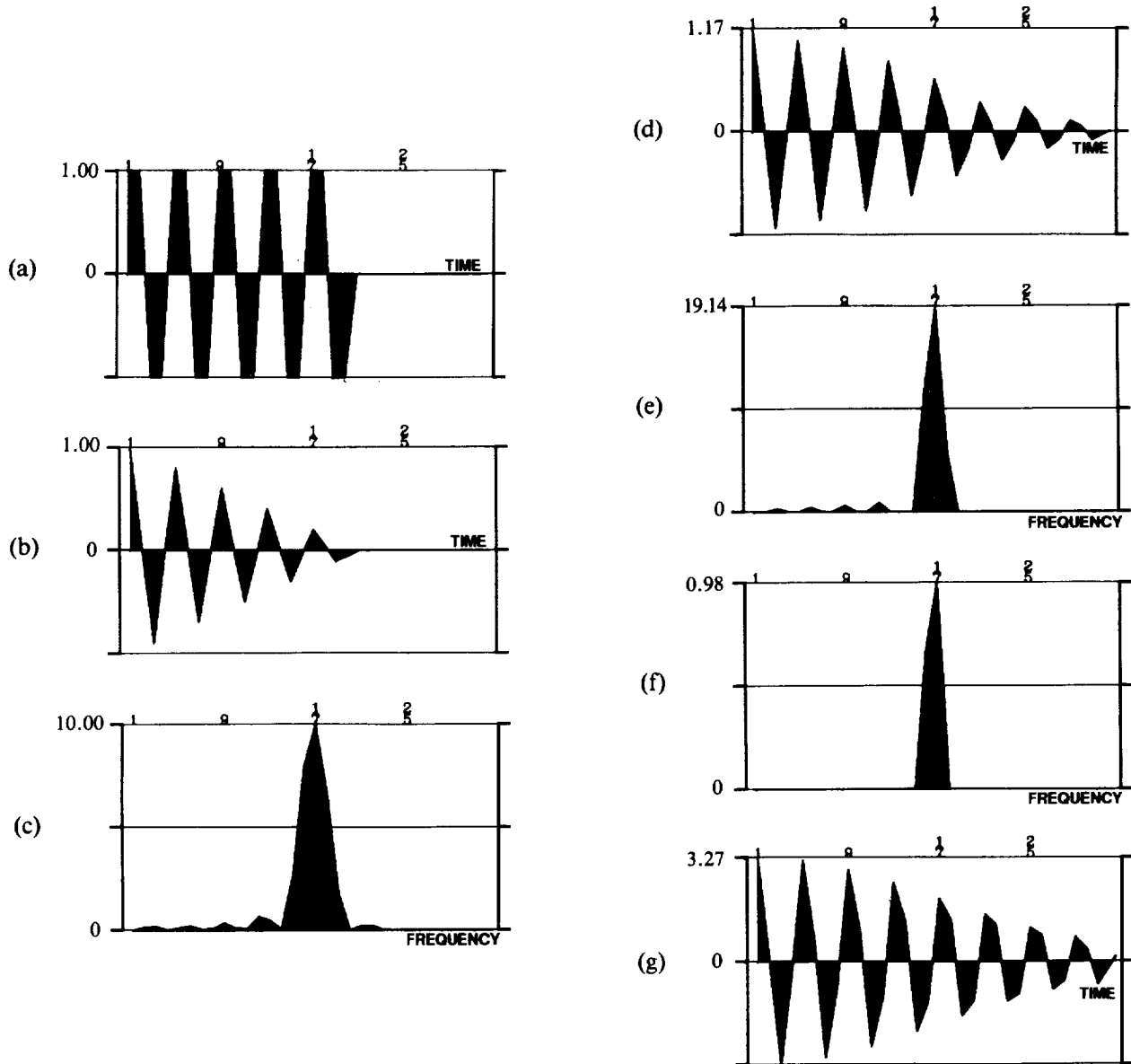


FIG. 5. Square wave example. (a) Original data. (b) Conventional autocorrelation. (c) Power spectrum [FT of (b)]. (d) Autocorrelation estimate [inverse FT of (e)]. (e) Spectrum calculated by iterative deconvolution from (c). (f) Maximum entropy power spectrum of (a). (g) Autocorrelation calculated from (f).

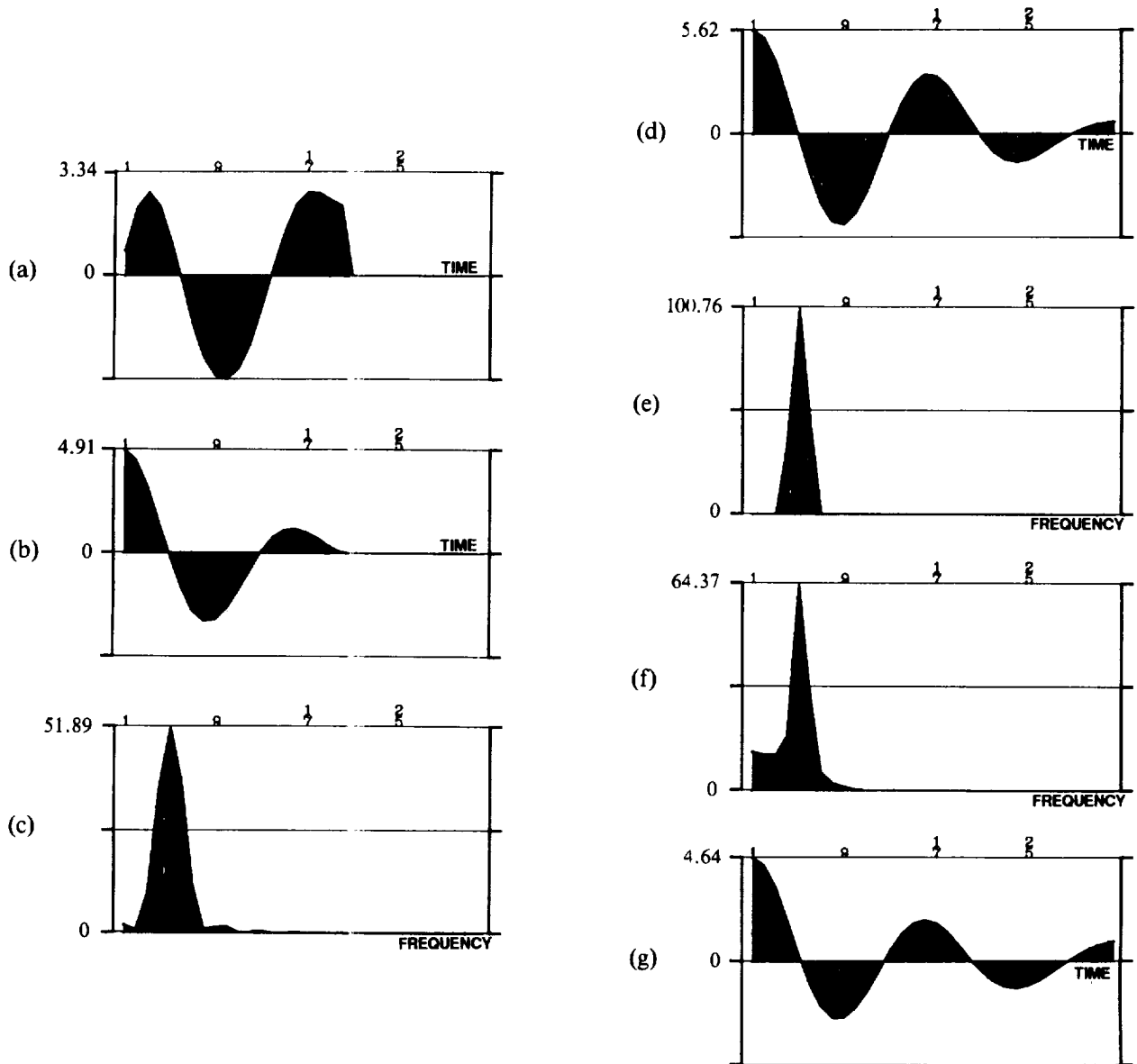


FIG. 6. Deconvolved prestack seismic data example. (a) Original data (b) Conventional autocorrelation. (c) Power spectrum [FT of (b)]. (d) Autocorrelation estimate [inverse FT of (e)]. (e) Spectrum calculated by iterative deconvolution from (c). (f) Maximum entropy power spectrum of (a). (g) Autocorrelation calculated from (f).

sixth and seventh zero crossings which are slightly delayed. In Figure 4e, the noise has caused the following changes from the noise-free Figure 3e result. There are modest changes in relative amplitude at several points and major changes in the first negative lobe, which is approximately one-third as large as it should be relative to the peak, and in the third negative lobe which is more than twice as large as it should be. The zero crossings agree, except for the third, which is advanced. In the noise-free case one may say that the autocorrelation of 20 lags of the function has been extended to good approximation to the first 28 lags of the autocorrelation of 34 lags of the function by the deconvolution. Even when large amounts of noise are present, the extension can still be useful. The maximum entropy noise-free result, Figure 3g, does not resemble any of the extended autocorrelations considered by the authors, up to 40 sample points of input data.

Using the conventional spectrum the two sinusoids are better resolved in the noisy data (Figure 4c) than in the noise-free data (Figure 3c), but this is an accidental effect of the noise. The noise-free iterative deconvolution spectrum (Figure 3e) partially resolves two peaks of approximately the same height. Further resolution could have been obtained by using more iterations. The maximum entropy spectrum in Figure 3f resolves the peaks even better, but the peak heights and areas are very different even though the input sinusoids are of equal strength. For the noisy spectra, the iterative technique resolves the peaks completely (Figure 4e) with the same number of iterations as in Figure 3e. Again this is accidental and due to noise. The important point is that the noise in the conventional spectrum (Figure 4c) has not been amplified relative to the main peaks by the deconvolution process. In the maximum entropy spectrum for the noisy data, Figure 4f, there is only one peak and the two sinusoids have not been resolved.

A 20 sample symmetric square wave with a 4 time sample period is considered in Figure 5. The conventional autocorrelation is triangular. The autocorrelation obtained by iterative deconvolution has been extended in a manner that more closely resembles the autocorrelation of an infinite length square wave; there is some distortion apparent at large lags. In order to preserve the characteristics of the triangular wave autocorrelation, frequencies other than the dominant or fundamental frequency, represented by sample 17 on the plots, must be present in the spectrum. This is seen in both the conventional and the modified spectra. The MEM method has resolved the dominant frequency, but other frequencies and harmonics are suppressed. The resulting autocorrelation is not quite as triangular as one would expect. In this example, MEM is perhaps not the most appropriate method.

An example of real seismic data is presented in Figure 6. The input consists of the 20 samples of deconvolved prestack data; the peak of the conventional spectrum occurs at the fifth sample. It is apparent that although very few low-frequency components are present in the conventional spectrum, the maximum entropy method estimates a sizeable low-frequency component. Our method does not have this disadvantage.

Since bias removal should increase autocorrelation amplitudes, we expect increased amplitudes for the iterative deconvolution (Figure 6e) and maximum entropy (Figure 6g) estimates compared to the conventional result (Figure 6b). Although both estimates show increases, the amplitudes of Figure 6e are greater, suggesting the iterative deconvolution

approach performed better. Also, both methods extend the autocorrelations in a reasonably consistent fashion.

EVALUATION

Sometimes the iterative deconvolution spectrum is not as peaked as the one obtained from maximum entropy. The constraints that lead to autocorrelation extension have the most effect at spectral valleys or notches that approach the zero baseline of the spectrum. If the spectrum that is input to the proposed method is flat and does not have notches in the spectrum, the constraints would be less effective.

However, the experience of the authors indicates that the iterative method of autocorrelation and spectral estimation has the following advantages over the maximum entropy method: The iterative method does not assume an autoregressive model for the input data as does the MEM. The iterative technique proposed is fairly insensitive to noise. This insensitivity results from the technique's attempting to improve the conventionally obtained spectrum through a gradual and stable iterative process. The maximum entropy method can result in a very different spectrum upon the addition of noise to the input. The maximum entropy method is sensitive to the order of the estimate. To do a reasonable job, some criteria (like Akaike's criteria) must be applied. This implies running diagnostics prior to computing the final MEM estimate. The iterative method could be applied in a hands-off fashion to sharpen the conventional spectral estimate. The peak frequency in the maximum entropy method can err by one sample and may have incorrect relative and absolute amplitudes. The iterative method appears to suffer from this problem to a lesser extent.

CONCLUSIONS

The iterative method cannot extend the autocorrelation indefinitely. The method's ability to extend the autocorrelation results from nonnegativity constraints on the spectrum. Since the unconstrained iterative deconvolution is a linear process, it cannot add new lag values to the autocorrelation.

In estimating the autocorrelation with the iterative method, the effect of the window used to produce the unbiased estimate is reduced, and the window is gradually made rectangular as the iterations proceed. The autocorrelation is extended as necessary in order to maintain a nonnegative spectrum at the end of every iteration. The smaller values of the autocorrelation corresponding to the smaller values of the triangular window can also be affected by the nonnegativity constraint more than the large values.

Naturally, there are no right or wrong answers when estimating power spectra (or autocorrelations) from short data sequences. Rather, the recorded data are assumed to be a segment of a larger sequence, and the ultimate issue is whether the model which generates the estimate is the same as that which generated the data.

Finally, since the method is recommended primarily for short data sequences, computer cost is not a major consideration.

ACKNOWLEDGMENTS

The authors thank the management of Shell Western Exploration and Production Inc. for their support. They are also deeply grateful to the Editor for his assistance in improving the manuscript.

REFERENCES

- Bartlett, M. S., 1948, Smoothing periodograms from time series with continuous spectra: *Nature*, **161**, 666-668.
- Blackman, R. W., and Tukey, J. W., 1958, *The measurement of power spectra*: Dover Publ. Inc.
- Bracewell, R. N., and Roberts, J. A., 1954, Ariel smoothing in radio astronomy: *Austral. J. Phy.*, **7**, 615-640.
- Bracewell, R. N., 1978, *The fast Fourier transform and its applications*: McGraw-Hill, 2nd ed.
- Burg, J. P., 1975, *Maximum entropy spectral analysis*: Ph.D dissertation, Stanford Univ.
- Chen, W. Y., and Stegan, G. R., 1974, Experiments with maximum entropy power spectra of sinusoids: *J. Geophys. Res.*, **79**, 3019-3022.
- Cooley, J. W., Lewis, P. A. W., and Welch, P. D., 1970, The application of the fast Fourier transform to the estimation of spectra and cross spectra: *J. Sound Vibration*, **12**, 339-352.
- Daniell, P. J., 1946, Discussion on symposium on autocorrelation in time series: *J. Roy. Statis. Soc.*, **8**, 88-90.
- Geckinli, N. C., and Yavuz, D., 1983, *Discrete Fourier transformation and its application to power spectra estimation*: Elsevier Scientific Publ. Co.
- Hill, N. R., 1973, *Deconvolution for resolution enhancement*: M.S. thesis, Univ. of New Orleans.
- Ioup, G. E., 1968, *Analysis of low energy atomic and molecular collisions: Semi-classical elastic scattering calculations and deconvolution of data*: Ph.D dissertation, Univ. of Florida.
- Ioup, G. E., and Ioup, J. W., 1983, Iterative deconvolution: *Geophysics*, **48**, 1287-1290.
- Jansson, P. E., 1984, *Deconvolution with applications in spectroscopy*: Academic Press Inc.
- Johnson, S. J., and Anderson, N., 1978, On power estimation in maximum entropy spectrum analysis: *Geophysics*, **43**, 681-690.
- Jurkevics, A., and Wiggins, R., 1984, A critique of seismic deconvolution methods: *Geophysics*, **49**, 2109-2116.
- Kanasewich, E. R., 1973, *Time sequence analysis in geophysics*: Univ. of Alberta Press.
- Lacoss, R. T., 1971, Data adaptive spectral analysis methods: *Geophysics*, **36**, 661-675.
- Lacoste, L. J. B., 1982, Deconvolution by successive approximations: *Geophysics*, **47**, 1724-1730.
- Papoulis, A., 1962, *The Fourier integral and its applications*: McGraw-Hill Book Co.
- Press, W. H., Flannery, B. P., Deukolsky, S. A., and Vetterling, W. T., 1986, *Numerical recipes: The art of scientific computing*: Cambridge Univ. Press.
- Ramaswamy, M., 1985, *Autocorrelation estimation using iterative spectral deconvolution*: M.S. Thesis, Univ. of New Orleans.
- Robinson, E. A., 1980, *Physical applications of stationary time series*: Macmillan.
- Welch, P. D., 1967, The use of fast Fourier transform for the estimation of power spectra: a method based on time averaging over short, modified periodograms: *Inst. Electr. Electron. Eng., Trans. Audio Electroacoust.*, **AU-15**, 70-73.
- Yoerger, E. J., 1978, *Application of iterative smoothing and deconvolution to two-dimensional images*: M.S. thesis, Univ. of New Orleans.
- Yoerger, E. J., and Ioup, G. E., 1983, Frequency domain shaping of ad hoc constraint corrections in iterative deconvolution: *J. Opt. Soc. Am.*, **73**, 1875.



1,
2,

Computers and Experiments in Stress Analysis

Proceedings of the fourth International Conference
on Computational Methods and Experimental
Measurements, Capri, Italy, May 1989

Editors:
G.M. Carlomagno
C.A. Brebbia

Computational Mechanics Publications
Southampton Boston

Springer-Verlag Berlin Heidelberg
New York London Paris Tokyo

**Enhanced Data from Analytical Instrumentation by
Deconvolution of Periodically Sampled Signals**

George E. Ioup*, Juliette W. Ioup*, Abolfazl Amini*,
Grayson H. Rayborn**, Dong Wang** and George M.
Wood***

**Department of Physics, University of New Orleans, New Orleans, LA 70148, USA*

***Department of Physics and Astronomy, University of Southern Mississippi, Hattiesburg, MS 39406-5046 USA*

****Instrument Research Division, NASA Langley Research Center, Hampton, VA 23665, USA*

ABSTRACT

Information contained in data that is in the form of a series of more-or-less resolved peaks is often unobtainable due to the limitations in resolution or response of the instrument. Adjusting the instrumental operating parameters to increase resolution usually has the effect of also decreasing the sensitivity and the signal-to-noise ratio, making detection of small signals difficult. If a mathematical representation of a shift invariant instrument response function that describes the broadening effect on the input can be defined, then it is possible by deconvolution to restore the resolution to some degree. This process is represented by the solution of the convolution integral, which is achieved for many common data types through the use of iterative or Fourier transformation techniques. Although deconvolution techniques are becoming widely used, particularly in spectroscopic, acoustic, astronomical, and geophysical applications, and appear to be straightforward, care must be exercised to prevent the generation of spurious peaks which may be interpreted as being real data. This is particularly true when the higher frequencies in the Fourier transform are important in recovering the information. This paper describes both iterative and Fourier techniques developed in the course of on-going studies of the deconvolution process, and discusses some of the pitfalls which should be avoided. Results of recent research in optimizing iterative techniques and instrumentation for deconvolution applications, and for evaluating and optimizing the efficacy of different methods of deconvolution for detecting peaks in specific classes of noisy data are also discussed.



Enhanced Data from Analytical Instrumentation by Deconvolution of Periodically Sampled Signals

George E. Ioup, Juliette W. Ioup, Abolfazl Amini

Department of Physics, University of New Orleans, New Orleans, LA 70148 USA

Grayson H. Rayborn, Dong Wang

Department of Physics and Astronomy, University of Southern Mississippi, Hattiesburg, MS 39406-5046 USA

George M. Wood

Instrument Research Division, NASA Langley Research Center, Hampton, VA 23665 USA

ABSTRACT

Information contained in data that are in the form of a series of more-or-less resolved peaks is often unobtainable due to the limitations in resolution or response of the instrument. Adjusting the instrumental operating parameters to increase resolution usually has the effect of also decreasing the sensitivity and the signal-to-noise ratio, making detection of small signals difficult. If a mathematical representation of a shift invariant instrument response function that describes the broadening effect on the input can be defined, then it is possible by deconvolution to restore the resolution to some degree. This process is represented by the solution of the convolution integral, which is achieved for many common data types through the use of iterative or Fourier transformation techniques. Although deconvolution techniques are becoming widely used, particularly in spectroscopic, acoustic, astronomical, and geophysical applications, and appear to be straightforward, care must be exercised to prevent the generation of spurious peaks which may be interpreted as being real data. This is particularly true when the higher frequencies in the Fourier transform are important in recovering the information. This paper describes both iterative and Fourier techniques developed in the course of on-going studies of the deconvolution process, and discusses some of the pitfalls which should be avoided. Results of recent research in optimizing iterative techniques and instrumentation for deconvolution applications, and for evaluating and optimizing the efficacy of different methods of deconvolution for detecting peaks in specific classes of noisy data are also discussed.

INTRODUCTION

When instruments are used in the analytical sense, the data are typically obtained by periodically sampling the magnitude of the dependent variable. The independent variable is most often time, but may be frequency, position, mass, wavelength, wave number,



or any other parameter as well. The sensitivity of such an instrument is defined to be the smallest increase in the intensity of the signal representing the magnitude of the dependent variable that can be measured, with the detection limit being the smallest measurable signal that appears above instrument background and noise. The resolution or resolving power is the smallest increment in the independent variable that can be identified in the output and is therefore a measure of the ability to detect changes in the parameter being measured.

The resolving power for a particular instrument is determined by the frequency response of the detection and recording circuitry and other factors influencing the output signal that represents a change in input. This is referred to as instrumental broadening, but in addition to the instrument response, it actually includes any parameters that affect the overall response of the system as well. Examples of these other sources are the interface between a sensor and the system upon which the measurement is being performed, mechanical or electronic limitations on the rate at which the independent variable can be scanned, and the presence of fundamental or environmental noise. Fundamental noise is that arising from the physics of the measurement process itself, while environmental noise results from externally imposed influences. With care, the latter can be made arbitrarily small, but fundamental noise has a limit below which it cannot be further reduced, therefore imposing a lower limit on detectability. The situation is, therefore, that a change in the input parameter is represented by an output signal whose response is dictated by the effects of instrumental broadening. Whenever these changes are slow or when only first order approximations are required, the signal obtained will represent adequately the variations in input. However, in many cases, valuable information is not observed or obtainable due to the broadening effects.

Signal averaging or differentiation are both useful techniques to improve the resolving power of the instrument. The most effective computational method is deconvolution which, however, is mathematically difficult to apply in that it tends to amplify noise and has other difficulties. In some cases deconvolution will result in spurious peaks that may be interpreted as being real if not carefully examined. When properly applied, however, deconvolution of the signal can yield an improved resolution, often much greater than can be obtained by careful tuning of the instrument or otherwise enhancing the signal, and sometimes even exceeding the theoretical limit of the resolving power. The improvement in resolution is determined in part by how accurately the response function (impulse response) can be determined for each point at which the deconvolution is to be carried out, and how completely the effect of noise can be addressed.

If the instrument response does not change appreciably while the measurement is being carried out, the response is called "shift invariant," and the relationship between the observed signal $h(x)$ and the input (or ideal) signal $f(y)$ is defined by the convolution integral

$$h(x) = \int_{-\infty}^{+\infty} f(y) g(x-y) dy = f * g \quad , \quad (1)$$

where g is the response function representing the broadening effects. The discrete form of this equation is given by

$$h_i = \sum_{j=-\infty}^{\infty} f_j g_{i-j} = f * g \quad (2)$$

Complete discussions of deconvolution and reviews of many of the techniques are given by Frieden,⁸ Robinson and Treitel,¹⁴ Mendel,²⁹ and Jansson.²²

In this paper a background in basic Fourier deconvolution is summarized, and mention is made of newer Fourier transform techniques which improve upon it. The source of sidelobes is discussed as well as why deconvolution generally amplifies noise and is therefore ill-conditioned. A review of iterative deconvolution techniques is given including recent developments. Examples of the pitfalls due to sidelobes and noise are presented. The optimization of iterative techniques is discussed as well as a new method for evaluating different deconvolution methods for their ability to detect true peaks and reject false peaks.

FOURIER DECONVOLUTION

Fourier deconvolution proceeds directly from the Convolution Theorem.⁵ This theorem holds that if $h(x)$ is the convolution of $f(x)$ and $g(x)$ as in Equations (1) or (2), then $H(s)$, the Fourier transform of $h(x)$, is the product of the Fourier transforms of $g(x)$ and $f(x)$:

$$H(s) = F(s) G(s) \quad (3)$$

As long as $G(s)$ is unequal to zero the transform of the ideal function $f(x)$ can be recovered by division, but when the experiment fails to transmit frequencies that are present in the ideal function, that is, $G(s)$ is zero for frequencies s for which $F(s)$ is not zero, information about $f(x)$ contained in these frequencies is lost, and $f(x)$ can not be perfectly restored. Bracewell and Roberts⁶ suggest that an initial approach in such cases might be to define a principal solution $F_p(s)$, an approximation to the transform of the ideal function, whose value is zero whenever $G(s)$ is zero. Thus,

$$F_p(s) = \begin{cases} H(s)/G(s) & (s:G(s) \neq 0) \\ 0 & (s:G(s) = 0) \end{cases} \quad (4)$$

The approximation to the ideal function, $f_p(x)$, is then obtained by taking the inverse transform of $F_p(s)$, and the process by which this resolution enhanced solution is obtained is called simple inverse filtering.

The loss of information about $F(s)$ at frequencies for which $G(s)=0$ often creates unwanted characteristics in the approximation $f_p(x)$. In many experiments the transform of the response function is non-zero (except perhaps at a few isolated points) for all frequencies below a certain critical "cut-off" frequency s_c and zero above this frequency. In these cases $F_p(s)$ is truncated. This usually gives rise to spurious peaks (Gibbs oscillations) which are not present in $f(x)$ and greatly complicates the interpretation of spectra enhanced by simple inverse filtering.

As the Convolution Theorem clearly shows, the transform of the measured function, $H(s)$, should be zero at values of s for which $G(s)$ is zero. Noise at these frequencies cannot have been transmitted through the system and is therefore called incompatible

noise.³⁰ Noise at frequencies s for which $G(s)$ is not zero is called compatible noise. Incompatible noise can be removed by bandpass filtering without further loss of information before Fourier deconvolution if $G(s)$ is known. Compatible noise which is present at frequencies for which $G(s)$ is small is an additional serious obstacle to accurate resolution enhancement by simple inverse filtering. Filtering which reduces or removes compatible noise necessarily forfeits part of the signal, and information needed for the accurate restoration of $f(x)$ is lost. In particular, noise tends to be more important at high frequencies so that low-pass filtering which decreases the bandpass of the approximation to the transform of the ideal function broadens the function itself, thereby partially tending to defeat the purpose of resolution enhancement.

For additive noise, the principal solution has the form $F_p(s) = [H(s) + N(s)]/G(s)$, where $N(s)$ is the transform of the noise. The example shown in Figure 1 includes plots of sample $|H(s)+N(s)|$ and $|G(s)|$ functions and the resulting $|F_p(s)|$, which is the noisy $F(s)$ truncated at the cutoff of $G(s)$. As the cutoff frequency is approached from below and $G(s)$ becomes smaller, the magnitude of N may exceed that of H , and hence noise predominates and is amplified by the deconvolution. In this case, the high frequency component of the transform domain spectrum is often deleted, a process defined as "low-pass inverse filtering." This reduces the effect of the noise but does not eliminate the Gibbs oscillations and it decreases the resolution as discussed above. (The application of a taper (window) to the transform can reduce these oscillations.²⁸)

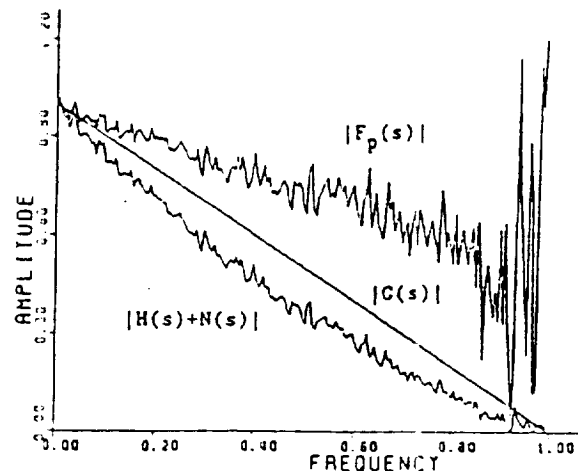


Figure 1. The magnitude of the Fourier transform of the principal solution for the transform of noisy measured data. $|H(s)+N(s)|$ is the magnitude of the transform of the noisy data. The magnitude of the transform of the impulse response is labeled $|G(s)|$. Simple inverse filtering yields a transform with magnitude $|F_p(s)|$.

A number of techniques have been developed to improve inverse filtering by restoring the lost resolution and correcting its tendency to create spurious peaks while controlling the effects of noise. Many of these methods use constraints to incorporate special knowledge of the ideal function into the deconvolution process. Deconvolution constrained to produce an approximation to the ideal function $f(x)$ that has as little negativity as possible,^{12 13 14} frequently referred to as either Minimum Negativity or the Howard extrapolation, is an example of this approach to deconvolution. A similar method was also developed by Gerchberg.⁹ Many experiments produce measurements of intensities which can be either positive or zero, but for which negative values can be created only by unwanted noise or sidelobes from deconvolution. Howard uses the minimum negativity constraint to extend the frequency spectrum of a deconvolved function expected to be positive by retaining initially only a small number of the lowest Fourier coefficients and restoring the lost coefficients one at a time so that each



successive coefficient produces an approximation to $f(x)$ that minimizes the sum of the squares of the negative values of the previous approximation.

The minimum negativity constraint has been applied to microwave spectra by Howard, extending the spectrum of $h(x)$ that has been curtailed by the measuring spectrometer. L. Wang and Rayborn³⁸ have extended the principle of minimum negativity directly to the deconvolution process itself, forming $F_p(s)$ and using the principle of minimum negativity to extend $F_p(s)$ beyond the cut-off frequency by first making $f_p(x)$ an even function.

Another technique for restoring the spectrum of a function truncated in deconvolution is to approximate the high frequency spectrum which has been truncated in deconvolution with the high frequency spectrum of a function of the expected shape.^{41 21} This method for extending the bandwidth uses simple inverse digital filtering to establish the size and location of peaks in the output of a laboratory spectrometer. The ideal peak shape for the instrument is determined either from a theoretical understanding of its performance or by experimental study and observation of an isolated peak. An artificial function is then formed by superposition of peaks of ideal shape of the sizes and at the locations determined by the inverse filtering. The Fourier transform of the artificial function is taken and the high frequency portion of this spectrum is extracted and used to replace the high frequency portion of the spectrum of the inverse filtered function which was truncated either naturally by the low bandpass of the spectrometer or deliberately because of the presence of noise at the high frequencies. Extending the Fourier spectrum in deconvolution by splicing the high frequency spectrum of an artificial function has been found to decrease the size of sidelobes created by inverse digital filtering by up to about 50 percent.

ITERATIVE DECONVOLUTION

One of the commonly used approaches to deconvolution is an iterative one, first proposed in its simplest form by van Cittert in 1931.³⁵ Excellent reviews are given by Frieden⁸ and Jansson.²² G. Ioup and J. Ioup¹⁷ summarize additional literature. The form of the van Cittert iterations is as follows:

$$\begin{aligned}
 f_1 &= h + (h - h * g) \\
 f_2 &= f_1 + (h - f_1 * g) \\
 &\vdots \\
 &\vdots \\
 f_n &= f_{n-1} + (h - f_{n-1} * g)
 \end{aligned}
 \tag{5}$$

The gradual nature of the iterations causes a controlled simultaneous increase in resolution and noise, allowing a compromise to be determined by the selection of iteration number. Because the iterations are accomplished in the function or time domain (as opposed to the Fourier transform domain), function domain constraints can be applied easily in an ad hoc fashion at each iteration. If the signal-to-noise ratio of the experimental data is low and more noise control is needed than that provided by the van Cittert iterations, an iterative noise removal technique proposed by Morrison,^{30 15 17 25 26} applied before the deconvolution, can give additional noise control.

The convergence conditions for the Morrison and van Cittert iterations are well established.^{9 16 10 11 8 17} There are many analytically and experimentally determined response functions for which the iterations do not converge. A modification of the deconvolution iteration called the reblurring or mirror image procedure which converges for any initial response function has been developed by Kawata and Ichioka²³ and independently by LaCoste.²⁴ Jansson²² gives background information and a discussion. An alternative always-convergent iterative noise removal and deconvolution technique was given by G. Ioup¹⁸ and applied to two-dimensional data by Whitehorn³⁹ and Whitehorn and G. Ioup.⁴⁰

One of the principal objections to the use of the iterative approach to deconvolution is the fact that it can be very slow for long data sets and impulse responses or for wide impulse responses. To overcome this problem the research group at the University of New Orleans has been investigating accelerated iterations and single filter application of the iterations in the Fourier transform domain.^{3 31} The single filter application is based on the transform domain representation of the iterations. The last of Equations (5) may be written in the transform domain as:

$$F_n = F_{n-1} + (H - F_{n-1}G) \quad (6)$$

By successive substitutions one may solve for F_n in terms of G and H to obtain

$$F_n = [1 - (1 - G)^{n+1}]H/G \quad (7)$$

Similar results have been obtained for Morrison's noise removal¹⁵ and the newer convergent iterative techniques of noise removal and deconvolution.^{39 40 18} Use of the so-called van Cittert or equivalent window makes possible the accomplishment of many iterations as a single filter. Because multiple convolutions imply expansions of the duration of the solution function in its independent variable, there is a possibility for serious wraparound error.³² Amini et al.³ and Ni et al.³¹ have shown that for many experimental data types wraparound error is negligible.

PITFALLS

Examples of effects on deconvolution of Gibbs oscillations and noise clarify the difficulties of the deconvolution process. Figure 2 contains the results of two approaches to deconvolution for mass spectrometric analysis of a gas containing oxygen and methane.²¹ Simple inverse filtering (not shown) gives large sidelobes which are the Gibbs oscillations. The irregular nature of these oscillations is due to the interference of the sidelobe patterns of the two main peaks. The artificial function approach (Curve B) reduces the spurious peaks somewhat but does not eliminate them. Iterative noise removal followed by iterative deconvolution with a nonnegativity constraint included gives Curve A. Because deconvolution with a normalized impulse response should preserve areas, the elimination of the negative spurious lobes by the use of a constraint reduces the positive lobes as well.²¹ Since the interference of the Gibbs oscillations due to the presence of two main peaks causes the adjacent positive and negative sidelobe areas to differ from each other, the area cancellation is incomplete and two small positive lobes remain after iterative deconvolution at mass to charge 16.0559 and 16.0963. These might be interpreted as small additional mass peaks if one is not aware of this pitfall and the need for careful analysis.

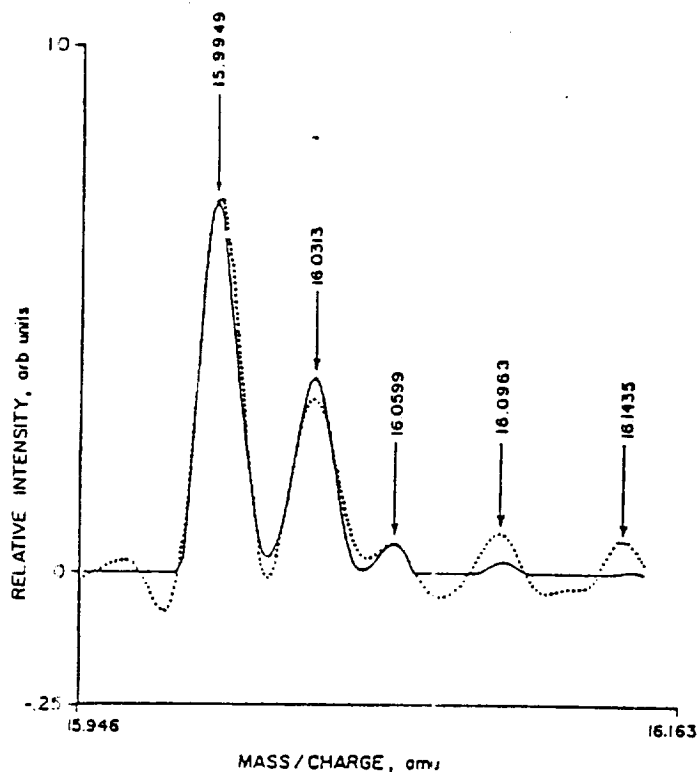


Figure 2. The deconvolution of the mass spectrometer analysis of a mixture of oxygen (mass 15.9949) and methane (mass 16.0313). Curve A: 30 noise removal and 50 deconvolution iterations. Curve B: function-continuation Fourier deconvolution.

Figures 3 and 4 show the effects of noise on a deconvolution of the synthetic data given by the curve in Figure 5, which is generated by convolving an ideal function consisting of three narrow-width, separated Gaussians of heights 100, 100, and 50 with a medium width Gaussian impulse response. For each example (Figures 3 and 4), different Gaussian distributed function domain noise has been added at a signal-to-noise ratio (signal peak to noise standard deviation) of 1000 to 1. Even though such noise is too small to be seen on a graph, the noise amplification by deconvolution (ill-conditioning) gives large noise spikes in the results of Figures 3 and 4. The original input function is also shown for comparison. If a wide Gaussian impulse response had been used the noise amplification would have been even worse.

One striking feature of Figures 3 and 4 is how much the deconvolved results differ from each other. Differences in the noise become dramatic after deconvolution. This behavior casts doubt on the ability of deconvolution methods to be optimized based on an average noise spectrum. Certainly any such optimization should be tested on specific noise realizations to understand whether the use of average noise properties is appropriate. An alternative approach, discussed in this paper, is to do many noise cases in a simulation and then to calculate statistics.

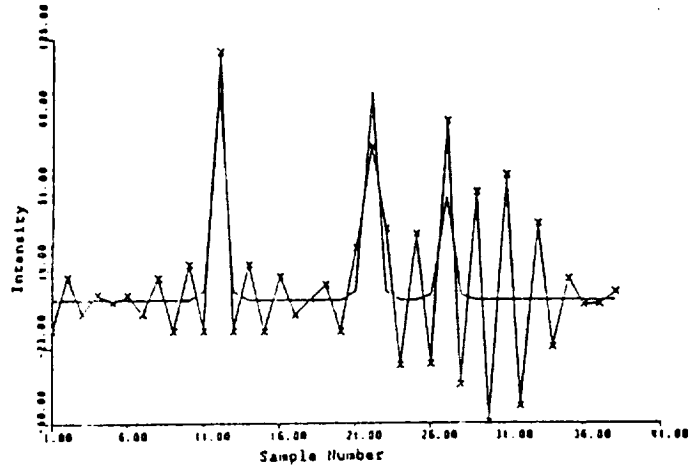


Figure 3. Deconvolution of the synthetic broadened data h of Figure 5. Unmarked curve is original input. Curve marked with x 's is deconvolution of a noisy h with $SNR=1000$. Noise is Gaussian distributed.

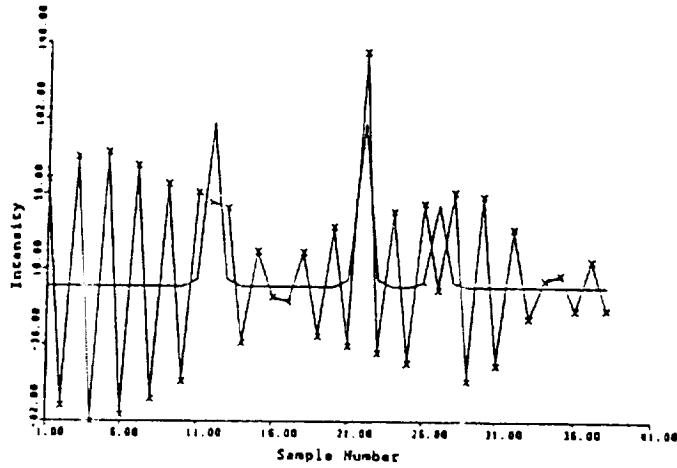


Figure 4. Same as Figure 3 except that a different noise set (still Gaussian distributed) is used to produce a noisy h with $SNR=1000$.

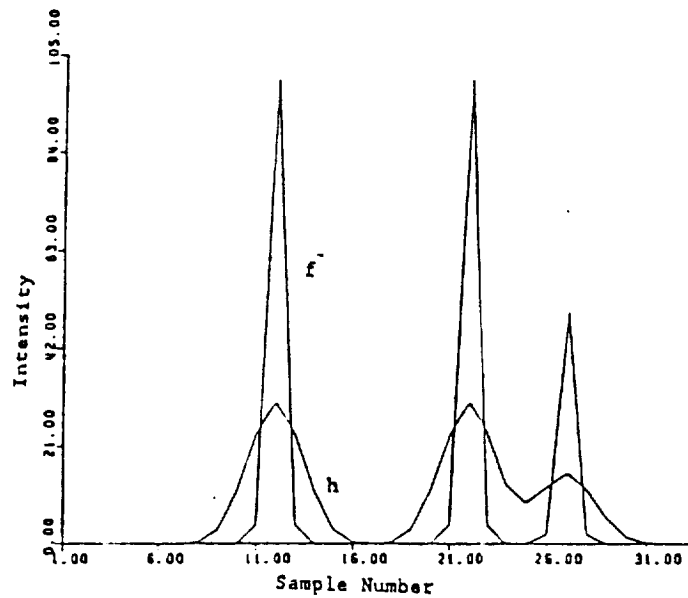


Figure 5. Input f and output h after convolution of f with a medium width Gaussian.



OPTIMIZATION OF ITERATIVE DECONVOLUTION

A long unanswered question for iterative methods has been how many iterations to use for a given data set. Experience and some trial and error for each data type have provided crude answers, but a systematic investigation did not begin until ten years ago. Wright⁴² initially investigated requirements for optimization of Morrison's iterative noise removal.^{30 16} Her work was extended by Wright and G. Ioup⁴³ and J. Ioup and G. Ioup.²⁰ Finally a very complete analysis was performed by Leclere²⁵ and co-workers.²⁶ Since then the method has been extended to van Cittert's iterations and to Morrison's and van Cittert's iterations applied sequentially.²⁷ The first optimization of noise removal and deconvolution iterations used sequentially was for G. Ioup's always-convergent method by Amini¹ and co-workers.^{2 4} The reblurring procedure has also been optimized.²

The initial hypothesis for the optimization studies is that for a given data type and signal-to-noise ratio (SNR), simulation with many different noise sets, and testing each for optimum iteration numbers, leads to reasonable statistics for the iteration number. It is assumed further that by varying the SNR, a smoothly varying set of the mean iteration numbers versus SNR can be generated with standard deviations, as well as that these standard deviations will not be too large. Although many problems present themselves in the course of the work, the final result is that useful curves of average iteration number versus SNR and average mean squared error of the deconvolved results versus SNR can be generated. Studies include narrow to wide Gaussian impulse responses as well as synthetic exploration seismic data. Several different noise types are included over SNR's from less than 1 to over 1000.

To answer the question of how changing the input model would affect the results, an input consisting of a rectangle function followed by a triangle function is substituted by El Saba⁷ for the three-Gaussian input shown in Figure 5. The optimization gives different optimum mean iteration number versus SNR curves, as expected. It is therefore important for experimentalists to do an optimization for the data type of interest. While there is some computer time involved, the labor is minimal since the optimization code exists. Once optimization results are obtained for a general data type, no further simulations are needed for experiments of the same type.

A by-product of the optimization of noise removal and deconvolution iterations used sequentially is the first solid answer to the question of when iterative noise removal was helpful and when it was not needed. By plotting the mean squared error after deconvolution versus SNR for sequential-use optimization on the same graph as the result for the optimization of deconvolution iterations alone, one can decide below which SNR noise removal is needed. The mean squared error will be smaller with noise removal at the lowest SNR's, but above some SNR value the noise removal will not improve the result significantly or at all. The mean squared error curves for a fairly narrow Gaussian impulse response are shown in Figure 6 and for a wide Gaussian in Figure 7 using the input given in Figure 5. The narrow Gaussian deconvolution is improved by noise removal up to a SNR of approximately 90. The wide Gaussian deconvolution is improved by noise removal for all SNR's included in Figure 7, i.e., up to SNR 150.

Although the mean squared error (L2 norm) is principally used in this work, the L1 norm for optimization has also been tested. It is important to emphasize that this method is not limited in the choice of optimization criterion, and that many others could be used. We are currently studying non-norm type measures.

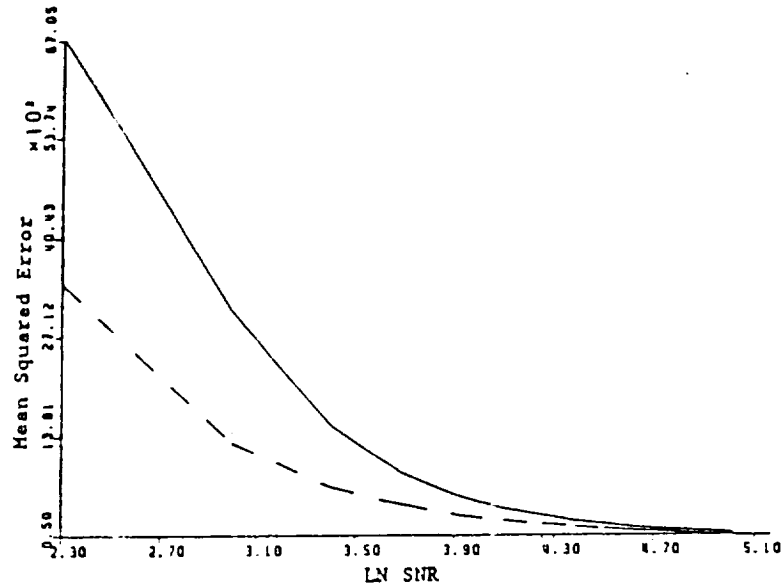


Figure 6. Mean squared error versus natural logarithm of SNR (a) after optimization of iterative deconvolution alone (solid line) and (b) after optimization of sequential application of iterative noise removal and deconvolution (dashed line) for a fairly narrow Gaussian impulse response.

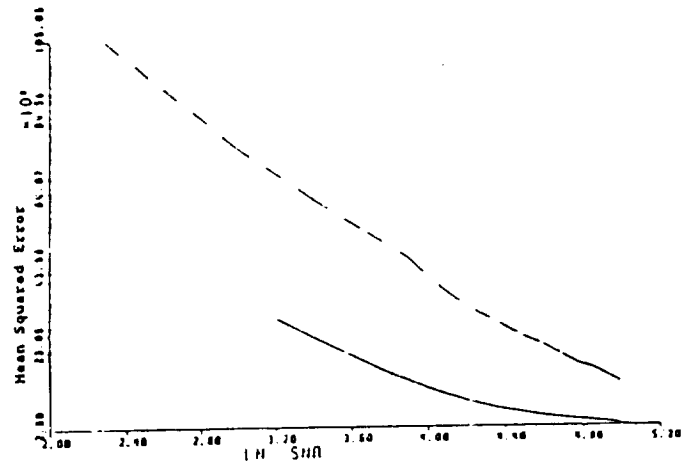


Figure 7. Same as Figure 6 with (a) iterative deconvolution optimized alone (dashed line) and (b) iterative noise removal and iterative deconvolution optimized together (solid line) for a wide Gaussian impulse response.

These studies have also provided a methodology for deciding how to optimize instrument design and operating parameters to achieve the best deconvolution results.¹⁹ In experiments with a compromise between SNR and resolution, an approach should be available to decide how to configure the instrument to obtain the needed experimental data. If deconvolution of the data is to be part of the process, then the optimization approach should include the deconvolution. Amini et al.⁴ have shown that a three-dimensional plot can be created with a surface of mean squared error after optimization of iterative deconvolution plotted versus SNR and resolution (impulse response width, for example) as the independent variables for systems with one degree of freedom. See Figure 8. Once the curve of SNR versus resolution is established for a given instrument in the SNR-resolution plane, an upward projection of this curve will give another curve at the intersection with the surface.¹⁹ The instrument resolution value corresponding to the minimum in the latter curve should give the best deconvolved result.



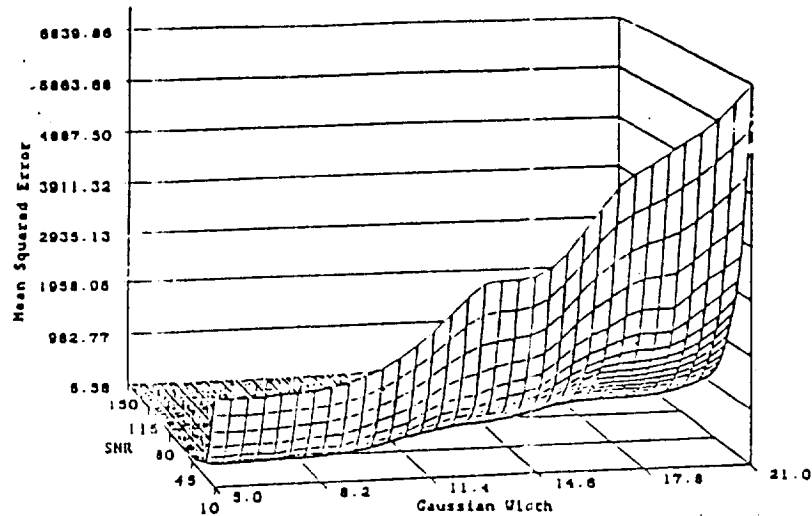


Figure 8. Surface of mean squared error after optimization of iterative deconvolution versus SNR and Gaussian impulse response width. The latter is a measure of resolution.

EVALUATION OF DECONVOLUTION ALGORITHMS

Systematic evaluation of deconvolution algorithms seldom takes place. Particular algorithms sometimes are applied to output of particular instruments and the results compared with known results of the instrument at high resolution in a qualitative fashion (e.g., J. Ioup et al.²¹). The technique may be used or discarded depending on whether it has distorted the spectrum unacceptably, created false, or ghost peaks, or simply used too much computer time. Sometimes synthetic spectra are generated, convolved with an assumed instrument function, and used to test the deconvolution algorithm by determining the square of the difference between the original spectrum and the deconvolution. As a figure of merit for evaluating deconvolution algorithms, this square difference criterion produces a large value for a spectrum which is faithfully deconvolved if it is merely translated slightly. Recently, the problem of evaluation of resolution enhancement has been attacked by regarding it as a problem of detecting an unresolved peak in the presence of both noise and the larger, fused peak.^{26 27 28} This point of view seems directly applicable to those spectral problems in which the presence or absence of a peak is the primary question. It also permits techniques long applied to the detection problem to be applied without modification to the problem of resolution enhancement, permitting for the first time judgements as to which deconvolution techniques are superior when the principal objective is to find a weak, fused peak and which are superior when the objective is to avoid falsely believing a weak peak to be present. Receiver Operating Characteristic, or ROC, curves are plots of the probability of falsely detecting an artifact of the deconvolution. Their application to the resolution problem shows that the efficacy of ideal low-pass filtering before deconvolution of a spectrum of fused Lorentzian peaks depends, of course, on the bandpass of the filter. For the example shown in Figure 9 a superior deconvolution as judged by the ROC curve produced occurs when about eleven of the 128 Fourier coefficients are retained. Of particular interest, however, is the fact that filtering with a narrower or wider bandpass, although each produce inferior deconvolutions, affects detection in different ways. Narrow-band filtering produces deconvolutions which are superior in avoiding false detections at low probabilities of detecting true peaks, while wide band filtering produces deconvolutions which better detect signal peaks when a relatively high rate of false alarms can be tolerated. When the gross efficacy of low-pass filtering prior to the application of an inverse digital filtering deconvolution algorithm is evaluated by maximizing the area under the resulting ROC curve, optimum

deconvolution is found to occur when only ten Fourier coefficients are retained in the low-pass filtering. When the efficacy of the filtering and deconvolution is evaluated by minimizing the square of the difference between the deconvolution and the original spectrum, a gentle minimum and, hence, optimum deconvolution is found when nineteen coefficients are kept. Thus, optimum deconvolution in the sense of minimum square difference does not produce optimum ability to detect peaks without creating spurious ghost peaks. Furthermore, when deconvolution with a minimum negativity constraint was evaluated using ROC curves³⁸ it was found that, although minimum negativity produced enhanced spectra whose peaks were easily interpreted visually, the ability to detect small, fused peaks in noise by means of a matched correlation filter was only marginally superior to optimum low-pass filtering. This result casts doubt on the deconvolution algorithms. It is clear that much work remains to be done in improving evaluation of deconvolution techniques; nonetheless, viewing resolution enhancement as a problem in detection offers promises of quantitative evaluation of deconvolution with a numerical appreciation of the risk of misidentifying a small peak discovered in deconvolution of noisy, fused spectra. Numerical assessment of the presence of ghosts and the failure to detect true peaks should greatly increase the utility of all deconvolution algorithms.

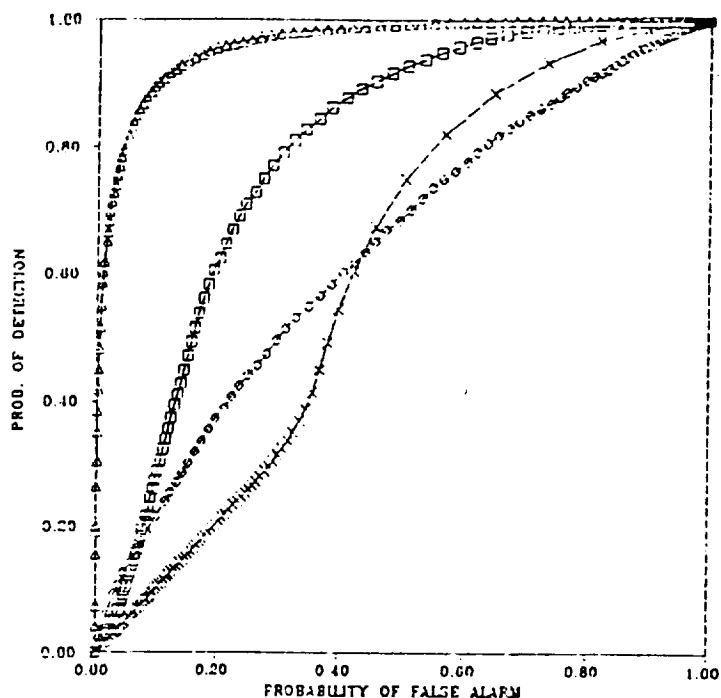


Figure 9. ROC curves (probability of detection versus probability of false alarm) for low pass filtering by varying the threshold at signal-to-noise ratio 3.183. -Square: cut-off number 39; triangle: 12; diamond: 3; cross: no cut off.

ACKNOWLEDGMENTS

The authors gratefully acknowledge the research support of the National Aeronautics and Space Administration under grants NAG-1-800 (USM) and NAG-1-804 (UNO) and the expert computer assistance of Mr. N. B. Day at UNO.

REFERENCES

1. Amini, A. M., Optimization of Convergent Iterative Noise Removal and Deconvolution and an Evaluation of Phase Shift Migration, Master's Thesis, University of New Orleans, 1984.
2. Amini, A. M., Ioup, G. E., Ioup, J. W., and Powe, R., Optimization of Convergent Iterative Deconvolution for Seismic Data, EOS Trans. Am. Geophys. Union, Vol. 67, p. 1088, 1986.
3. Amini, A. M., Bensusied, T. A., Ioup, G. E., and Ioup, J. W., Single Filter Application of Always-Convergent-Iterative Deconvolution to Seismic Data, EOS Trans. Amer. Geophys. Union, Vol. 68, p. 1380, 1987.
4. Amini, A. M., Ioup, G. E., and Ioup, J. W., Optimization of Convergent Iterative Deconvolution for Physical Data, Bull. Am. Phys. Soc., Vol. 33, p. 669, 1988.
5. Bracewell, R. N., The Fourier Transform and Its Applications. McGraw-Hill, New York, 2nd ed., revised, 1986.
6. Bracewell, R. N. and Roberts, J. A., Aerial smoothing in radio astronomy, Austral. J. Phys., Vol. 7, pp. 615-640, 1954.
7. El-Saba, A. M., Effect of Input on Optimization of Morrison's Iterative Noise Removal for Deconvolution, Master's Thesis, University of New Orleans, 1986.
8. Frieden, B. R., Image Enhancement and Restoration, in Picture Processing and Digital Filtering, T.S. Huang, Ed., Springer-Verlag, Berlin and New York, pp. 177-248, 1975; 2nd updated edition, 1979.
9. Gerchberg, R. W., Super-resolution through error energy reduction, Opt. Acta, Vol. 21, pp. 709-720, 1974.
10. Hill, N. R., Deconvolution for Resolution Enhancement, Master's Thesis, University of New Orleans, 1973.
11. Hill, N. R. and Ioup, G. E., 1976, Convergence of the van Cittert iterative method of deconvolution, J. Opt. Soc. Am., Vol. 66, pp. 487- 89, 1976.
12. Howard, S. J., Continuation of discrete Fourier spectra using a minimum-negativity constraint, J. Opt. Soc. Am., Vol. 71, pp. 819-824, 1981.
13. Howard, S. J., Fast Algorithm for Implementing the Minimum-Negativity Constraint for Fourier Spectrum Extrapolation, Appl. Opt., Vol. 25, p. 1670-1675, 1986.
14. Howard, S. J., Fast Algorithm for Implementing the Minimum-Negativity Constraint for Fourier Spectrum Extrapolation, Part II., Appl. Opt., Vol. 27, pp. 3190-3196, 1988.
15. Ioup, G. E., Analysis of Low Energy Atomic and Molecular Collisions: Semiclassical Elastic Scattering Calculations and Deconvolution of Data, Ph.D. Dissertation, University of Florida, 333 pages, 1968.
16. Ioup, G. E., Always-Convergent Iterative Noise Removal and Deconvolution, Bull. Am. Phys. Soc., Vol. 26, p. 1213, 1981.
17. Ioup, G. E. and Ioup, J. W., Iterative deconvolution, Geophysics Vol. 48, pp. 1287-1290, 1983.
18. Ioup, G. E., Ioup, J. W., and Radford, M. E., Application of Always-Convergent Iterative Noise Removal and Deconvolution to Seismic Data, Geophysics, Vol. 50, p. 717, 1985.
19. Ioup, G. E., Amini, A. M., and Ioup, J. W., Determination of Instrumentation Parameters for Optimum Resolution with Deconvolution, Bull. Am. Phys. Soc., Vol. 33, pp. 705-706, 1988.
20. Ioup, J. W. and Ioup, G. E., Optimum Use of Morrison's Noise Removal Method Prior to Linear Deconvolution, Bull. Am. Phys. Soc., Vol. 26, p. 1213, 1981.
21. Ioup, J. W., Ioup, G. E., Rayborn, G. H., Wood, G. M., and Upchurch, B. T., Iterative and Function - Continuation Fourier Deconvolution Methods for Enhancing Mass Spectrometer Resolution, Int. J. Mass Spectrom. and Ion Processes, Vol. 55, pp. 93-109,

1983-1984.

22. Jansson, P. E., *Deconvolution with Applications in Spectroscopy*, Academic Press, New York, 1984.
23. Kawata, S. and Y. Ichioka, Y., Iterative image restoration for linearly degraded images. I. Basis, *J. Opt. Soc. Am.*, Vol. 70, pp. 762-768; II. Reblurring procedure, *J. Opt. Soc. Am.*, Vol. 70, pp. 768-772, 1980.
24. LaCoste, L. J. B., Deconvolution by successive approximations, *Geophysics*, Vol. 47, pp. 1724-1730, 1982.
25. Leclere, J. H., *Optimum Use of Morrison's Iterative Method of Noise Removal for Deconvolution*, Master's Thesis, University of New Orleans, 1984.
26. Leclere, J. H., Ioup, G. E., and Ioup, J. W., A Statistical Optimization Study of Iterative Noise Removal for Deconvolution, *EOS Trans. Am. Geophys. Union*, Vol. 66, p. 983, 1985.
27. Leclere, J. H., Ioup, G. E., and Ioup, J. W., Statistical Optimization of Morrison's Iterative Noise Removal and van Cittert's Iterative Deconvolution, *Bull. Am. Phys. Soc.*, Vol. 33, p. 669, 1988.
28. Marple, S. Lawrence, *Digital Spectral Analysis with Applications*, Prentice-Hall, New Jersey, 1987.
29. Mendel, J. M., *Optimal Seismic Deconvolution*, Academic Press, New York, 1983.
30. Morrison, J. D., On the Optimum Use of Ionization Efficiency Data, *J. Chem. Phys.*, Vol. 39, pp. 200-207, 1963.
31. Ni, H., Amini, A. M., Bensueid, T. A., Ioup, G. E., and Ioup, J. W., Single Filter Application of Always-Convergent Iterative Deconvolution to Physical Data, *Bull. Am. Phys. Soc.*, Vol. 33, p. 669, 1988.
32. Oppenheim, A. V. and Schaffer, R. W., *Digital Signal Processing*, Prentice-Hall, New Jersey, 1975.
33. Rayborn, G. H. and Wang, D., Viewing Resolution as a Problem in Deconvolution: The Use of Receiver Operating Characteristics in Evaluating Deconvolution Algorithms, *Bull. Am. Phys. Soc.*, Vol. 33, P. 2201, 1988.
34. Robinson, E. A. and Treitel, S., *Geophysical Signal Analysis*, Prentice-Hall, New York, 1980.
35. van Cittert, P. H., Zum Einfluss der Spaltbreite auf die Intensitätsverteilung in Spektrallinien, *Z. Physik*, Vol. 69, pp. 298- 308, 1931.
36. Wang, D., The Use of Receiver Operating Characteristic Curves to Discriminate Between Deconvolution Algorithms, Master's Thesis, University of Southern Mississippi, 1988.
37. Wang, D., and Rayborn, G. H., Evaluation of Algorithms for Spectral Enhancement Using ROC Curves, *Bull. Am. Phys. Soc.*, Vol. 33, p. 372, 1988.
38. Wang, L. and Rayborn, G. H., Evaluation of the Minimum Negativity Constraint in Deconvolution, *Bull. Am. Phys. Soc.*, Vol. 33, p. 2201, 1988.
39. Whitehorn, M. A., Always-Convergent Iterative Noise Removal and Deconvolution for Image Data, Master's Thesis, University of New Orleans, 1981.
40. Whitehorn, M. A. and Ioup, G. E., Always-Convergent Iterative Noise Removal and Deconvolution for Two-Dimensional Images, *Bull. Am. Phys. Soc.*, Vol. 26, p. 1213, 1981.
41. Wood, G. M., Rayborn, G. H., Ioup, J. W., Ioup, G. E., Upchurch, B. T., and Howard, S. J., Data Enhancement and Analysis through Mathematical Deconvolution of Signals from Scientific Measuring Instruments, *ICIASF '81 Record*, pp. 25-37, 1981.
42. Wright, K. A. R., 1980, A Study of Morrison's Iterative Noise Removal Method, Master's Thesis, University of New Orleans, 1980.
43. Wright, K. A. R. and Ioup, G. E., Optimum Use of Morrison's Noise Removal Method for Noise Minimization, *Bull. Am. Phys. Soc.*, Vol. 26, p. 1213, 1981.

Computers and Experiments in Stress Analysis

Proceedings of the fourth International Conference
on Computational Methods and Experimental
Measurements, Capri, Italy, May 1989

Editors:
G.M. Carlomagno
C.A. Brebbia

Computational Mechanics Publications
Southampton Boston

Springer-Verlag Berlin Heidelberg
New York London Paris Tokyo

G.M. CARLOMAGNO
Department of Mechanical Engineering
Universita degli Studi di Napoli
P.le Tecchio 80
80125 Napoli
Italy

C.A. BREBBIA
Computational Mechanics Institute
Ashurst Lodge
Ashurst, Southampton
SO4 2AA
U.K.

British Library Cataloguing in Publication Data
Computers and experiments in stress analysis.

1. Stress analysis. Applications of microcomputer systems

I. Carlomagno, G.M. (Giovanni M) II. Brebbia, C.A. (Carlos Alberto), 1938-
620.1'123'0285416
ISBN 1-85312-033-2
ISBN 1-85312-031-6 set

Library of Congress Catalog Card Number 89-60541

ISBN 1-85312-033-2 Computational Mechanics Publications Southampton
ISBN 0-945824-18-1 Computational Mechanics Publications Boston
ISBN 3-540-51111-3 Springer Verlag Berlin Heidelberg New York
London Paris Tokyo
ISBN 0-387-51111-3 Springer Verlag New York Heidelberg Berlin
London Paris Tokyo

ISBN 1-85312-031-6
ISBN 3-540-51112-1 2 volume set
ISBN 0-387-51112-1

This work is subject to copyright. All rights are reserved, whether the whole or part of the material is concerned, specifically the rights of translation, reprinting, re-use of illustrations, recitation, broadcasting, reproduction on microfilms or in any other way, and storage in data banks. Duplication of this publication or parts thereof is only permitted under the provisions of the German Copyright Law of September 9, 1965, in its version of June 24, 1985, and a copyright fee must always be paid. Violations fall under the prosecution act of the German Copyright Law.

© Computational Mechanics Publications 1989
© Springer-Verlag Berlin Heidelberg 1989

Printed in Great Britain by The Bath Press Limited, Avon

The use of registered names, trademarks etc. in this publication does not imply, even in the absence of a specific statement, that such names are exempt from the relevant protective laws and regulations and therefore free for general use.

SECTION

Modelling of
R.C.H. Che

The Use of
Brittle Com
R.C.H. Che

Nonlinear F
Walls
I.D. Lajos

The Bound
Problems w
J.A.M. Car

Comparison
Heater Test
S. Heuserm

Numerical S
Michael B.

SECTION

INVITED C
Inversion of
Motion Data
M.D. Tijm

INVITED C
Realistic Sim
G.F. Pinza

INVITED C
A Time-Dep
Inhomogene
Ezio Facciol

ORIGINAL PAGE IS
OF POOR QUALITY

(2) how much analog precision is needed in the connections in the network, (3) the number of training examples the network must see before it can be expected to form reliable generalizations, and (4) the efficiency with which a network extracts information from the training data.

John Denker, Daniel Schwartz, Ben Wittner, Sara Solla, John Hopfield, Richard Howard, and Lawrence Jackel, Complex Systems, in press (1987).

14:42
O18 2

An Analog VLSI System for Neural Network Learning Experiments DANIEL B. SCHWARTZ and RICHARD E. HOWARD AT&T Bell Laboratories.

Because the complexity available from standard VLSI has grown far beyond our ability to simulate it, it has become interesting in its own right. Adaptive neural network models are an example of a class of complex systems where a mapping directly onto VLSI is of great practical and fundamental interest. However, the continuously variable connections required for adaption are not easily represented in a digital world. We are building a collection of analog circuits from standard digital CMOS with variable strength analog connections based upon charge storage by a pair of MOS capacitors. The capacitors are tied together by a string of FETs, allowing the connection strength to be monotonically varied by moving charge between them. Our current designs have 7 bits of analog depth of both polarities. The chips have about 10^3 connections and can easily be cascaded to make larger networks. The available computational speed is dominated by i/o bandwidth of the host controller. We will discuss use of such chips and their limitations.

14:54

O18 3 Specific Heat for a Boson System with Anharmonicity. M.S. Wartak, C.Y. Fong, Department of Physics, University of California, Davis. -- We used the model Hamiltonian

$$H = \sum_{i=1}^N \left[\epsilon b_i^\dagger b_i - \Gamma_i b_i^\dagger b_i^\dagger b_i b_i + \Delta (b_{i+1}^\dagger b_i^\dagger + b_{i+1} b_i^\dagger) \right]$$

to study the thermodynamic properties of the one-dimensional boson system with on-site anharmonicity, and with Δ much smaller than ϵ . For the calculation of partition function we have used the path-integral method. The Dyson equation is solved in the nearest-neighbor approximation. The resulting expression for the free energy is evaluated in the static approximation using the steepest descent method. The behavior of specific heat for different values of Γ and Δ is examined.

15:06
O18 4

cancel

Color Induced Transitions in the Presence of a Nonlinear Potential. G. P. TSIRONIS, P. GRIGOLINI, University of California, San Diego. -- We show that the negative diffusion coefficients exhibited by current approaches to the Fokker-Planck equation for non-Markovian and bistable processes result from assuming that the system reaches a conventional steady state. By lifting this assumption we show that when a critical value of the noise correlation time τ is exceeded, the process of escape over a barrier agrees with an exact prediction for the large- τ regime and thus that the linear response approximation behind our theory produces exact results for arbitrary correlation times.

1. G. P. Tsironis, P. Grigolini, "Rate processes activated by color noise: Bridging two exact limits", UCSD preprint
2. J. Masoliver, B. J. West, K. Lindenberg, Phys. Rev. A 35, 3086 (1987)

15:18

O18 5 Surface Loss in a Parabolic-Equation Model.

MARINA E.M. HEAD and W. JOBST, Naval Oceanographic Office and ELEANOR S. HOLMES, Science Applications International Corporation. -- Ocean-surface loss of acoustic energy is often given as a function $SL(\theta)$ of the grazing angle θ . If $p(z)$ is the complex acoustic-pressure field (from a parabolic-equation model) as a function of depth z near the surface, a Fourier transform $F(K)$ of $p(z)$ yields pressure as a function of the vertical wave number K . K is proportional to $\sin \theta$, thus $F(K)$ is a function $G(\theta)$ of θ . We account for the surface loss by multiplying $G(\theta)$ by a loss function $L(\theta)$ -- related to $SL(\theta)$ -- before transforming back to physical space. The method also is applicable to bottom loss. Numerical implementation, angular resolution, and limitations of the method are discussed. Numerical examples are presented.

15:30

O18 6 Effects of Noise on Pressure and Modal Amplitude Matched Field Processors.* GEORGE M. FRICHTER, IV, JULIETTE W. IOUP, Univ. of New Orleans.** GEORGE B. SMITH, Xavier Univ., GEORGE E. IOUP,** Univ. of New Orleans, CHRISTOPHER FEUILLADE, Syntek, GRAYSON H. RAYBORN, Univ. of Southern Miss.** and DONALD DEL BALZO, NORDA--Modal amplitude matched field processing for acoustic signals received by a vertical array of hydrophones is used to determine the effects of spatially correlated and uncorrelated noise fields on pressure and modal amplitude matched field processors. Various amounts of white isotropic noise and spatially correlated noise as calculated by a normal mode noise model are combined with the field due to a submerged acoustic source to produce simulated cross spectral matrices. A phone-to-mode space mapping is then used to obtain the corresponding cross amplitude correlation matrices. Both conventional and maximum likelihood processing are used. Results show that spatially uncorrelated noise degrades modal amplitude processors more than spatially correlated noise.

**Supported in part by ONR/NORDA Contract N00014-87-K-600

15:42

O18 7 A Review of Underwater Acoustic Propagation Models Emphasizing Coupled Full-Wave Range-Dependent Propagation.

JOSEPH E. MURPHY, University of New Orleans, New Orleans, LA 70148; STANLEY A. CHIN-BING, Naval Ocean Research and Development Activity, NSTL, MS 39529-5004. -- Underwater acoustics is usually not discussed at APS meetings, but rather is confined to peer review meetings. However, given the close proximity of the Navy's lead ocean environmental RDT&E laboratory, the Naval Ocean Research and Development Activity (NORDA) located 45 miles from New Orleans, we take this opportunity to present a review of ocean acoustic propagation modeling. In the ocean, the index of refraction is variable; acoustic transmission paths are curved and the coupling of the refracted, reflected, and diffracted acoustic fields from boundaries give rise to complicated classical physics problems. The prominent acoustic models are based on normal mode, parabolic approximation, FFT, and modified ray methods. Each of these include a limited number of physical mechanisms. We have therefore developed a coupled full-wave range-dependent ocean acoustic propagation and scattering model based on the finite element method. This model is superior especially at low frequencies. Numerical simulations will be presented showing the effect of a fractal under-ice interface with ice keel on the fully coupled range-dependent underwater acoustic field.

15:54

O18 8 Determination of Instrumentation Parameters for Spectrum Resolution with Deconvolution. GEORGE E. IOUP, ABOLFAZL M. AMINI, and JULIETTE W. IOUP, Univ. of New Orleans**--An important design and parameter selection

problem for many instruments is the compromise between resolution and signal-to-noise ratio (SNR). An improvement in instrumental resolution is usually accompanied by a decrease in SNR. Resolution can often be improved for shift-invariant instruments after the data are taken by the use of deconvolution. The optimum design and operation of the instrument cannot be presumed to be the same with and without deconvolution, however. We present a methodology for determining optimum instrument configuration when deconvolution is used. In its simplest form, a surface of the error after deconvolution versus SNR and instrument resolution is generated. A given instrument will have a curve in the SNR-instrument resolution plane. The minimum in the intersection of the upward projection of this curve with the surface determines the optimum parameters. Examples of these surfaces and their use will be given.

**Supported in part by NASA Grant NAG-1-804

16:06

O189 Electron Localization in Water Clusters: Surface and Internal States. R. N. BARNETT, UZI LANDMAN, C. L. CLEVELAND AND JOSHUA JORTNER, School of Physics, Georgia Institute of Technology, Atlanta, Ga. 30332--Electron attachment and localization in water clusters, $(H_2O)_n$ ($n=8-128$) are studied using path-integral molecular dynamics simulations.¹ The electron-water molecule interaction is described via a newly developed pseudopotential which includes Coulomb, polarization, exclusion and exchange contributions. For small and intermediate size clusters ($n=8-32$), the energetically favored localization mode involves a surface state and the calculated excess electron binding energies agree with experiment. In larger clusters internal localization (solvation) is favored. In both cases electron localization is accompanied by large cluster molecular reorganization. The cluster size dependence, energetics, structure and temperature dependence are discussed.

1. R. N. Barnett, Uzi Landman, C. L. Cleveland and J. Jortner, Phys. Rev. Lett. **59**, 811 (1987).
*Work supported by U.S. DOE, Grant No. FG05-86KR45234.

16:18

O1810 Many-Electron States for Small Cu-O Rings Modeled by Hubbard and Extended Hubbard Models. YU ZHOU and SAMUEL P. BOWEN, Virginia Tech.--The low lying states of small rings of atoms are studied for varying numbers of electrons and holes in the Hubbard and the extended Hubbard model. Particular interest is focused on the binding energy of hole pairs of different separations in the many electron Bloch states that comprise the low-lying multiplets. The analytic structure of the states and the ground state energies will be compared with numerical values for several different chain lengths and electron numbers.

16:30

O1811 Hole Propagation and Pairing in a Model for CuO_2 H.Y. CHOI and E.J. MELE, University of Pennsylvania--We construct a model for the dynamics of the holes in the nearly half filled Hubbard model on a square lattice. An interaction of these carriers with an antiferromagnetic background produces a self localization of the holes to form a gas of spin polarons. The resulting polarons are found to be relatively light, and propagate through the two dimensional structure by coupling to background spin fluctuations. A pairing potential is derived for

the hole polarons on the resulting Fermi surface, which is mediated by exchange of the linearized spin waves. In the simplest model this provides a long range attractive interaction in an $l = 2$ state; however, we will discuss a refinement of this model, which favors singlet pairing in an $l = 0$ state.

Supplementary Program

01812

Photoemission Spectra of Narrow band systems P.S. Riseborough, Polytechnic University, In the heavy fermion systems there is a large discrepancy between the experimentally measured density of states and the density of states obtained from local density functional band structure calculations. This discrepancy is clearly indicative of manybody effects. Arko and collaborators* have recently discovered similar manybody anomalies can be found in the normal narrow band Uranium systems. We have performed calculations using an N fold degenerate Hubbard model, utilizing an expansion in the coulomb interaction. The infinite set of diagrams containing independent single loops have been evaluated. This approximation should be exact in the limit $N \rightarrow \infty$. We obtain a qualitative agreement with the experimental findings.
*A.J. Arko, B.W. Yates, D.D. Koelling, B.P. Dunlap Z. Zolnierak, A.W. Mitchell, D.J. Lam, C.G. Olson and M. del Giudice, preprint

SESSION O19: HYDROGEN IN METALS I

Thursday afternoon, 24 March 1988

Mardi Gras K at 14:30

P. Richards, presiding

14:30

O191 Anomalous Proton Spin-Lattice Relaxation at High Temperatures in BCC Transition Metal-Hydrogen Solid Solution Systems. R. G. BARNES, J-W. HAN, L. LICHTY and D. R. TORGESON, Ames Laboratory* and Department of Physics, Iowa State University--We report anomalous behavior of the proton spin-lattice relaxation time T_1 at very high temperatures (up to 1000 K) for hydrogen in solution in the b.c.c. metals V, Nb and their alloys. Besides the usual T_1 minimum at intermediate temperatures (~ 225 K) characterized by the mean dwell time for hopping, $\tau_d = \exp(E_s/k_B T)$, T_1 again decreases sharply at higher temperatures instead of returning to the value T_{1s} determined by the conduction electron contribution to $(T_1)^{-1}$. This decrease is well-described by an additional contribution to $(T_1)^{-1}$ of the form $\exp[-(U-E)/k_B T]$, consistent with excitation of hydrogen to a state of highly correlated motion, where U is the excitation energy and E is the activation energy for the correlation time τ_L in that state, i.e., $\tau_L = \alpha \exp(E/k_B T)$, and $E < U$. Changes in hydrogen diffusion associated with such a state have also been sought.¹

*Operated for the USDOE by Iowa State University under contract No. W-7405-Eng-82.

1. R. M. Cotts, J. L. Billeter, et al., abstract this meeting.

14:42

O192 Search for an Hydrogen Diffusion Anomaly in a BCC Transition Metal Alloy. R. M. COTTS and J. L. BILLETER, Cornell University; J-W. HAN, L. LICHTY, D. R. TORGESON and R. G. BARNES, Ames Laboratory -

method which combines a modification of earlier suggestions^{1,2} and subspace diagonalization, realizing advantages of both methods for a matrix expressed in a planewave basis. Comparison of asymptotic convergence rates for several iteration methods shows that the combined method is at least a factor of three better than the best previously known method. The method is implemented in a planewave basis with separable nonlocal pseudopotentials so that computational effort scales as $N \log N$ for a basis of N planewaves.

- 1 M.C. Payne, J.D. Joannopoulos, D.C. Allan, M.P. Teter, and D.H. Vanderbilt, *Phys. Rev. Lett.* **56**, 2656 (1986).
- 2 A. Williams and J. Soler, *Bull. Am. Phys. Soc.* **32**, 562 (1987).

11:12

N182 Solution to the Initial Value Problem for the Quantum Nonlinear Schrödinger Equation. M. J. POTASEK and B. YURKE, AT&T Bell Laboratories -- The quantum nonlinear Schrödinger equation provides an integrable quantum field theory that has been solved by a number of methods. Most recently, Gutkin^{1,2} has developed an intertwining operator technique for obtaining the time evolution of the field operators. Using Gutkin's formalism, we show how to obtain the exact time evolution of an initial Schrödinger state vector. The suitability of this formalism for numerical computation with application to pulse propagation in optical fibers will be discussed.

1. E. Gutkin, *Ann. Inst. Henri Poincaré* **3**, 285 (1986).
2. E. Gutkin, *J. Func. Anal.* (1987).

11:24

N183 Statistical Optimization of Morrison's Iterative Noise Removal and van Cittert's Iterative Deconvolution. JAMES H. LECLERE, GEORGE E. IOUP, and JULIETTE W. IOUP, Univ. of New Orleans**--Morrison's iterative noise removal and van Cittert's iterative deconvolution have been used to remove experimental broadening for various physical data types. Heretofore the number of iterations needed and other conditions of use have been determined by trial and error. We have developed a statistical optimization procedure to determine optimum use of the methods for any computer-generated noise type and any signal-to-noise ratio domain of interest. We report the results for L1 and L2 norm optimization and several noise types for a signal-to-noise ratio domain from 2 to over 1000. The contrast between point successive and point simultaneous iterations is also discussed as is the effect of allowing the deconvolved result to expand as the iterations proceed. Combined optimization of the two techniques is presented.

- **Supported in part by NASA Grant NAG-1-485
¹G. E. Ioup and J. W. Ioup, *Geophysics* **48**, 1287-1290 (1983)

11:36

N184 Optimization of Convergent Iterative Deconvolution for Physical Data. ABOLFAZL M. AMINI, GEORGE E. IOUP, and JULIETTE W. IOUP, Univ. of New Orleans***--Statistical computer simulation is used to optimize the always-convergent iterative noise removal and deconvolution technique of Ioup.¹ By considering the mean square error versus iteration number for 50 noisy data sets, one can calculate the mean optimum iteration number and its standard deviation, as well as the average mean square error and its standard deviation. Data with peak-to-standard-deviation signal-to-noise ratios (SNR) varying from 10 to 150 are considered. By applying the iterative deconvolution alone, it is shown that there exists an SNR, for any

given impulse response and data type, above which it is not beneficial to precede the deconvolution with the noise removal.

- **Supported in part by NASA Grants NAG-1-485 and NAG-1-804
¹G. E. Ioup, *Bull. Am. Phys. Soc.* **26**, 1213 (1981)

11:48

N185 Single Filter Application of Always-Convergent-Iterative Deconvolution to Physical Data. HAIHONG NI, ABOLFAZL M. AMINI, TAHAR A. BENSUEID, GEORGE E. IOUP, and JULIETTE W. IOUP, Univ. of New Orleans**--Single filter application of any iterative technique, when possible, presents significant computational economic advantage, but it should not be used until its performance is evaluated against that of the iterations. Wraparound errors associated with a finite length DFT calculation of the filter must be considered. The optimization of the always-convergent iterative technique of Ioup¹ for noisy data is reported in the preceding abstract. In this investigation the sensitivity to wraparound of the DFT single filter equivalent window is established by gradually increasing the zero padding of the data for peak to standard deviation signal-to-noise ratios varying from 10 to 150. It is found that the wraparound error is small enough to be negligible, even when almost no zero padding is used. These results show that very rapid application of iterative deconvolution to physical data is possible.

- **Supported in part by NASA Grants NAG-1-485 and NAG-1-804
¹G. E. Ioup, *Bull. Am. Phys. Soc.* **26**, 1213 (1981)

12:00

N186 Non-Separable Numerical Evaluation of VGV Term in the Schwinger Variational Method. C.A. Weatherford, Florida A&M U.;***--A numerical method is presented for the evaluation of the VGV term which appears in the denominator of the Schwinger variational expression for the T-matrix.^{1,2} The method employs an evaluation of a partial differential equation for the GV part, and then is followed by the calculation of a two dimensional integral. An application to electron scattering from a minimal basis set H₂ model is presented. The possibility for efficient evaluation on vector computers is explored.

- *Supported by NSF grant PHY-8711805 and NASA grant NCC 2-492
 1. W.M. Huo, T.L. Gibson, M.A.P. Lima, and V. McKoy, *Phys. Rev.* **A36**, 1632 (1987).
 2. W.M. Huo, M.A.P. Lima, T.L. Gibson, and V. McKoy, *Phys. Rev.* **A36**, 1642 (1987).

12:12

cancel
N187 Generalized Fourier series for non-linear quantum mechanics. J. DIAZ BEJARANO and A. MARTIN SANCHEZ, Universidad de Extremadura, Badajoz.-- A simple generalization of the usual Fourier series using the generalized exponential and circular functions is presented. The functions themselves are developed in a new, more simple way. They are solutions of common linear and non-linear wave equations. The series are given in terms of Jacobi elliptic functions in a form as similar as possible to the usual Fourier presentation. Several examples are given that correspond to the most usual textbook Fourier series.
 Thanks are due to CAICYT (project nº 1179-84).

100

1189 An Extension Theory for Lattice Green Functions. A. SCHWALM and M. K. SCHWALM, U. of N. Dakota--A method presented of using the known Green functions or densities of states (DOS) for a given lattice Hamiltonian H to find Green functions or DOS for any lattice Hamiltonian H_e expressible as a rational function of H , i.e. $H_e = f(H)$. The formalism is further developed to permit using the known Green functions and DOS of two Hamiltonians H and K to obtain those of any Hamiltonian H_e in the algebra generated by the direct products ($H \otimes I$) and ($I \otimes K$), where I is the identity. Namely,

$$H_e = \sum a_{mn} (H^m \otimes K^n), \text{ with } a_{mn} \text{ real numbers.}$$

Results may be obtained either analytically or numerically. Other properties such as electrical conductivity are also extended from H and K to H_e . A study is presented of two examples, (i) The Cartesian product of two Sierpinski fractal lattice Hamiltonians, also a hierarchical fractal which is infinitely connected with spectral dimension $4 \ln 3 / \ln 5 = 2.730\dots$ (ii) 2D and 3D plaid lattice Hamiltonians formed as products of 1D Fibonacci chains. These lattices are quasi-periodic and admit inflation/deflation transformations, but do not have 5-fold rotation.

11810 Rydberg States of the Rare-Gas Van der Waals Dimers. NING YI DU and C. H. GREENE, Louisiana State U. --Multichannel quantum defect theory is adapted to describe bound and autoionizing Rydberg states of the rare gas dimers. As in our earlier paper¹, related to a similar study by de Prunele², a nonperturbative Fermi-type analysis combines readily with MQDT, giving an enormous simplification. This permits the description of complicated avoided crossings among Rydberg state potential curves, e.g. for ArHe, XeHe, without requiring a large-scale ab initio calculation. Autoionizing resonance structures in the photoionization cross section are also calculated between the fine-structure-split ionization thresholds, accounting partially for observations of Dehmer and Pratt.³

¹Supported in part by the National Science Foundation
 W. Y. Du and C. H. Greene, Phys. Rev. A 36, 971 (1987).
²E. de Prunele, Phys. Rev. A 35, 496 (1987); also Phys. Rev. A 36, 3015 (1987).
³P. M. Dehmer and S. T. Pratt, J. Chem. Phys. 77, 4804 (1982).

SESSION I19: GENERAL MECHANICAL PROPERTIES AND NDE

Wednesday morning, 23 March 1988

Mardi Gras K at 8:00;

R. C. Cook, presiding

8:00

1191 Acoustic Axes In TI, TII And RI, RII Lath Group Crystals. DAVID Y. CHUNG, Howard University. --- There are six and seven elastic constants for TI (RI) and TII (RII) group crystals respectively. In an earlier paper, Khatkevich¹ indicated that the crystals of TI (RI) are related to TII (RII) by a rotation of an angle ϕ about the 4-fold (3-fold) axis. This rotation of acoustic axis is the only distinction between the two groups so far as the acoustic properties are concerned. In the present work, we like to show that by the use of so-called invariant constants, this rotation of ϕ comes out naturally from the inherent properties of these constants. Invariant constants are the elastic constants which are independent of the specific coordinate system being used. The detail expressions of ϕ for TI, TII and RI, RII groups will be presented at the meeting.

1.A. G. Khatkevich, Sov. Phys. Crystallography, 6, 561 (1962).

2.T. P. Srinivasan, J. of Math. and Mech., 19, 1019 (1970).

8:12

1192 The Frenkel-Kontorova Model With Nonconvex Interparticle Interactions and Strain Gradients. S. Marianer and A. R. Bishop, LANL. --We study the statics and dynamics of a chain of atoms moving in a periodic potential with nonlinear, nonconvex interparticle interactions, and with strain gradients which we model by including next nearest neighbors' interactions through the discrete Hamiltonian $H = \sum_n \dot{u}_n^2/2 + \alpha(u_{n+1}-u_n)^4 + \beta(u_{n+1}-u_n)^2 + \gamma(u_{n+1}-2u_n+u_{n-1})^2 - \cos u_n$. We obtain the phase diagram within an ansatz of periodically modulated configurations. These generalize the homogeneous (for $\beta < 1/8$) and dimerized (for $\beta > 1/8$) configurations already reported for $\gamma=0$, and are given by: $u_n = na_1 + b_1$ for $n=1\dots N$, and $u_n = na_2 + b_2$ for $n=N+1\dots N+M$. The dynamics of transitions between different configurations when the parameters are varied is also investigated and we show that these are dominated by nucleation processes, which occur on short time scales compared with the subsequent slow growth. Possible relation of the model to the dynamics of twin boundaries recently observed in the copper-oxide high-temperature superconductors is discussed.

8:24

1193 Temperature Dependence of Third Order Elastic Constants of $KMnF_3$. W. CAO, G.R. BARSCH, Penn State U., W. JIANG, M.A. BREAZEALE, U. of Tennessee. --We have measured the three nonlinearity parameters along the principal symmetry directions for $KMnF_3$ from 298 to 350K by means of acoustic second harmonic generation. In conjunction with our earlier data on the temperature dependence of the pressure derivatives of the elastic constants the complete set of the six third order elastic constants has been determined in this temperature range. For C_{111} , C_{112} , C_{123} and C_{166} the temperature dependence is linear, indicating that the effect of the ferroelastic transition at 186K (manifest in elastic anomalies) is no longer present above 300K, and permitting us to eliminate the effect of zero point and thermal motion by extrapolation to absolute zero. The static T.O.E. constants thus obtained differ significantly from the R.T. values. Both static and R.T. values exhibit large deviations from the Cauchy relations. The results are also compared with those for other perovskites.

*Supported by Office of Naval Research under Contract No. N00014-82-K-0339.

8:36

1194 Always-Convergent Iterative Deconvolution for Acoustic Non-Destructive Evaluation. EDWARD J. MURPHY, JULIETTE W. IOUP, and GEORGE E. IOUP, Univ. of New Orleans, DORON KISHONI, Coll. of William and Mary and NASA Langley Res. Cen. --Acoustic energy sources generally have a finite time duration and a ringing shape which can make the evaluation of individual reflections difficult. Deconvolution can be an important tool for signal analysis. In this work the detected acoustic signals are deconvolved using the Always-Convergent Method of Ioup.¹ The Always-Convergent technique is applied to data recorded during the quantitative analysis of materials through Non-Destructive Evaluation in which ultrasonic signals are used to detect flaws in substances such as composites. An important part of processing the signal is the normalization since it is useful to know the strengths of the reflections. Various methods of normalization are investigated and the most effective method is found to be the one which uses the change in the sum of the absolute values of the amplitudes in the signal before and after processing. Results of the application to actual data are shown.

¹G. E. Ioup, Bull. Am. Phys. Soc. 26, 1213 (1981)

8:48

1195 Thermal Properties of PEEK (poly-ether-ether-ketone) Based Materials* Ryan Giedd, Ewan

showed that the directivity index (DI) of an infinitely populated spherical shell array was about equal to that of a sphere. Extrapolating to discrete elements, this means the shell requires far fewer elements. They did not compute DI using amplitude shading, due to the impractical cost of such systems at that time. Today's technology removes that constraint. This work revisits the problem with shading, using an approach for choosing the amplitude shading coefficients that maximizes DI [H.S.C. Wang, *J. Acoust. Soc. Am.* 57, 1076-1084 (1975)]. Calculations have been made for the DI of shaded cubic volumetric arrays, forming beams perpendicular to one of its faces, in the presence of isotropic noise. Results show that for 27 and 125 element arrays with element matrix spacings of 1/2 wavelength, a full 10 log (number of elements) can be obtained for DI. Work is underway to investigate larger arrays and smaller spacings. The approach will also be extended to nonisotropic noise fields. [Work supported by NORDA and NOSC exploratory development programs.]

9:00

H7. Least-squares and single-filter always-convergent iterative deconvolution of transient signals for correlation processing. James H. Leclere, George E. Ioup,¹⁾ Juliette W. Ioup,²⁾ and Robert L. Field (Code 244, NORDA, Stennis Space Center, MS 39529)

Correlation processing for distributed sensors is most accurate for short pulses and those whose autocorrelation is sharply spiked. For longer transient signals, multipath arrivals at each sensor have significant interference with each other, and it is difficult to identify individual arrival times. Deconvolution of the received signal to sharpen the transients is one method to decrease the overlap and increase the accuracy with which travel times can be identified. Deconvolution can also be applied after cross correlation to sharpen the autocorrelation of the transients. Least-squares deconvolution is the most commonly used approach for acoustic signals. It has the disadvantage of being computer intensive when filters for long transients are needed. An alternative approach, the single-filter application of the always-convergent iterative technique, is faster and provides variable control for noise. The two techniques are compared for actual underwater acoustic multipath transient signals. Single filter application of always-convergent iterative noise removal is compared to the use of a modified Blackman-Harris window for noise control.⁴⁾ Also at the Department of Physics, University of New Orleans.

9:05

H8. Comparison of double and triple cross correlation for arrival time identification of amplitude- and frequency-modulated acoustic transient signals. Juliette W. Ioup,¹⁾ George E. Ioup,²⁾ Robert L. Field, and James H. Leclere (Code 244, NORDA, Stennis Space Center, MS 39529)

The triple cross correlation of three signals is a simultaneous function of two lags. It is an alternative to cross correlations taken two at a time for determining the lags for a given source at three distributed sensors. It should offer improvement in arrival time identification only when the statistics of the signal have significant third moment components. In this study, amplitude- and frequency-modulated synthetic transient signals are propagated over several possible paths to three sensors, and the triple correlation of the received pulses computed, as well as the cross correlations of the same three signals two at a time. The efficacy of these two approaches is compared for a variety of amplitude- and frequency-modulated transient signals and multipath interference conditions.³⁾ Also at the Department of Physics, University of New Orleans.

9:10

H9. *In situ* acoustic calibration for a large aperture array. Barbara J. Sotirin (Marine Physical Laboratory A-005, Scripps Institution of Oceanography, La Jolla, CA 92093)

During September 1987, a large aperture acoustic array was deployed vertically in the Northeast Pacific to study low-frequency noise in the

edge of individual element amplitude and phase response for accurate results. Two *in situ* methods of array calibration are described and results from the September experiment are presented. The first method used transmissions from a low-frequency source of known location and power level. Simulating the conditions encountered during the transmission, the power arriving at the array was predicted by several acoustic propagation models. By comparing the array response at specific frequencies to the response predicted by the models, an absolute calibration was obtained. An error curve for the phase data was generated by unwrapping the phase, accounting for a sampling offset in the array, and subtracting a multiple linear regression curve. The second method determines relative amplitude levels by examining the average ambient noise power output of a specified frequency band across the array. Using spectral, coherence, and directionality plots, the level of self-noise in the array was shown to be below that of the ambient noise being measured. These two independent methods provide a consistent set of element calibration values used for array beamforming. [Work supported by ONT.]

9:15

H10. Abstract withdrawn.

9:20

H11. Matched-mode processing corrections for array tilt and bottom type. James A. Mercer (Applied Physics Laboratory, University of Washington, Seattle, WA 98105)

In a related effort, Homer Bucker has shown that matched-mode processing for an unknown sound-speed environment can be significantly improved if correction factors for the mode-line amplitude functions can be determined. The correction factors are obtained when a source with known location is available to calibrate the system. This paper describes the results of applying the same techniques for simulated cases of unknown array tilt and bottom characteristics.

9:25

H12. Self-consistent modeling of signal and noise in a three-dimensional environment. John S. Perkins, W. A. Kuperman, and F. Ingenito (U.S. Naval Research Laboratory, Code 5160, Washington, DC 20375-5000)

Previous propagation work is extended to model surface noise, shipping, and signal sources in a fully three-dimensional environment. The noise cross-spectral density matrix for a vertical array is computed as the sum of a local contribution and propagation from distant small patches of ocean surface. Propagation from any point to the array is made efficient

GP12A-4 1330h POSTER

Role of Remanent Magnetization in the MAGSAT Crustal Anomaly Field in the SW Indian Ocean

L Fullerton and J Roark (Astronomy Program, University of Maryland, College Park, MD 20742),
H Frey and H Thomas (Laboratory for Terrestrial Physics/Goddard Space Flight Center, Greenbelt MD 20771; 301-286-5450)

The MAGSAT regional crustal magnetic anomalies in the SW Indian-Antarctic Ocean are due to a combination of induced plus viscous remanent magnetization and TRM in Cretaceous Quiet Zone (KQZ) regions. Two broad, roughly parallel, SW to NE trending, multi-peaked lobes of positive reduced-to-pole (RTP) anomalies dominate the region, one lying south of Africa and the other north of Antarctica. Some of the peaks of these anomalies correlate well with the location of submarine plateaus which are tectonic conjugates; i.e., formed together but now separated. But the shape, location of many of the peaks and amplitude contrast of the northern lobe, which runs from the Agulhas Plateau northeastward to the Madagascar Ridge, appears to be controlled mostly by TRM in KQZ crust; structural characteristics (i.e., thickened crust) account for only about 20% of the total anomaly amplitude. Based on modeling results, the TRM contribution varies from about 10 A/m over the Mozambique Plateau and Basin) to about 3 A/m over the Agulhas Plateau, Transkei Basin and Madagascar Ridge (TRM assumed distributed through layer 2). This inferred differential TRM is consistent with available drill core data. The southwestern portion of the Enderby Abyssal Plain has a 3nT positive MAGSAT anomaly over it which is centered south of the Conrad Rise. This entire area is KQZ crust, and the anomaly seems little related to the Conrad structure. The centroid of another 3 nT anomaly which lies between the Maud Rise and Astrid Ridge may also be controlled by the KQZ crust rather than the structural features which flank this portion of the extreme southwest Enderby Basin. Overall there is good correspondence between the MAGSAT RTP anomalies observed for conjugate plateaus and adjacent ocean basins in that portions formed together at the same time but now well separated seem to have similar TRM contributions to the total anomaly contrasts observed. Surprisingly, it may be possible to use MAGSAT data to infer the limits of KQZ crust where this is poorly known.

GP12A-5 1330h POSTER

Magnetization Contrast of the Pacific Cretaceous Quiet Zone Based on Magsat Data

P B Toft and J Artani-Hamed (Dept. of Geological Sciences, McGill University, Montreal, Quebec, H3A 2A7, Canada; 514-398-8052)

The absolute value of magnetization of oceanic lithosphere is poorly known. Information from drill holes is only for the uppermost 0.2 km and that from ophiolites is scattered and sparse. Magnetic anomaly inversion gives only a value of magnetization contrast.

A constraint on the absolute value may be obtained from Magsat data and the Pacific Cretaceous Quiet Zone (QZ) of normal polarity. There are few Magsat anomalies over the east Pacific, and most large anomalies in the west Pacific are correlated with plateaus and seamounts. An anomaly over the Cretaceous Hess Rise, for example is modelled from topography and crustal thickness with a total magnetization contrast of 10,000 A (magnetization x thickness).

In the central Pacific, however, are anomalies that are not obviously correlated with topographic features. Some of these may be due to a magnetization contrast between the QZ and its surroundings: if the magnetic signatures of the narrow bands of normal and reversed magnetizations surrounding the QZ sum to zero at satellite altitude, and if there is no susceptibility contrast across the QZ boundary, then Magsat anomalies may result from an edge effect of the QZ.

To test this hypothesis, the magnetic anomaly of the QZ is calculated at 400 km and it is filtered to simulate removal of long wavelengths overlapping the core field that are extracted from Magsat data along with the core field. The QZ with a total magnetization of about 10,000 A produces 500-1000 km wavelength features spatially associated with the QZ boundary, which are similar in magnitude, wavelength, and location to observed Magsat anomalies. Both the Pacific QZ and isolated plateaus, such as the Hess Rise, indicate a total magnetization of about 10,000 A for the Pacific oceanic lithosphere.

GP12A-6 1330h POSTER

The Intensity of Magnetization of Oceanic Basalts as a Function of Age; Compiled Data from ODP and DSDP Basalts.

J E Pariso and H P Johnson (School of Oceanography, University of Washington, Seattle, WA 98195; 206-543-8542)
H. Sakai (Dept. of Earth Sciences, Toyama University, Toyama, Japan)

In contrast to the original Vine-Matthews model of the magnetization of oceanic crust, we now know that oceanic rocks are subject to changing physical and chemical conditions which have the potential to modify the magnetic properties of crustal rocks. The variation in the intensity of magnetization (J) of oceanic basalts was initially investigated by Bleil and Petersen (1983), who compiled paleomagnetic data from DSDP Legs 1-65. A more recent study at the University of Washington focussed on a re-examination of drilled basalts (0-155 Ma), and includes all of the DSDP and new ODP drill

rock samples. These data were filtered to remove samples with anomalous geochemistry and from non-mid-ocean ridge environments. These new results show that, on average, J for oceanic basalts (1) steadily decrease from 0 to 35 Ma, (2) increase from 35 to 50 Ma, and (3) exhibit no significant change between 90 and 140 Ma. The mean value of J all studied basalts is 3.5 A/m.

The observed decrease in J from 0-35 Ma is consistent with our understanding of the effect of progressive low temperature oxidation on the intensity of natural remanent magnetization. The 35-50 Ma increase must be due to either a submarine process which effects oceanic basalts of this age, or a change in the intensity of the paleomagnetic field. The lack of variation in J between 50 and 140 Ma is not consistent with recent models which predict that basalts formed during the Cretaceous Normal Magnetic Superchron should have substantially higher values of J than basalts formed before, or after, the Superchron. Therefore, we suggest that the high magnetic fields measured by MAGSAT over the Cretaceous Quiet Zones in the Atlantic ocean result from (1) a thicker extrusive layer, or (2) an increased contribution from the lower, intrusive layers of oceanic crust.

GP12A-7 1330h POSTER

Deconvolution for Increased Resolution in AEM Data

Clyde J Bergeron, Jr, George E Ioup, Juliette W Ioup, Long B Trinh, and Abolfazl M Amini (Physics Department and Geophysical Research Laboratory, University of New Orleans, New Orleans, LA 70148; (504) 286-6341)

Deconvolution is a standard technique for removing the effect of the instrument or other response functions from data. In airborne electromagnetic (AEM) measurements, there is an effective impulse response for the AEM measuring device due to the large footprint of the device. We present approximate line and point impulse response functions calculated from the Modified Image Method (MIM) representation of the AEM field. We apply these functions in an iterative deconvolution of data produced from two-dimensional models. The deconvolved results in general show an increase in the effective resolution of the AEM data. (Work supported in part by the U. S. Army Cold Regions Research and Engineering Laboratory.)

GP12A-8 1330h POSTER

Three-dimensional magnetotelluric modeling using difference equations

RANDALL MACKIE and THEODORE MADDEN (Both at: Dept. of Earth, Atmospheric, and Planetary Sciences, M.I.T., Cambridge, MA 02139)

We have developed numerical algorithms for computing the electromagnetic response of a fully inhomogeneous, 3D earth model due to a uniform current source far above the earth (this is the magnetotelluric response). Our algorithms are finite difference algorithms, but they are based on the integral forms of Maxwell's equations rather than the differential forms. This eliminates the need to approximate derivatives of earth properties; indeed, one only needs be concerned with the issue of taking averages of earth properties.

Finite difference algorithms invariably lead to large systems of equations to be solved, especially for realistic 3D earth models. We have investigated relaxation methods (conjugate direction algorithms) and direct methods for solving these systems quickly and accurately. The relaxation solutions are quick, give reasonable answers, and do not require large amounts of computer storage. We have found that a multiple scaling technique used in conjunction with relaxation methods works especially well. The direct solutions are more computer intensive than the relaxation methods because they can require large amounts of storage space and involve doing many matrix inversions. The solutions from our algorithms compare well with the solutions from Wannamaker's integral equation algorithm.

GP12A-9 1330h POSTER

MIM Inversion of AEM Data for Groundwater

Juliette W Ioup, and Clyde J Bergeron, Jr (Physics Department and Geophysical Research Laboratory, University of New Orleans, New Orleans, LA 70148; (504) 286-6715)

The Modified Image Method (MIM) for inversion of airborne electromagnetic (AEM) measurements can be applied to groundwater studies. The effective depth and conductivity of the groundwater is determined from the simultaneous measurements of the AEM transmitter/receiver system altitude and the complex low frequency secondary field. The inversion of the high frequency AEM data allows a determination of the average

conductivity of the overburden layer. The results of such an analysis of data from a groundwater survey performed by the Dighen Company in Michigan will be presented.

GP12B CA: 317 Mon 1330h
Magnetic Methods in Studies of Global Change II

Presiding: R Karlin, Univ of Nevada, Reno; R Negrini, California State Univ

GP12B-1 1330h

Determination of Paleoenvironmental Conditions From Soils Using Rock Magnetic Techniques

Michael J Singer (Dept. of Land, Air and Water Resources, Univ. of Calif., Davis, CA 95616)
Bruce Moskowitz and Kenneth L Verosub (Both at: Dept. of Geology, Univ. of Calif., Davis, CA 95616)
Pinchas Fine (Institute of Soils and Water, Volcani Center, P.O. Box 6, Bet Dagan, ISRAEL)

Soils are sensitive indicators of paleoenvironmental conditions, and horizon by horizon chemical analysis of a soil can provide detailed information about climate and climate change. We have been using rock magnetic techniques to supplement traditional wet chemical methods for tracing the movement and transformation of iron in soils. Our work has shown that enhancement of the magnetic susceptibility of a soil is not a surficial process, as was previously believed, and that the increase in susceptibility results from the retention of inherited magnetite as well as from the precipitation of pedogenic magnetite. Both of these factors are influenced by the water content of the soil, and the enhancement process ceases when a soil becomes poorly drained. We have also found that morphological discontinuities found in soils often have a corresponding magnetic susceptibility anomaly so that susceptibility measurements can be used to evaluate the suitability of soil sequences for detailed pedological analysis. Our one enigmatic result is that the ratio $X_{\text{arm}}/Z_{\text{arm}}$ appears to be independent of soil horizon and particle size fraction within a soil. This result implies that the ferromagnetic particles in a soil fall within a narrow size range.

GP12B-2 1345h

Diagnosis for Greigite (Fe₃S₄) in Cretaceous Basals, North Slope, Alaska, and Holocene Sediments, Lake Michigan

R L Reynolds, A Nicholson, M B Goldhaber (USGS, MS 964, Box 25046, Denver, CO 80225, 303-236-1303)
S M Colman (USGS, Woods Hole, MA 02543)
J W King (Univ. of Rhode Island, Narragansett, RI 02882)
C A Rice, M L Tuttle, and D M Sherman (USGS, Denver, CO 80225)

The presence of postdepositional greigite (Fe₃S₄; ferrimagnetic) can distort depositional magnetic records and thereby jeopardize paleoenvironmental interpretations based on magnetic susceptibility (MS) and remanent magnetization. Our studies have provided means to identify greigite and evaluate its effects. Using X-ray diffraction, thermomagnetic signature, and Mossbauer spectra, we have identified abundant greigite in Upper Cretaceous mudstones from the Simpson Peninsula, North Slope, Alaska, but have found little evidence of it in Holocene mud from southern Lake Michigan.

Greigite dominates magnetic properties of the Cretaceous mudstones, which have a mean MS of 5.9×10^{-4} (vol 51) and a mean NRM magnitude of 6.6×10^{-2} A/m. Geochemically, these mudstones resemble many recent marine sediments: Acid-volatile sulfur (AVS); from greigite and nonmagnetic monosulfide) ranges from 0.02% to 0.20% (by weight); disulfide S (from pyrite) ranges from 0.02% to 0.46%, and the ratio of AVS plus disulfide S to organic carbon averages 0.34.

Comparison of magnetic properties with the distribution of sulfur species in Holocene mud from southern Lake Michigan suggests the presence of greigite and pyrite. Neither mineral, however, appears to obscure the detrital magnetic record, except perhaps in shallow (<20 cm) intervals in some cores. In these shallow intervals, three cores achieve maximum sulfur values (AVS 0.02 to 0.16; disulfide S 0.012 to 0.24 %), mostly within the ranges of the Alaskan mudstones. In one core, the AVS profile mimics the MS profile, both reaching their maximum (AVS 0.02; MS 4.4×10^{-4}) at 6 cm. In the upper 10 cm of another core, high AVS content (maximum 0.16%) corresponds to relatively high MS (4.1×10^{-4}) and NRM (1.1×10^{-2} A/m). Both of these results suggest that some of the AVS may be in the form of greigite. In the latter core, however, high MS also correlates with high sand content, indicating that detrital oxides contribute much more to MS than does greigite. This finding is supported by examination of magnetic separates.

**Determination of Design and Operation Parameters
for Upper Atmospheric Research Instrumentation
to Yield Optimum Resolution with Deconvolution**

NASA Grant NAG 1-804

FINAL REPORT

APPENDIX 5

Dr. George E. Ioup, Principal Investigator
Dr. Juliette W. Ioup, Principal Investigator
Department of Physics
University of New Orleans
New Orleans, LA 70148

DETERMINATION OF DESIGN AND OPERATION PARAMETERS
FOR UPPER ATMOSPHERIC RESEARCH INSTRUMENTATION
TO YIELD OPTIMUM RESOLUTION WITH DECONVOLUTION

NASA GRANT NAG 1-804

APPLICATIONS OF THE MODIFIED IMAGE METHOD TO THE AEM STUDY OF SEA ICE

FINAL REPORT

29 Aug 1989

Dr. Clyde J. Bergeron, Jr., Principal Investigator
Dr. Juliette W. Ioup, Principal Investigator
Dr. George E. Ioup, Principal Investigator
Department of Physics
University of New Orleans
New Orleans, LA 70148

INTRODUCTION

Classical image theory may provide a simple method for calculating the secondary field produced by a conducting structure in response to an applied field. The three-dimensional screening distribution that is induced in the conductor is replaced by an image (or a distribution of images) of the primary source. When the primary field is magnetic, classical image theory may be used in the case of a "perfect" conductor (high frequencies and/or high conductivities) or for the response of a superconductor to a constant magnetic field. The general criterion for the applicability of classical image theory is that the weighted average depth of the screening current distribution (the superconducting penetration depth or the complex skin depth in the ohmic case) be much less than the altitude of the primary source above the conducting surface.

The essential constraint on the image sources for the magnetic case is that they produce a secondary field at the surface of the conductor whose normal component, B_{sn} , is equal but opposite to the normal component of the primary field, B_{pn} , thus satisfying the continuity condition on B_n at the interface. A symmetry constraint on the tangential components, B_{pt} and B_{st} , results in their equality. Thus

$$\vec{B}(\text{surface}) = \vec{B}_p + \vec{B}_s = 2 B_{pt} \hat{T} \quad , \quad (1)$$



where \hat{T} is a unit vector in the conducting surface. The conductor surface is generally termed the image surface.

Only simple interface geometries allow for simple distributions of image sources. A plane interface requires only one image source to satisfy the electromagnetic boundary conditions on B_n . In this case the secondary field produced by the induced current distribution is accurately replicated in the nonconducting halfspace by the field of a single image source. An alternate source distribution to the image source is provided by a surface current \vec{K} which is given by $\vec{K} = \hat{n} \times \vec{B}$ at the image surface, where \hat{n} is the normal to the surface. Thus \vec{K} is given by

$$\vec{K} = 2 B_{pt} \hat{T}' \quad , \quad (2)$$

where \hat{T}' is a unit vector tangent to the surface but perpendicular to \hat{T} and \hat{n} . The secondary field produced by the surface current distribution \vec{K} is identical to the field produced by the image source, but this calculation is less direct since it involves an integration over the surface.

The modified image method (MIM) has all the elements of the classical image theory EXCEPT that the image surface is relocated to one weighted average screening length BELOW the conducting surface. For the ohmic case this distance is complex and is given by $[\exp(-i\pi/4)/\sqrt{2}]\delta$, where δ is the electromagnetic skin depth $\delta = \sqrt{2/(\mu_0\sigma\omega)}$. For a plane layered conducting medium, δ is modified by a complex correction factor, \tilde{Q} (Bergeron et al., 1987). The complex image field produced by this



assumption is in good agreement with the secondary field given by the one-dimensional Sommerfeld theory (Sommerfeld, 1909).

For non-planar conducting models (two- and three-dimensional), there is no general prescription for determining a distribution of image sources that will satisfy the electromagnetic boundary condition, and in general none exist. The standard methods of calculating the secondary field produced by two- and three-dimensional structures (e.g., the finite element method (Lee and Morrison, 1985)) are generally of an iterative nature and hence computationally slow.

MIM provides a fast, efficient, but approximate method for calculating the secondary field. We assume the general validity of Eq. (2), which defines a surface screening current distribution \vec{K} in terms of the tangential component of \vec{B}_p . This screening distribution is at a complex skin depth, $[\exp(-i\pi/4)/\sqrt{2}]\delta$, below the conducting surface, where now \hat{n} is the LOCAL normal to the conducting surface. Equation 2 gives \vec{K} in terms of the primary field alone. The heart of this approximation is that the relation $B_{st} \approx B_{pt}$ is still valid.

In the context of the MIM theory, the primary field \vec{B}_p on the image surface is a formally complex function, since it is a function of the primary source strength (real), the lateral displacement of the source from the image surface point (real), and the vertical separation between the source and the image surface point, $h + \delta_{eff}$ (complex). It follows that \vec{B}_p and \vec{K} in the image plane, given by Eq. (2), and the secondary field



generated at the detector by \vec{K} are complex, i.e., the secondary field is not in phase with the primary field at the detector. Thus in the image-source surface a discontinuous change in a model parameter results in a local discontinuous vertical displacement of the source surface. That is, a discontinuous change in σ_1 , σ_2 or d_1 for a two-layer model, results in a discontinuous change in δ_{eff} , and hence a vertical shift in the source surface.

In this approximation the source surface is now disjointed and the strength of the secondary surface distribution is calculated locally in various areal cells of the surface. The individual contributions of these source surface cells are summed up at the detector coil location. In general the area of a surface cell is decomposed into Cartesian components

$$\vec{da} = da \hat{n} = \alpha da \hat{i} + \beta da \hat{j} + \gamma da \hat{k} \quad ,$$

where α , β , and γ are direction cosines with respect to the x, y, and z axes, respectively.

There are two facts that render the assumption of the general validity of Eq. (2) at least plausible. The first is that the field is screened from the interior of the conductor independent of its geometry, i.e., $B_{interior} \approx 0$. The second is that Eq. (2) provides for the approximate satisfaction of the electromagnetic boundary condition at the image surface. \vec{K} produces a stepwise discontinuity in B_t at the image surface from $2B_{pt}$ to approximately zero, and likewise implies that $B_n = 0$ at the surface, thus satisfying the boundary conditions on B_n .



The secondary field produced by \vec{K} of Eq. (2) is easily and rapidly calculated, taking about 1 sec/survey point for fairly arbitrary two-dimensional models. See Table 2.

The ultimate utility of this approximate method of calculating secondary fields produced by two- and three-dimensional structures depends on how well these MIM fields agree with secondary fields generated by other methods of calculation and with scaled model laboratory measurements and survey results.

In this report we give the resultant numerical calculations of the MIM secondary fields produced by models of ice keels. The specific models studied were:

- 1) rectangular trough models in which we examine the dependence of the secondary maximum (in ppm of the primary field) and the secondary field half maximum width (in meters) on keel depth, width, and bird altitude.

- 2) a triangular ice keel model which we label the Berkeley model, identical to one used by Becker et al. (1987).

We compare the results of the MIM two-dimensional field with the Berkeley two-dimensional calculation and to a one-dimensional Sommerfeld calculation.

- 3) a "CRREL" model which is based on an Arctic sea-ice survey ground truth data set provided by CRREL (bird altitude, ice and snow freeboard, and keel depth versus range).

THEORY

In this section we include the "working equations"



which are used in the numerical computations of the secondary fields produced by the current distribution given by Eq. (2) for two-dimensional structures. We also include the MIM and Sommerfeld one-dimensional formulations which result in fields that exactly track the geometry of the model. The two-dimensional MIM approximation produces fields that vary more smoothly but still generally track the model. There is one exception to this rule which will be pointed out and discussed later in this report.

Table 1 illustrates and defines the notation used for the normalized secondary field detected by the various possible permutations of horizontal coil pairs.

Table 1

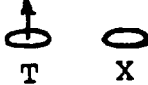
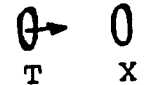
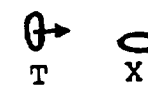
name	coil pair	diagram	normalized secondary field
horizontal coplanar		 T X	$ZZ = H_{sz}/H_p$
horizontal coaxial		 T X	$XX = H_{sx}/H_p$
horizontal mixed 1		 T X	$ZX = H_{sx}/H_p$
horizontal mixed 2		 T X	$XZ = H_{sz}/H_p$



Table 2 gives the total CPU time per survey point for a line survey and the horizontal surface element dimensions.

Table 2

Field	sec/survey point	step sizes	
XX } XZ }	1.34	$\Delta x = 0.5 \delta_1$	$\Delta y = 1.0 \delta_1$
ZZ } ZX }	1.74	$\Delta x = 0.5 \delta_1$	$\Delta y = 1.0 \delta_1$

One-dimensional Fields

MIM

$$ZZ = \frac{2R_M^2 - 1}{(1 + R_M^2)^{5/2}}$$

$$R_M = \frac{2h + (1-i) \tilde{Q} \delta_1}{x_d} \quad (3a)$$

$$XX = \frac{-\frac{1}{2}(R_M^2 - 2)}{(1 + R_M^2)^{5/2}}$$

(3b)

$$ZX = \frac{3R_M}{(1 + R_M^2)^{5/2}}$$

(3c)

$$XZ = \frac{-3R_M}{(1 + R_M^2)^{5/2}}$$

(3d)

Note: $\frac{|ZZ|}{|XX|} = \frac{2R_M^2 - 1}{\frac{1}{2}(R_M^2 - 2)} \approx \frac{2R_M^2}{\frac{1}{2}R_M^2} \approx 4$

Two-Dimensional Fields

Horizontal surface elements:

$$\frac{\Delta B_z}{B_{zp}} = \Delta z z_h = \frac{6x_p^3 \tilde{h} \Delta x \Delta y}{4\pi R^3 R'^5} (e^2 - x x_p), \quad e^2 = x^2 + y^2 \quad (5a)$$

$$R = (x^2 + y^2 + \tilde{h}^2)^{1/2}$$

$$R' = ((x-x_p)^2 + y^2 + \tilde{h}^2)^{1/2}$$

$$\tilde{h} = h_0 + \left(\frac{1-i}{2}\right) S_1 R$$

$$\frac{\Delta B_x}{B_{zp}} = \Delta z X_h = \frac{-6x_p^3 \tilde{h}^2 \Delta x \Delta y}{4\pi R^3 R'^5} (x - x_0) \quad (5c)$$

$$\frac{\Delta B_x}{B_{zp}} = \Delta X X_h = \frac{x_p^3 \tilde{h} \Delta x \Delta y}{4\pi R^3 R'^5} [2(x-x_p)^2 - (y^2 + \tilde{h}^2)] \quad (5b)$$

$$\frac{\Delta B_z}{B_{xp}} = \Delta X z_h = \frac{x_p^3 \Delta x \Delta y}{4\pi R^3 R'^5} [(x-x_0) \{3y^2 + 2x(x-x_0)\} - x(y^2 + \tilde{h}^2)] \quad (5d)$$

Vertical surface elements:

$$\Delta z z_v = \frac{2x_p^3 x \Delta y \Delta z}{4\pi R^3 R'^5} [2\tilde{h}^2 - (x-x_0)^2 - y^2] \quad (6a)$$

$$\Delta X X_v = \frac{3x_p^3 \Delta y \Delta z}{4\pi R^3 R'^5} [(x-x_0)(y^2 - \tilde{h}^2)] \quad (6b)$$

$$\Delta z X_v = \frac{2x_p^3 \tilde{h} \Delta y \Delta z}{4\pi R^3 R'^5} [2(\tilde{h}^2 + y^2) - (x-x_0)^2] \quad (6c)$$

$$\Delta X z_v = \frac{-3x_p^3 \Delta y \Delta z}{4\pi R^3 R'^5} [(x-x_0)(x\tilde{h})] \quad (6d)$$

Note: The contribution of vertical surface elements to the models that are used in these calculations is small compared to the horizontal elements and so has not been included in the section presenting results.

With the detector located at the origin of the coordinate system, the transmitter has Cartesian coordinates $(x_0, 0, 0)$ and an element in the source surface has Cartesian coordinates $(x, y, -h)$. R is the complex distance between a source element and the detector, and R' is the complex distance between a source element and the transmitter.

RESULTS

In this section we discuss the results of the investigations in the context of the tasks set forth in the contract.

Task 1: The implementation of a MIM halfspace inversion algorithm for AEM data.

This task has been completed, and a printout of the code and a magnetic tape containing the code has been delivered to CRREL.

Task 2: Implementation of a MIM algorithm to calculate approximate AEM signatures of ice keels as functions of their width and depth.

This task has been completed. MIM two-dimensional computer codes for rectangular and triangular sea ice keel models have also been delivered to CRREL in both printout and magnetic tape forms. We were initially tasked to produce algorithms and sample calculations of the MIM two-dimensional ZZ fields (horizontal coplanar coil configuration). We have extended that task to include the XX (horizontal coaxial coils) and ZX fields. These calculations have been applied to two ice keel models. For the CRREL model based on ground truth data of an ice keel in Prudhoe Bay, the ZZ and XX fields have been inverted using the one-dimensional MIM inversion to produce values for the model parameters. The Berkeley model (Becker et al., 1987) is a triangular ice keel for which the XX field has been calculated using a finite element method. We compare results of these two



calculations. A detailed discussion follows.

Task 3: Implementation of an analytic continuation algorithm of AEM data.

The feasibility of analytically continuing AEM data up and down 10 m by a Taylor's series expansion of the MIM field has been demonstrated. A preliminary report of these results was made at the American Geophysical Union meeting in San Francisco in Dec 1988, and the abstract published (Bergeron et al., 1988). A more detailed discussion and illustration of this work follows below.

Task 4: Deconvolution algorithm for ice keel signal signatures.

The results for the preceding tasks show that the two-dimensional MIM ice keel fields (with the exception of the ZX and probably the XZ fields) track the one-dimensional fields in a "smoothed out" way. It is anticipated that an efficient deconvolution algorithm of the two-dimensional fields by a line impulse source signal will sharpen the two-dimensional fields and bring them into closer agreement with the one-dimensional fields, thereby bringing one-dimensional inversion results of the two-dimensional fields into closer agreement with the input model.

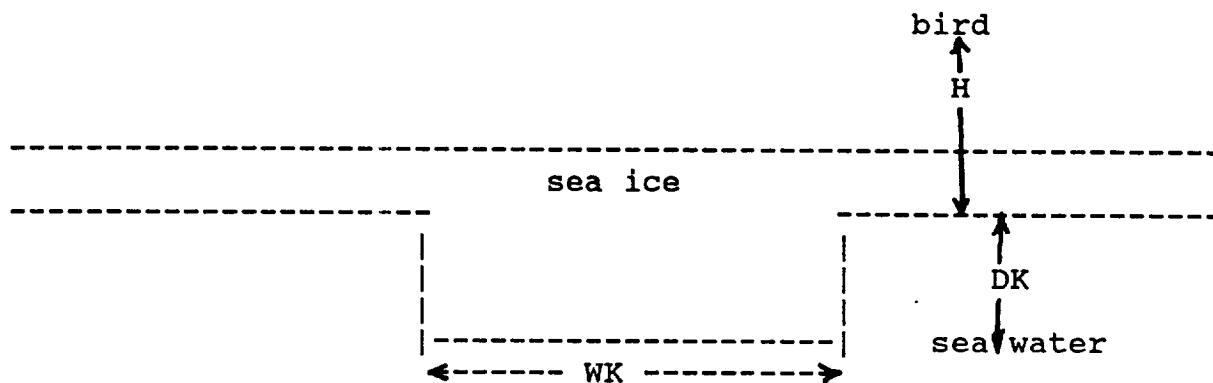


TASK TWO

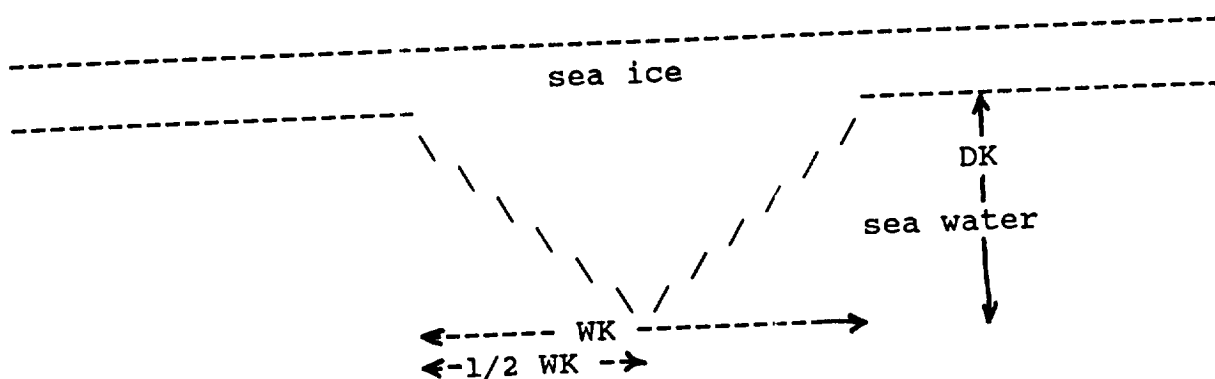
Approximate ZZ MIM Signal Signatures of Rectangular and Triangular Ice Keels

The sea ice is assumed to be transparent to the AEM field, i.e., its conductivity is assumed negligible. All lengths in these models are scaled to the AEM skin depth in sea water and all fields calculated are for the horizontal coplanar ZZ coil configuration.

Rectangular Keel



Triangular Keel



Definition of variables:

H = altitude of bird above sea water/ice interface

WK = width of ice keel

DK = depth of ice keel

DX = numerical integration increment parallel to survey path

DY = numerical integration increment perpendicular to survey path

XO = coil spacing in AEM bird (for example, if the coil spacing is 6 m and XO is 0.6, then the skin depth is 10 m; the altitude of the bird above the seawater is 3.0 m if H = 3.0, and the width and depth of the keel are 10 m if WK and DK are 1.0)

In Figures 2-1 through 2-11, H_z/H_p is plotted versus range (in skin depths) for rectangular and triangular keel models. The keels are centered at zero for various combinations of WK, DK, and H. The solid and dashed curves are the real and quadrature signals, respectively. The larger pairs of signals



are produced by the rectangular keels.

In Figures 2-12 and 2-13, AMP is the maximum signal in ppm produced by the ice keel as the bird passes overhead. Figure 2-12 shows AMP versus WK, and of course the signal saturates at about 600 ppm. This is the difference in the signals produced at altitudes of $H = 3$ and $H+DK = 4$. Figure 2-13 shows the variation in AMP with keel depth DK for a fixed keel width. The saturated value of AMP in this case is about 140 ppm.

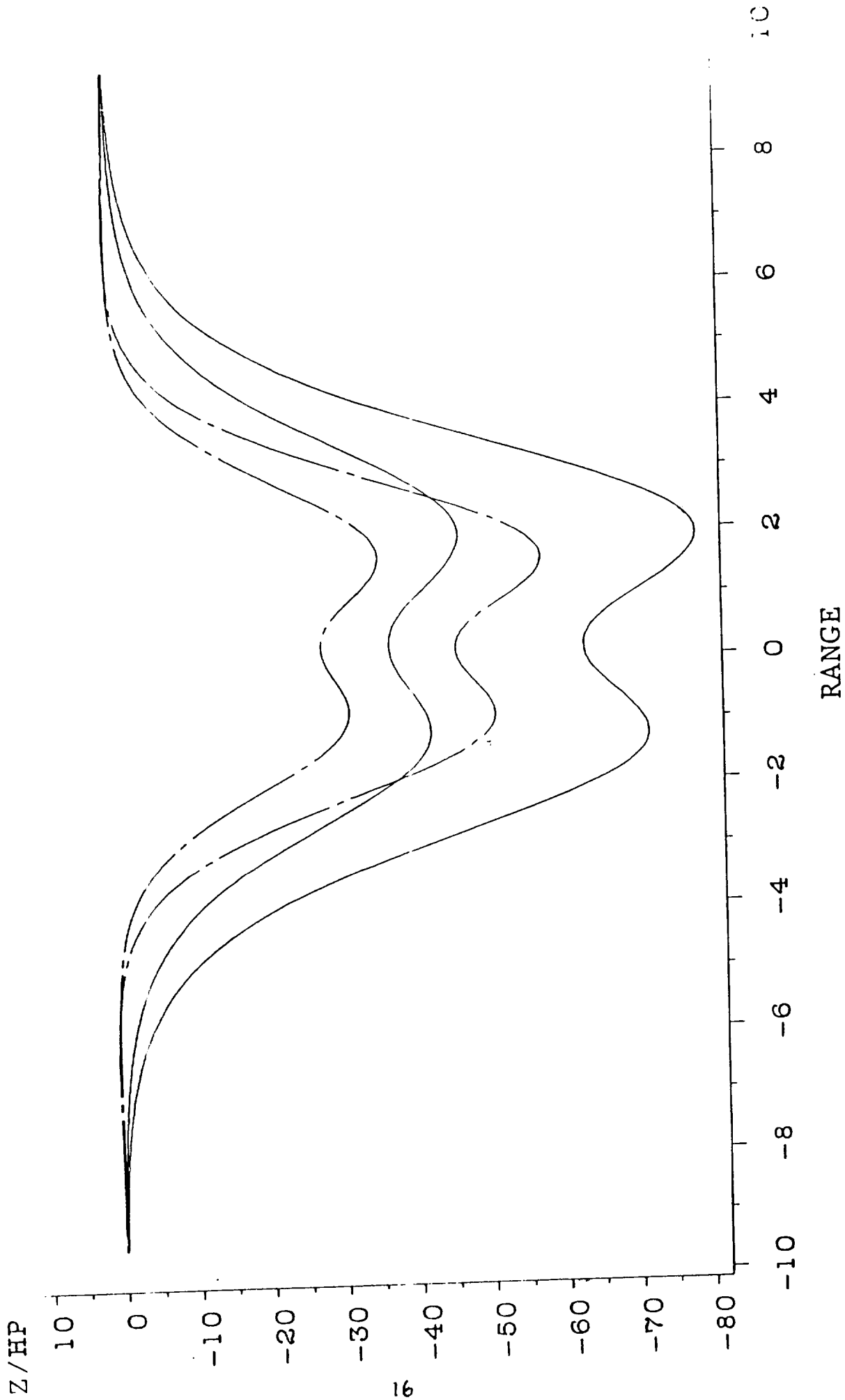
In Figures 2-14, 2-15, and 2-16 the 50% signal level signature width (WIDTH) is plotted versus keel width for constant keel depth, or versus keel depth for constant keel width. Note that the residual 50% signal width for narrow ice keels ($WK < 4$) is approximately 7 for $H = 3$. Thus narrow ice keels produce a 50% width signal approximately equal to twice the bird altitude plus ice thickness.



RECT. & TRIAN. KEEL

WK=1 DK=1

H=3 X0=0.6 DX=0.1 DY=1





RECT. & TRIAN. KEEL

$WK=1$ $DK=1$

$H=5$ $X0=0.6$ $DX=0.1$ $DY=1$

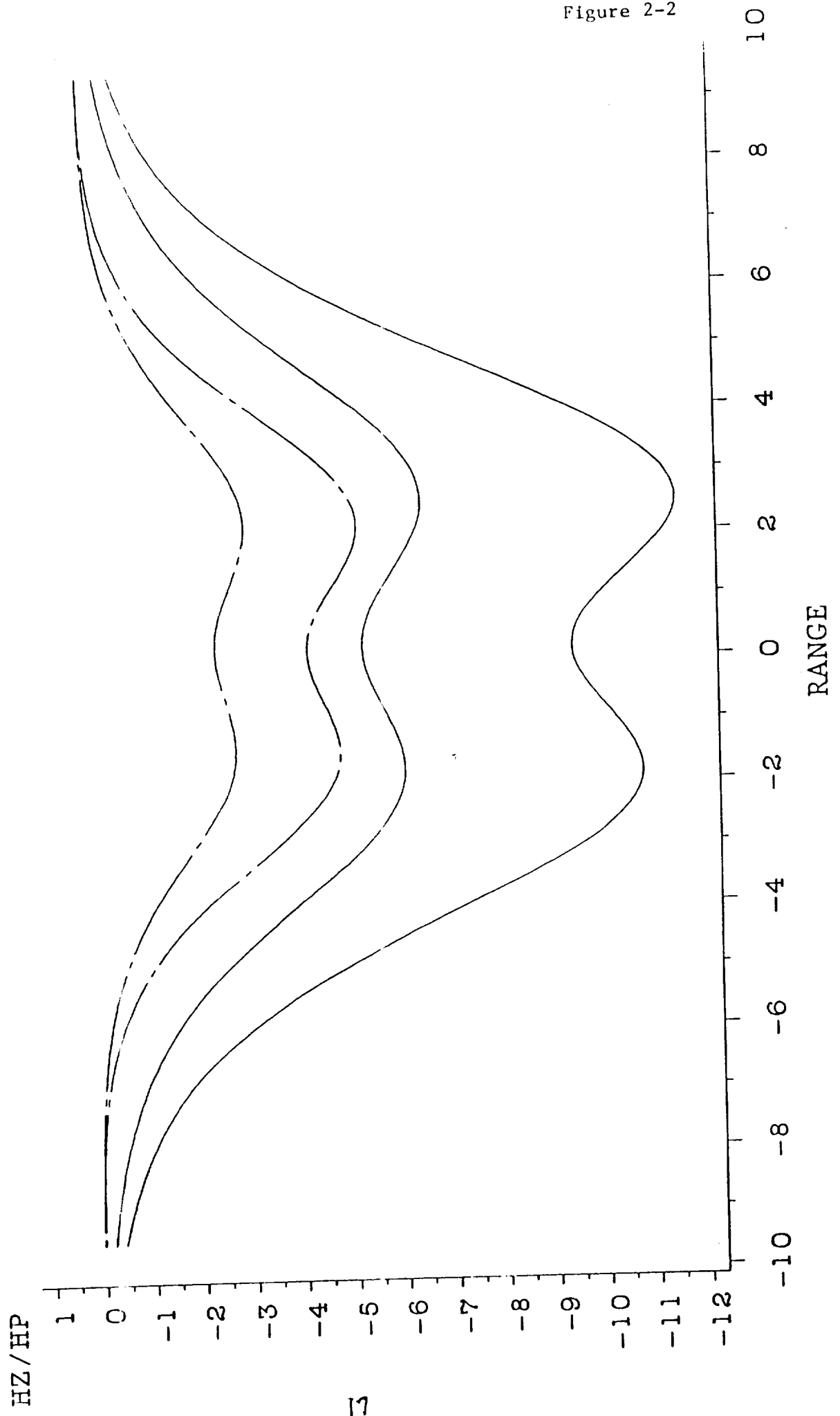


Figure 2-2



RECT. & TRIAN. KEEL

WK=1 DK=3

H=3 X0=0.6 DX=0.1 DY=1

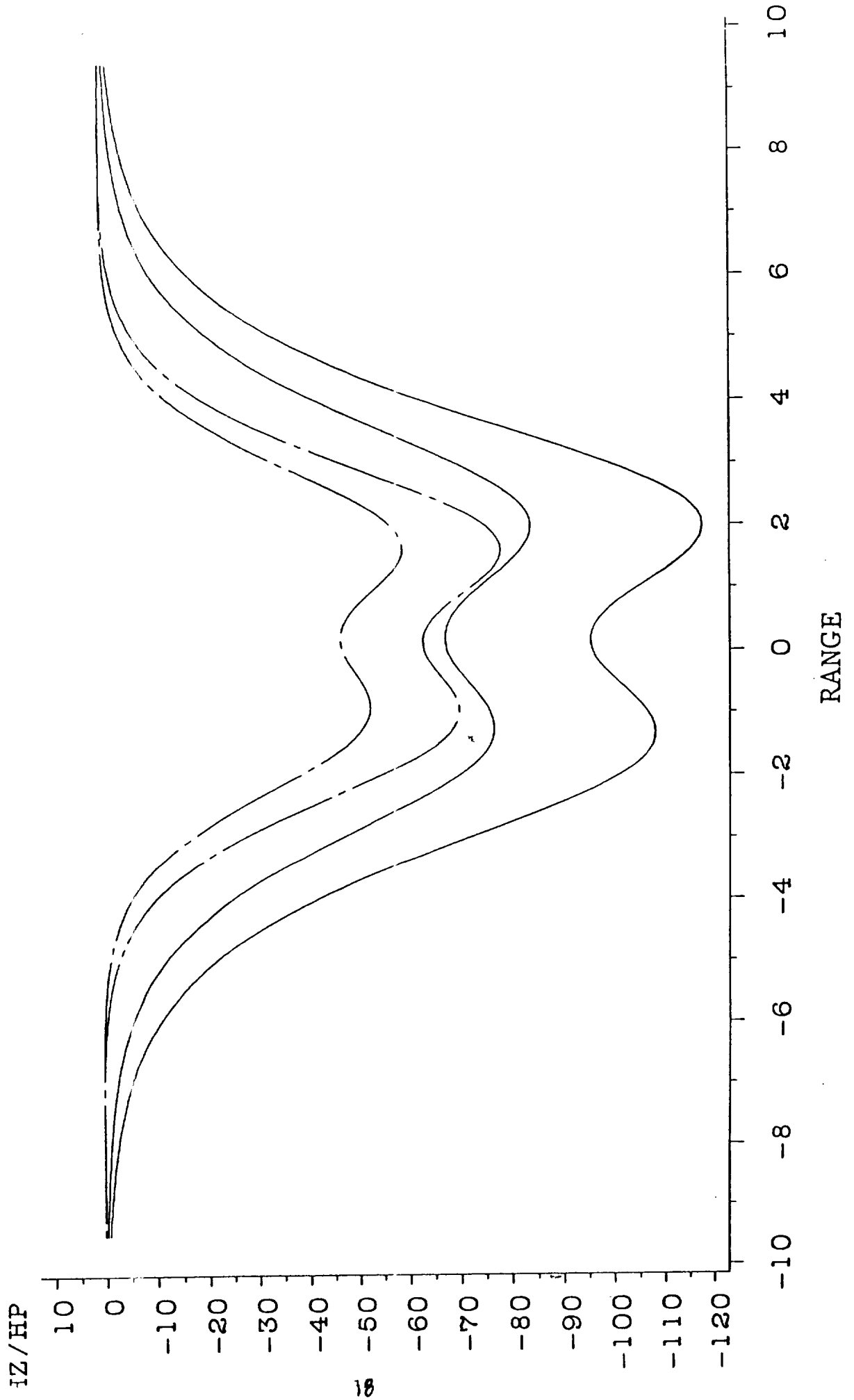


Figure 2-3

RECT. & TRIAN. KEEL

WK=2 DK=1

H=3 X0=0.6 DX=0.1 DY=1

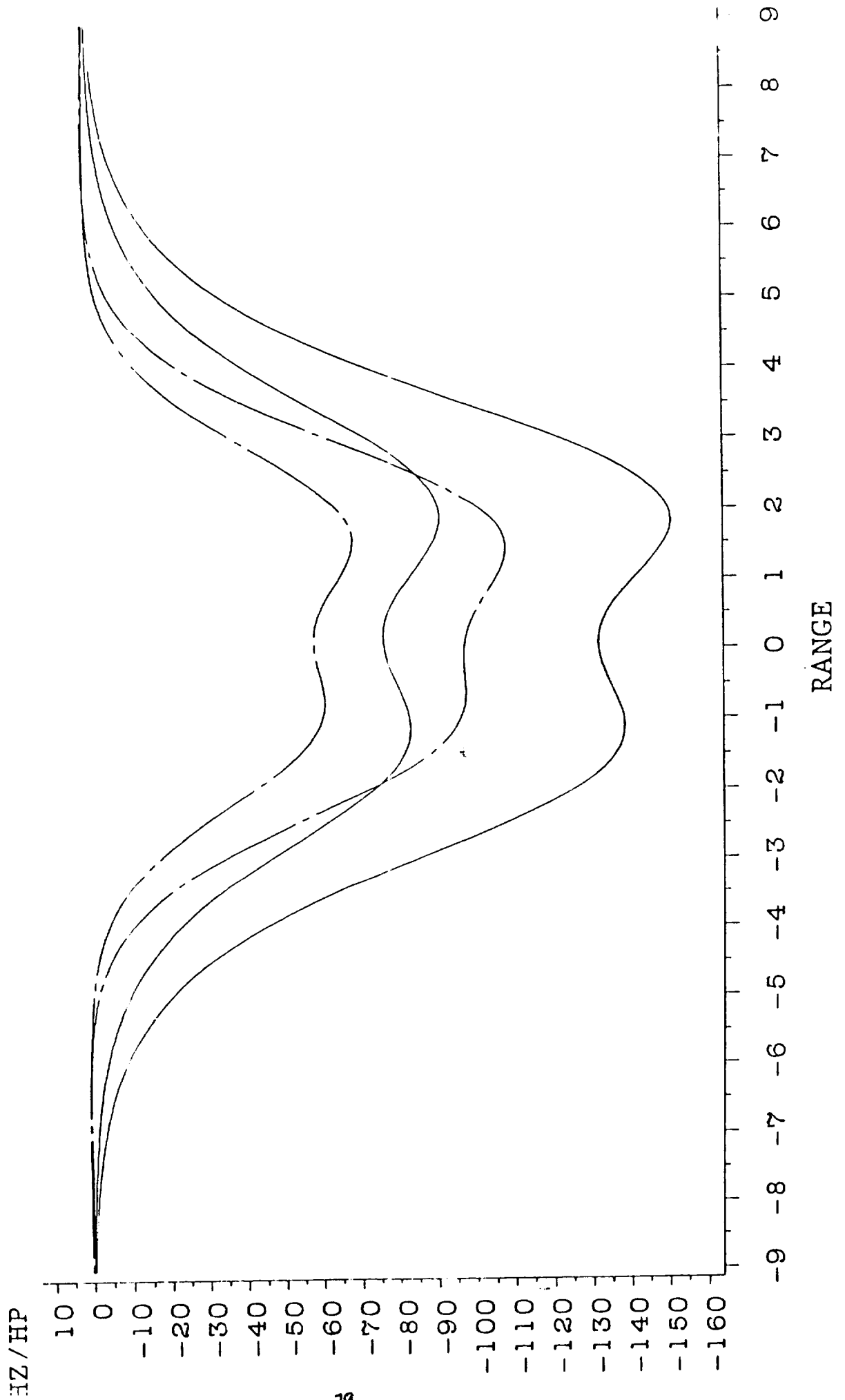


Figure 2-4

RECT. & TRIAN. KEEL

WK= 3 DK=1

H=3 X0=0.6 DX=0.1 DY=1

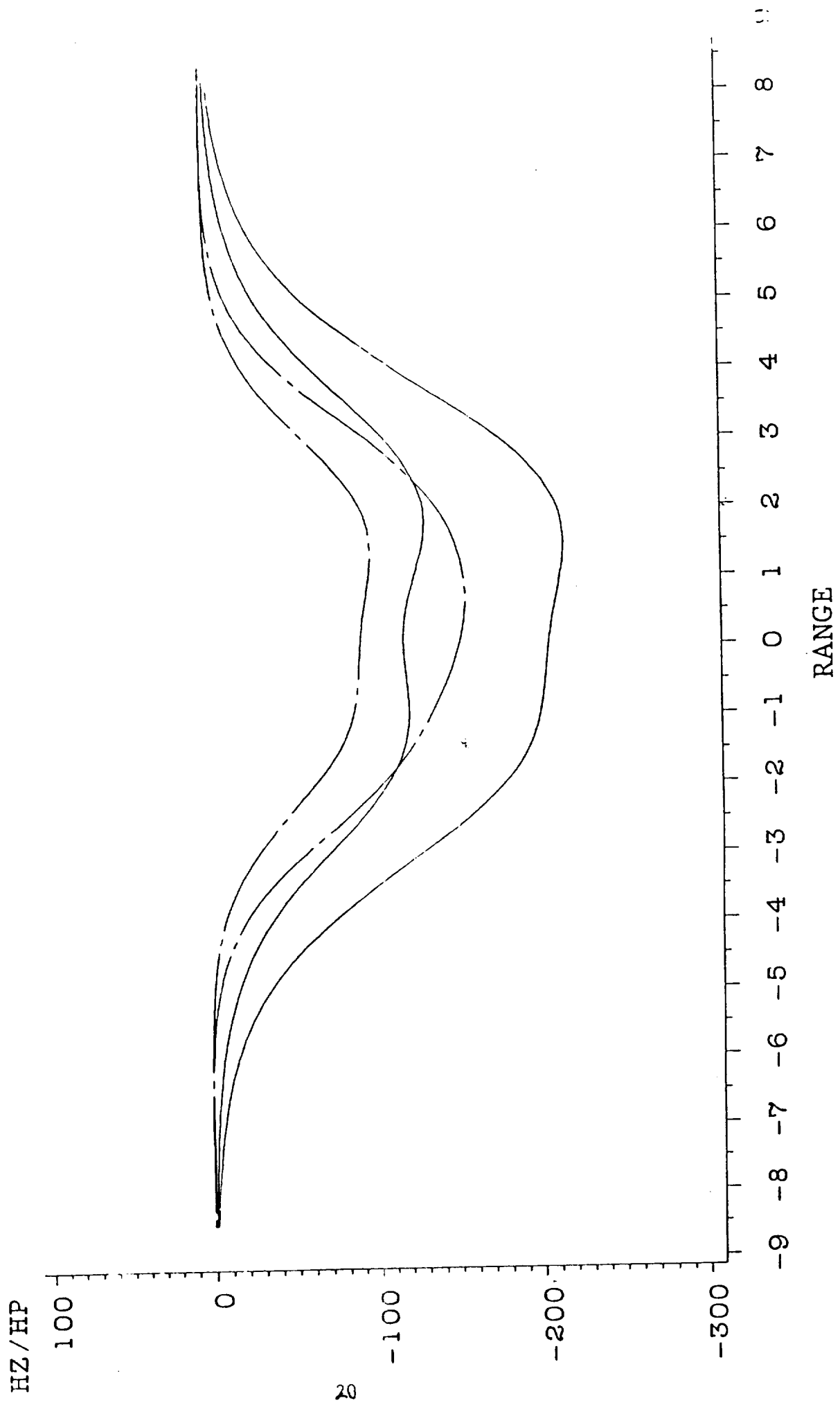


Figure 2-5



RECT. & TRIAN. KEEL
WK= 4 DK=1
H=3 X0=0.6 DX=0.1 DY=1

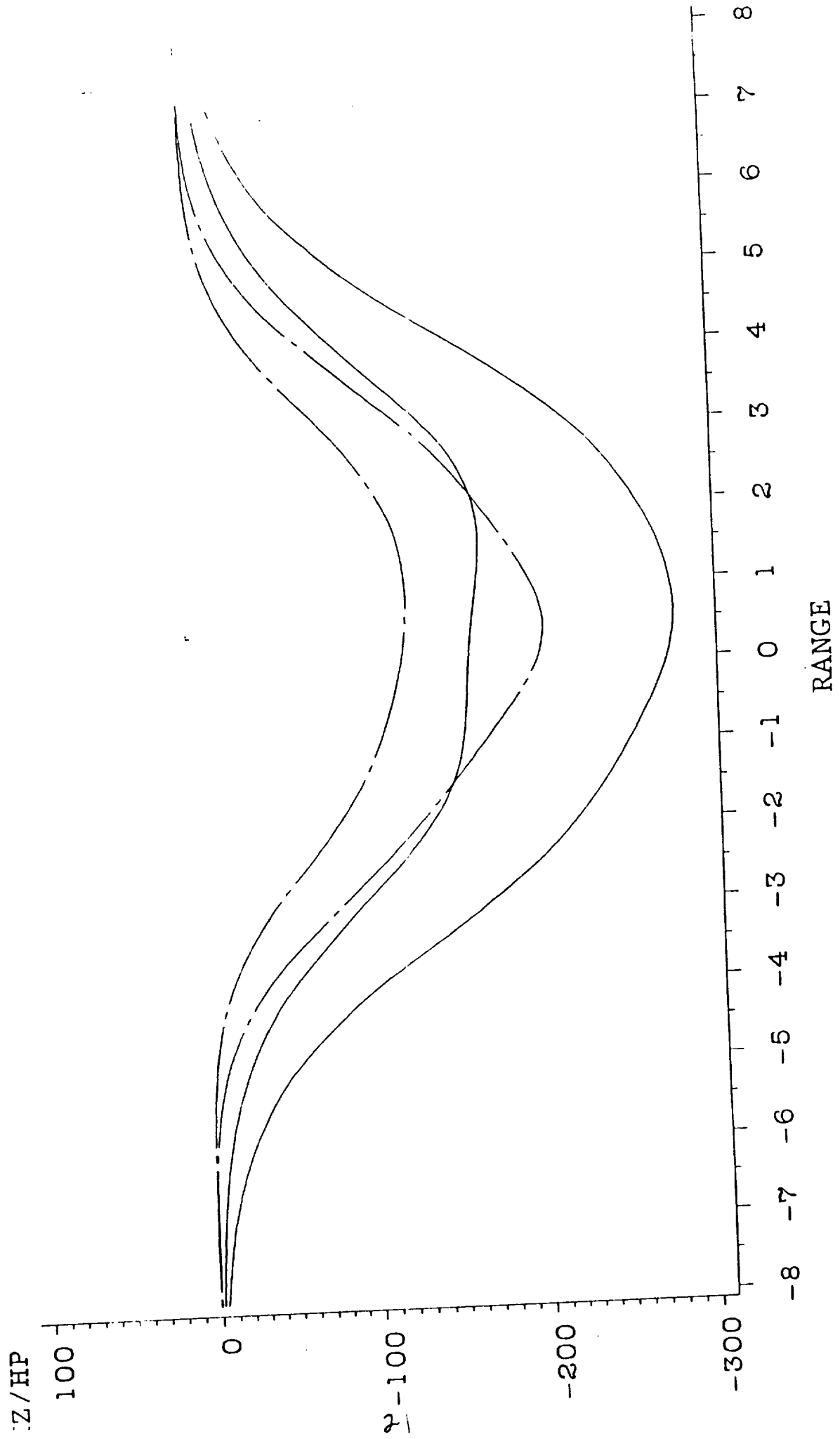


Figure 2-6

RECT. & TRIAN. KEEL

WK=2 DK=6

H=3 X0=0.6 DX=0.1 DY=1

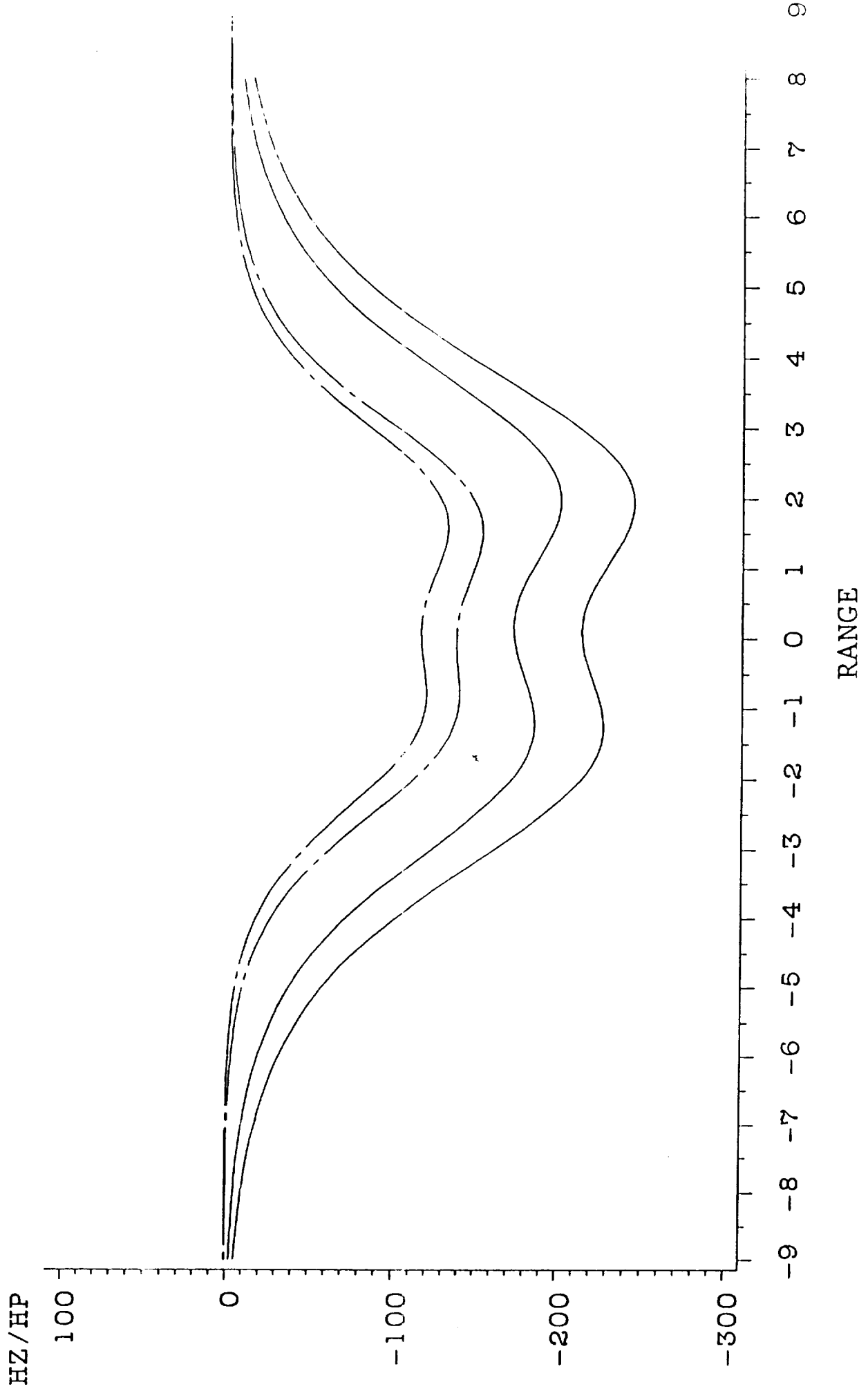


Figure 2-7

RECT. & TRIAN. KEEL

WK= 3 DK=6

H=3 X0=0.6 DX=0.1 DY=1

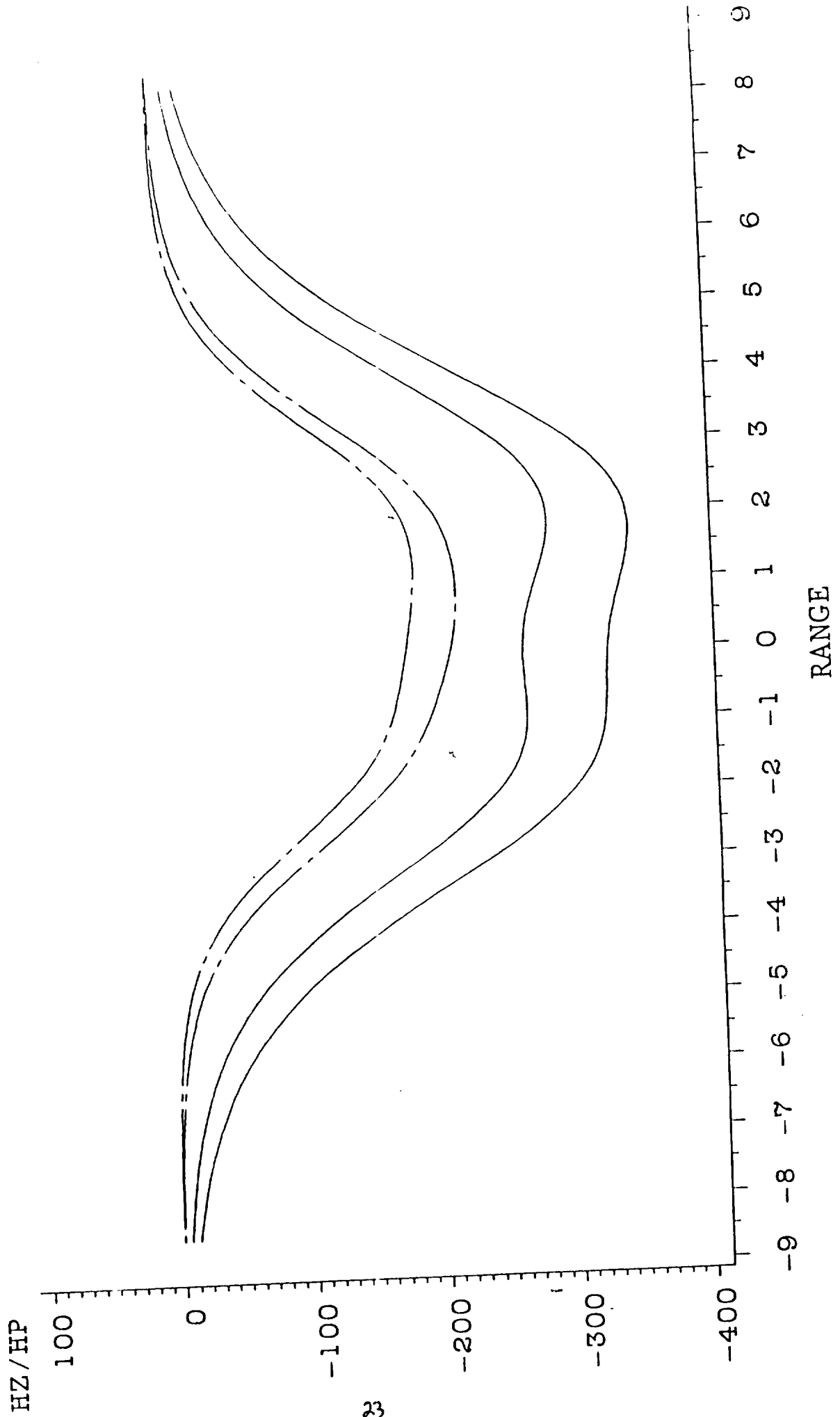


Figure 2-8



RECT. & TRIAN. KEEL

WK= 4 DK=6

H=3 X0=0.6 DX=0.1 DY=1

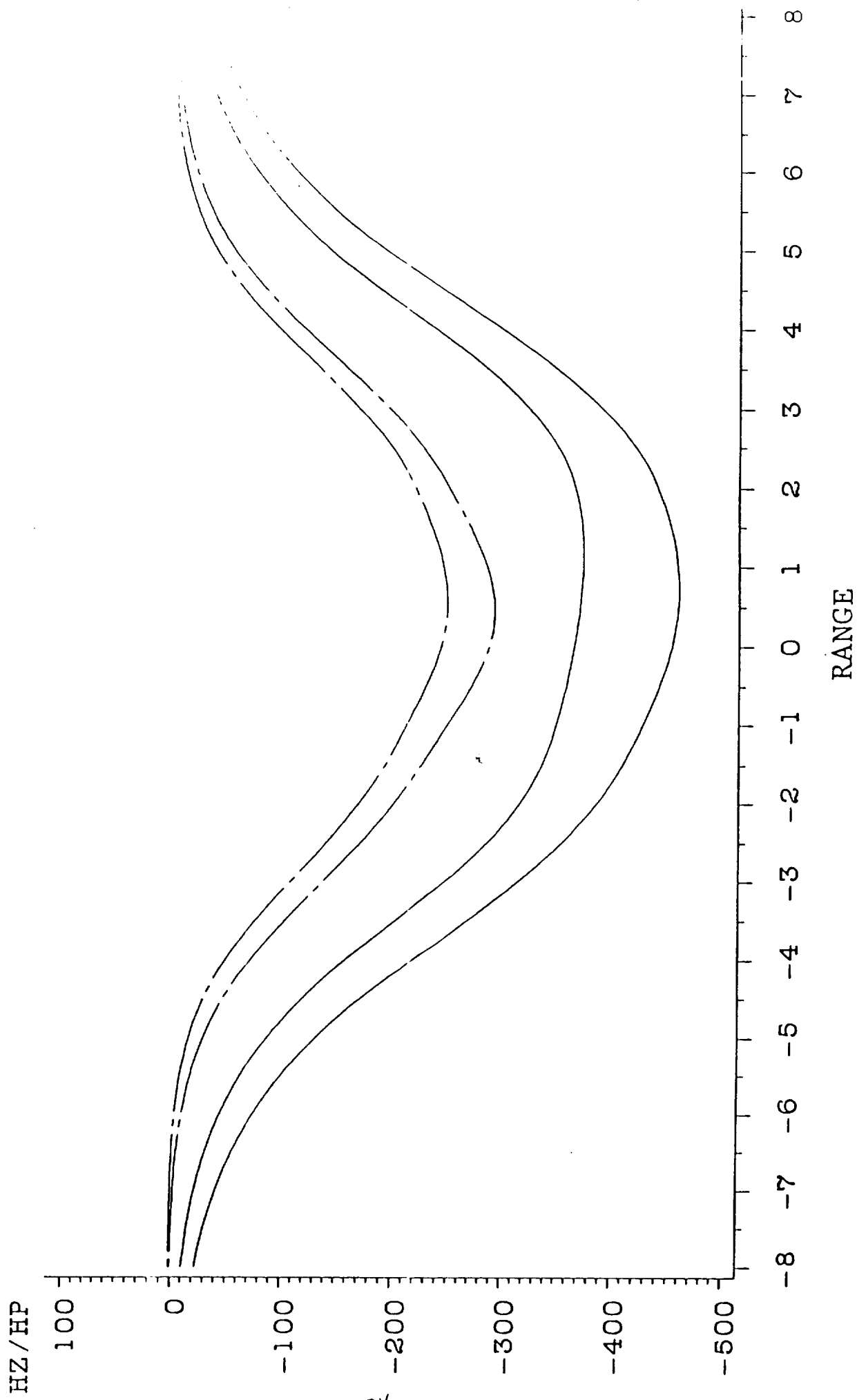


Figure 2-9



RECT. & TRIAN. KEEL

WK= 5 DK=6

H=3 X0=0.6 DX=0.1 DY=1

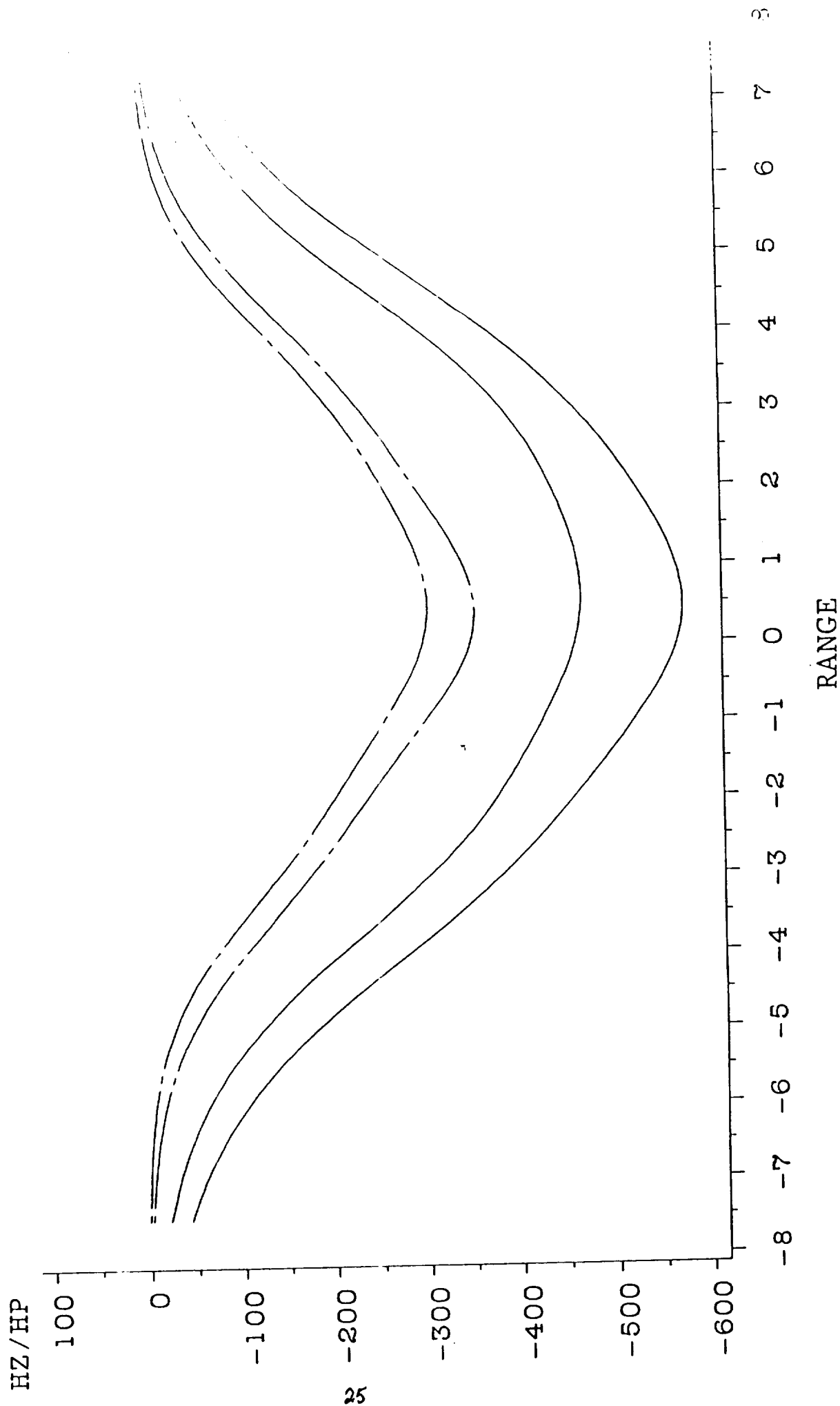


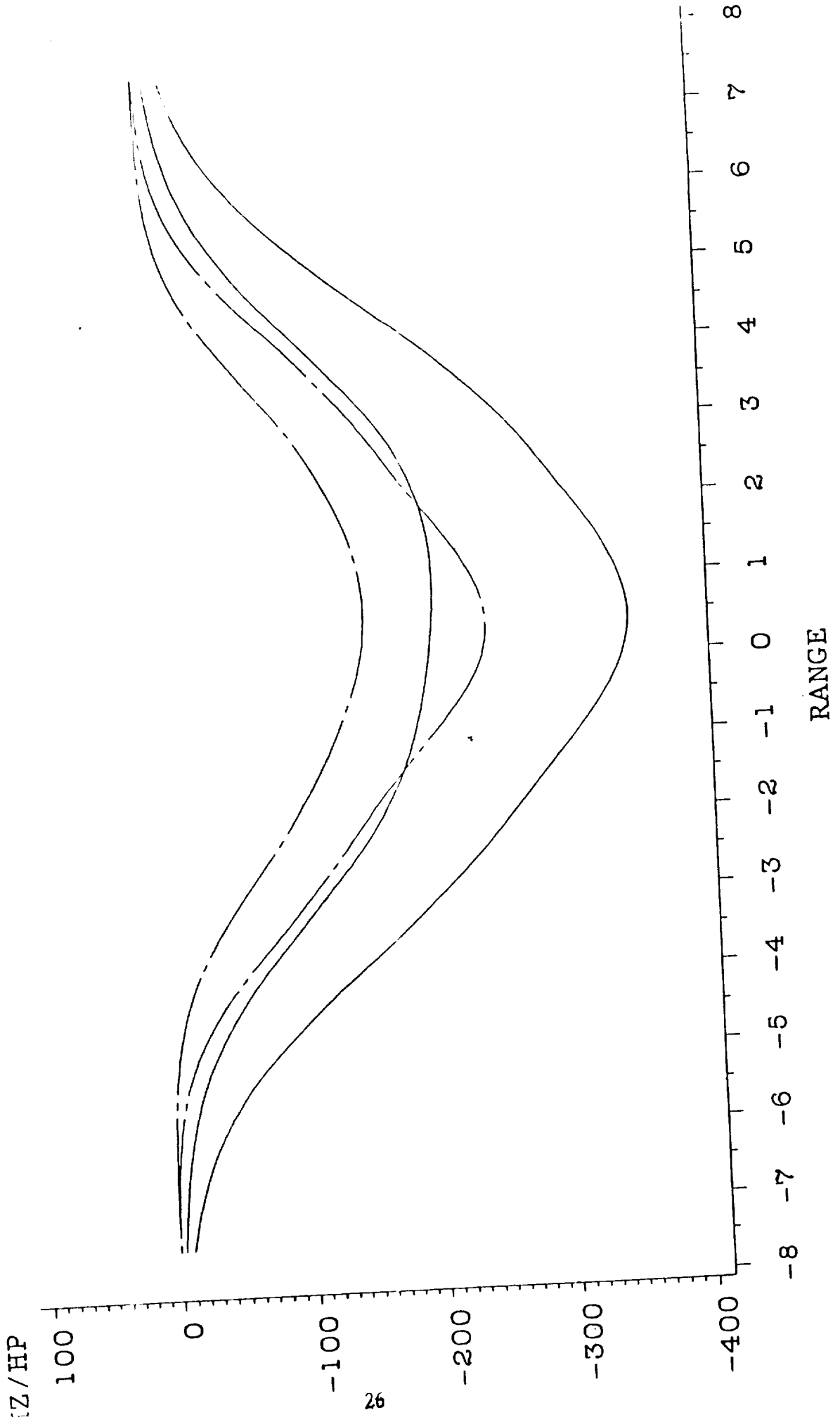
Figure 2-10



RECT. & TRIAN. KEEL

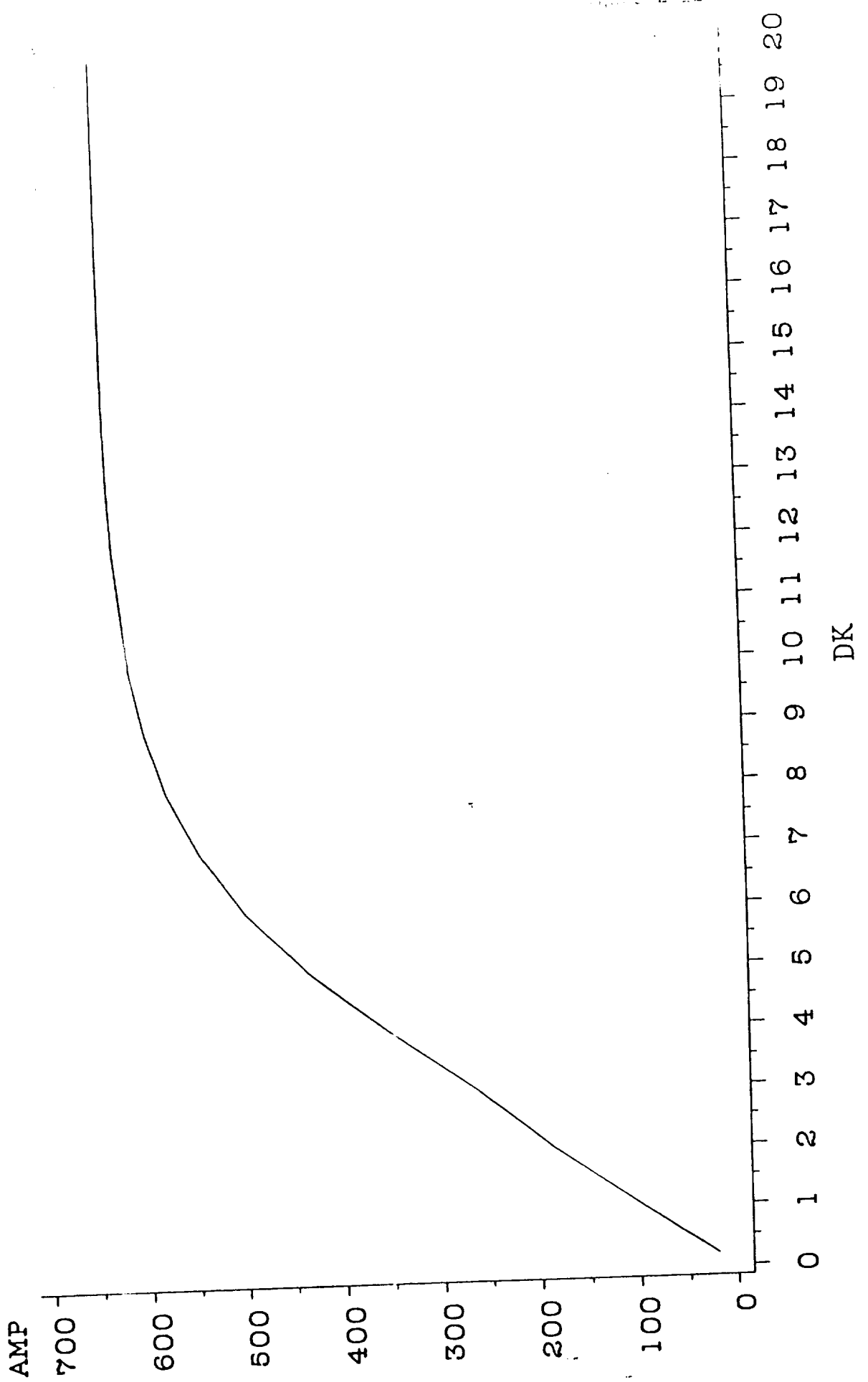
WK= 5 DK=1

H=3 X0=0.6 DX=0.1 DY=1



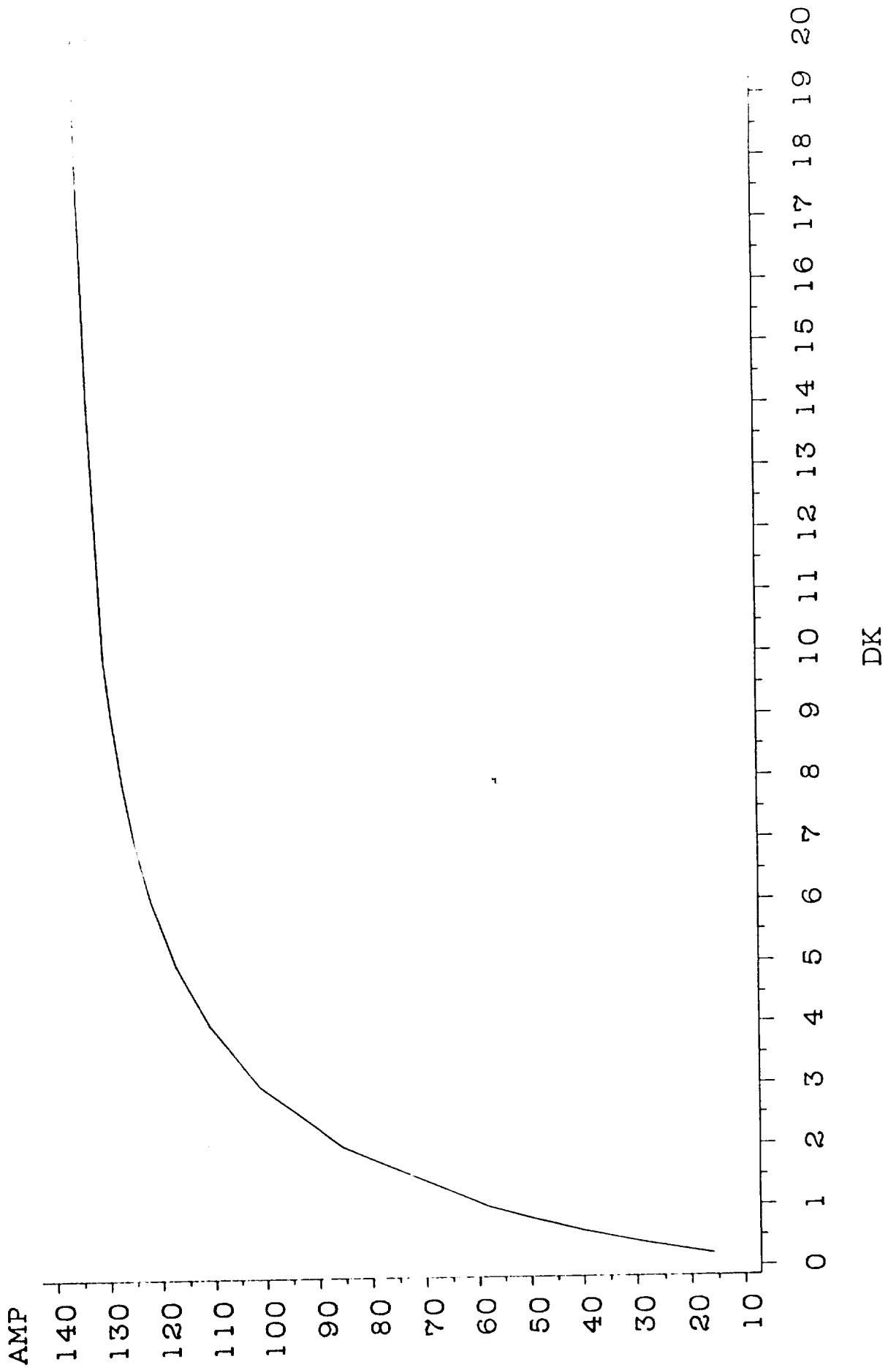


RECT. TROUGH
H=3 COIL=0.6
DX=0.1 DY=1 WK=1.0

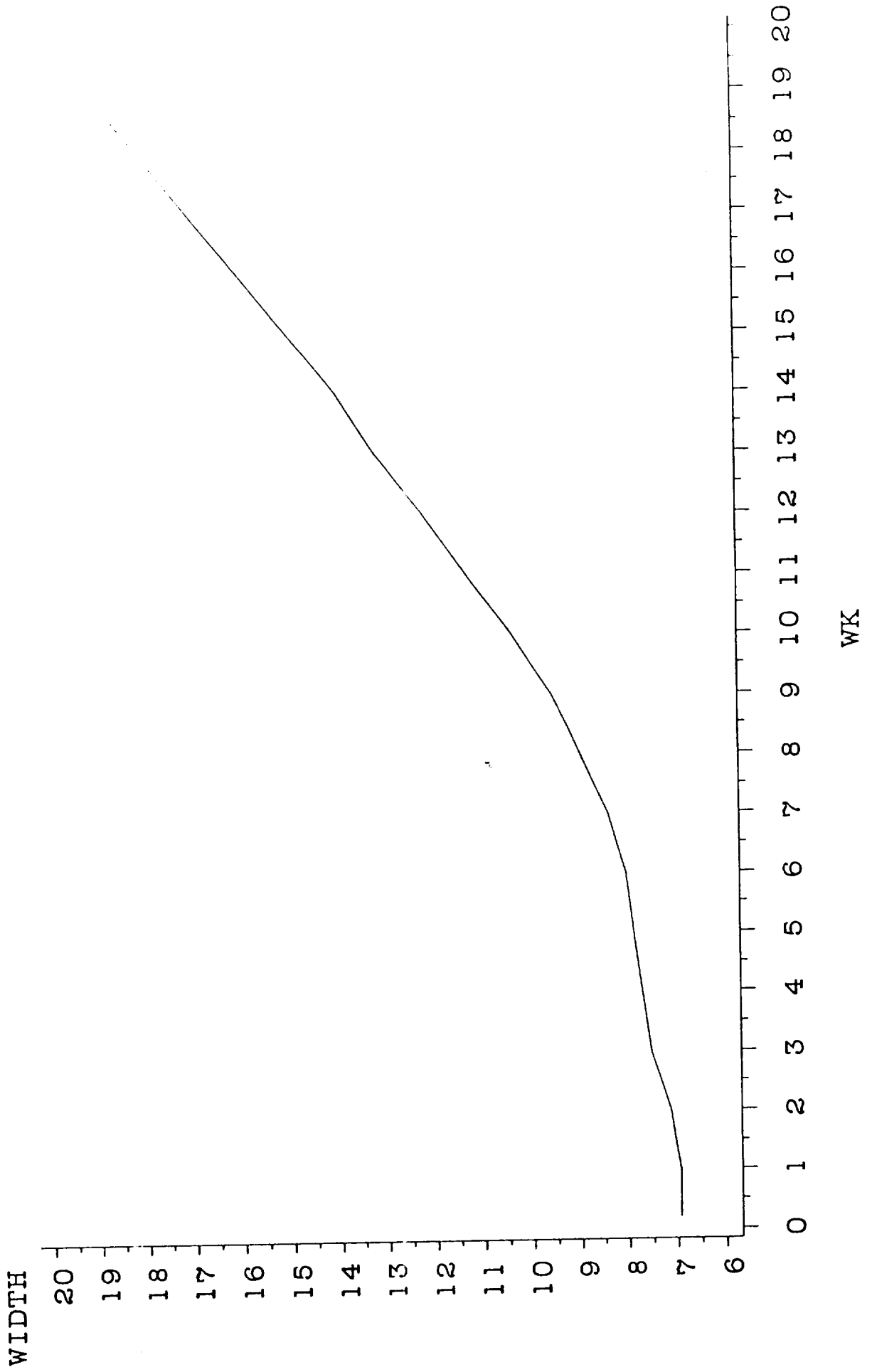




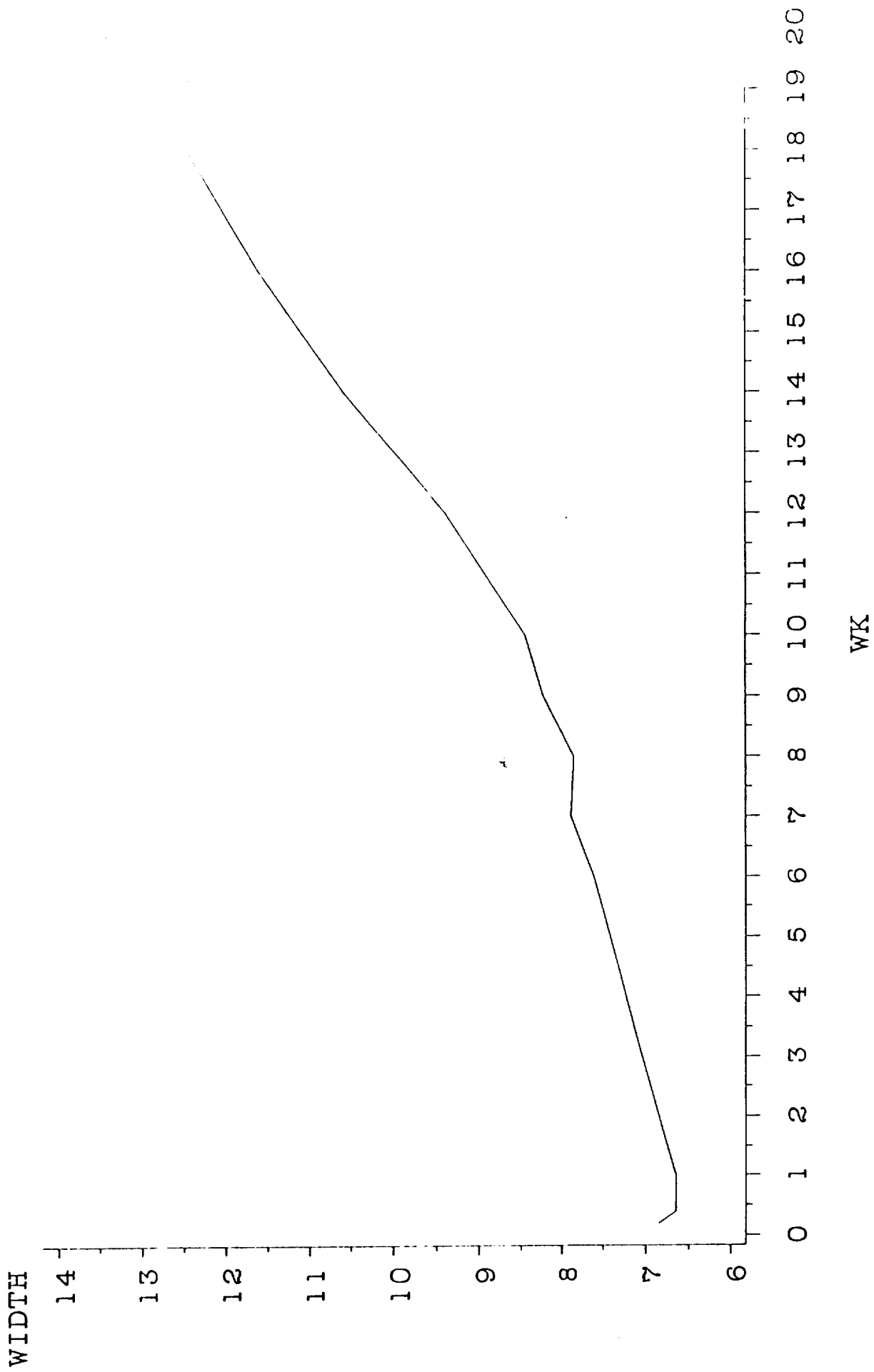
TRIANGLE KEEL
H=3 COIL=0.6
WK=1 DX=0.1 DY=1



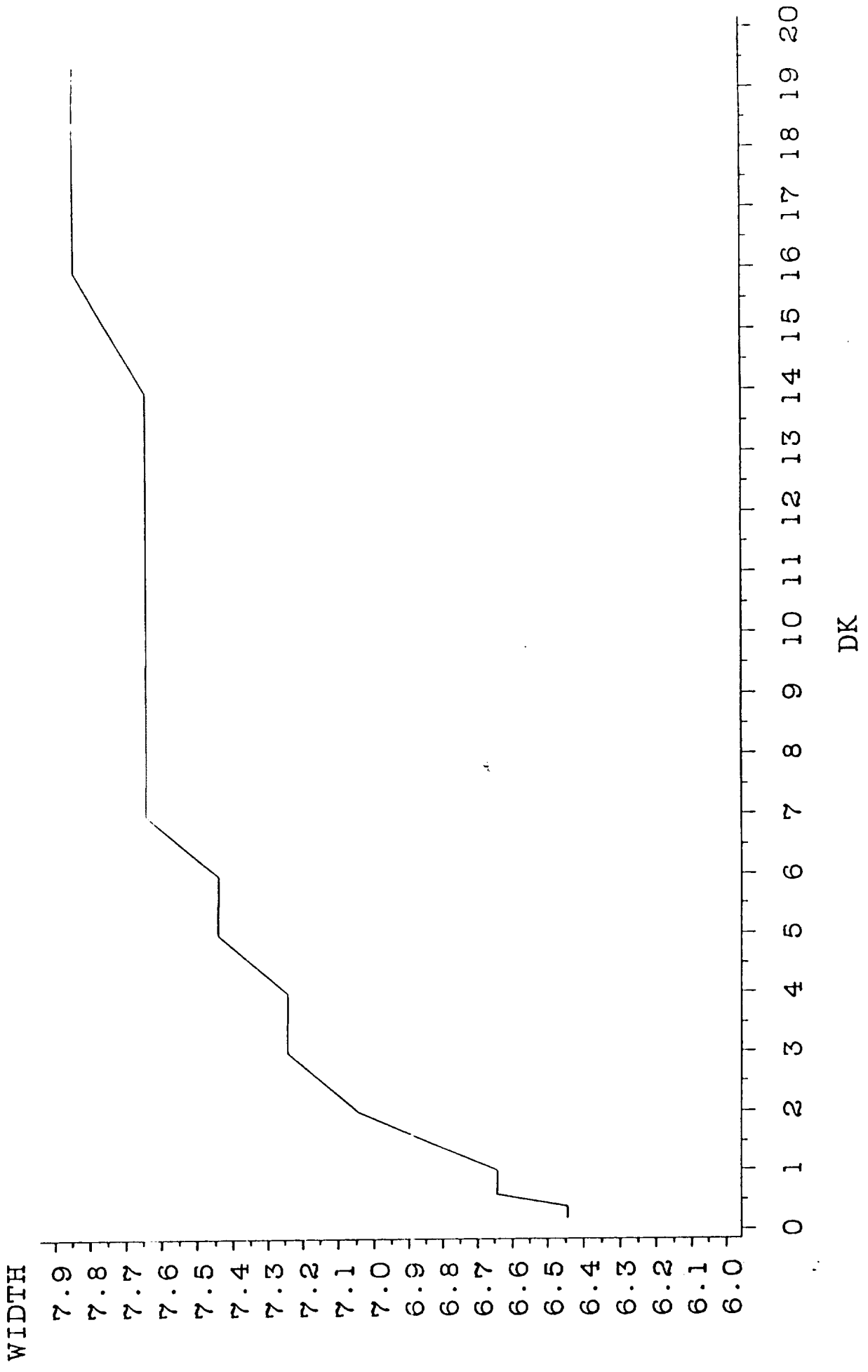
RECT. TROUGH
H=3 COIL=0.6
DX=0.1 DY=1 DK=1.0



TRIANGLE KEEL
H=3 COIL=0.6
DK=1 DX=0.1 DY=1



TRIANGLE KEEL
H=3 COIL=0.6
WK=1 DX=0.1 DY=1



Berkeley Triangular Keel Model

The XX response of the triangular keel model shown in the bottom of Fig. B-1 was calculated by Becker et al. (1985) by means of a finite element algorithm. The results of the calculation at ten survey points are shown in the upper half of Fig. B-1. This numerical procedure reportedly required 30 minutes on a Cray supercomputer. The range of the calculation is only approximately three times the keel width--not enough to reach the homogeneous halfspace values of the Sommerfeld one-dimensional field of -312 ppm inphase, -62 quadrature. The same model is shown in Fig. B-2 but range, keel width, and keel depth are displayed in units of skin depth, which is 5.03 m given the assumed values for sea conductivity and bird transmitter frequency. The MIM one-dimensional and approximate two-dimensional fields for the XX coil configuration are shown in Fig. B-3 for the same model parameters. The first feature to note in these curves is the displacement of the minimum in the two-dimensional fields relative to the one-dimensional fields. This is caused by our computational scheme, and since this discrepancy continually reoccurs a brief explanation is required. The minimum values for the two-dimensional fields occur at about -6 m on the range scale. This is the approximate coordinate of the receiver coil when the transmitting coil is at the origin, which is the coordinate of the keel bottom relative to the model. At this location of the transmitter, the smallest currents are induced in the model and hence a minimum signal is detected at



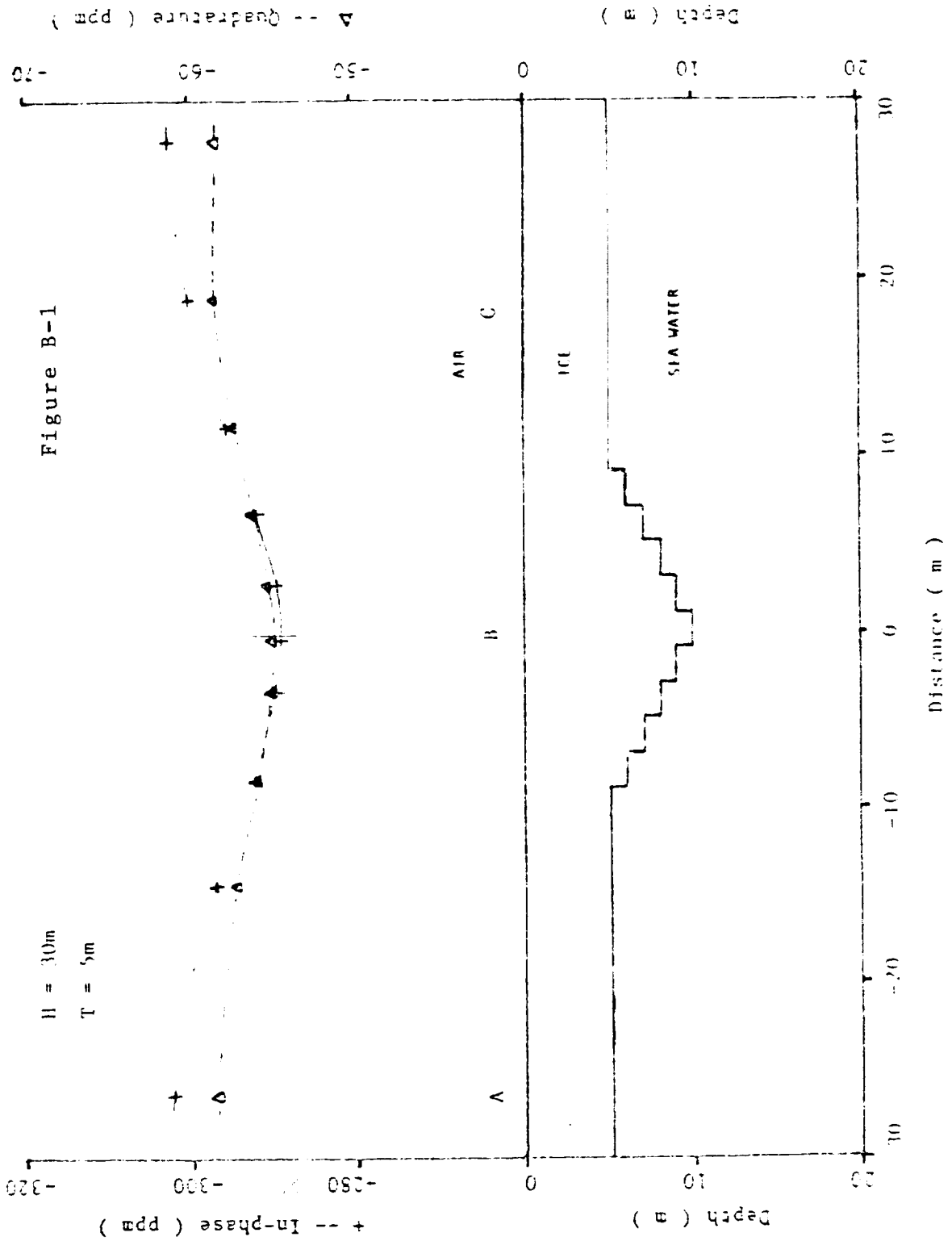
the receiver coil. On the other hand, in the one-dimensional case, the altitude of the bird above the homogeneous halfspace is taken to be the vertical separation of the receiver coil above the model. This distance is a maximum when the receiver coil is directly above the bottom of the keel. Thus it is at this location where the one-dimensional field minimum occurs.

The MIM XX two-dimensional field is in fair agreement with the Berkeley calculation. The signal widths of the two curves are approximately the same. The minimum field for the MIM two-dimensional calculation is intermediate between the Berkeley two-dimensional calculation and the MIM one-dimensional field minima.

Figure B-4 shows the two-dimensional MIM fields for the ZZ coil configuration. The signal is broader and the maximum change in signal is smaller than for the XX configuration. No ZZ field was reported in the Berkeley report.

Finally, the ZX MIM one- and two-dimensional fields are displayed in Fig. B-5. This figure clearly shows that the MIM approximation predicts that the ZX field produces a keel signature that is very different from the one-dimensional signal. The leading edge downslope in the model produces a tracking downslope in the one-dimensional fields but a large positive hump two-dimensional signal and a nearly mirror negative hump indicative of the keel upslope. The peak to peak separation is approximately 25 m, which is comparable to the keel width of 18 m.





HX system response Model 1

ORIGINAL PAGE IS OF POOR QUALITY

Figure B-2

$WK=18 M$ $DKMAX=5 M$

$\delta_1 = 5.033 M$

7-19-89

$\Delta x = 0.4 \delta_1$

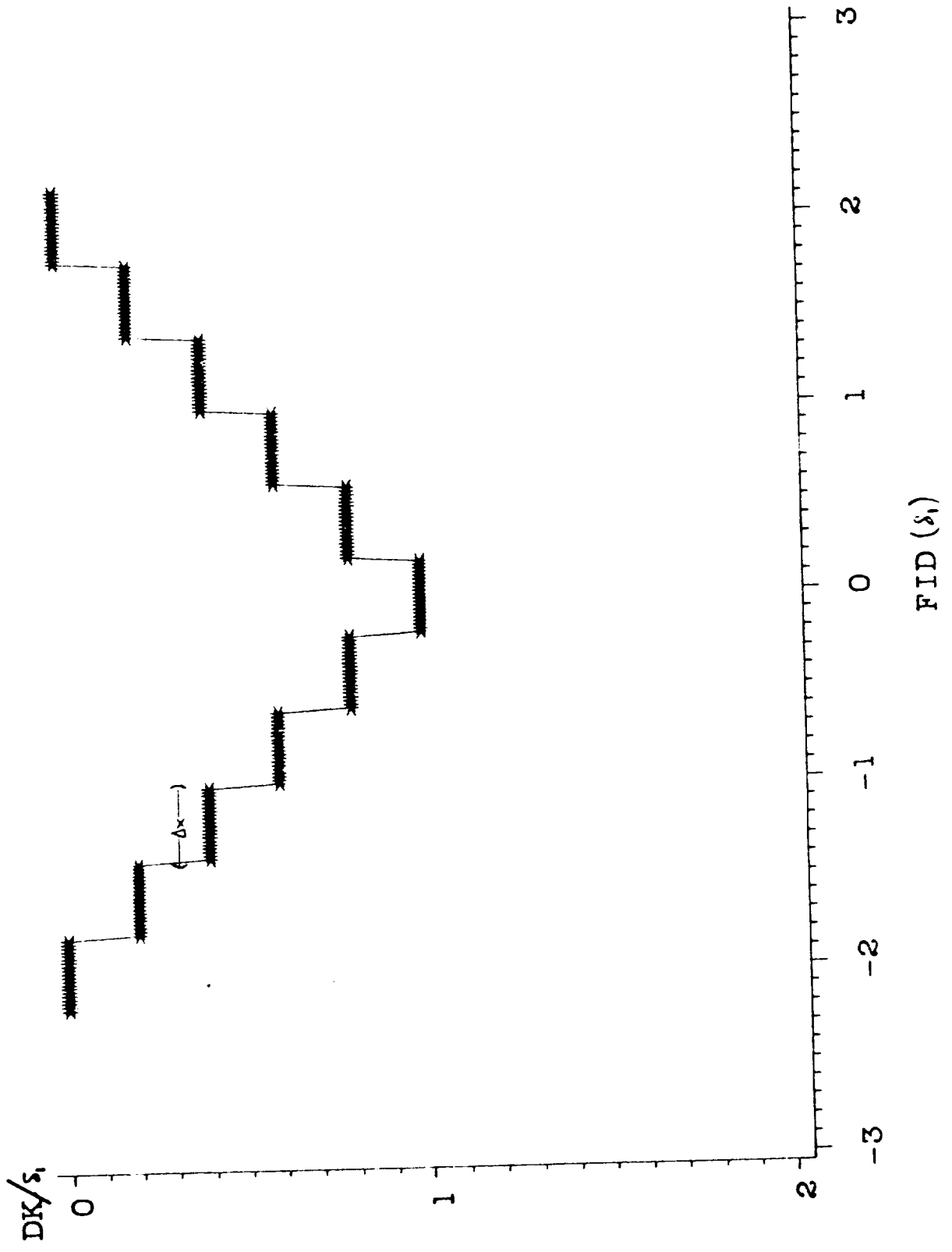


Figure B-3

X DIPOLE: XX FIELD
TRIAN. KEEL: TX AT X0
H=35 DK=5 WK=18 X0=6.5
07-11-89

$\Delta x = 2.01m$; $\Delta y = 5.033m$

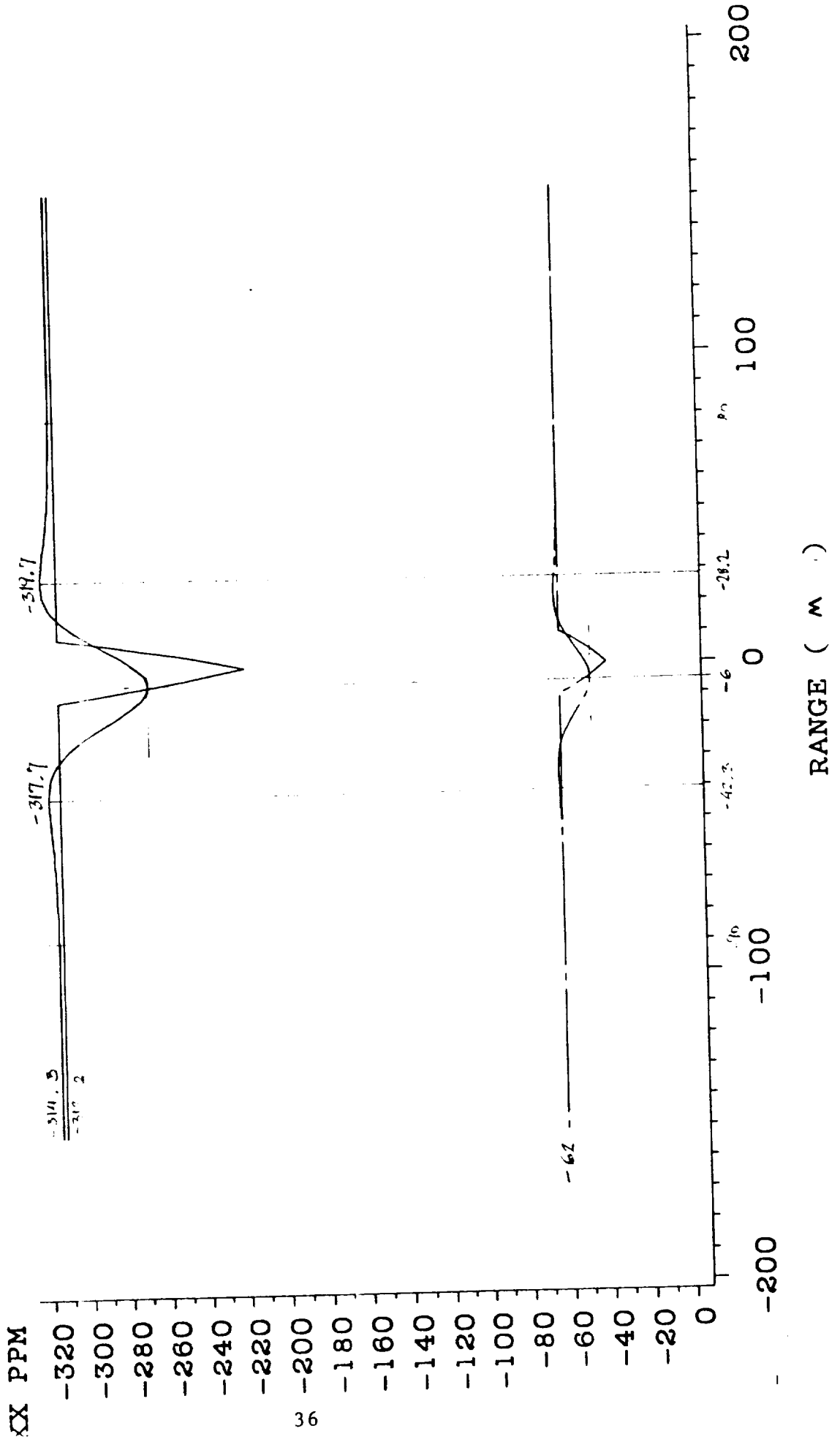
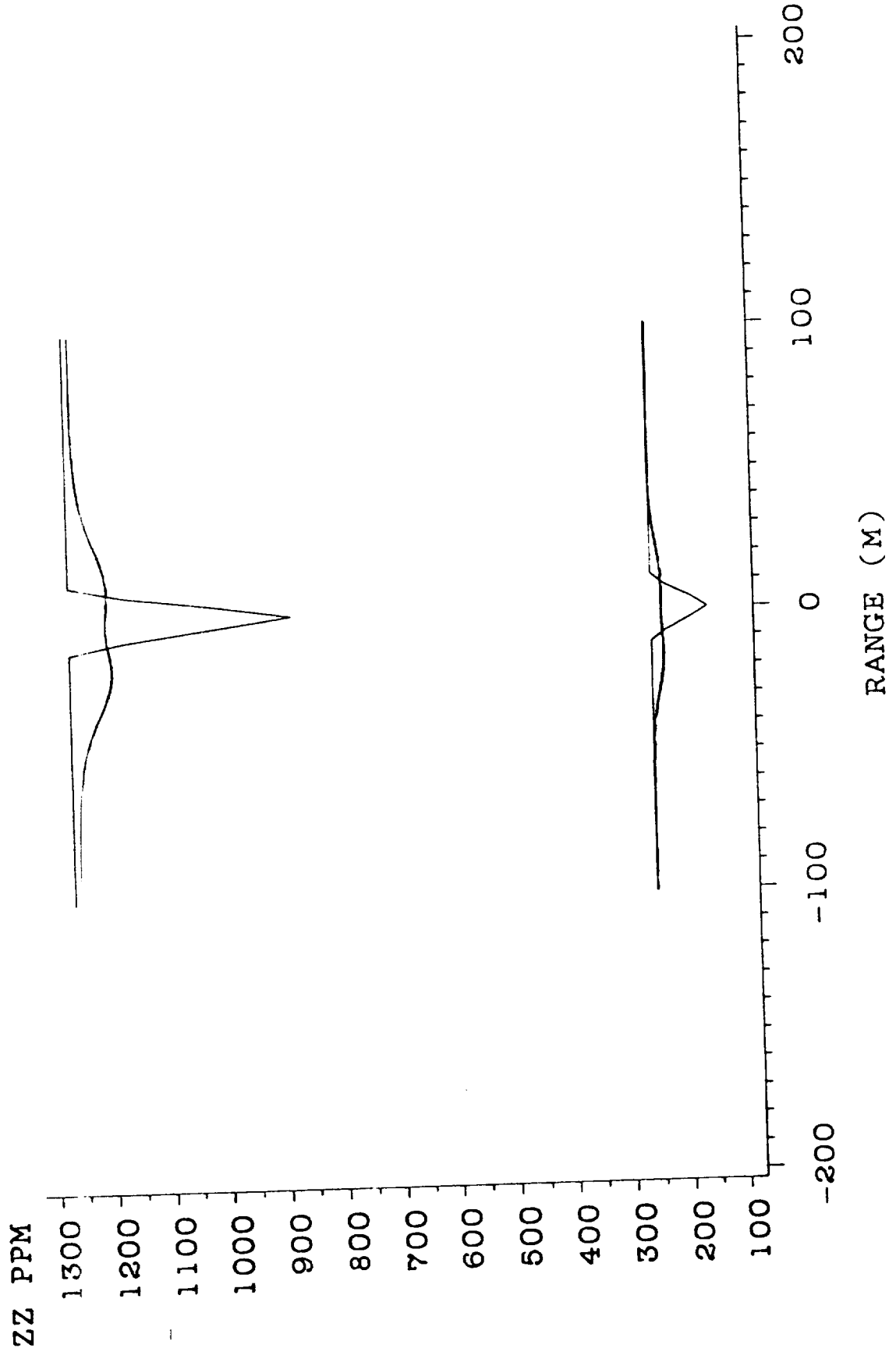


Figure B-4

Z DIPOLE: FIELD

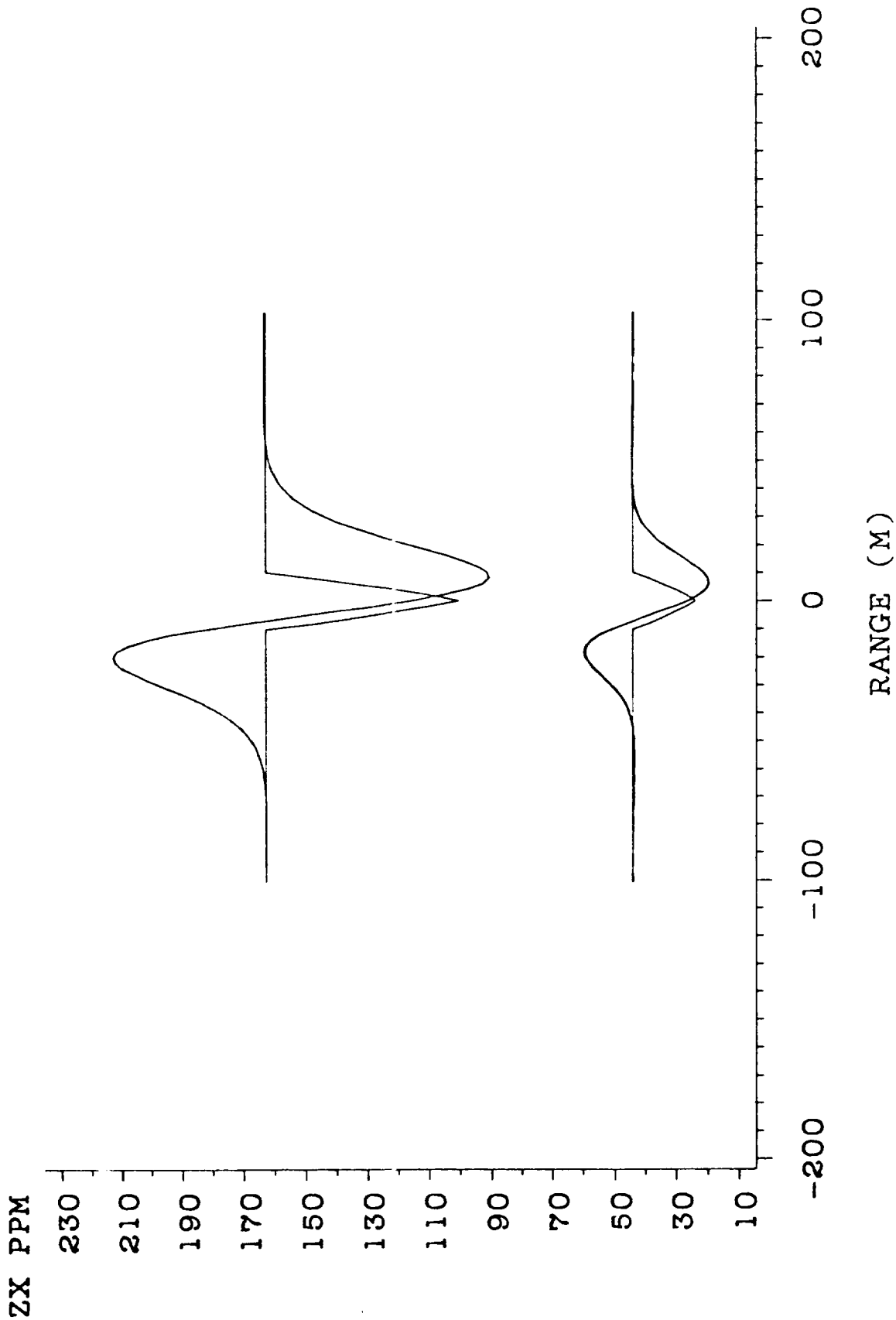
TRIAN. KEEL: TX AT X0

H=35M WK=18M DK=5M X0=6.5M DEL1=5M
08-04-89



Z DIPOLE: FIELD
'TRIAN. KEEL: TX AT X0
H=35M WK=18M DK=5M X0=6.5M DEL1=5M
08-04-89

Figure B-5





CRREL Model

Figure C-1 through C-9 are the results of ground truth measurements of a Frudhoe Bay ice keel by CRREL personnel and contractors. The ordinant of the figure is the total ice/snow thickness, i.e., snow cover plus freeboard plus ice keel. A uniform thickness region has been added to each end of the keel in order to demonstrate that the two-dimensional MIM calculations of AEM fields are in agreement with the one-dimensional field in the uniform thickness regions of the model. Figure C-2 shows the altimeter reading of the bird-to-snow vertical distance measured during a helicopter traverse of the keel. The final model parameter used in these calculations is the sea conductivity, $\sigma = 3.1 \text{ S/m}$.

Figures C-3, C-4, and C-5 show the results of one- and two-dimensional calculations for the ZZ coil configuration (horizontal coplanar). Figure C-3 shows the inphase and quadrature one- and two-dimensional ZZ fields. Both fields track the model but the two-dimensional results are smoother and the variations are smaller than the one-dimensional results. Figures C-4 and C-5 show the results of the one-dimensional MIM inversion of the one- and two-dimensional fields. Figure C-4 gives the ice thickness (inverse distance from bird to sea surface minus the laser altimeter reading) and Figure C-5 the inversion results for the sea conductivity. The inversion results for the one-dimensional fields are in close agreement with the input model whereas the two-dimensional results indicate a smoother keel no

as dependent on the model.

Figures C-6, C-7, and C-8 show results of the same calculations for the XX configuration (horizontal coaxial). A comparison of Figures C-4 and C-6 shows that the XX two-dimensional field to be closer to its one-dimensional counterpart than is true for the two- and one-dimensional fields for the ZZ configuration. This observation is confirmed by the MIM inversion results (ice thickness and conductivity) for the XX fields shown in Figures C-7 and C-8. Figure C-9 shows the one- and two-dimensional fields for the mixed coil configurations ZX (vertical transmitter dipole/horizontal receiver coil axis). The most striking feature of these curves is the large difference between the two- and one-dimensional fields at the leading edge of the keel. The two-dimensional results show an enhanced secondary field whereas the one-dimensional field falls off with increasing distance between bird and sea surface. Thus a ZX field would seem to provide a signature for a sudden increase in ice thickness. In this model the effect on the ZX field of the sudden decrease in ice thickness at about 100 m downrange (Figure C-1) tends to be canceled by the increasing altitude of the bird over the same portion of the range (Figure C-2). Nevertheless the two-dimensional fields do show a relatively sharp decrease from 80 to 110 m: a mirror image trailing edge response to the initial leading edge response. This is more clearly seen in the ZX field of Figure C-10 in which the model has been modified to a constant bird altitude of 18 m.

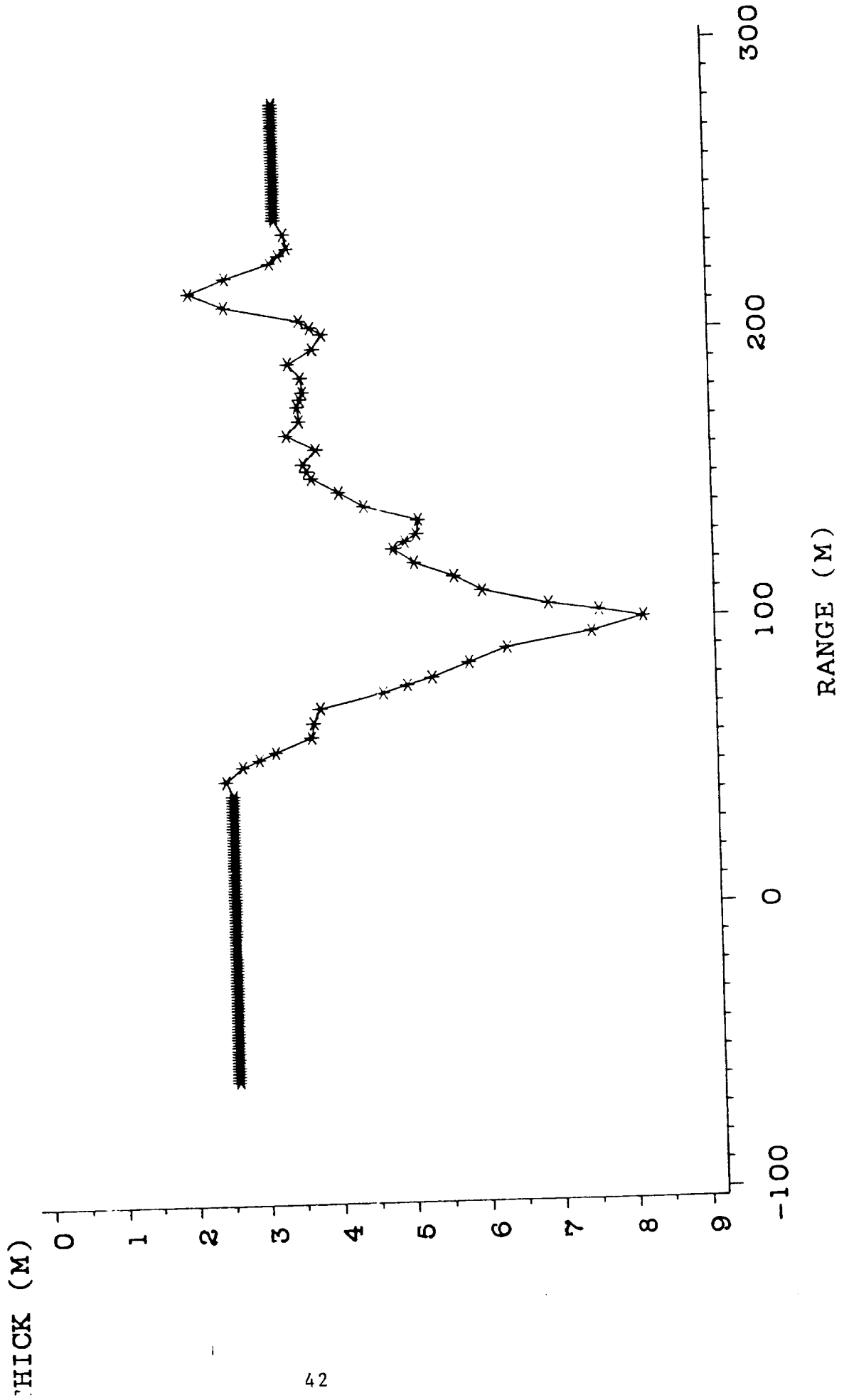


In principle these departures of the two-dimensional calculation for the ZX configuration from the one-dimensional ZX fields can be compared to the measured ZX response of scaled edge models (Dallal, 1985). Dallal measured the ZX field in the time domain over a sheet of brass as a function of distance from the edge of the sheet. It is possible for us to calculate the ZX field for such models in the frequency domain over a sufficiently large range of frequencies and then Fourier transform these results for $ZX(\omega)$ into $ZX(t)$, thereby allowing a comparison of the MIM approximation of $ZX(t)$ with the scale model measurements.



Figure C-1

CRELLE MODEL
COIL=3M FREQ=811HZ DEL1=10M
08-14-89



CRELLE MODEL
COIL=3M FREQ=811HZ DEL1=10M
08-14-89

Figure C-2

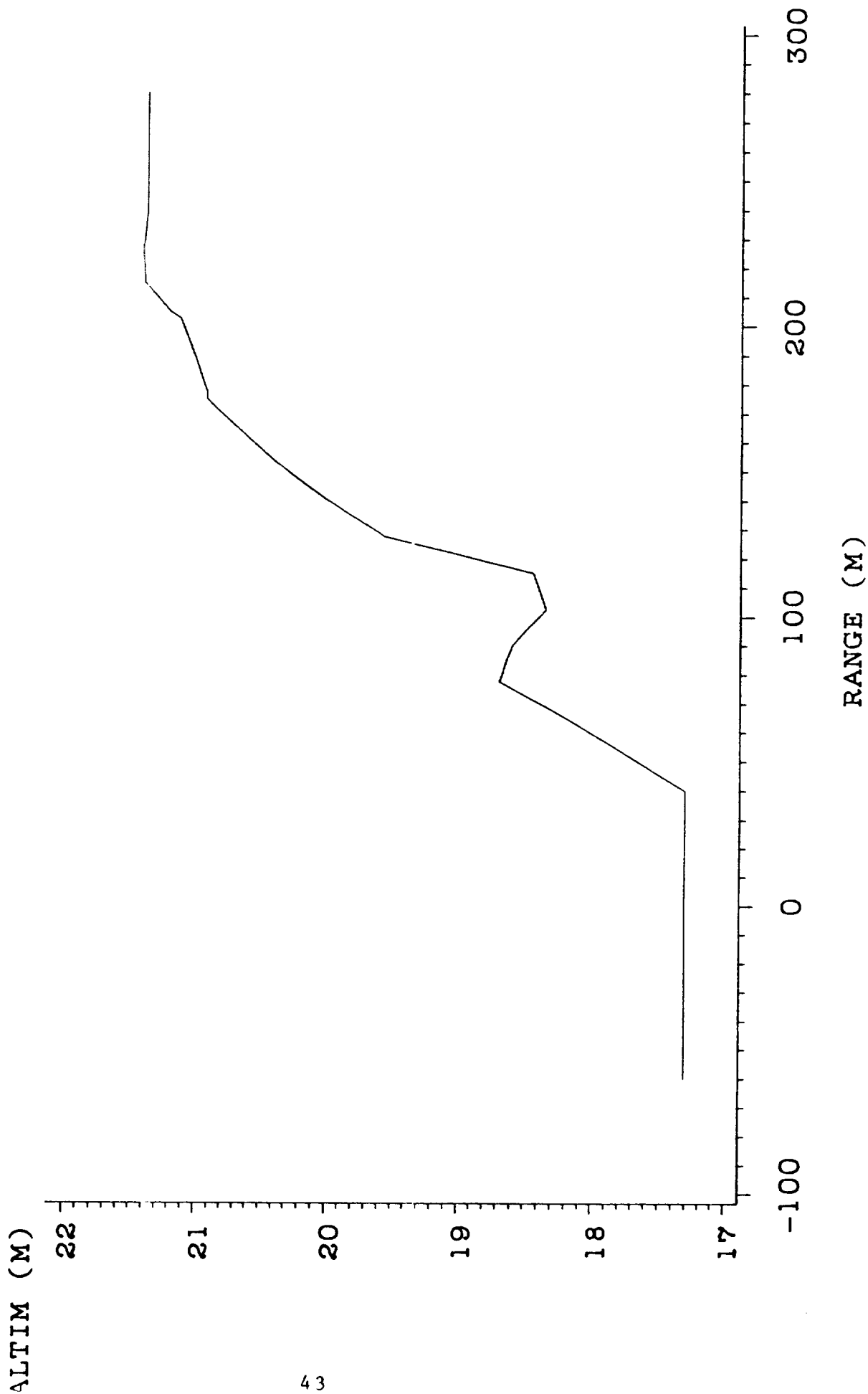


Figure C-3

MIM-MIM

CRREL MODEL: X0=3M DEL1=10M FREQ=811HZ

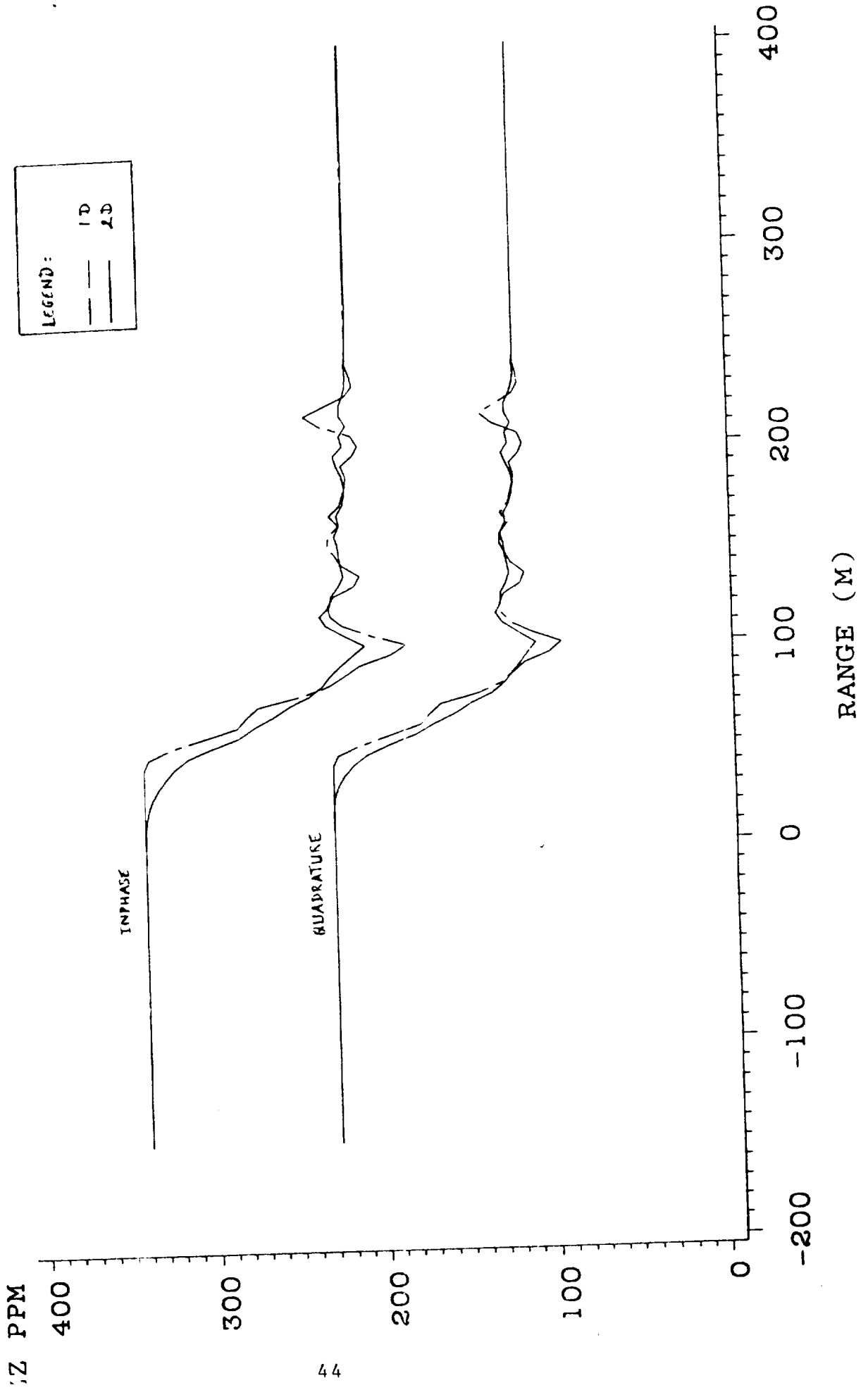


Figure C-4

ZZ FIELD: MIM - MIM

CRREL MODEL: X0=3M DEL1=10M FREQ=811HZ

INVERSE ICE THICKNESS

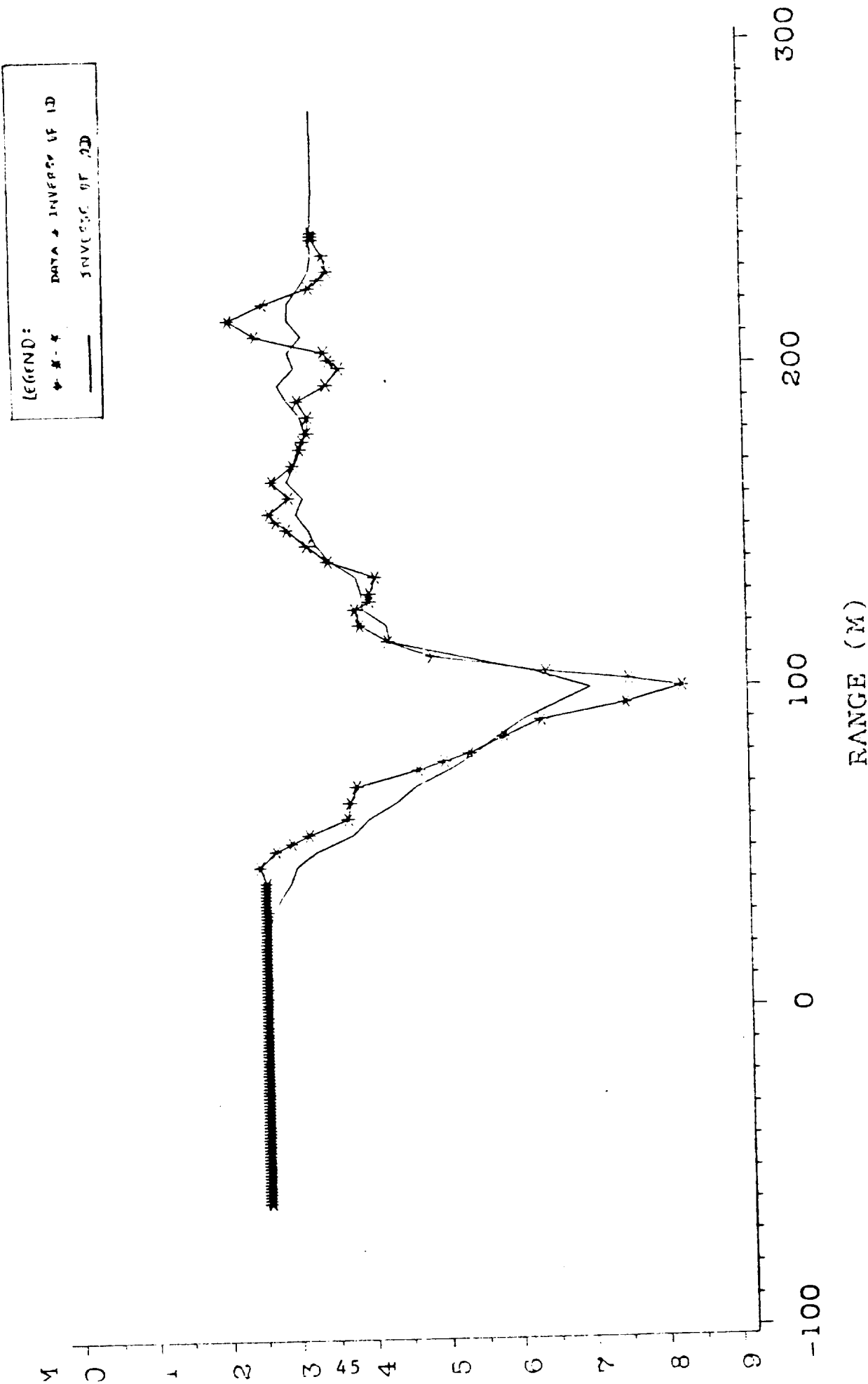


Figure C-5

ZZ FIELD: MIM - MIM
CRREL MODEL: X0=3M DEL1=10M FREQ=811HZ
INVERSE CONDUCTIVITY

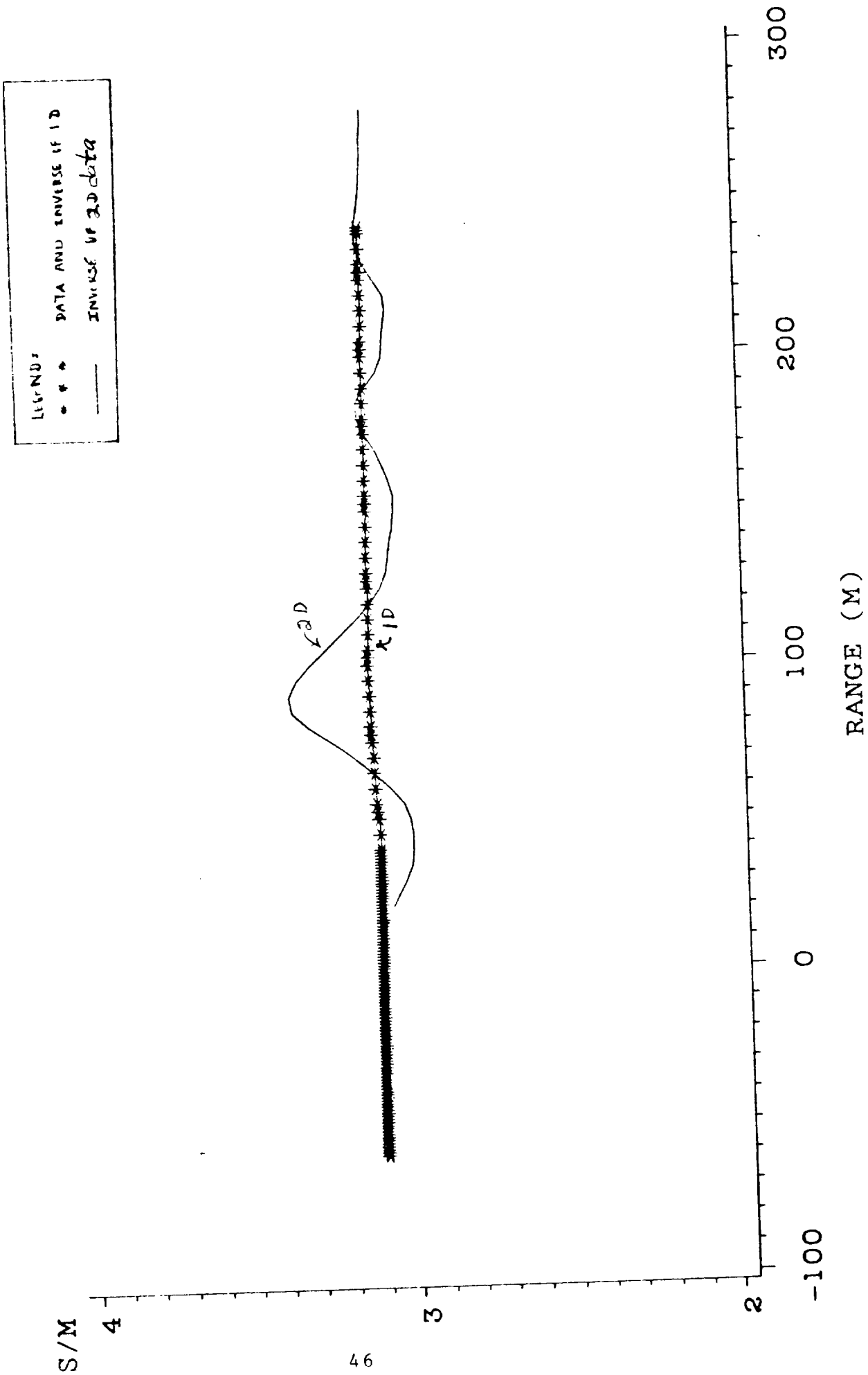


Figure C-6

MIM-MIM

CRREL MODEL: X0=3M DEL1=10M FREQ=811HZ

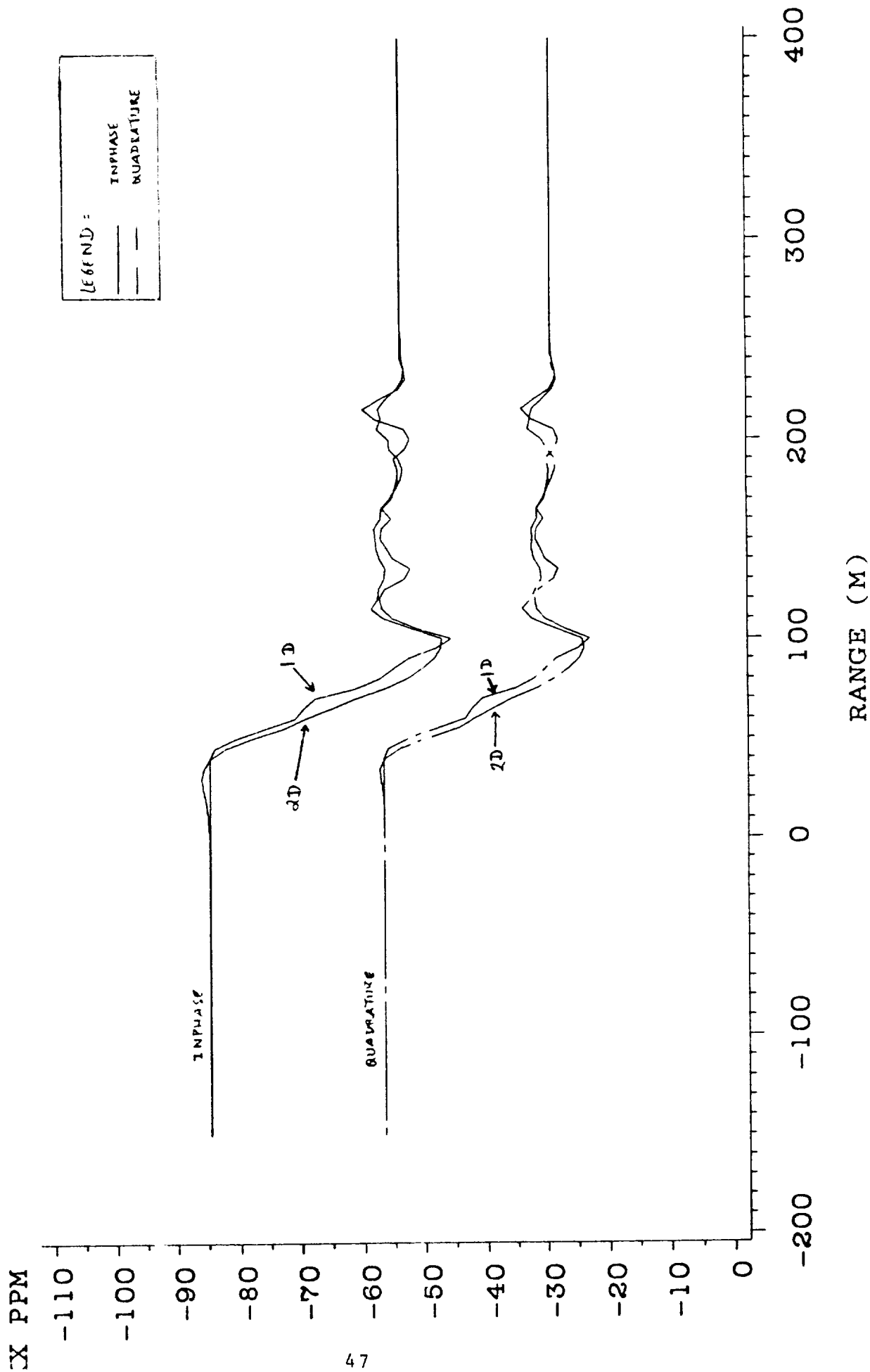




Figure C-7

XX FIELD

CRREL MODEL: X0=3M DEL1=10M FREQ=811HZ
INVERSE ICE THICKNESS

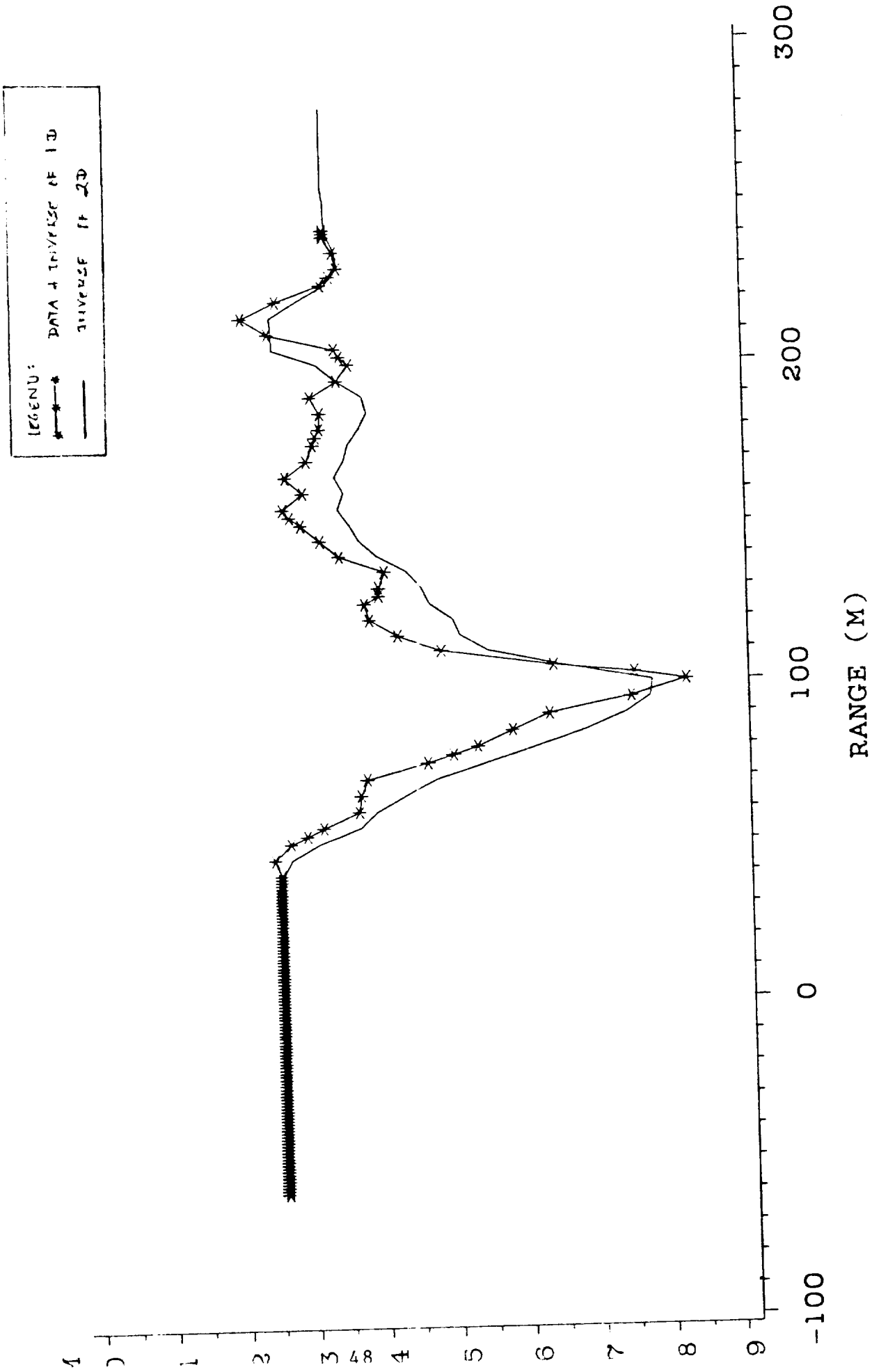
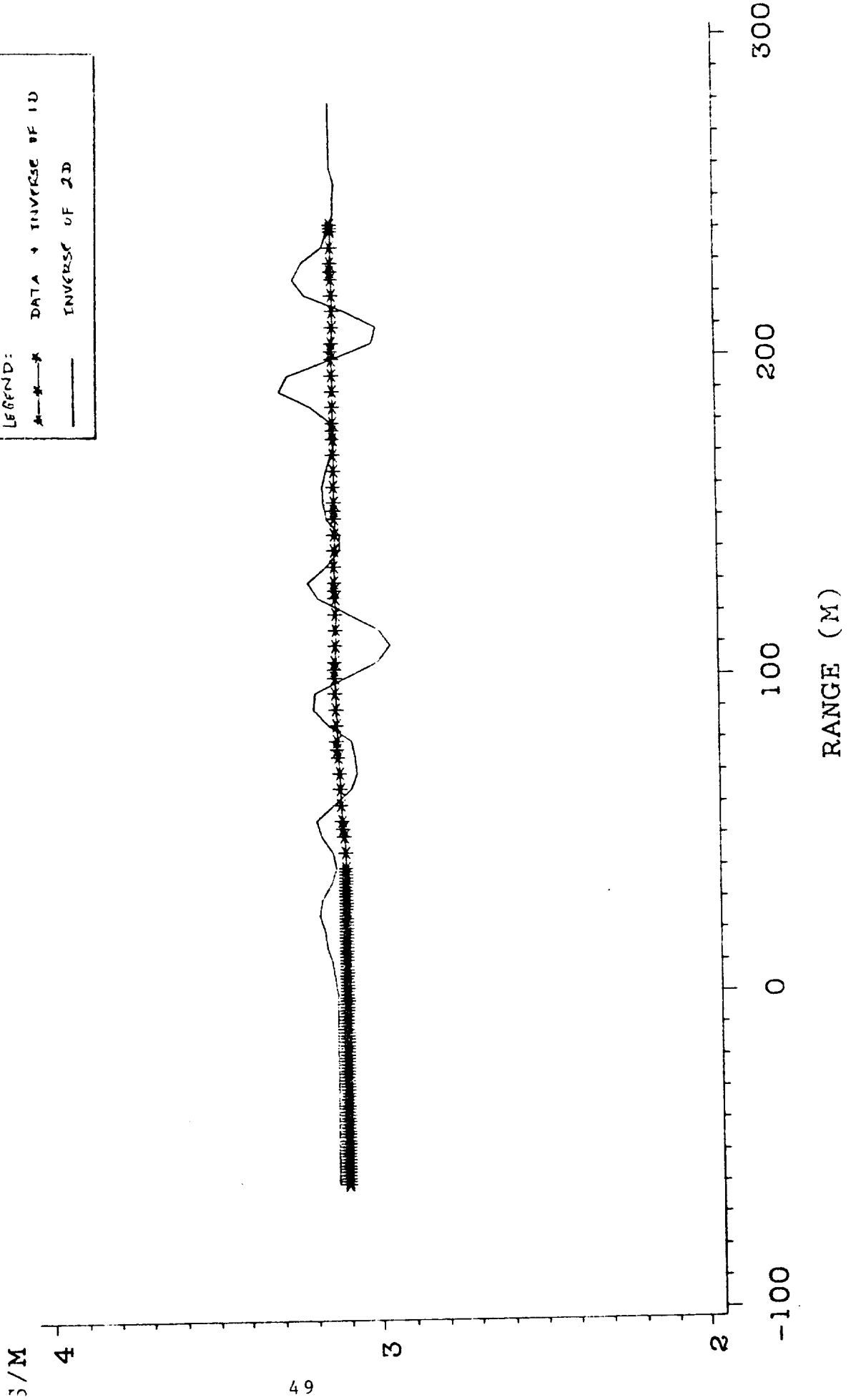
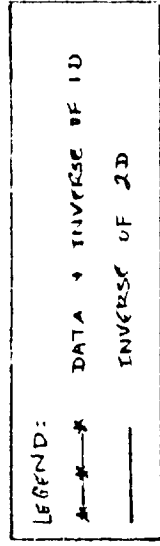


Figure C-8

XX FIELD

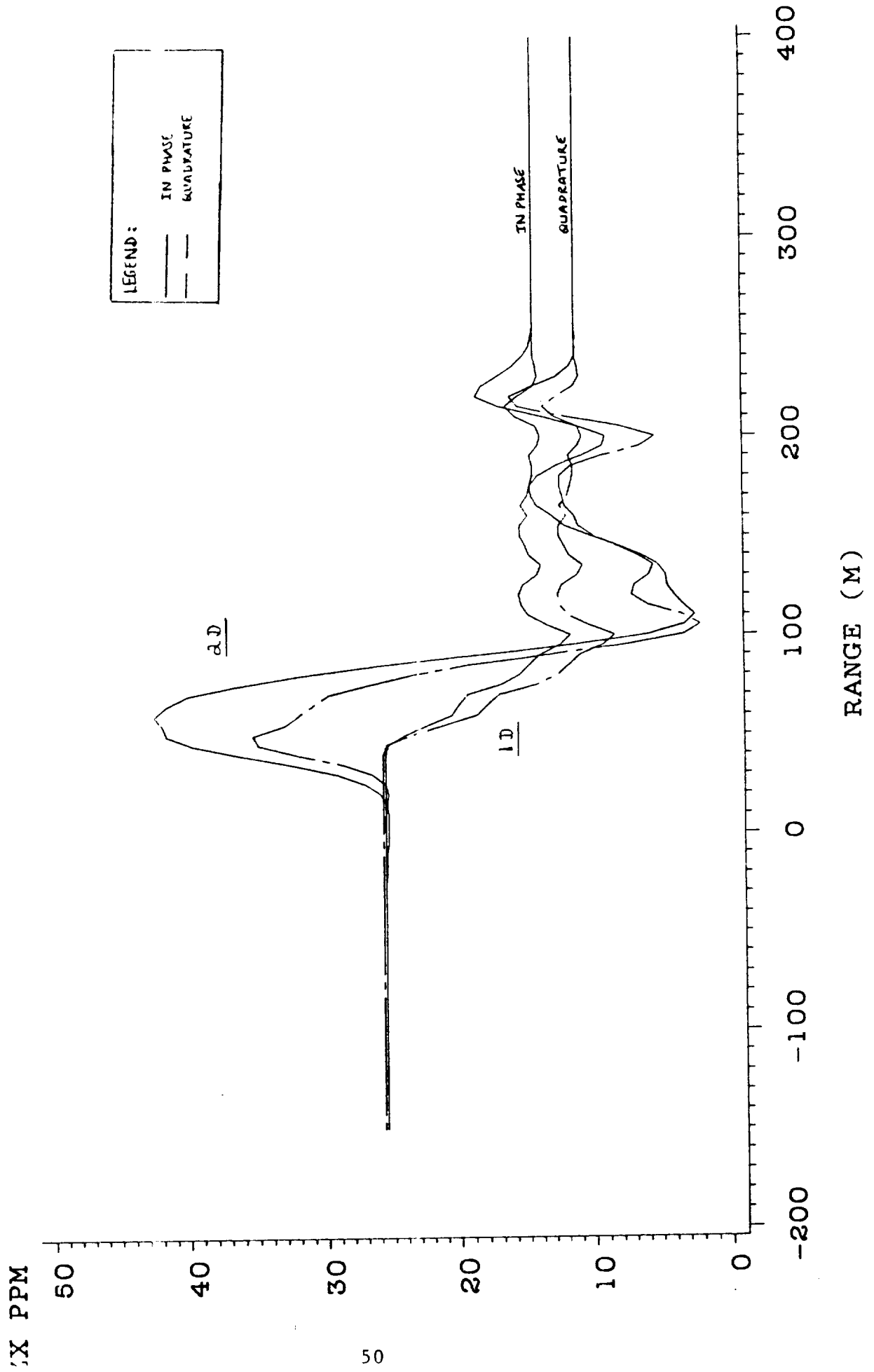
CRREL MODEL: X0=3M DEL1=10M FREQ=811HZ
INVERSE CONDUCTIVITY



MIM-MIM

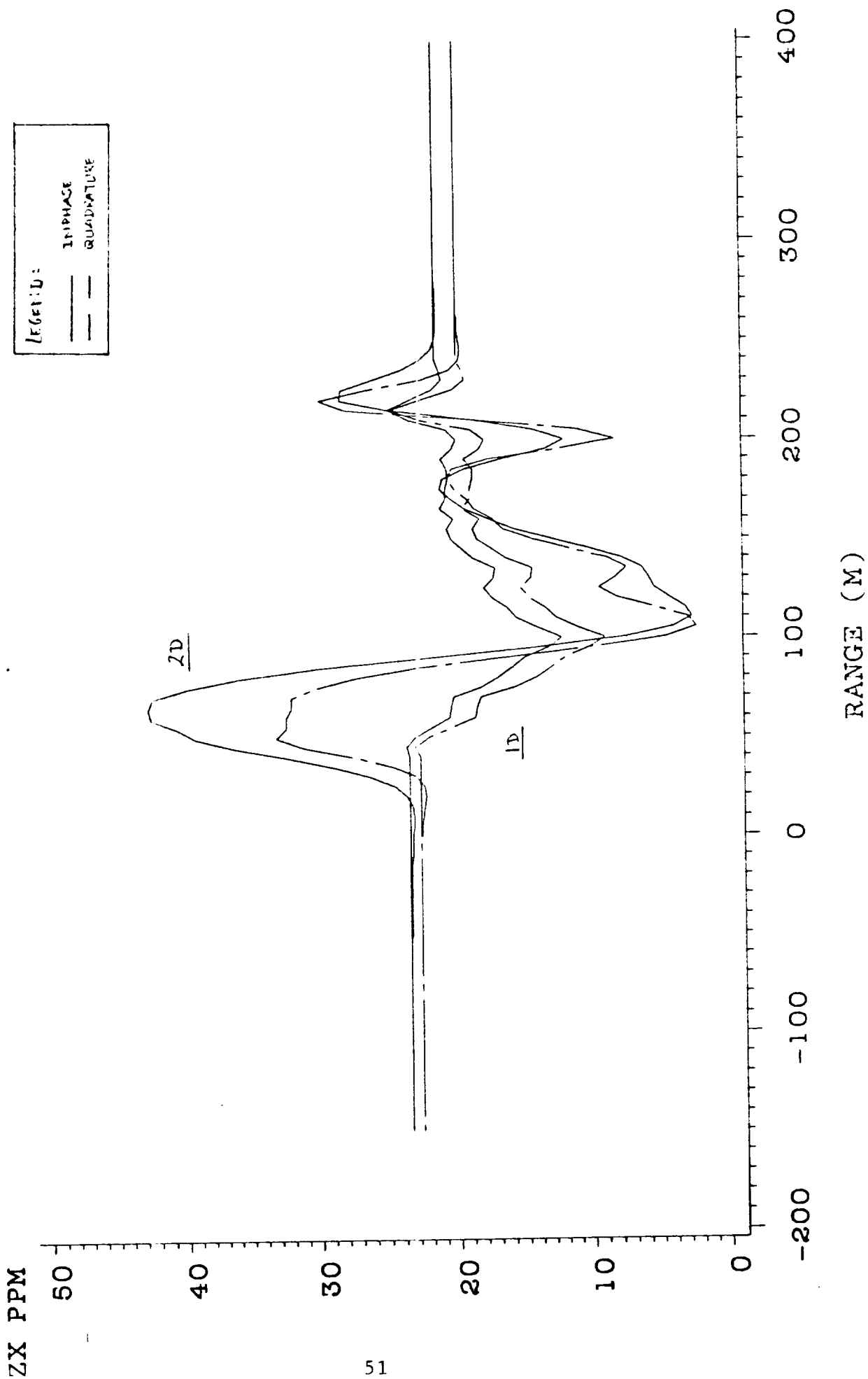
Figure C-9

CRREL MODEL: X0=3M DEL1=10M FREQ=811HZ



MIM-MIM ALTIM=18M
CRREL MODEL: X0=3M DEL1=10M FREQ=811HZ

Figure C-10



TASK THREE

Analytic Continuation of AEM Signal

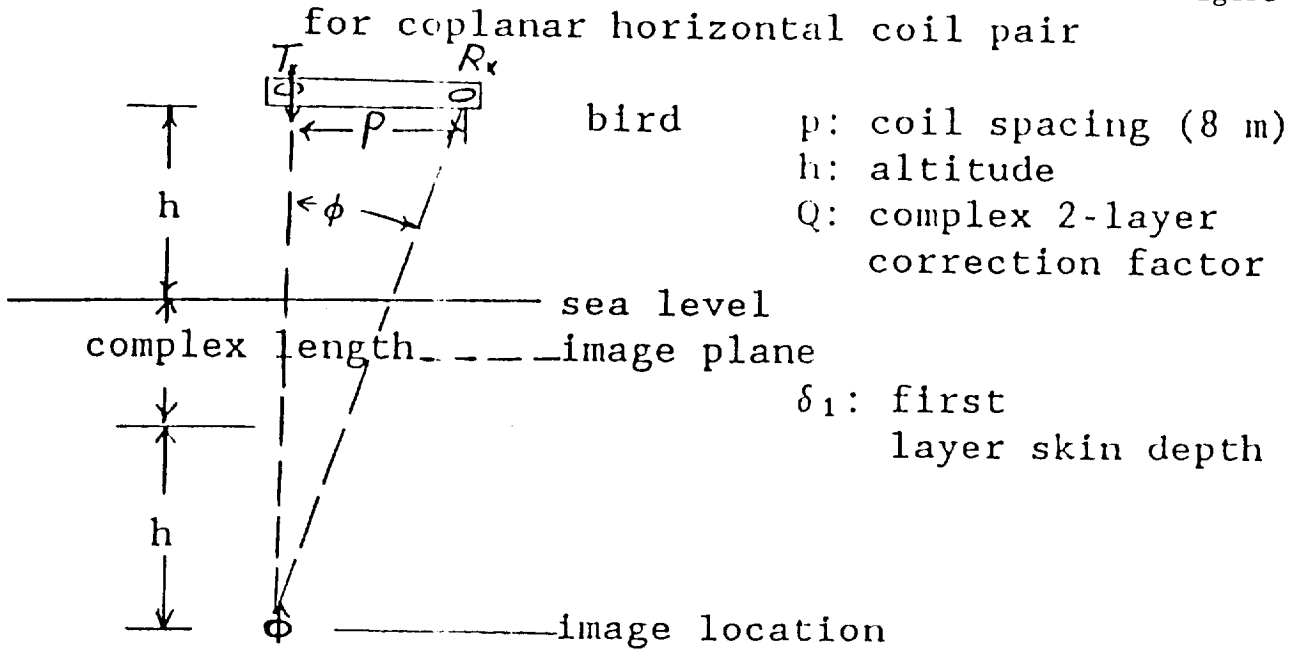
Figure 3-1 is a summary sheet of the MIM model along with the indicated Taylor's series expansion of the vertical component Z of the normalized secondary field (Bergeron et al., 1988). Figure 3-2 shows the smoothed laser altimeter versus range of a Prudhoe Bay survey line. It, along with an assumed conductivity of 2.7 S/m, constitutes a uniform halfspace model. The Sommerfeld integral expression, T_0 , for a secondary field is employed with this model to generate the inphase (real) and quadrature (imaginary) fields shown in Figs. 3-3 and 3-4. Figures 3-5 and 3-6 show the absolute percent difference between the Sommerfeld field calculated directly at a 40 m altitude and the fields shown in Fig. 3-3 and 3-4 and which are analytically continued to $h = 40$ m, i.e.,

$$\% |\Delta Z/Z| = | \{ [Z_S(40) - Z_{\text{cont to } 40(h)}] / Z_S(40) \} \times 100 \quad .$$

Figures 3-7 and 3-8 show the percent errors that result from an upward continuation of a signal from 30 m as a function of altitude for skin depths of 5 and 25 m, respectively. Figures 3-9 and 3-10 show the corresponding percent errors that result from a downward continuation of a signal from 50 m. All of the figures indicate that a smaller error occurs for an upward continuation than a downward continuation. The utility of the technique depends on the subtlety of the anomaly that one is searching for in the data. Only if the error produced by the continuation of the data to a fixed reference altitude is less than the anticipated anomaly signal will this procedure be useful.

MIM MODEL

Figure 3-1



Taylor's Expansion of Z in altitude

$$Z(h_0) = \sum_{n=0}^N \left(\frac{d^n Z}{dh^n} \right)_h (h_0 - h)^n$$

$$\frac{d^n Z}{dh^n} = \frac{d^n Z}{dR^n} \left(\frac{2}{p} \right)^n$$



Figure 3-2

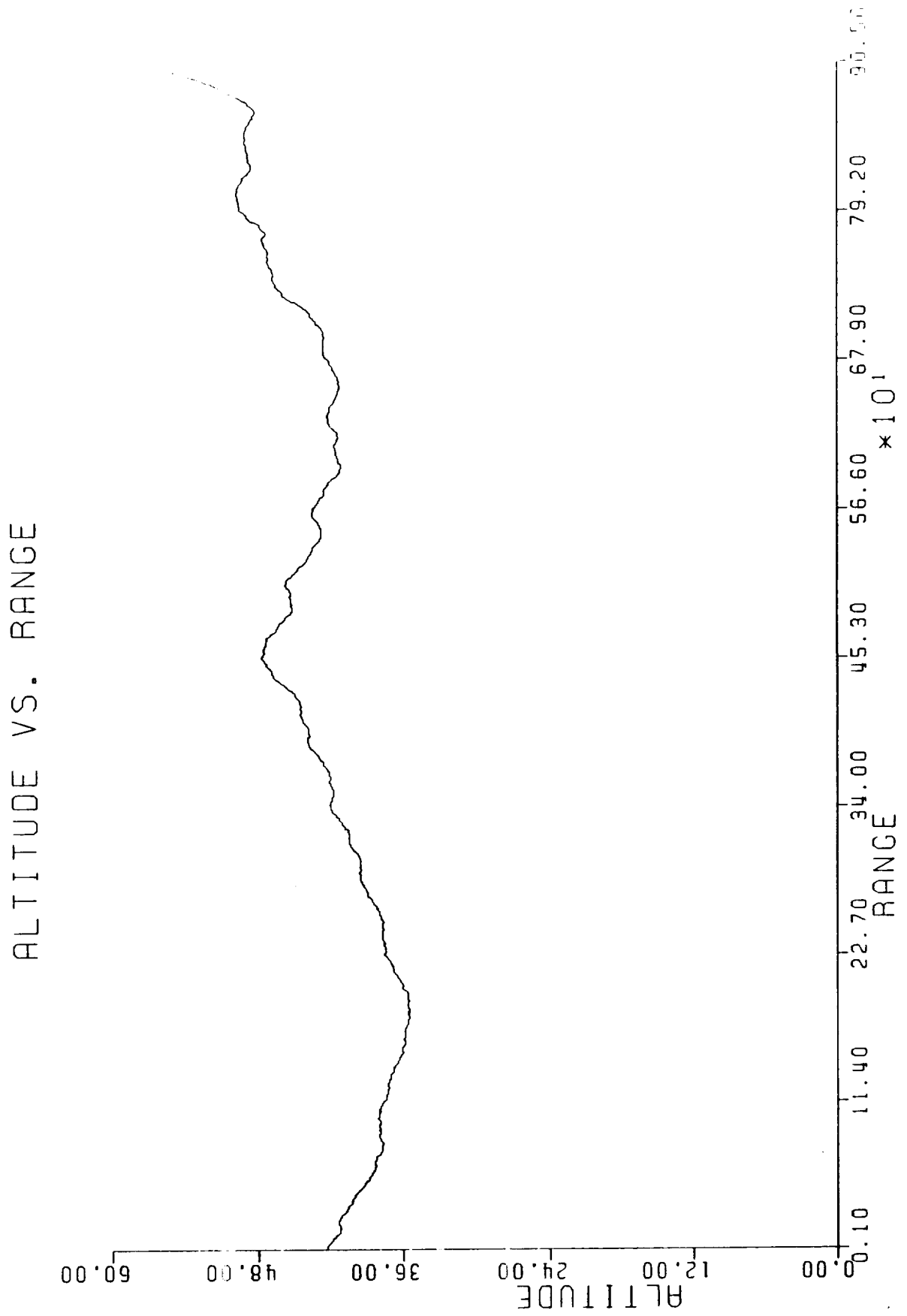




Figure 3-3

REAL Z (SOM) FIELD

H=40/DELTA=25

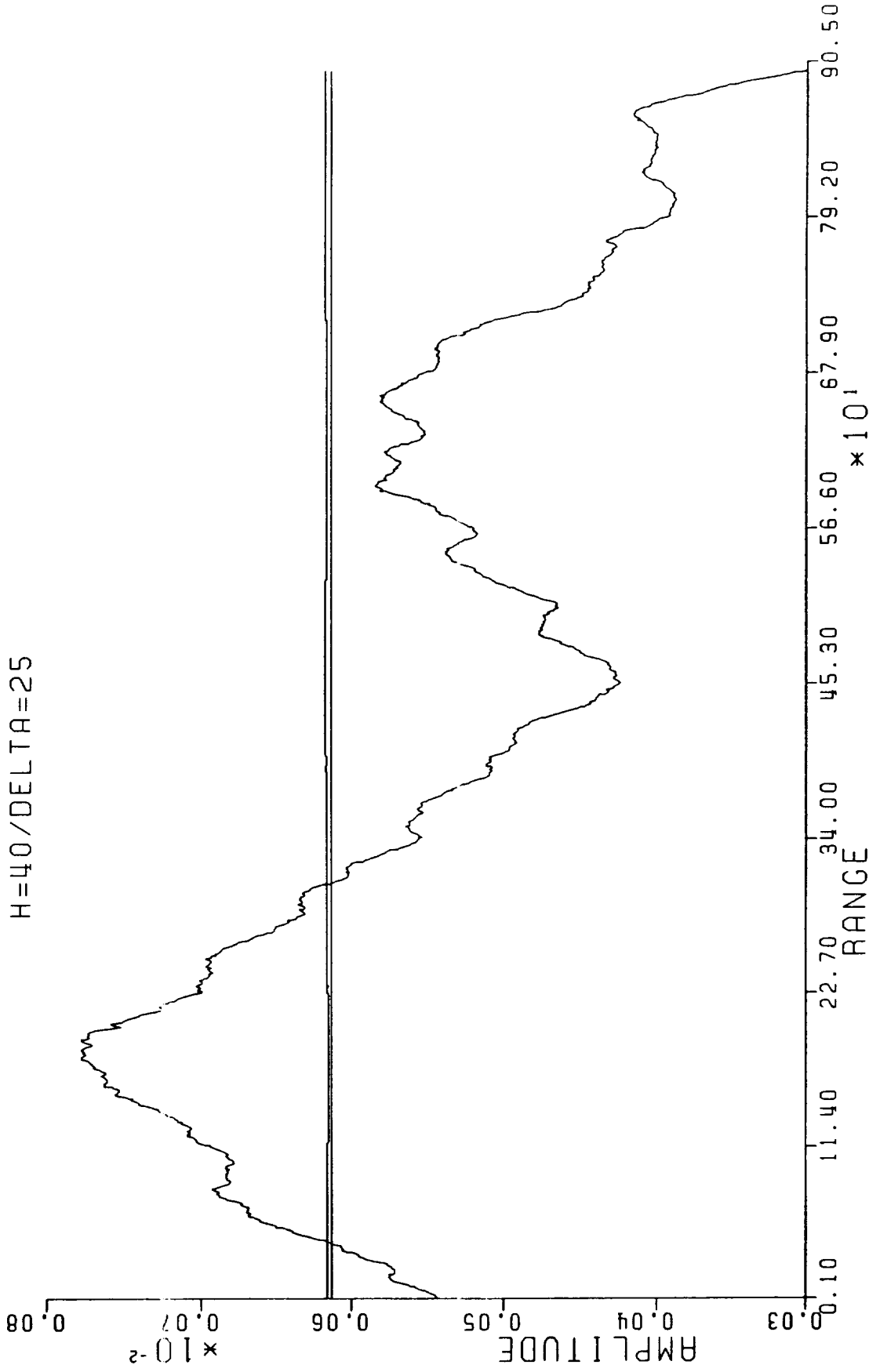




Figure 3-4

IMAGINARY ZSOM

H=40/DELTA=25

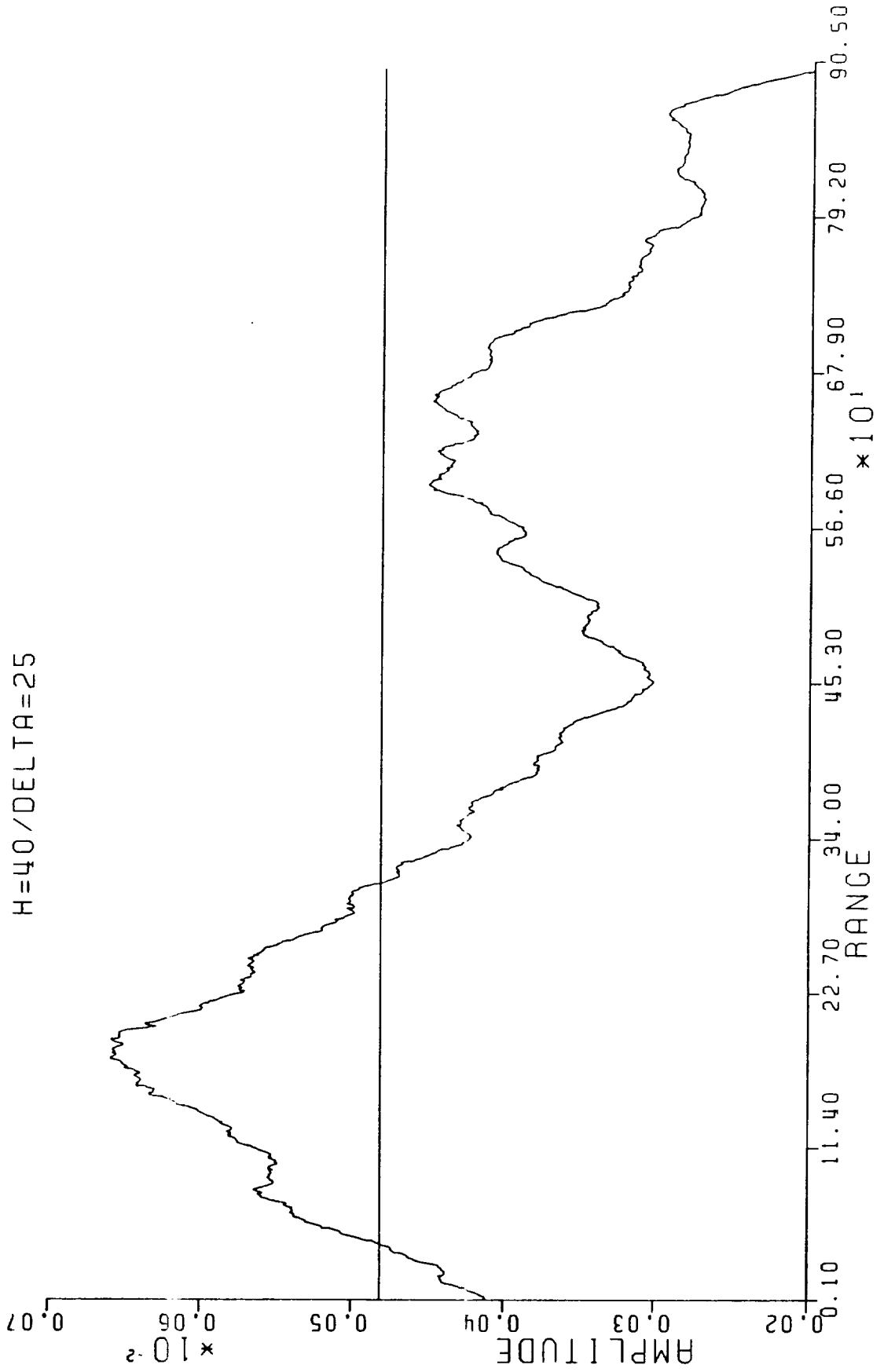




Figure 3-5

ERROR REAL ZMIM/ZSOM

H=40/DELTA=25

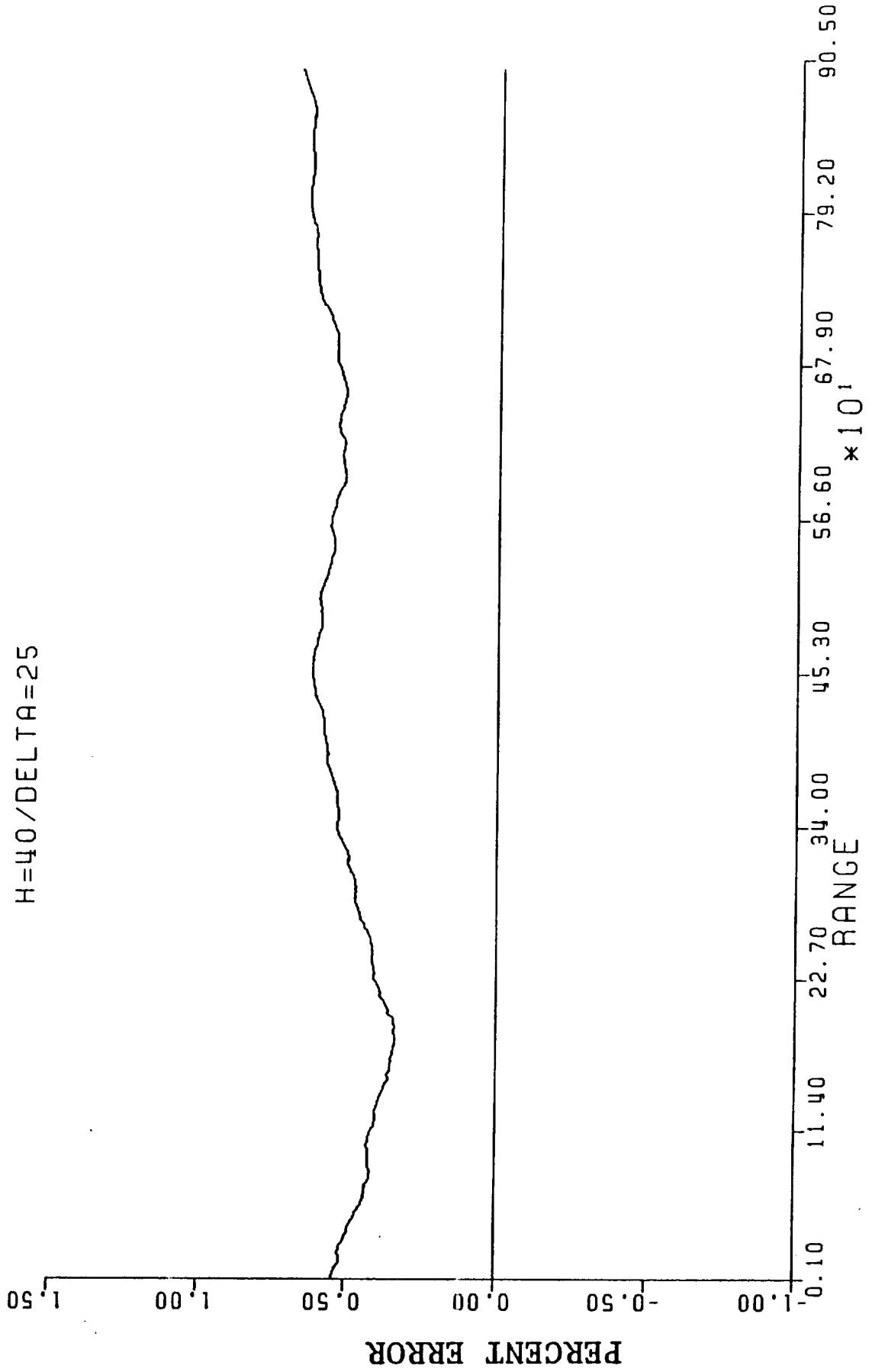
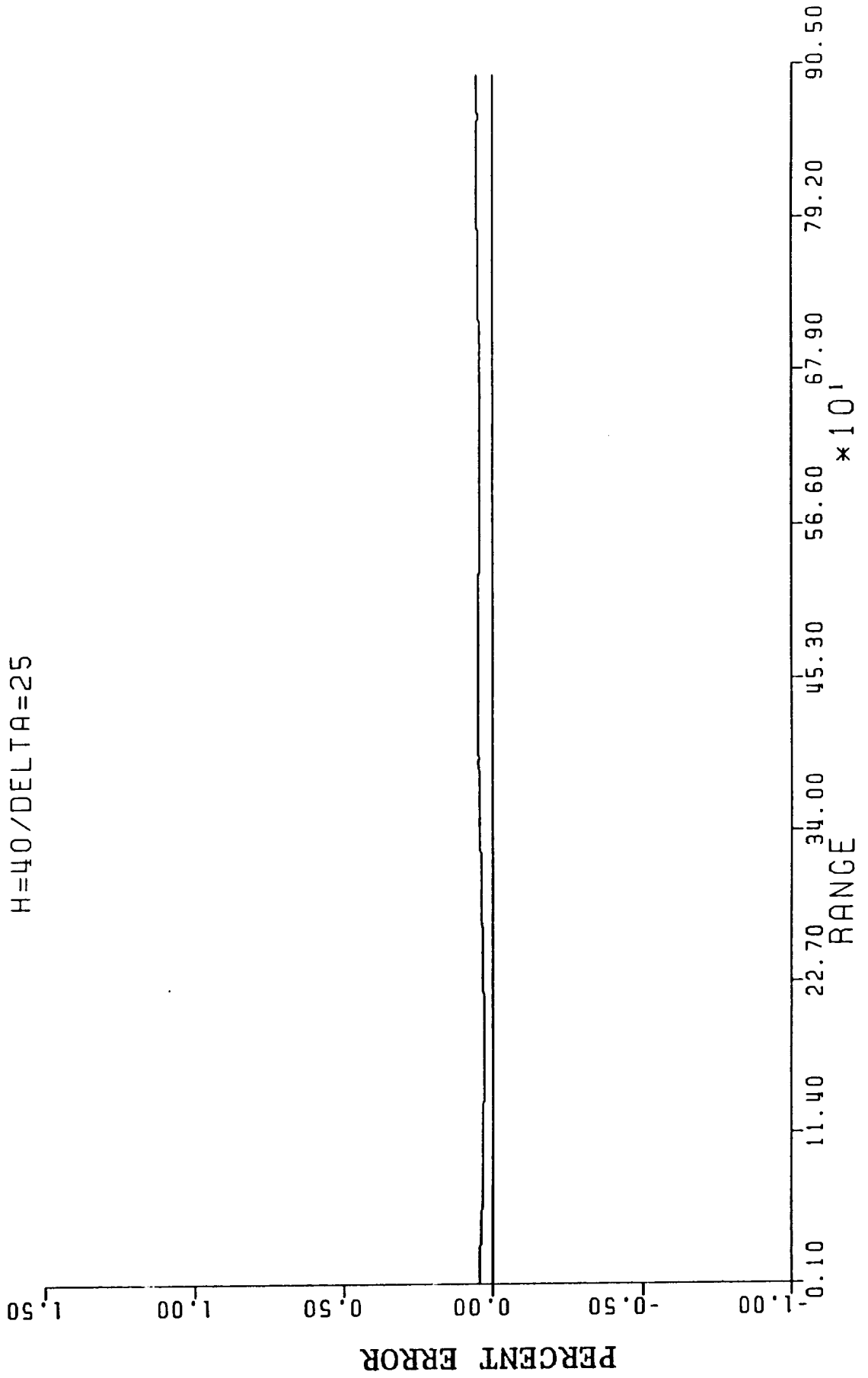




Figure 3-6

ERROR IMAG ZMIM/ZSOM

H=40/DELTA=25



UPWARD CONTINUATION (30 → 50 m)

ERROR VS. ALTITUDE

H0=30/DELTA=5

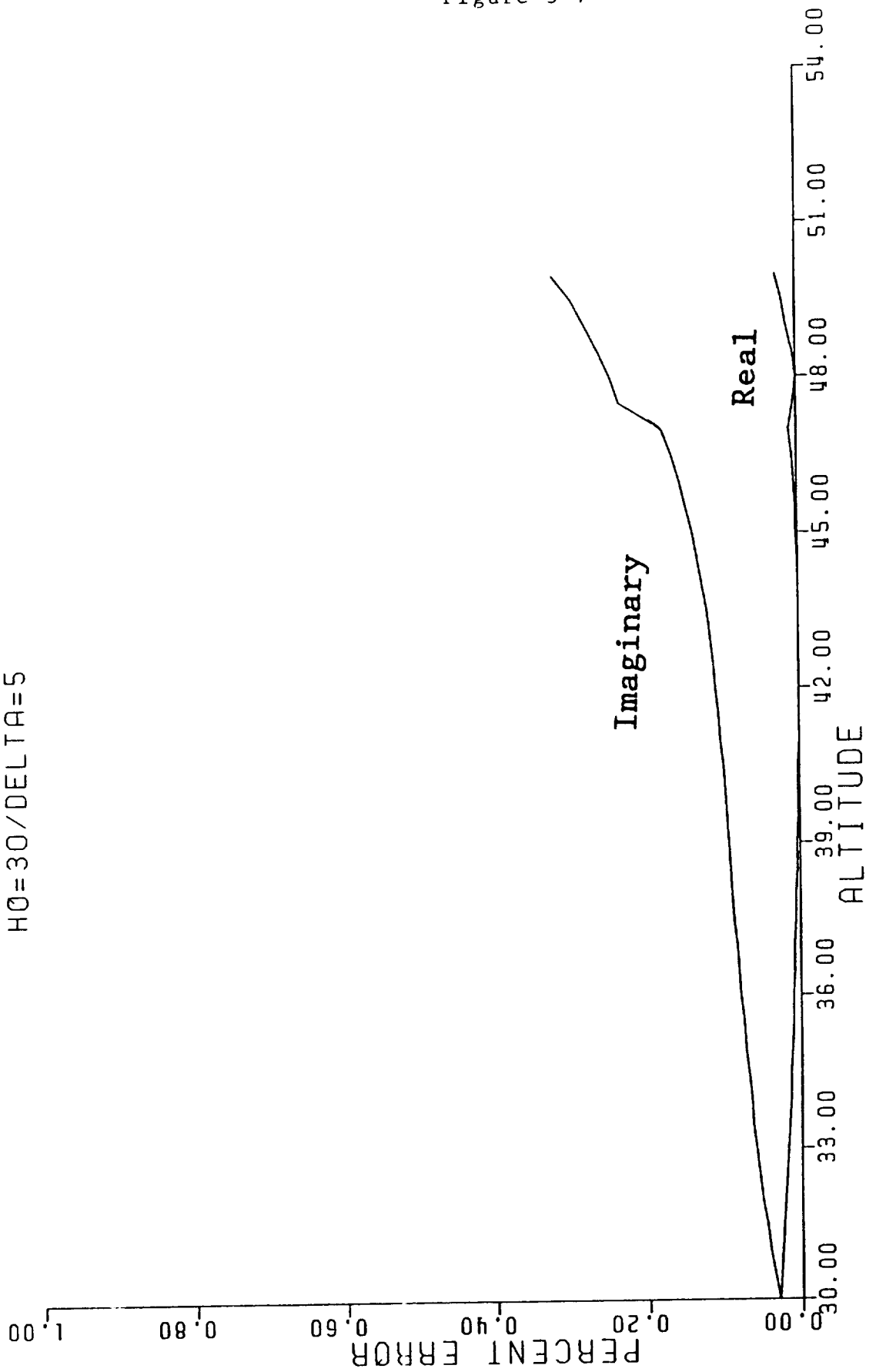


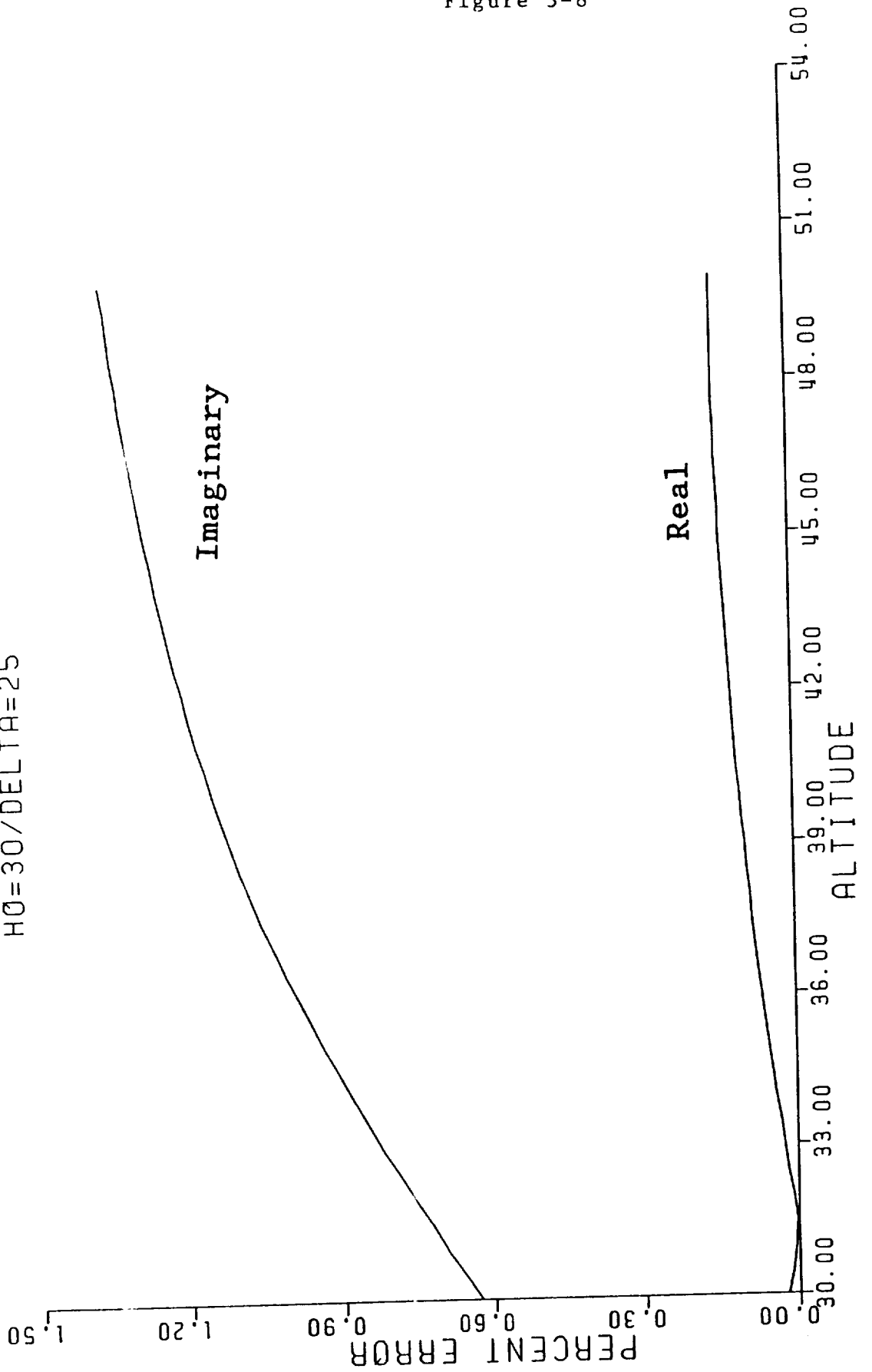
Figure 3-7

Figure 3-8

UPWARD CONTINUATION (30 → 50 m)

ERROR VS. ALTITUDE

$H_0 = 30 / \Delta T = 25$



DOWNWARD CONTINUATION (50 → 30 m)

ERROR VS. AMPLITUDE

H0=50/DELTA=5

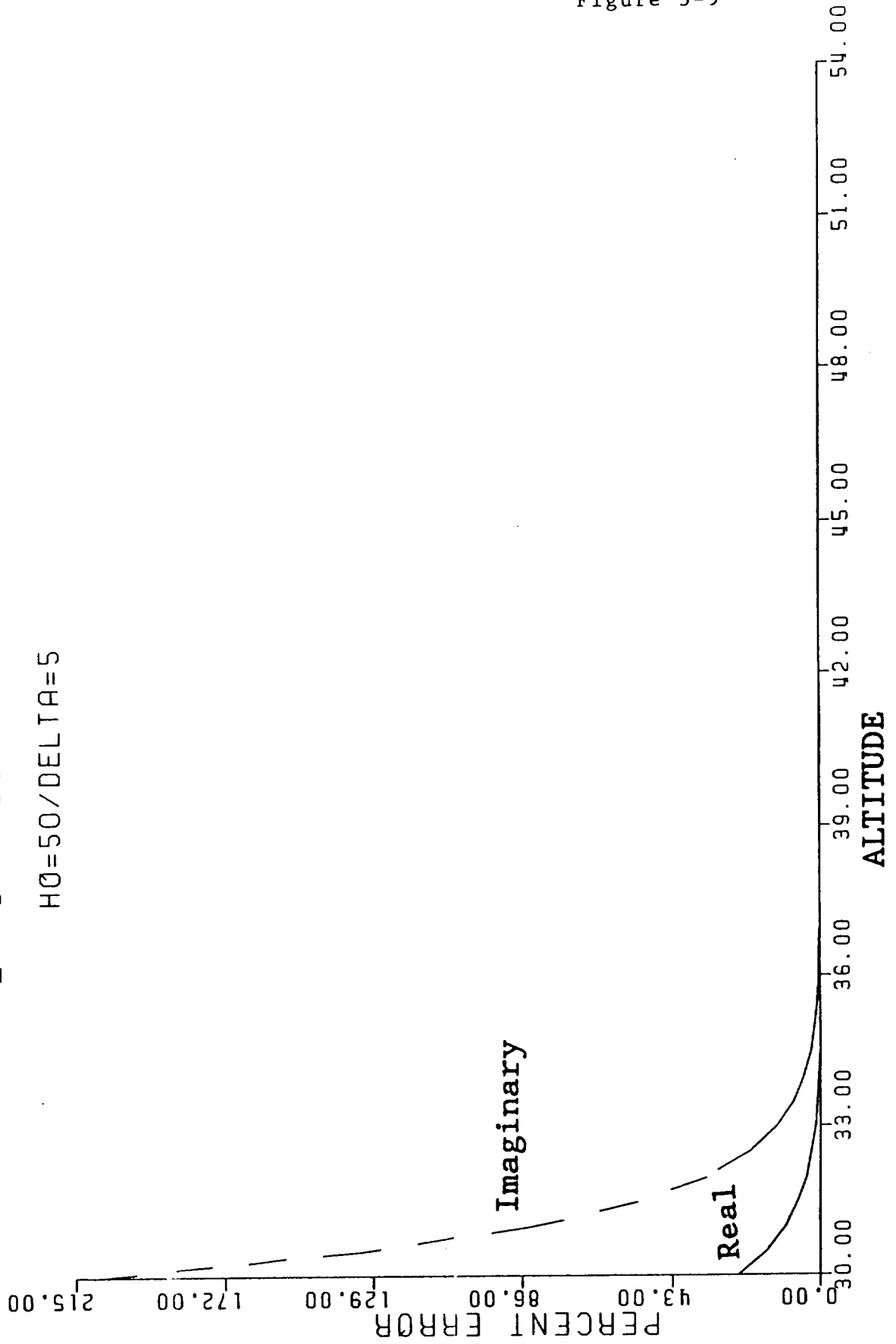


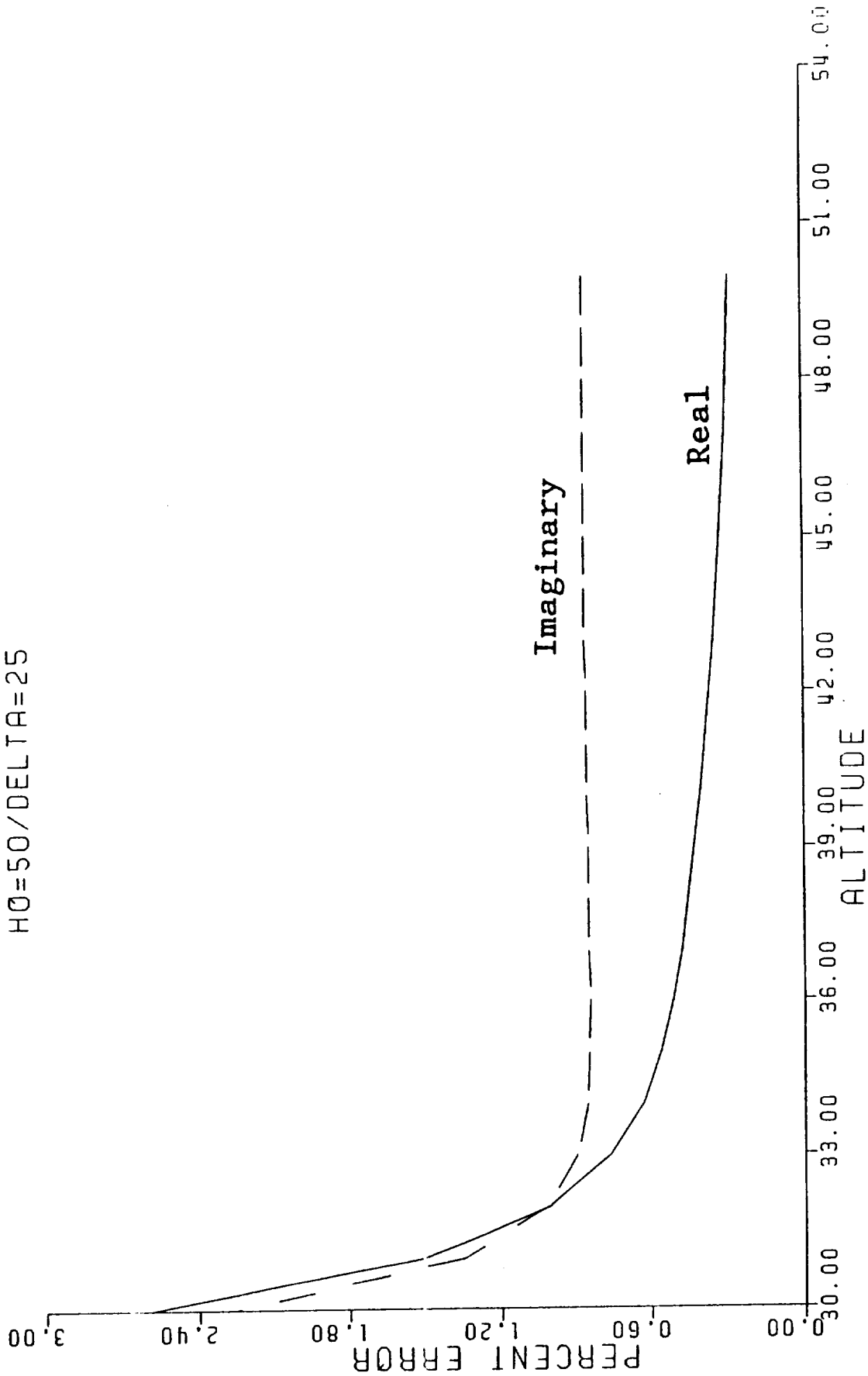
Figure 3-9

Figure 3-10

DOWNWARD CONTINUATION (50 → 30 m)

ERROR VS. ALTITUDE

$H_0 = 50 / \Delta T = 25$



TASK FOUR

Deconvolution of a keel signal

Figure 4-1 shows the one- and two-dimensional inphase and quadrature fields produced for a rectangular keel model of width 90 m and depth 5 m. Figure 4-2 shows the inphase one- and two-dimensional fields, again along with the result of a deconvolution of the two-dimensional field by a line impulse function. The signal width of the deconvolved fields is narrowed, which is the desired result. Gibbs oscillations are introduced by the deconvolution process. Similar results are shown in Figure 4-3 for the quadrature component of the fields. The step in the deconvolved two-dimensional quadrature field at about 20 m is probably an artifact of the line impulse function used in the calculation.

Figures 4-4 through 4-7 show the results of a one-dimensional inversion of the fields displayed in Figures 4-1 through 4-3. Figures 4-4 and 4-5 illustrate ice thickness and ice conductivity results for the one- and two-dimensional fields, and Figures 4-6 and 4-7 show the one-dimensional results, again along with those for the two-dimensional deconvolved fields.

The deconvolved two-dimensional inversion results are not noticeably different from those of the original two-dimensional fields. The chief benefit of the deconvolution process that can be seen in this example is the narrowing of the keel signal. Further investigation with a variety of models should be pursued.

MIM-MIM ALTIM=35M
RECT. MODEL: X0=6.5M DEL1=5M FREQ=2500HZ

Figure 4-1

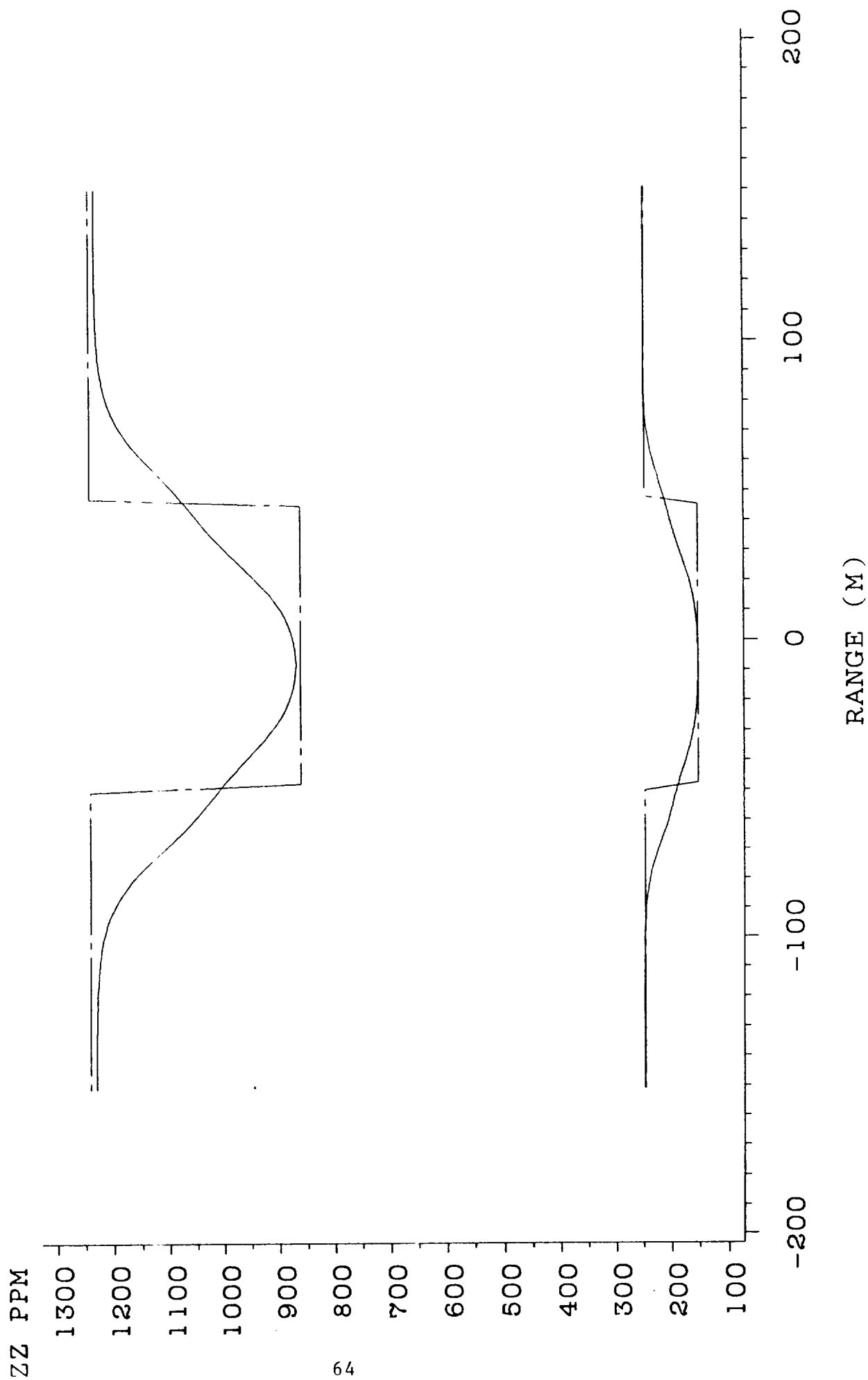


Figure 4-2

MIM-MIM

RECT MODEL: X0=6.5M DEL1=5M FREQ=2500HZ

ALTIM=35M

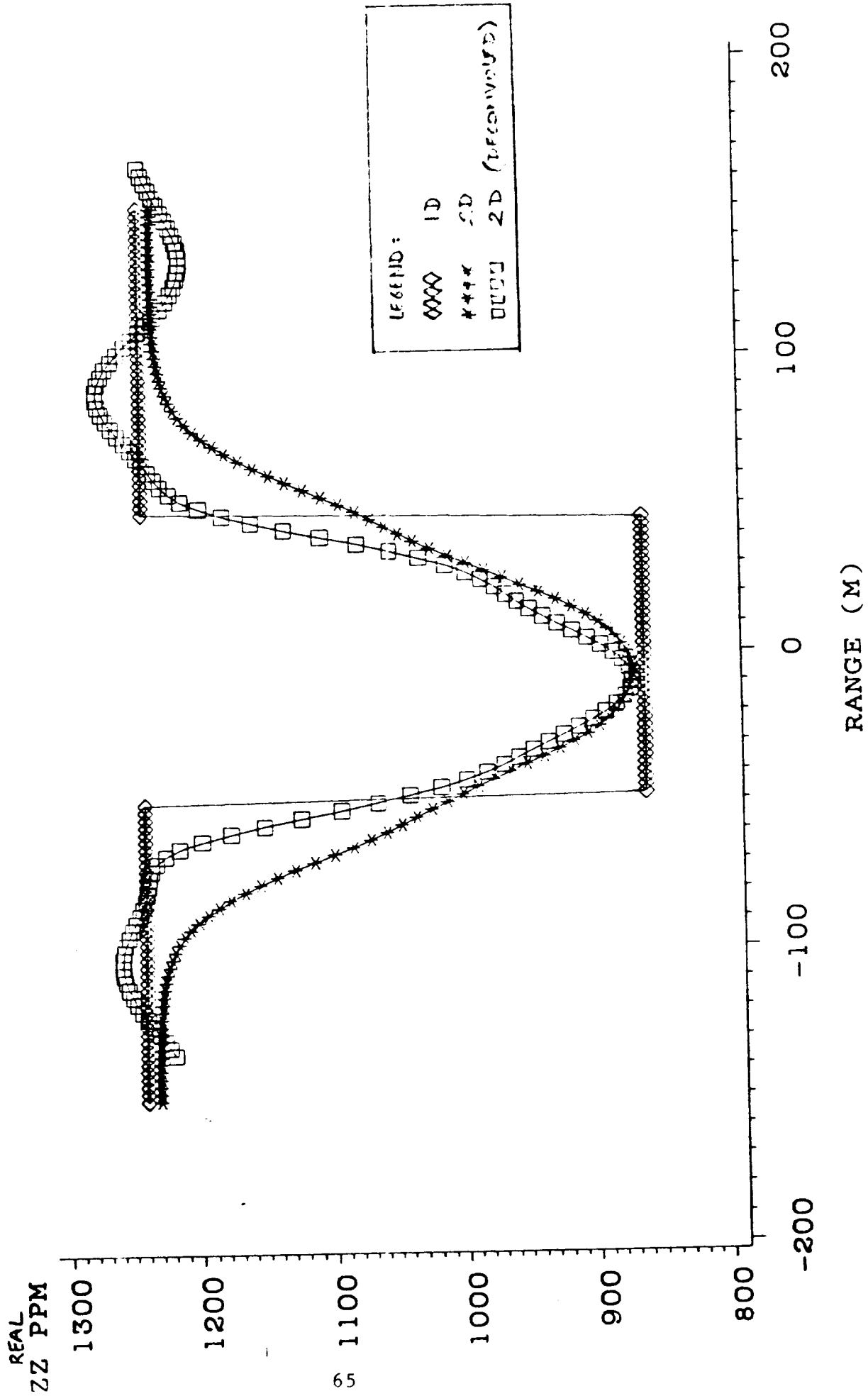


Figure 4-3

MIM-MIM

RECT MODEL: X0=6.5M DEL1=5M FREQ=2500HZ

ALTIM=35M

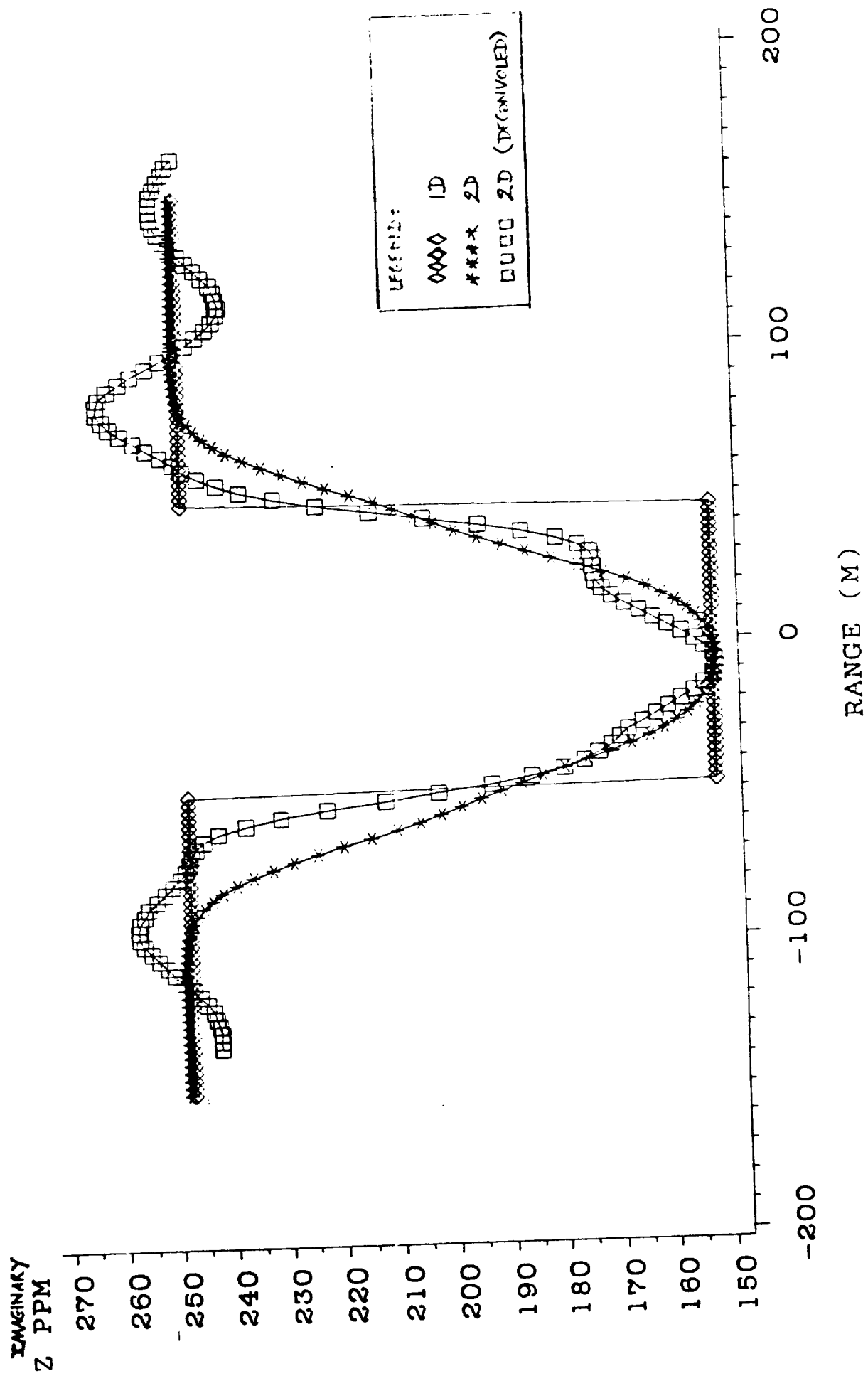




Figure 4-4

ZZ FIELD: MIM-MIM
RECT MODEL: X0=6.5M DEL1=5M FREQ=2500HZ
INVERSE ICE THICKNESS

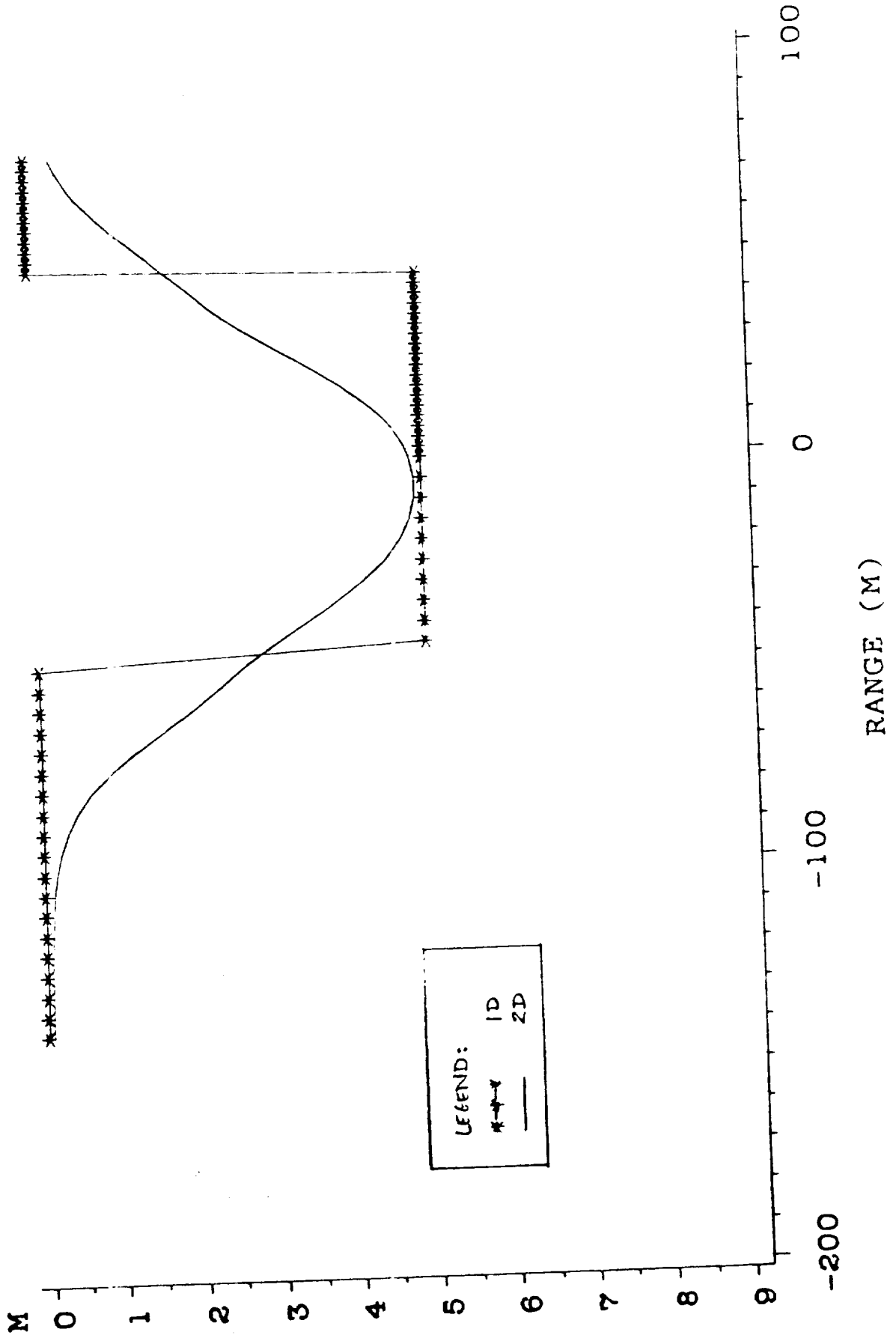


Figure 4-5

ZZ FIELD: MIM-MIM
RECT MODEL: X0=6.5M DEL1=5M FREQ=2500HZ
INVERSE CONDUCTIVITY

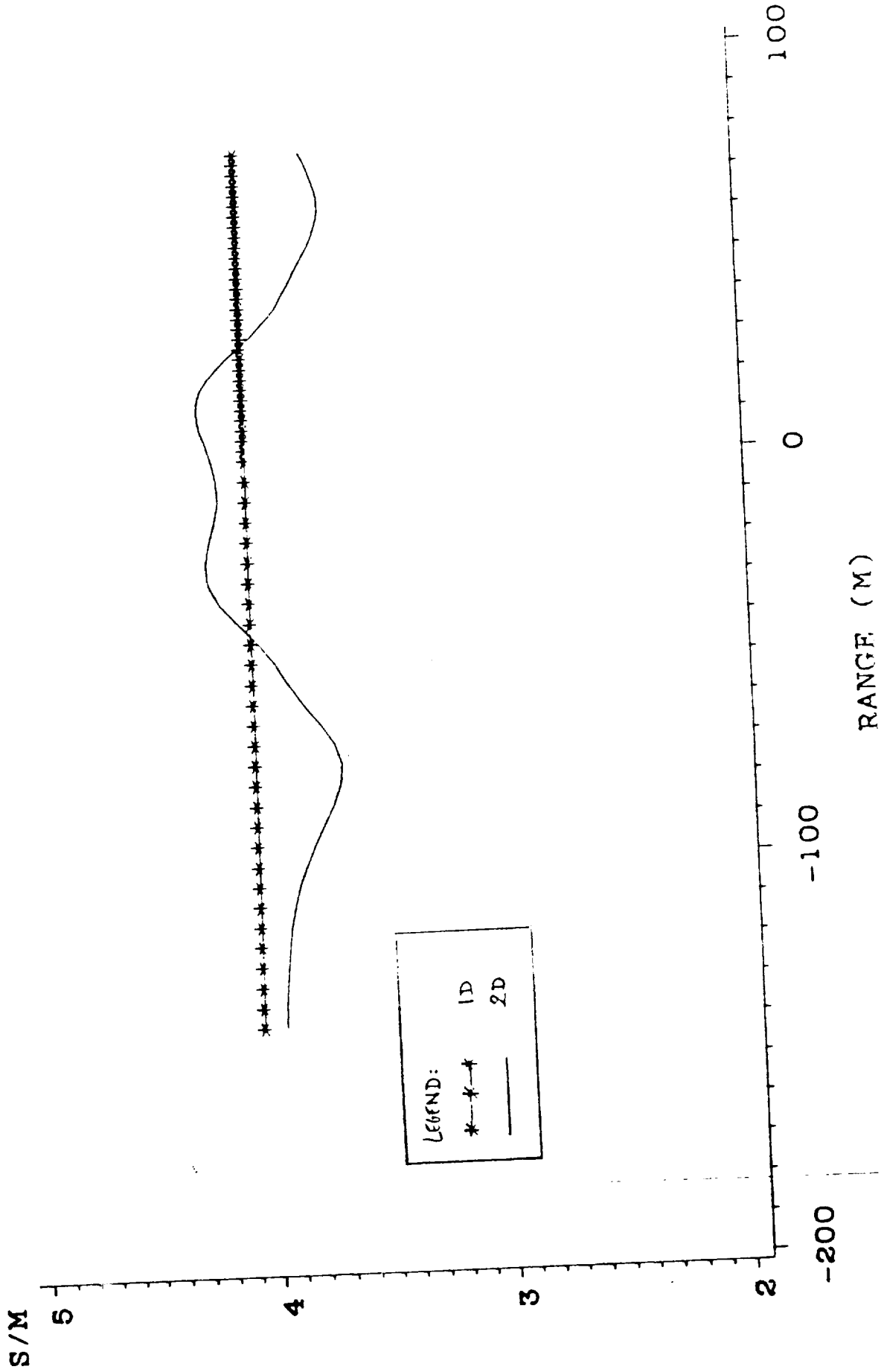
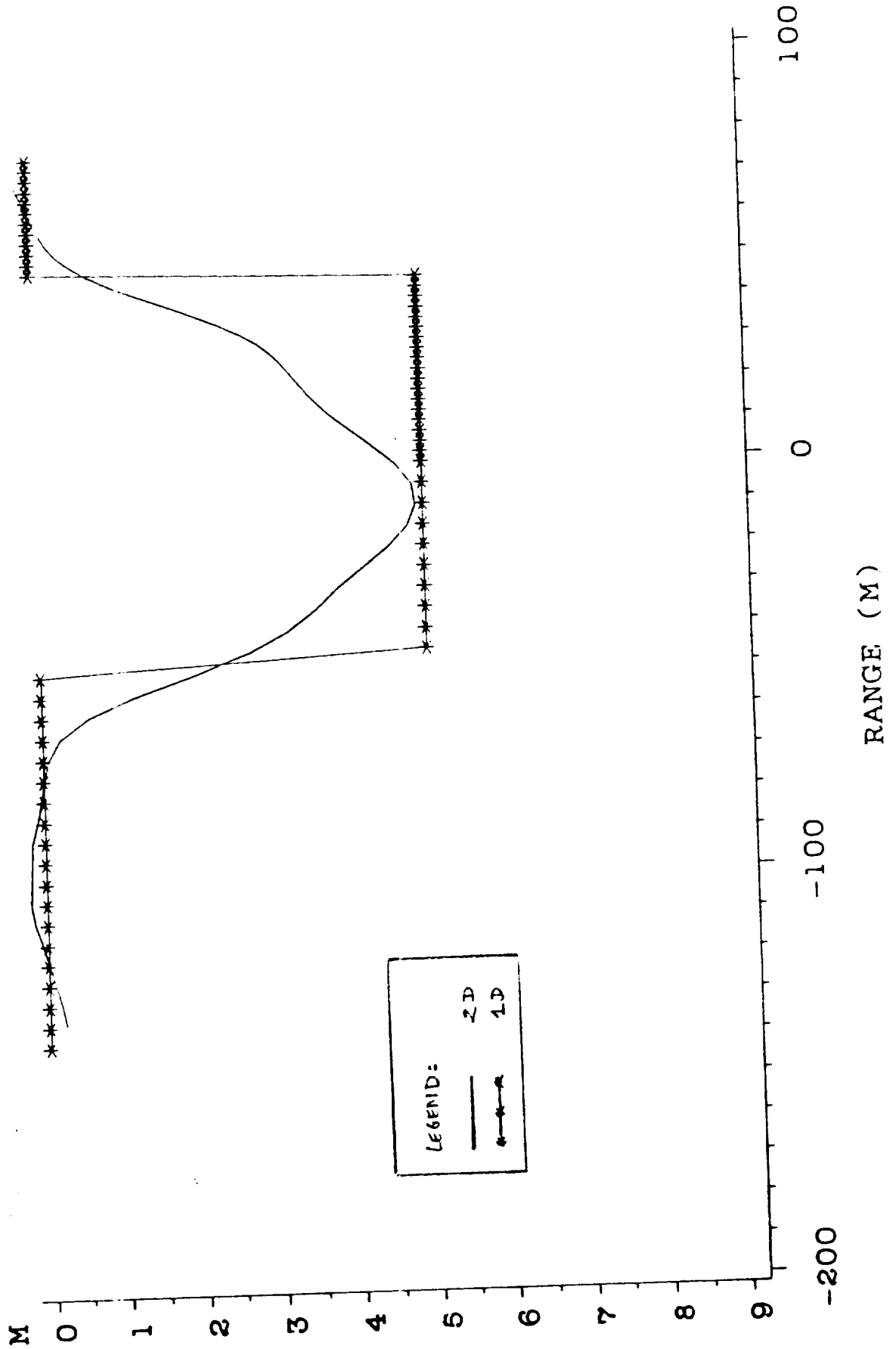


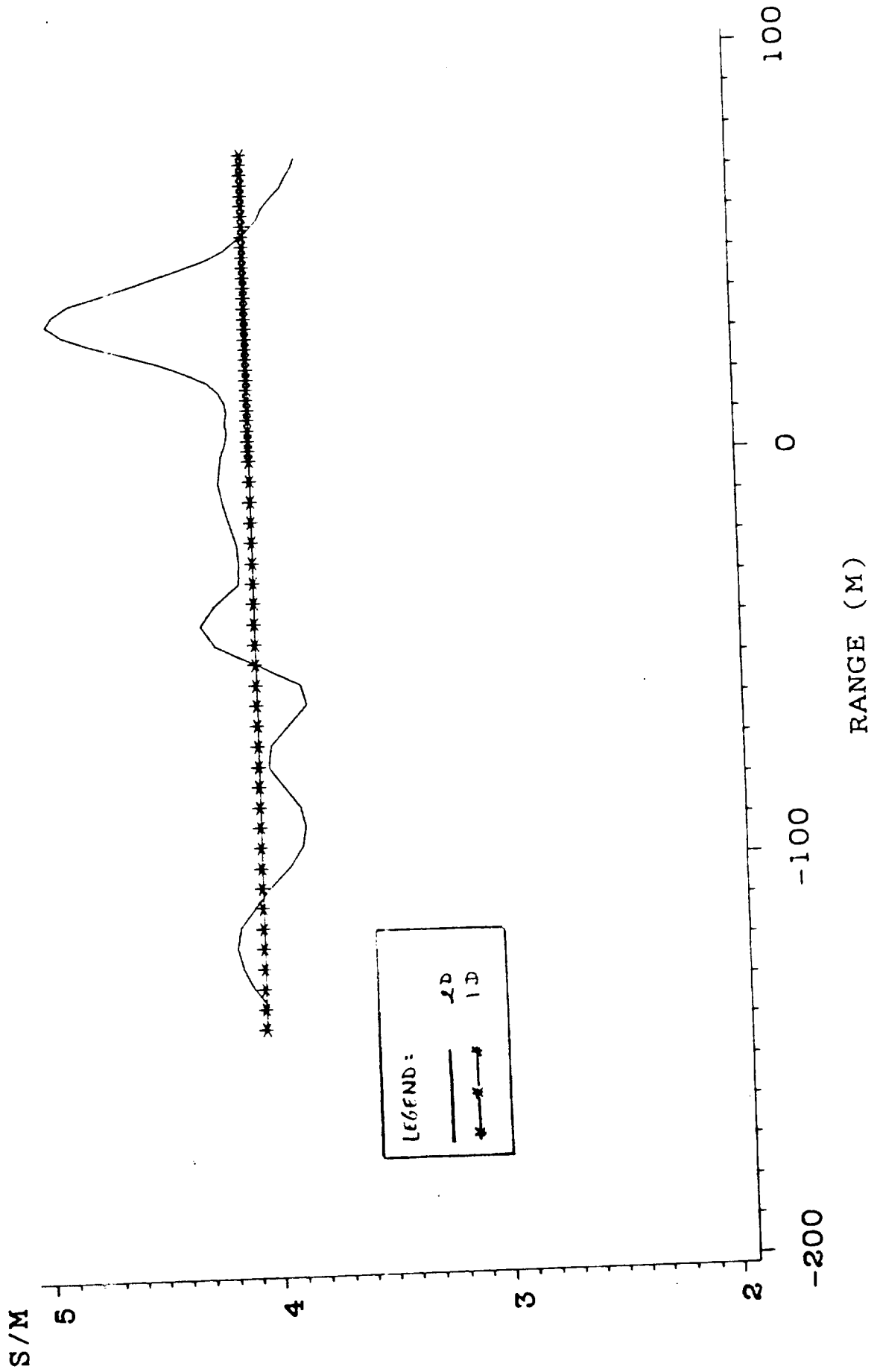
Figure 4-6

DECONVOLED ZZ FIELD: MIM-MIM
RECT MODEL: X0=6.5M DEL1=5M FREQ=2500HZ
INVERSE ICE THICKNESS





DECONVOLED ZZ FIELD: MIM-MIM Figure 4-7
 RECT MODEL: X0=6.5M DEL1=5M FREQ=2500HZ
 INVERSE CONDUCTIVITY





CONCLUSION

The manner in which most of the tasks were completed exceeded initial specifications, e.g., the calculation of the XX and ZX ice keel fields.

The validation of the MIM two- and three-dimensional fields by comparison with the results of more accurate (but more CPU time consuming) numerical calculations and model measurements should be the primary thrust in a continuing investigation.

REFERENCES

A. Becker, G. Liu, and H. F. Morrison, 1987, Airborne Electromagnetic Sensing of Sea Ice Thickness, Final Report, CRREL.

Clyde J. Bergeron, Juliette W. Ioup, and Gus A. Michel, 1987, Application of MIM to inversion of synthetic AEM bathymetric data, *Geophysics* 52, 794-801.

Clyde J. Bergeron, Terry L. Morris, and Juliette W. Ioup, 1988, Up-down continuation of AEM data, *EOS Trans. Amer. Geophys. Union* 69, 1169.

Stanley L. Dallal, 1985, Electromagnetic Scale Modelling for the Detection of Fractures and Cavities, M. S. Thesis, University of California, Berkeley.

K. H. Lee and H. F. Morrison, 1985, A numerical solution for the electromagnetic scattering by a two-dimensional inhomogeneity, *Geophysics* 50, 466-472.

A. N. Sommerfeld, 1909, The propagation of waves in wireless telegraphy, *Ann. Phys.* 28, 665-736.

**Determination of Design and Operation Parameters
for Upper Atmospheric Research Instrumentation
to Yield Optimum Resolution with Deconvolution**

NASA Grant NAG 1-804

FINAL REPORT

APPENDIX 6

**Dr. George E. Ioup, Principal Investigator
Dr. Juliette W. Ioup, Principal Investigator
Department of Physics
University of New Orleans
New Orleans, LA 70148**

Status Report

15 Jan 1990

NASA Grant NAG-1-804

Determination of Design and Operation Parameters for Upper
Atmospheric Research Instrumentation to Yield Optimum Resolution
with Deconvolution

Analysis of Response of the Arctic Sea Ice Environment
to AEM Fields

Clyde J. Bergeron and Juliette W. Ioup
Department of Physics, University of New Orleans

Sea Ice Inversion

The MIM inversion of sea ice AEM data taken at two frequencies, 1000 Hz (f_{10}) and 250 kHz (f_{hi}), proceeds as follows.

The low frequency data are first inverted to give $(h + d_1)$ and σ_2 , where h is the altitude of the bird above the sea ice, d is the ice thickness, and σ_2 is the electrical conductivity of the sea. This inversion assumes the following:

1. The skin depth of the sea ice $\delta_1(10)$ is much greater than the thickness of the sea ice and hence the sea ice is effectively transparent to the low frequency primary signal.
2. The sea bottom does not affect the secondary field. This assumption is valid provided that the sea depth d_2 is greater than twice the low frequency skin depth of the sea, i.e., $d_2 > 2$

$\delta_2(10)$. These two assumptions allow a halfspace inversion. The algebra and computer algorithms for the halfspace inversion are given in the Appendix.

It is assumed that the altitude h is independently determined by a radar or laser altimeter. Thus the inversion results in a local value for the sea ice thickness d_1 and the conductivity of the sea water, σ_2 . These results are employed in the inversion of the high frequency data to determine the sea ice conductivity.

Outline of high frequency inversion

First a halfspace inversion of the high frequency data is performed. This produces an effective skin depth δ_{eff} which lies in the range $\delta_2 \leq \delta_{eff} \leq \delta_1$, and is a function of ice thickness d_1 . The effective high frequency skin depth is combined with the altimeter reading h to form the ratio $A_{eff} = 2h/\delta_{eff}$. The ad hoc normalization function employed in MIM inversion is a function of A_{eff} , i.e.,

$$Z_{MIM} \approx Z_s(\text{normalized}) = F(A_{eff}) Z_s .$$

For $d_1 \ll \delta_1$, $\delta_{eff} = \delta_2$ and for $d_1 > 2\delta_1$, then $\delta_{eff} = \delta_1$. Since d_1 is known from the low frequency inversion, this latter case may be recognized and hence the first layer conductivity σ_1 is determined from δ_{eff} by

$$\sigma_1 = 2/[\mu_0 f(hi) \delta_{eff}^2] ,$$

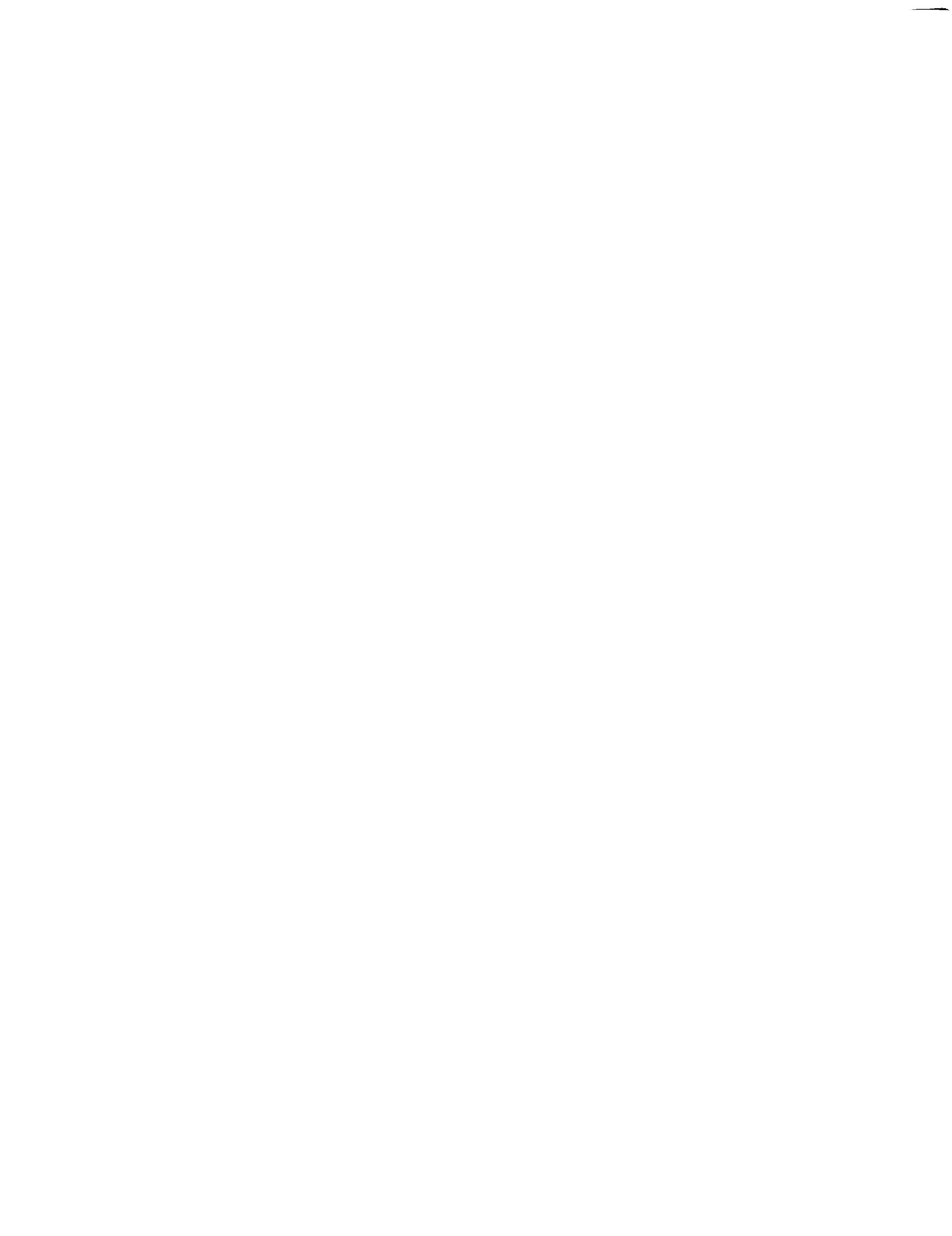
$$\omega = 2\pi \frac{f}{Hz}$$

where μ_0 is the vacuum magnetic permittivity. The condition $d_1 > 2 \delta_1$ only occurs for thick ($d_1 \geq 10m$), highly conducting (σ_1

> 0.027 S/m) sea ice. For the intermediate, more general situation where δ_{eff}/d_1 is of the order of unity, the inversion procedure to be used is that described below.

The MIM relationship between the complex two-layer correction factor Q and the high frequency AEM field is algebraically transformed into two simultaneous transcendental real equations with argument d_1/δ_1 , where δ_1 is the unknown quantity. All other quantities in these equations are known. Each of these equations has in general several roots, BUT only one common root. The explicit functions that occur respectively in these equations are $\tan(d_1/\delta_1)$ and $\tanh(d_1/\delta_1)$. A root-finding algorithm is first applied to the $\tan(d_1/\delta_1)$ equation. When a root is determined, that root is inserted in the $\tanh(d_1/\delta_1)$ equation to test if it is also a root of the $\tanh(d_1/\delta_1)$ equation. If not, the algorithm continues in its determination of the real roots of the $\tan(d_1/\delta_1)$ equation until the root is found that simultaneously satisfies both equations. The first layer skin depth δ_1 and conductivity σ_1 are given by that simultaneous root.

The range of applicability of the root finding algorithm is given by $0.02 < d_1/\delta_1 < 2.5$. These limits can be understood in physical terms. For $d_1/\delta_1 > 2.5$ the sea ice is effectively a halfspace as has been already noted, and a two layer model is inappropriate. For $d_1/\delta_1 < 0.02$ the perturbation produced on the secondary AEM field by the sea ice cover is lost in the computer "noise" caused by roundoff, etc., and will



certainly be undetectable in the noise and drift present in even ideal real data, where noise and drift are greater than about 1 ppm.

The lower ice thickness limit on the detectability of sea ice conductivity is illustrated in the following table which assumes a value of sea water conductivity of $\sigma_2 = 2.7$ S/m and an operating frequency of 250 KHz.

σ_2/σ_1	δ_1	minimum d_1
100	~ 6 m	~ 0.1 m
1000	~ 20 m	~ 0.3 m

The algebraic details of this procedure and the root finding algorithm are given in the Appendix.

Results

The MIM inversion procedure that has been described is applied to several sea ice models. In all of the models used the low and high frequencies assumed for the AEM system are 1 kHz and 250 kHz, respectively; the altitude of the AEM bird is 25 m; the conductivity of the sea water σ_2 is 2.7 S/m; and the conductivity of the sea ice σ_1 for each model has input values of 0.027 S/m, 0.0054 S/m, and 0.0027 S/m. Thus the ratio K of the conductivities of sea water to sea ice has the values 100, 500, and 1000, respectively.

With these general conditions, the first model of ice

thickness versus range (fiducial number) is given in Figure 1. The ice thickness increases linearly with increasing range. The results of the inversion for σ_1 are shown in Figure 2. The inversion values for σ_1 are in fair agreement with the input values except for the case with $\sigma_1 = 0.027$ S/m. The problem occurs at an ice thickness of approximately 9.5 m. For $\sigma_1 = 0.027$ S/m the skin depth of the sea ice is about 6 m, thus the ratio of ice thickness to skin depth (which is the argument of both the tan and tanh functions) is about $\pi/2$, where the tangent becomes singular and double valued. More importantly, in the immediate vicinity of $\pi/2$, $\tan(d_1/\delta_1)$ varies rapidly. In spite of this, the root finding inversion algorithm still works when the exact forward MIM field ZZ(MIM) is used as the input field (see Table 1). When a simultaneous root cannot be found for the normalized Sommerfeld field in the vicinity of $\pi/2$, a value of 1.55 is assumed for x . See Table 2. It is the residual differences between the normalized Sommerfeld field (or real field data) and the exact MIM field that causes the root finding algorithm that we are currently using to fail for $x = d_1/\delta_1 = \pi/2$.

It should be noted that this value of $\pi/2$ will most likely not be encountered in field surveys where ice conductivities will generally be less than 0.0054 S/m ($K = 500$). Table 3 shows that for $K = 500$, x is less than $\pi/2$ for sea ice thicknesses up to 20 m.

A shallow ice keel model is shown in Figure 3. Figure 4

shows the values of σ_1 for this model produced by the inversion algorithm for $K = 100, 500, \text{ and } 1000$. These results are also listed in Tables 5, 6, and 7.

In all of the tables we have included the results of the halfspace inversion of the high frequency data which gives σ_{eff} . It can be seen for the case $K = 100$ when $x > 2.4$, $\sigma_{\text{eff}} = \sigma_{\text{input}}$. This demonstrates that when the ice thickness is greater than 2.4 skin depths, a halfspace inversion yields good results for the ice conductivity. Although values of $x > 2.4$ will probably not be found in survey data taken at a high frequency of 250 kHz, still higher frequencies of about 1 MHz will bring x into this range.

Finally, the results of the inversion are shown in Figure 3 for a shallow ice keel model. The tabulated results are shown in Tables 5, 6, and 7.

In summary, the present inversion algorithm for σ_1 works well except in the vicinity of $d_1/\delta_1 = \pi/2$. We are continuing efforts to modify and improve the existing algorithm.

Figure 1

SEA ICE: INVERT SOM ZZ(HI)

K=100,500,1000 H=25 SIG2=2.7 F=1KHZ,250KHZ X0=3

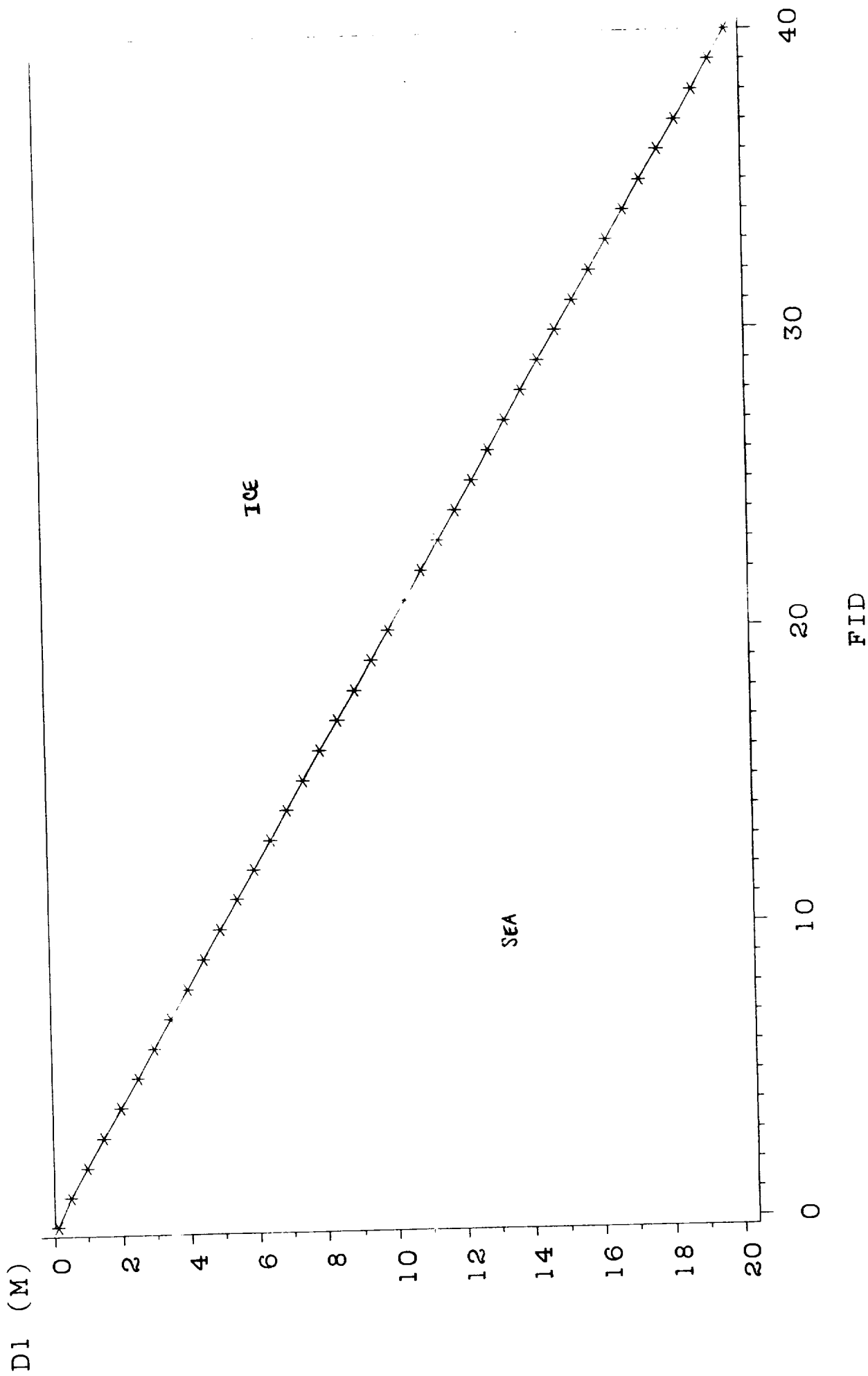
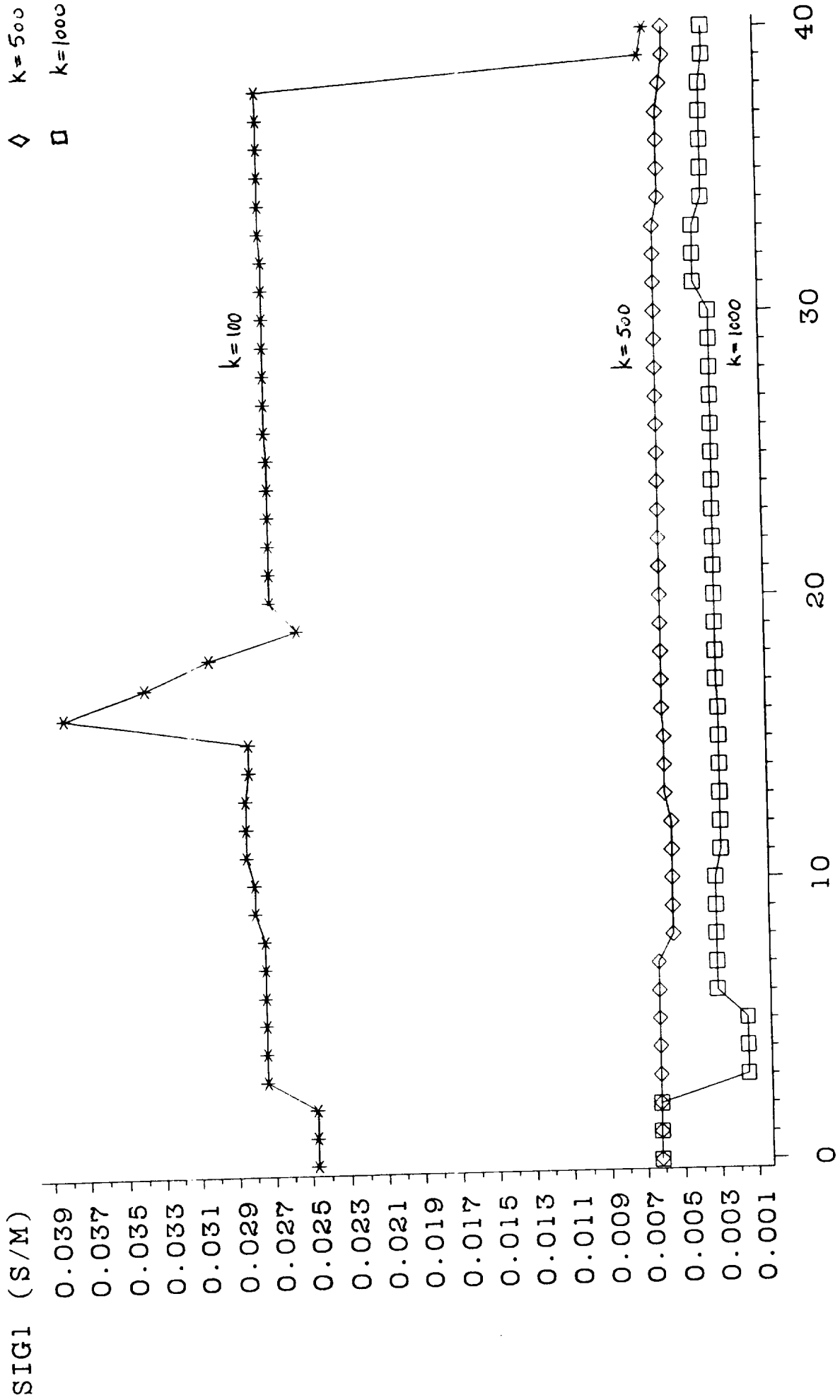


Figure 2

SEA ICE: INVERT SOM ZZ(HI)

$K=100, 500, 1000$ $H=25$ $SIG2=2.7$ $F=1$ $KHZ, 250$ KHZ $X0=3$

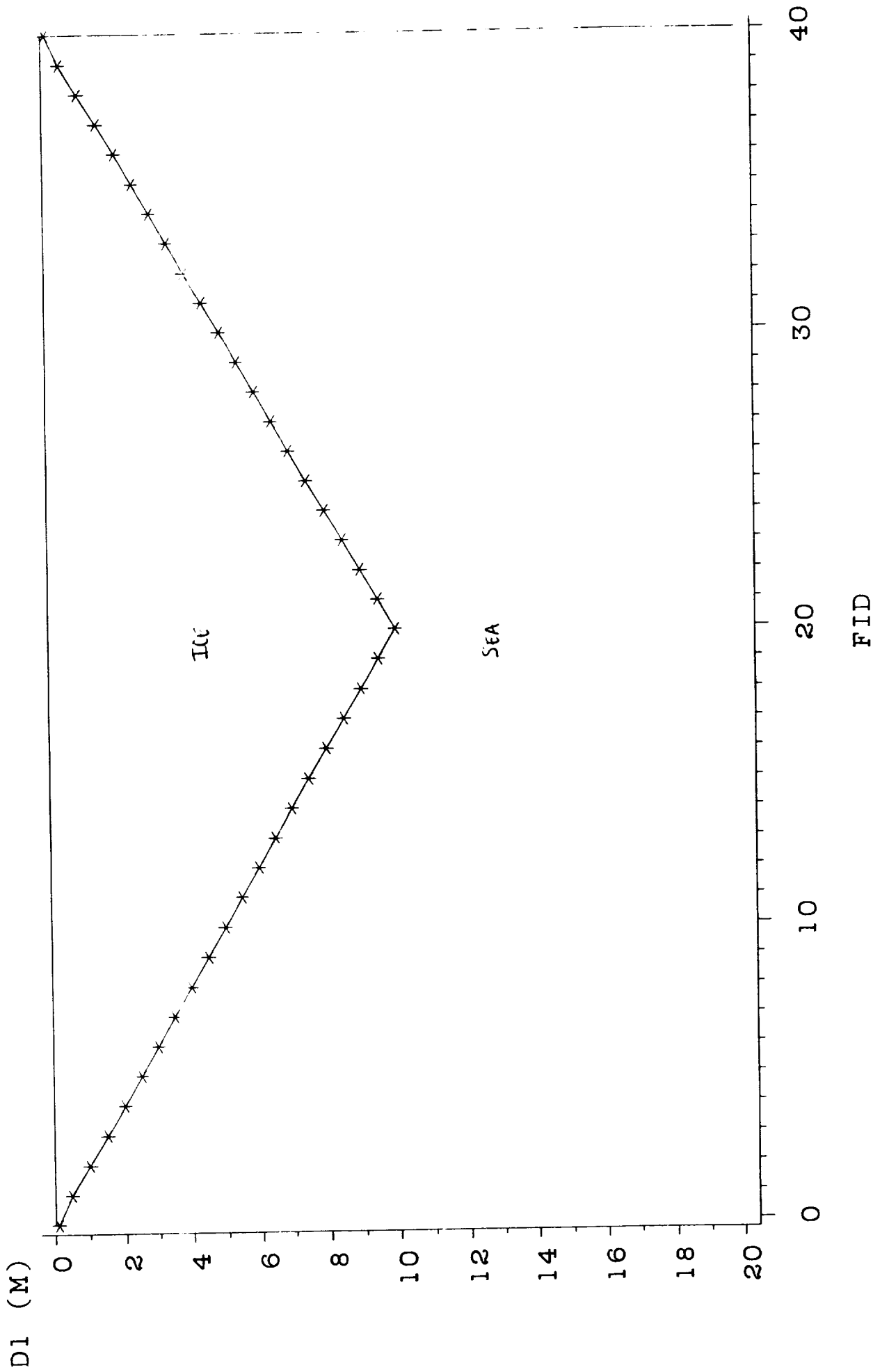
* $k=100$
◇ $k=500$
□ $k=1000$



FID

SEA ICE: INVERT SOM ZZ(HI)
K=100,500,1000 H=25 SIG2=2.7 F=1KHZ,250KHZ X0=3

Figure 3



SEA ICE: INVERT SOM ZZ(HI) Figure 4
 K=100,500,1000 H=25 SIG2=2.7 F=1KHZ,250KHZ X0=3

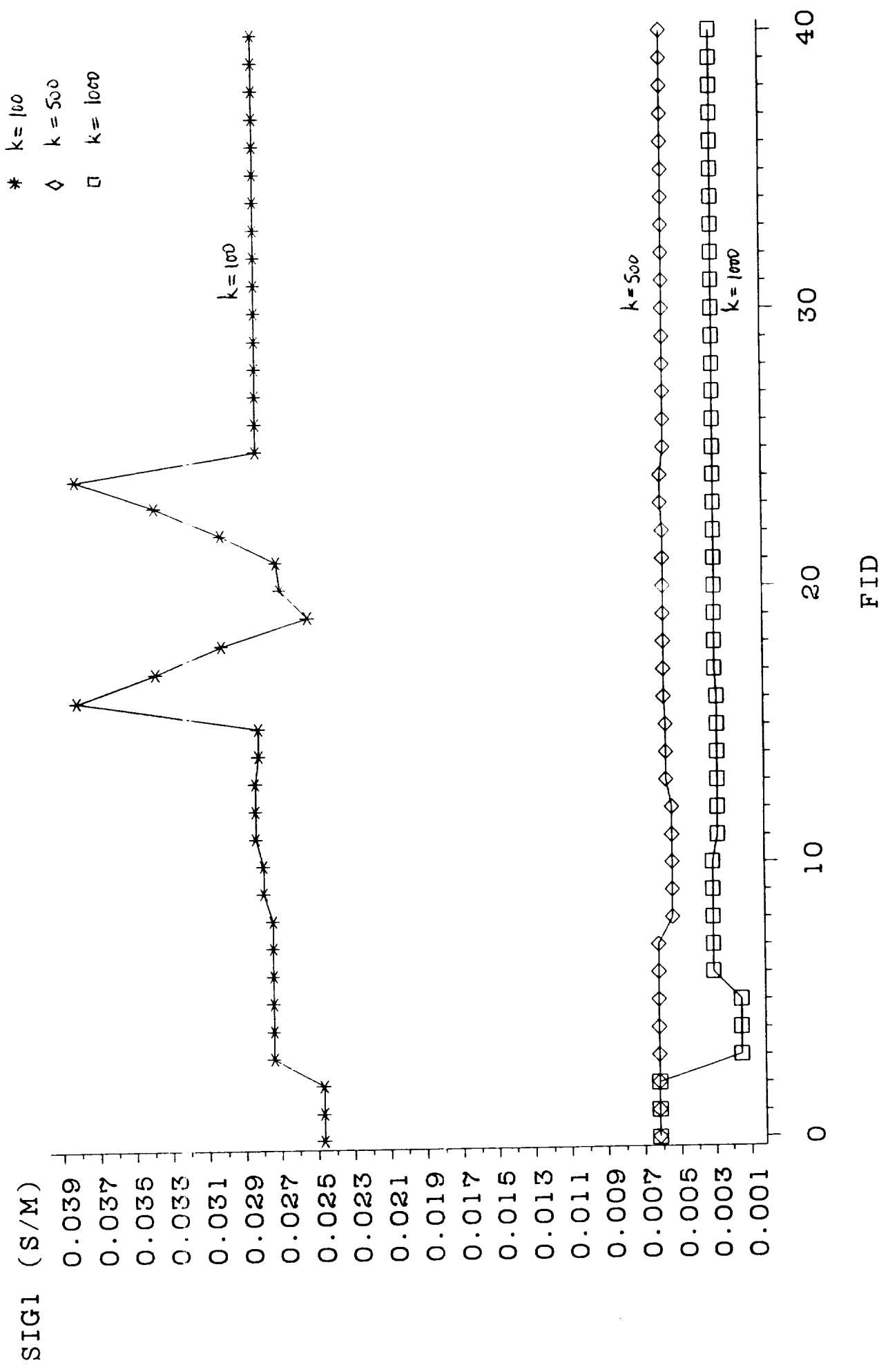


TABLE 1

=====

SIGMA1 (ACTUAL)=0.027 S/M

WORKING WITH

ZZMIM

XSTART= 0.5000000

KNOW D1 AND SIG2, SOLVE FOR X=D1/DELTA1 AND HENCE SIG1.

SIGeff IS THE HALF-SPACE EFFECTIVE CONDUCTIVITY,

AND IT IS COMPUTED ONLY WHEN INVERTING ZZSOM

FID	D1	X	SIG1	SIGeff
0.0	0.1	0.0156	0.0247	2.6960
1.0	0.5	0.0781	0.0247	2.5941
2.0	1.0	0.1563	0.0247	2.2813
3.0	1.5	0.2344	0.0247	1.7051
4.0	2.0	0.3250	0.0268	1.1303
5.0	2.5	0.4063	0.0268	0.7022
6.0	3.0	0.4875	0.0268	0.4009
7.0	3.5	0.5687	0.0268	0.2198
8.0	4.0	0.6500	0.0268	0.1332
9.0	4.5	0.7312	0.0268	0.0884
10.0	5.0	0.8125	0.0268	0.0613
11.0	5.5	0.9000	0.0271	0.0461
12.0	6.0	0.9818	0.0271	0.0373
13.0	6.5	1.0636	0.0271	0.0315
14.0	7.0	1.1455	0.0271	0.0277
15.0	7.5	1.2273	0.0271	0.0253
16.0	8.0	1.3091	0.0271	0.0238
17.0	8.5	1.3909	0.0271	0.0228
18.0	9.0	1.4727	0.0271	0.0224
19.0	9.5	1.5500	0.0270	0.0221
20.0	10.0	1.6355	0.0271	0.0222
21.0	10.5	1.7172	0.0271	0.0223
22.0	11.0	1.7990	0.0271	0.0226
23.0	11.5	1.8808	0.0271	0.0230
24.0	12.0	1.9626	0.0271	0.0234
25.0	12.5	2.0443	0.0271	0.0237
26.0	13.0	2.1218	0.0270	0.0241
27.0	13.5	2.2035	0.0270	0.0244
28.0	14.0	2.2851	0.0270	0.0247
29.0	14.5	2.3667	0.0270	0.0250
30.0	15.0	2.4483	0.0270	0.0252
31.0	15.5	2.5299	0.0270	0.0254
32.0	16.0	2.6115	0.0270	0.0255
33.0	16.5	2.6931	0.0270	0.0257
34.0	17.0	2.7747	0.0270	0.0258
35.0	17.5	2.8563	0.0270	0.0258
36.0	18.0	2.9379	0.0270	0.0259
37.0	18.5	3.0195	0.0270	0.0259
38.0	19.0	3.1012	0.0270	0.0259
39.0	19.5	3.1828	0.0270	0.0259
40.0	20.0	3.2644	0.0270	0.0259

TABLE 2

=====

SIGMA1 (ACTUAL)=0.027 S/M

WORKING WITH

ZZSOM

XSTART= 0.5000000

KNOW D1 AND SIG2, SOLVE FOR X=D1/DELT1 AND HENCE SIG1.

SIGeff IS THE HALF-SPACE EFFECTIVE CONDUCTIVITY,

AND IT IS COMPUTED ONLY WHEN INVERTING ZZSOM

FID	D1	X	SIG1	SIGeff
0.0	0.1	0.0156	0.0247	2.6973
1.0	0.5	0.0781	0.0247	2.5953
2.0	1.0	0.1563	0.0247	2.2816
3.0	1.5	0.2344	0.0247	1.7033
4.0	2.0	0.3375	0.0289	1.1265
5.0	2.5	0.4087	0.0271	0.6976
6.0	3.0	0.4904	0.0271	0.3973
7.0	3.5	0.5722	0.0271	0.2178
8.0	4.0	0.6664	0.0281	0.1324
9.0	4.5	0.7497	0.0281	0.0884
10.0	5.0	0.8330	0.0281	0.0619
11.0	5.5	0.9163	0.0281	0.0471
12.0	6.0	0.9996	0.0281	0.0386
13.0	6.5	1.0829	0.0281	0.0330
14.0	7.0	1.1662	0.0281	0.0294
15.0	7.5	1.2495	0.0281	0.0270
16.0	8.0	1.5500	0.0380	0.0256
17.0	8.5	1.5500	0.0337	0.0247
18.0	9.0	1.5500	0.0301	0.0242
19.0	9.5	1.4875	0.0248	0.0240
20.0	10.0	1.5500	0.0243	0.0240
21.0	10.5	1.7131	0.0270	0.0241
22.0	11.0	1.7947	0.0270	0.0244
23.0	11.5	1.8763	0.0270	0.0247
24.0	12.0	1.9579	0.0270	0.0250
25.0	12.5	2.0394	0.0270	0.0253
26.0	13.0	2.1210	0.0270	0.0256
27.0	13.5	2.2026	0.0270	0.0259
28.0	14.0	2.2842	0.0270	0.0261
29.0	14.5	2.3657	0.0270	0.0264
30.0	15.0	2.4473	0.0270	0.0265
31.0	15.5	2.5289	0.0270	0.0267
32.0	16.0	2.6105	0.0270	0.0268
33.0	16.5	2.6921	0.0270	0.0269
34.0	17.0	2.7736	0.0270	0.0270
35.0	17.5	2.8552	0.0270	0.0271
36.0	18.0	2.9383	0.0270	0.0271
37.0	18.5	3.0199	0.0270	0.0271
38.0	19.0	3.1024	0.0270	0.0271
39.0	19.5	1.5500	0.0064	0.0271
40.0	20.0	1.5500	0.0061	0.0271

TABLE 3

=====

SIGMA1 (ACTUAL)=0.0054 S/M
WORKING WITH
ZZSOM

XSTART= 0.5000000

KNOW D1 AND SIG2, SOLVE FOR X=D1/DELT1 AND HENCE SIG1.
SIGeff IS THE HALF-SPACE EFFECTIVE CONDUCTIVITY,
AND IT IS COMPUTED ONLY WHEN INVERTING ZZSOM

FID	D1	X	SIG1	SIGeff
0.0	0.1	0.0078	0.0062	2.6998
1.0	0.5	0.0391	0.0062	2.6784
2.0	1.0	0.0781	0.0062	2.6794
3.0	1.5	0.1172	0.0062	2.5616
4.0	2.0	0.1563	0.0062	2.3817
5.0	2.5	0.1953	0.0062	2.1671
6.0	3.0	0.2344	0.0062	1.7031
7.0	3.5	0.2734	0.0062	1.1052
8.0	4.0	0.2930	0.0054	0.7481
9.0	4.5	0.3296	0.0054	0.5329
10.0	5.0	0.3662	0.0054	0.3495
11.0	5.5	0.4028	0.0054	0.2399
12.0	6.0	0.4395	0.0054	0.1807
13.0	6.5	0.4886	0.0057	0.1303
14.0	7.0	0.5262	0.0057	0.0979
15.0	7.5	0.5637	0.0057	0.0723
16.0	8.0	0.6076	0.0058	0.0536
17.0	8.5	0.6455	0.0058	0.0414
18.0	9.0	0.6835	0.0058	0.0325
19.0	9.5	0.7215	0.0058	0.0264
20.0	10.0	0.7595	0.0058	0.0213
21.0	10.5	0.7974	0.0058	0.0178
22.0	11.0	0.8354	0.0058	0.0148
23.0	11.5	0.8734	0.0058	0.0126
24.0	12.0	0.9114	0.0058	0.0109
25.0	12.5	0.9493	0.0058	0.0097
26.0	13.0	0.9873	0.0058	0.0087
27.0	13.5	1.1253	0.0070	0.0082
28.0	14.0	1.1670	0.0070	0.0075
29.0	14.5	1.2086	0.0070	0.0070
30.0	15.0	1.2503	0.0070	0.0066
31.0	15.5	1.2112	0.0062	0.0063
32.0	16.0	1.2503	0.0062	0.0060
33.0	16.5	1.2894	0.0062	0.0058
34.0	17.0	1.3285	0.0062	0.0056
35.0	17.5	1.3675	0.0062	0.0055
36.0	18.0	1.4066	0.0062	0.0054
37.0	18.5	1.5500	0.0071	0.0053
38.0	19.0	1.5500	0.0067	0.0052
39.0	19.5	1.5500	0.0064	0.0052
40.0	20.0	1.5500	0.0061	0.0051

TABLE 4

=====

SIGMA1 (ACTUAL)=0.0027 S/M

WORKING WITH

ZZSOM

XSTART= 0.5000000

KNOW D1 AND SIG2, SOLVE FOR X=D1/DELTA1 AND HENCE SIG1.

SIGeff IS THE HALF-SPACE EFFECTIVE CONDUCTIVITY,

AND IT IS COMPUTED ONLY WHEN INVERTING ZZSOM

FID	D1	X	SIG1	SIGeff
0.0	0.1	0.0078	0.0062	2.7001
1.0	0.5	0.0391	0.0062	2.6894
2.0	1.0	0.0781	0.0062	2.7387
3.0	1.5	0.0586	0.0015	2.7221
4.0	2.0	0.0781	0.0015	2.7030
5.0	2.5	0.0977	0.0015	2.7093
6.0	3.0	0.1672	0.0031	2.3818
7.0	3.5	0.1951	0.0031	1.6995
8.0	4.0	0.2229	0.0031	1.2689
9.0	4.5	0.2508	0.0031	1.0030
10.0	5.0	0.2786	0.0031	0.7038
11.0	5.5	0.2874	0.0028	0.5150
12.0	6.0	0.3135	0.0028	0.4217
13.0	6.5	0.3396	0.0028	0.3189
14.0	7.0	0.3657	0.0028	0.2518
15.0	7.5	0.3918	0.0028	0.1897
16.0	8.0	0.4180	0.0028	0.1405
17.0	8.5	0.4566	0.0029	0.1086
18.0	9.0	0.4835	0.0029	0.0843
19.0	9.5	0.5103	0.0029	0.0680
20.0	10.0	0.5372	0.0029	0.0528
21.0	10.5	0.5640	0.0029	0.0426
22.0	11.0	0.5909	0.0029	0.0332
23.0	11.5	0.6177	0.0029	0.0265
24.0	12.0	0.6446	0.0029	0.0217
25.0	12.5	0.6715	0.0029	0.0180
26.0	13.0	0.6983	0.0029	0.0151
27.0	13.5	0.7252	0.0029	0.0128
28.0	14.0	0.7520	0.0029	0.0109
29.0	14.5	0.7789	0.0029	0.0095
30.0	15.0	0.8058	0.0029	0.0083
31.0	15.5	0.9326	0.0037	0.0073
32.0	16.0	0.9627	0.0037	0.0067
33.0	16.5	0.9928	0.0037	0.0061
34.0	17.0	1.0229	0.0037	0.0055
35.0	17.5	1.0529	0.0037	0.0051
36.0	18.0	1.0830	0.0037	0.0047
37.0	18.5	1.1131	0.0037	0.0044
38.0	19.0	1.1432	0.0037	0.0041
39.0	19.5	1.1733	0.0037	0.0038
40.0	20.0	1.2034	0.0037	0.0036

TABLE 5

=====

SIGMA1 (ACTUAL)=0.027 S/M

WORKING WITH

ZZSOM

XSTART= 0.5000000

KNOW D1 AND SIG2, SOLVE FOR X=D1/DELTA1 AND HENCE SIG1.

SIGeff IS THE HALF-SPACE EFFECTIVE CONDUCTIVITY,

AND IT IS COMPUTED ONLY WHEN INVERTING ZZSOM

FID	D1	X	SIG1	SIGeff
0.0	0.1	0.0156	0.0247	2.6973
1.0	0.5	0.0781	0.0247	2.5953
2.0	1.0	0.1563	0.0247	2.2046
3.0	1.5	0.2469	0.0274	1.6041
4.0	2.0	0.3292	0.0274	1.0232
5.0	2.5	0.4115	0.0274	0.6057
6.0	3.0	0.4938	0.0274	0.3527
7.0	3.5	0.5760	0.0274	0.2107
8.0	4.0	0.6583	0.0274	0.1324
9.0	4.5	0.7469	0.0279	0.0884
10.0	5.0	0.8299	0.0279	0.0631
11.0	5.5	0.9191	0.0283	0.0481
12.0	6.0	1.0027	0.0283	0.0388
13.0	6.5	1.0862	0.0283	0.0330
14.0	7.0	1.1652	0.0281	0.0294
15.0	7.5	1.2484	0.0281	0.0270
16.0	8.0	1.5500	0.0380	0.0256
17.0	8.5	1.5500	0.0337	0.0247
18.0	9.0	1.5500	0.0301	0.0242
19.0	9.5	1.5000	0.0253	0.0240
20.0	10.0	1.6274	0.0268	0.0241
21.0	9.5	1.5500	0.0270	0.0240
22.0	9.0	1.5500	0.0301	0.0242
23.0	8.5	1.5500	0.0337	0.0247
24.0	8.0	1.5500	0.0380	0.0256
25.0	7.5	1.2500	0.0281	0.0270
26.0	7.0	1.1667	0.0281	0.0294
27.0	6.5	1.0833	0.0281	0.0330
28.0	6.0	1.0000	0.0281	0.0388
29.0	5.5	0.9167	0.0281	0.0481
30.0	5.0	0.8333	0.0281	0.0631
31.0	4.5	0.7500	0.0281	0.0884
32.0	4.0	0.6667	0.0281	0.1324
33.0	3.5	0.5833	0.0281	0.2107
34.0	3.0	0.5000	0.0281	0.3527
35.0	2.5	0.4167	0.0281	0.6057
36.0	2.0	0.3333	0.0281	1.0232
37.0	1.5	0.2500	0.0281	1.6041
38.0	1.0	0.1667	0.0281	2.2046
39.0	0.5	0.0833	0.0281	2.5953
40.0	0.1	0.0167	0.0281	2.6973

TABLE 6

=====

SIGMA1 (ACTUAL)=0.0054 S/M

WORKING WITH

ZZSOM

XSTART= 0.5000000

KNOW D1 AND SIG2, SOLVE FOR X=D1/DELTA1 AND HENCE SIG1.

SIGeff IS THE HALF-SPACE EFFECTIVE CONDUCTIVITY,

AND IT IS COMPUTED ONLY WHEN INVERTING ZZSOM

FID	D1	X	SIG1	SIGeff
0.0	0.1	0.0078	0.0062	2.6998
1.0	0.5	0.0391	0.0062	2.6784
2.0	1.0	0.0781	0.0062	2.5848
3.0	1.5	0.1172	0.0062	2.3914
4.0	2.0	0.1563	0.0062	2.0990
5.0	2.5	0.1953	0.0062	1.7409
6.0	3.0	0.2344	0.0062	1.3686
7.0	3.5	0.2734	0.0062	1.0287
8.0	4.0	0.2930	0.0054	0.7481
9.0	4.5	0.3296	0.0054	0.5329
10.0	5.0	0.3662	0.0054	0.3759
11.0	5.5	0.4028	0.0054	0.2650
12.0	6.0	0.4395	0.0054	0.1879
13.0	6.5	0.4886	0.0057	0.1348
14.0	7.0	0.5262	0.0057	0.0979
15.0	7.5	0.5637	0.0057	0.0723
16.0	8.0	0.6076	0.0058	0.0544
17.0	8.5	0.6455	0.0058	0.0417
18.0	9.0	0.6835	0.0058	0.0325
19.0	9.5	0.7215	0.0058	0.0259
20.0	10.0	0.7595	0.0058	0.0210
21.0	9.5	0.7215	0.0058	0.0259
22.0	9.0	0.6835	0.0058	0.0325
23.0	8.5	0.6500	0.0059	0.0417
24.0	8.0	0.6118	0.0059	0.0544
25.0	7.5	0.5646	0.0057	0.0723
26.0	7.0	0.5269	0.0057	0.0979
27.0	6.5	0.4893	0.0057	0.1348
28.0	6.0	0.4517	0.0057	0.1879
29.0	5.5	0.4140	0.0057	0.2650
30.0	5.0	0.3764	0.0057	0.3759
31.0	4.5	0.3387	0.0057	0.5329
32.0	4.0	0.3011	0.0057	0.7481
33.0	3.5	0.2635	0.0057	1.0287
34.0	3.0	0.2258	0.0057	1.3686
35.0	2.5	0.1882	0.0057	1.7409
36.0	2.0	0.1506	0.0057	2.0990
37.0	1.5	0.1129	0.0057	2.3914
38.0	1.0	0.0753	0.0057	2.5848
39.0	0.5	0.0376	0.0057	2.6784
40.0	0.1	0.0075	0.0057	2.6998

TABLE 7

=====

SIGMA1 (ACTUAL)=0.0027 S/M
 WORKING WITH
 ZZSOM

XSTART= 0.5000000

KNOW D1 AND SIG2, SOLVE FOR X=D1/DELTA1 AND HENCE SIG1.
 SIGeff IS THE HALF-SPACE EFFECTIVE CONDUCTIVITY,
 AND IT IS COMPUTED ONLY WHEN INVERTING ZZSOM

FID	D1	X	SIG1	SIGeff
0.0	0.1	0.0078	0.0062	2.7001
1.0	0.5	0.0391	0.0062	2.6894
2.0	1.0	0.0781	0.0062	2.6414
3.0	1.5	0.0586	0.0015	2.5379
4.0	2.0	0.0781	0.0015	2.3690
5.0	2.5	0.0977	0.0015	2.1376
6.0	3.0	0.1672	0.0031	1.8600
7.0	3.5	0.1951	0.0031	1.5616
8.0	4.0	0.2229	0.0031	1.2689
9.0	4.5	0.2508	0.0031	1.0030
10.0	5.0	0.2786	0.0031	0.7760
11.0	5.5	0.2874	0.0028	0.5912
12.0	6.0	0.3135	0.0028	0.4462
13.0	6.5	0.3396	0.0028	0.3353
14.0	7.0	0.3657	0.0028	0.2518
15.0	7.5	0.3918	0.0028	0.1897
16.0	8.0	0.4180	0.0028	0.1437
17.0	8.5	0.4566	0.0029	0.1096
18.0	9.0	0.4835	0.0029	0.0843
19.0	9.5	0.5103	0.0029	0.0654
20.0	10.0	0.5372	0.0029	0.0513
21.0	9.5	0.5103	0.0029	0.0654
22.0	9.0	0.4835	0.0029	0.0843
23.0	8.5	0.4566	0.0029	0.1096
24.0	8.0	0.4297	0.0029	0.1437
25.0	7.5	0.4029	0.0029	0.1897
26.0	7.0	0.3760	0.0029	0.2518
27.0	6.5	0.3492	0.0029	0.3353
28.0	6.0	0.3223	0.0029	0.4462
29.0	5.5	0.2954	0.0029	0.5912
30.0	5.0	0.2686	0.0029	0.7760
31.0	4.5	0.2417	0.0029	1.0030
32.0	4.0	0.2149	0.0029	1.2689
33.0	3.5	0.1880	0.0029	1.5616
34.0	3.0	0.1612	0.0029	1.8600
35.0	2.5	0.1343	0.0029	2.1376
36.0	2.0	0.1074	0.0029	2.3690
37.0	1.5	0.0806	0.0029	2.5379
38.0	1.0	0.0537	0.0029	2.6414
39.0	0.5	0.0269	0.0029	2.6894
40.0	0.1	0.0054	0.0029	2.7001

Appendix

The MIM representation of the normalized secondary field produced by induced ohmic currents in a two-layered conducting model (see Figure 1) for a horizontal coplanar coil pair is given by

$$(H_s/H_p) = ZZ = [2R^2 - 1]/[R^2 + 1]^{5/2} \quad (A-1)$$

and

$$R = [2h + (1-i) Q \delta_1]/\rho \quad , \quad (A-2)$$

where $[2h + (1-i) Q \delta_1]$ is the complex vertical distance separating the primary dipole source from the image source, h is the real altitude of the bird above the first layer surface, $[(1-i) Q \delta_1]/2$ is the complex distance below the first layer surface of the image plane, ρ is the coil spacing, δ_1 is the first layer (sea ice) skin depth, and finally Q is the two-layer correction factor given by

$$Q = [(\delta_1/\delta_2) + \tanh\{(1+i)d_1/\delta_1\}]/[1 + (\delta_1/\delta_2) \tanh\{(1+i)d_1/\delta_1\}] \quad . \quad (A-3)$$

d_1 is the first layer thickness and δ_2 is the skin depth of the second layer (sea water). The thickness or depth of the second layer, d_2 , is assumed to be greater than $2 \delta_2$ in this analysis. (In order to determine the sea depth, a third lower frequency signal must be employed.) The R function can be interpreted geometrically as $\cotan \phi$, where ϕ is the complex angle indicated in Figure 1.

In all MIM inversion schemes, Equation (A-2) is inverted by means of a polynomial expression which gives R as a function of ZZ :

$$R = 1/s - as - bs^3 - cs^5 - ds^7, \quad (A-4)$$

where $s = (ZZ/2)^{1/3}$, and for this coil configuration, $a = 1$, $b = 9/8$, $c = 31/12$, and $d = 267/384$. This inverted relationship is of paramount importance in all MIM inversion routines, i.e., from the value of R calculated from the AEM fields the values of the model parameters are determined.

Halfspace inversion

A halfspace inversion is defined by the condition $Q = 1$. Thus Equation (A-2) can be inverted to give values for the bird altitude h and the skin depth δ_1 :

$$2h/\rho = R_1 + R_2$$

$$\delta_1/\rho = -R_2,$$

where R_1 and R_2 are the real and imaginary components of R . In the event that the conditions which make $Q = 1$ are not satisfied ($Q = 1$ if $\sigma_2 = \sigma_1$ or $d_1 > 2\delta_1$), then the halfspace inversion results in an effective skin depth and bird altitude.

Two layer inversion for sea ice conductivity

In this inversion it is assumed that the only unknown is the first layer skin depth, i.e., the altitude, the second layer skin depth, and the first layer thickness are known from the altimeter reading and the low frequency inversion results. The algebraic manipulations of Equations (A-2) and (A-3) that result in the two simultaneous equations mentioned in the narrative proceed as follows:

First $Q\delta_1$ is solved for explicitly from Equation (A-2)

to produce

$$Q\delta_1 = [\rho R(hi) - 2h]/(1 - i) \quad . \quad (A-5)$$

Next the expression for Q from Equation (A-3) is substituted into Equation (A-5) and the resultant equation is rearranged to solve explicitly for $\tanh((1+i)d_1/\delta_1)$:

$$\begin{aligned} \tanh((1+i)d_1/\delta_1) &= [(C - 1)(\delta_2/\delta_1)]/[1 - C\delta_2/\delta_1] \\ &= D(\delta_1, \delta_2 C) \quad . \quad (A-6) \end{aligned}$$

C is a known complex number given by

$$C = [\rho R(hi) - 2h]/[(1 - i)\delta_2] \quad ,$$

and D is a complex function of the unknown δ_1 and the known quantities C and δ_2 . If we set $D = D_1 + i D_2$ and expand $\tanh((1+i)d_1/\delta_1)$ by

$$\begin{aligned} \tanh((1+i)d_1/\delta_1) &= [\tanh(d_1/\delta_1) + i \tan(d_1/\delta_1)]/[1 + \\ &\quad i \tanh(d_1/\delta_1) \tan(d_1/\delta_1)] \quad , \end{aligned}$$

we get

$$\begin{aligned} &[\tanh(d_1/\delta_1) + i \tan(d_1/\delta_1)]/[1 + i \tanh(d_1/\delta_1) \tan(d_1/\delta_1)] \\ &= D_1 + i D_2 \quad . \quad (A-7) \end{aligned}$$

Finally, if we equate the real and imaginary parts of Equation (A-7), we find

$$\begin{aligned} \tanh(d_1/\delta_1) &= D_1 - D_2 \tan(d_1/\delta_1) \tanh(d_1/\delta_1) \\ \tan(d_1/\delta_1) &= D_2 + D_1 \tan(d_1/\delta_1) \tanh(d_1/\delta_1) \end{aligned}$$

These can be combined to give

$$D_2 \tan^2(d_1/\delta_1) - (D_1^2 + D_2^2 - 1) \tan(d_1/\delta_1) - D_2 = 0 \quad (A-8a)$$

and

$$D_1 \tanh^2(d_1/\delta_1) - (D_1^2 + D_2^2 + 1) \tanh(d_1/\delta_1) + D_1 = 0 \quad . \quad (A-8b)$$

Both of these equations are of the quadratic form $a x^2 + b x + c$, and hence explicit expressions for $\tanh(d_1/\delta_1)$ and $\tan(d_1/\delta_1)$ can be written. But first it should be noted that for the tan equation, $a = -c = D_2$, and thus

$$\tan(d_1/\delta_1) = -b/2a \pm [(b/2a)^2 + 1]^{1/2} ,$$

and similarly for the tanh equation, since $a = c = D_1$,

$$\tanh(d_1/\delta_1) = -b/2a \pm [(b/2a)^2 - 1]^{1/2} .$$

The physical constraint that the roots of these equations be real and positive results in the following solutions:

$$\tan(d_1/\delta_1) = F_1(d_1/\delta_1) + [F_1^2(d_1/\delta_1) + 1]^{1/2} \quad (\text{A-9a})$$

for $0 \leq (d_1/\delta_1) < \pi/2$, and

$$\tan(d_1/\delta_1) = F_1 - [F_1^2 + 1]^{1/2} , \quad (\text{A-9b})$$

for $\pi/2 \leq (d_1/\delta_1) < \pi$, where

$$F_1 = [D_1^2 + D_2^2 - 1]/(2 D_2) .$$

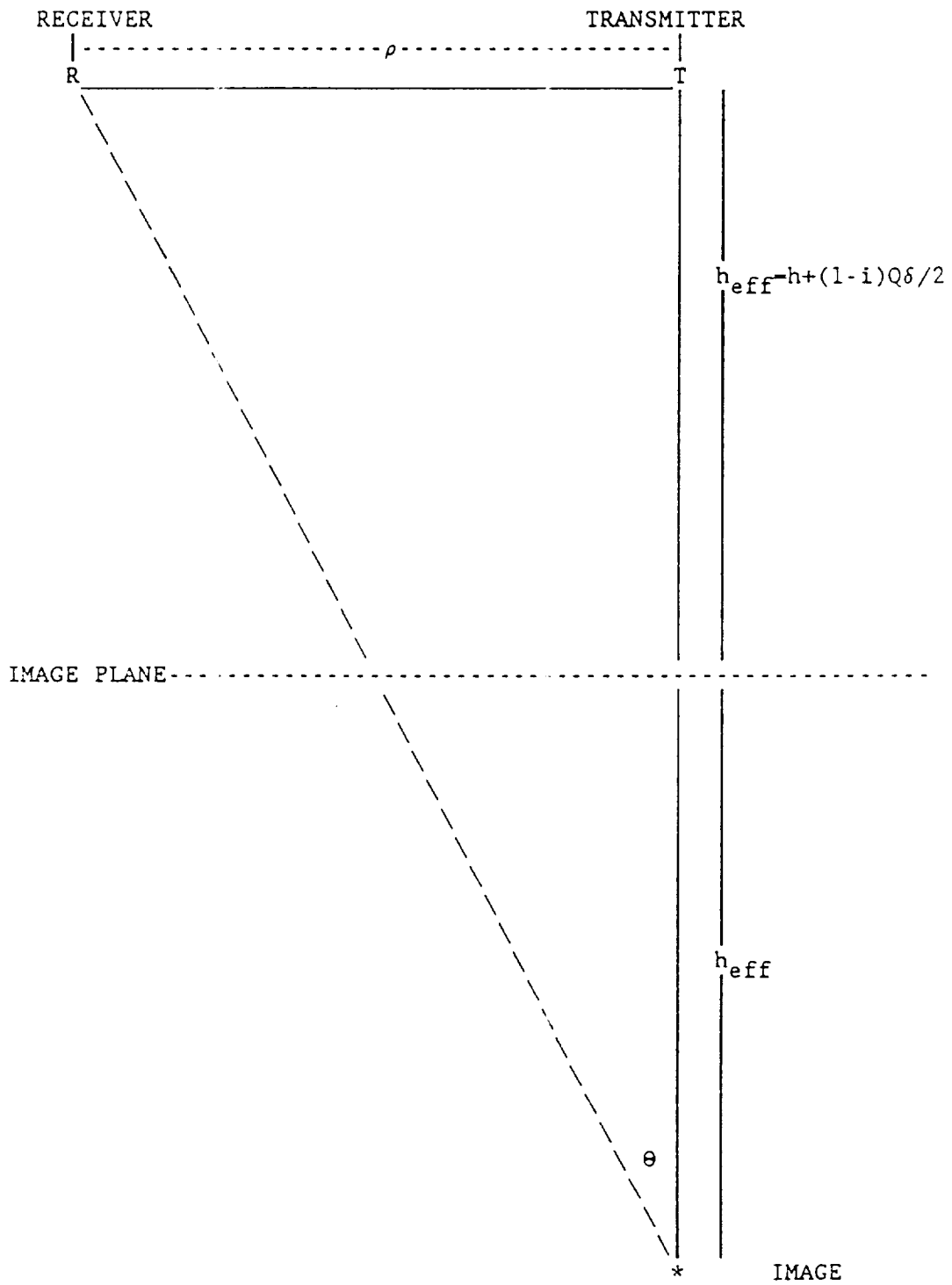
$$\tanh(d_1/\delta_1) = F_2 + [F_2^2 - 1]^{1/2} , \quad (\text{A-10})$$

where

$$F_2 = [D_1^2 + D_2^2 + 1]/(2 D_1) .$$

A root finding algorithm given below is used to find the real positive roots of Equation (A-9a) or (A-9b). These roots are substituted into Equation (A-10) to find the one root of Equation (A-9a) or (A-9b) that is simultaneously a root of Equation (A-10). This value of (d_1/δ_1) is used to determine δ_1 and in turn σ_1 .

FIGURE 1 - Appendix





Updated Status Report

15 Mar 1990

NASA Grant NAG-1-804

Determination of Design and Operation Parameters for Upper
Atmospheric Research Instrumentation to Yield Optimum Resolution
with Deconvolution

Analysis of Response of the Arctic Sea Ice Environment
to AEM Fields

Clyde J. Bergeron and Juliette W. Ioup
Department of Physics, University of New Orleans

Sea Ice Inversion

The MIM inversion of sea ice AEM data taken at two frequencies, 1000 Hz (f_{10}) and 250 kHz (f_{hi}), and for two AEM coil configurations, horizontal coplanar and vertical coaxial, is outlined below.

The low frequency data are first inverted to give $(h + d_1)$ and σ_2 , where h is the altitude of the bird above the sea ice, d is the ice thickness, and σ_2 is the electrical conductivity of the sea. This inversion assumes the following:

1. The skin depth of the sea ice $\delta_1(10)$ is much greater than the thickness of the sea ice and hence the sea ice is effectively transparent to the low frequency primary signal.
2. The sea bottom does not affect the secondary field. This assumption is valid provided that the sea depth d_2 is greater

than twice the low frequency skin depth of the sea, i.e., $d_2 > 2\delta_2(10)$. These two assumptions allow a halfspace inversion. The algebra and computer algorithms for the halfspace inversion are given in the Appendix.

It is assumed that the altitude h is independently determined by a radar or laser altimeter. Thus the inversion results in a local value for the sea ice thickness d_1 and the conductivity of the sea water, σ_2 . These results are employed in the inversion of the high frequency data to determine the sea ice conductivity.

Outline of high frequency inversion

First a halfspace inversion of the high frequency data is performed. This produces an effective skin depth δ_{eff} which lies in the range $\delta_2 \leq \delta_{\text{eff}} \leq \delta_1$, and is a function of ice thickness d_1 . The effective high frequency skin depth is combined with the altimeter reading h to form the ratio $A_{\text{eff}} = 2h/\delta_{\text{eff}}$. The ad hoc normalization function employed in MIM inversion is a function of A_{eff} , i.e.,

MIM field = Normalized field = $F(A_{\text{eff}})$ Sommerfeld field .
It turns out that the same normalization function $F(A_{\text{eff}})$ may be employed for both coil configurations.

For $d_1 \ll \delta_1$, $\delta_{\text{eff}} \approx \delta_2$ and for $d_1 > 2\delta_1$, then $\delta_{\text{eff}} \approx \delta_1$. Since d_1 is known from the low frequency inversion, this latter case may be recognized and hence the first layer conductivity σ_1 is determined from δ_{eff} by

$$\sigma_1 = 2/[\mu_0 f(hi) \delta_{eff}^2] \quad ,$$

where μ_0 is the vacuum magnetic permittivity. The condition $d_1 > 2 \delta_1$ only occurs for thick ($d_1 \geq 10m$), highly conducting ($\sigma_1 > 0.027 \text{ S/m}$) sea ice. For the intermediate, more general situation where δ_{eff}/d_1 is of the order of unity, the inversion procedure to be used is that described below.

The MIM relationship between the complex two-layer correction factor Q and the high frequency AEM field is algebraically transformed into two simultaneous transcendental real equations with argument d_1/δ_1 , where δ_1 is the unknown quantity. All other quantities in these equations are known. Each of these equations has in general several roots, BUT only one common root. The explicit functions that occur respectively in these equations are $\tan(d_1/\delta_1)$ and $\tanh(d_1/\delta_1)$. A root-finding algorithm is first applied to the $\tan(d_1/\delta_1)$ equation. When a root is determined, that root is inserted in the $\tanh(d_1/\delta_1)$ equation to test if it is also a root of the $\tanh(d_1/\delta_1)$ equation. If not, the algorithm continues in its determination of the real roots of the $\tan(d_1/\delta_1)$ equation until the root is found that simultaneously satisfies both equations. The first layer skin depth δ_1 and conductivity σ_1 are given by that simultaneous root.

The range of applicability of the root finding algorithm is given by $0.02 < d_1/\delta_1 < 2.5$. These limits can be understood in physical terms. For $d_1/\delta_1 > 2.5$ the sea ice is effectively a halfspace as has been already noted, and a two

layer model is inappropriate. For $d_1/\delta_1 < 0.02$ the perturbation produced on the secondary AEM field by the sea ice cover is lost in the computer "noise" caused by roundoff, etc., and will certainly be undetectable in the noise and drift present in even ideal real data, where noise and drift are greater than about 1 ppm.

The lower ice thickness limit on the detectability of sea ice conductivity is illustrated in the following table which assumes a value of sea water conductivity of $\sigma_2 = 2.7$ S/m and an operating frequency of 250 Khz.

σ_2/σ_1	δ_1	minimum d_1
100	~ 6 m	~ 0.1 m
1000	~ 20 m	~ 0.3 m

The algebraic details of this procedure and the root finding algorithm are given in the Appendix.

Results

The MIM inversion procedure that has been described is applied to several sea ice models. In all of the models used the low and high frequencies assumed for the AEM system are 1 kHz and 250 kHz, respectively; the altitude of the AEM bird is 25 m; the conductivity of the sea water σ_2 is 2.7 S/m; and the conductivity of the sea ice σ_1 for each model has input values of 0.027 S/m, 0.0054 S/m, and 0.0027 S/m. Thus the ratio K of the

conductivities of sea water to sea ice has the values 100, 500, and 1000, respectively.

With these general conditions, the first model of ice thickness versus range (fiducial number) is given in Figure 1. The ice thickness increases linearly with increasing range.

Horizontal Coplanar Case

The results of the inversion of the ZZ field for σ_1 are shown in Figure 2. The inversion values for σ_1 are in fair agreement with the input values except for the case with $\sigma_1 = 0.027$ S/m. The problem occurs at an ice thickness of approximately 9.5 m. For $\sigma_1 = 0.027$ S/m the skin depth of the sea ice is about 6 m, thus the ratio of ice thickness to skin depth (which is the argument of both the tan and tanh functions) is about $\pi/2$, where the tangent becomes singular and double valued. More importantly, in the immediate vicinity of $\pi/2$, $\tan(d_1/\delta_1)$ varies rapidly. In spite of this, the root finding inversion algorithm still works when the exact forward MIM field ZZ(MIM) is used as the input field (see Table 1). When a simultaneous root cannot be found for the normalized Sommerfeld field in the vicinity of $\pi/2$, a value of 1.55 is assumed for x . See Table 2. It is the residual differences between the normalized Sommerfeld field (or real field data) and the exact MIM field that causes the root finding algorithm that we are currently using to fail for $x = d_1/\delta_1 = \pi/2$.

It should be noted that this value of $\pi/2$ will most

likely not be encountered in field surveys where ice conductivities will generally be less than 0.0054 S/m ($K = 500$). Table 3 shows that for $K = 500$, x is less than $\pi/2$ for sea ice thicknesses up to 20 m.

A shallow ice keel model is shown in Figure 3. Figure 4 shows the values of σ_1 for this model produced by the inversion algorithm for $K = 100, 500, \text{ and } 1000$. These results are also listed in Tables 5, 6, and 7.

In all of the tables we have included the results of the halfspace inversion of the high frequency data which gives σ_{eff} . It can be seen for the case $K = 100$ when $x > 2.4$, $\sigma_{\text{eff}} = \sigma_{\text{input}}$. This demonstrates that when the ice thickness is greater than 2.4 skin depths, a halfspace inversion yields good results for the ice conductivity. Although values of $x > 2.4$ will probably not be found in survey data taken at a high frequency of 250 kHz, still higher frequencies of about 1 MHz will bring x into this range.

Finally, the results of the inversion are shown in Figure 3 for a shallow ice keel model. The tabulated results are shown in Tables 5, 6, and 7.

In summary, the present inversion algorithm for σ_1 works well except in the vicinity of $d_1/\delta_1 = \pi/2$. We are continuing efforts to modify and improve the existing algorithm.

Vertical Coaxial Case

Results similar to the horizontal coplanar case are

obtained for this coil configuration.

Appendix

The MIM representation of the normalized secondary field produced by induced ohmic currents in a two-layered conducting model (see Figure 1) for a horizontal coplanar coil pair is given by

$$(H_s/H_p) = ZZ = [2R^2 - 1]/[R^2 + i]^{5/2} \quad (A-1a)$$

and for a vertical coaxial coil pair is given by

$$(H_s/H_p) = XX = [R^2 - 2]/[R^2 + 1]^{5/2} \quad , \quad (A-1b)$$

where for both cases

$$R = [2h + (1-i) Q \delta_1]/\rho \quad , \quad (A-2)$$

and $[2h + (1-i) Q \delta_1]$ is the complex vertical distance separating the primary dipole source from the image source, h is the real altitude of the bird above the first layer surface, $[(1-i) Q \delta_1]/2$ is the complex distance below the first layer surface of the image plane, ρ is the coil spacing, δ_1 is the first layer (sea ice) skin depth, and finally Q is the two-layer correction factor given by

$$Q = [(\delta_1/\delta_2) + \tanh((1+i)d_1/\delta_1)]/[1 + (\delta_1/\delta_2) \tanh((1+i)d_1/\delta_1)] \quad . \quad (A-3)$$

d_1 is the first layer thickness and δ_2 is the skin depth of the second layer (sea water). The thickness or depth of the second layer, d_2 , is assumed to be greater than $2 \delta_2$ in this analysis. (In order to determine the sea depth, a third lower frequency signal must be employed.) The R function can be interpreted geometrically as $\cotan \phi$, where ϕ is the complex angle indicated

in Figure 1.

In MIM inversion schemes for both cases, Equation (A-2) is inverted by means of a polynomial expression which gives R as a function of ZZ or XX:

$$1/R = as + bs^3 + cs^5 + ds^7 + es^9 \quad , \quad (A-4)$$

where $s = (ZZ/2)^{1/3}$ for the horizontal coplanar configuration and $(2XX)^{1/3}$ for the vertical coaxial case. The values for the coefficients for the two coil configurations are given in the following table. These inverted relationships are of paramount importance in all MIM inversion routines, i.e., the values of the model parameters are determined from the value of R calculated from the AEM fields.

coil configuration	a	b	c	d	e
horizontal coplanar	1	1	2.069	-3	125.1
vertical coaxial	1	1.5	1.125	32.08	203.7

Halfspace inversions

A halfspace inversion is defined by the condition $Q = 1$. Thus Equation (A-2) can be inverted to give values for the bird altitude h and the skin depth δ_1 :

$$2h/\rho = R_1 + R_2$$

$$\delta_1/\rho = -R_2 \quad ,$$

where R_1 and R_2 are the real and imaginary components of R. In the event that the conditions which make $Q = 1$ are not satisfied ($Q = 1$ if $\sigma_2 = \sigma_1$ or $d_1 > 2 \delta_1$), then the halfspace inversion results in an effective skin depth and bird altitude.



Two layer inversion for sea ice conductivity

In this inversion it is assumed that the only unknown is the first layer skin depth, i.e., the altitude, the second layer skin depth, and the first layer thickness are known from the altimeter reading and the low frequency inversion results. The algebraic manipulations of Equations (A-2) and (A-3) that result in the two simultaneous equations mentioned in the narrative proceed as follows:

First $Q\delta_1$ is solved for explicitly from Equation (A-2) to produce

$$Q\delta_1 = [\rho R(h_i) - 2h]/(1 - i) \quad (A-5)$$

Next the expression for Q from Equation (A-3) is substituted into Equation (A-5) and the resultant equation is rearranged to solve explicitly for $\tanh((1+i)d_1/\delta_1)$:

$$\begin{aligned} \tanh((1+i)d_1/\delta_1) &= [(C - 1)(\delta_2/\delta_1)]/[1 - C\delta_2/\delta_1] \\ &= D(\delta_1, \delta_2 C) \quad (A-6) \end{aligned}$$

C is a known complex number given by

$$C = [\rho R(h_i) - 2h]/[(1 - i)\delta_2]$$

and D is a complex function of the unknown δ_1 and the known quantities C and δ_2 . If we set $D = D_1 + i D_2$ and expand $\tanh((1+i)d_1/\delta_1)$ by

$$\tanh((1+i)d_1/\delta_1) = [\tanh(d_1/\delta_1) + i \tan(d_1/\delta_1)]/[1 + i \tanh(d_1/\delta_1) \tan(d_1/\delta_1)]$$

we get

$$[\tanh(d_1/\delta_1) + i \tan(d_1/\delta_1)]/[1 + i \tanh(d_1/\delta_1) \tan(d_1/\delta_1)]$$

$$= D_1 + i D_2 \quad (A-7)$$

Finally, if we equate the real and imaginary parts of Equation (A-7), we find

$$\tanh(d_1/\delta_1) = D_1 - D_2 \tan(d_1/\delta_1) \tanh(d_1/\delta_1)$$

$$\tan(d_1/\delta_1) = D_2 + D_1 \tan(d_1/\delta_1) \tanh(d_1/\delta_1)$$

These can be combined to give

$$D_2 \tan^2(d_1/\delta_1) - (D_1^2 + D_2^2 - 1) \tan(d_1/\delta_1) - D_2 = 0 \quad (A-8a)$$

and

$$D_1 \tanh^2(d_1/\delta_1) - (D_1^2 + D_2^2 + 1) \tanh(d_1/\delta_1) + D_1 = 0 \quad (A-8b)$$

Both of these equations are of the quadratic form $a x^2 + b x + c$, and hence explicit expressions for $\tanh(d_1/\delta_1)$ and $\tan(d_1/\delta_1)$ can be written. But first it should be noted that for the \tan equation, $a = -c = D_2$, and thus

$$\tan(d_1/\delta_1) = -b/2a \pm [(b/2a)^2 + 1]^{1/2},$$

and similarly for the \tanh equation, since $a = c = D_1$,

$$\tanh(d_1/\delta_1) = -b/2a \pm [(b/2a)^2 - 1]^{1/2}.$$

The physical constraint that the roots of these equations be real and positive results in the following solutions:

$$\tan(d_1/\delta_1) = F_1(d_1/\delta_1) + [F_1^2(d_1/\delta_1) + 1]^{1/2} \quad (A-9a)$$

for $0 \leq (d_1/\delta_1) < \pi/2$, and

$$\tan(d_1/\delta_1) = F_1 - [F_1^2 + 1]^{1/2}, \quad (A-9b)$$

for $\pi/2 \leq (d_1/\delta_1) < \pi$, where

$$F_1 = [D_1^2 + D_2^2 - 1]/(2 D_2).$$

$$\tanh(d_1/\delta_1) = F_2 + [F_2^2 - 1]^{1/2}, \quad (A-10)$$

where

$$F_2 = [D_1^2 + D_2^2 + 1]/(2 D_1) \quad .$$

A root finding algorithm given below is used to find the real positive roots of Equation (A-9a) or (A-9b). These roots are substituted into Equation (A-10) to find the one root of Equation (A-9a) or (A-9b) that is simultaneously a root of Equation (A-10). This value of (d_1/δ_1) is used to determine δ_1 and in turn σ_1 .

Figure 1

SEA ICE: INVERT SOM ZZ(HI)

K=100,500,1000 H=25 SIG2=2.7 F=1KHZ,250KHZ X0=3

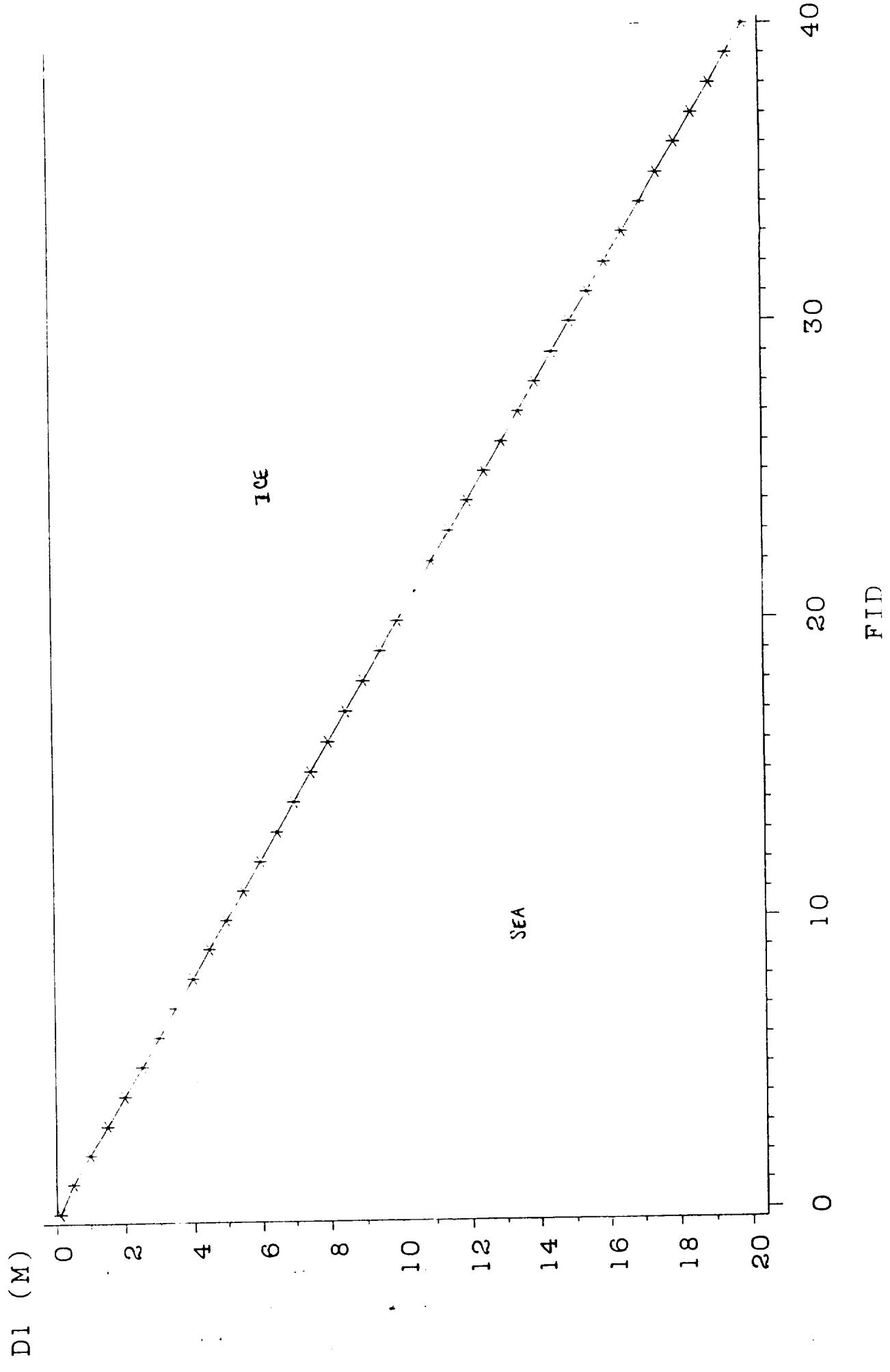
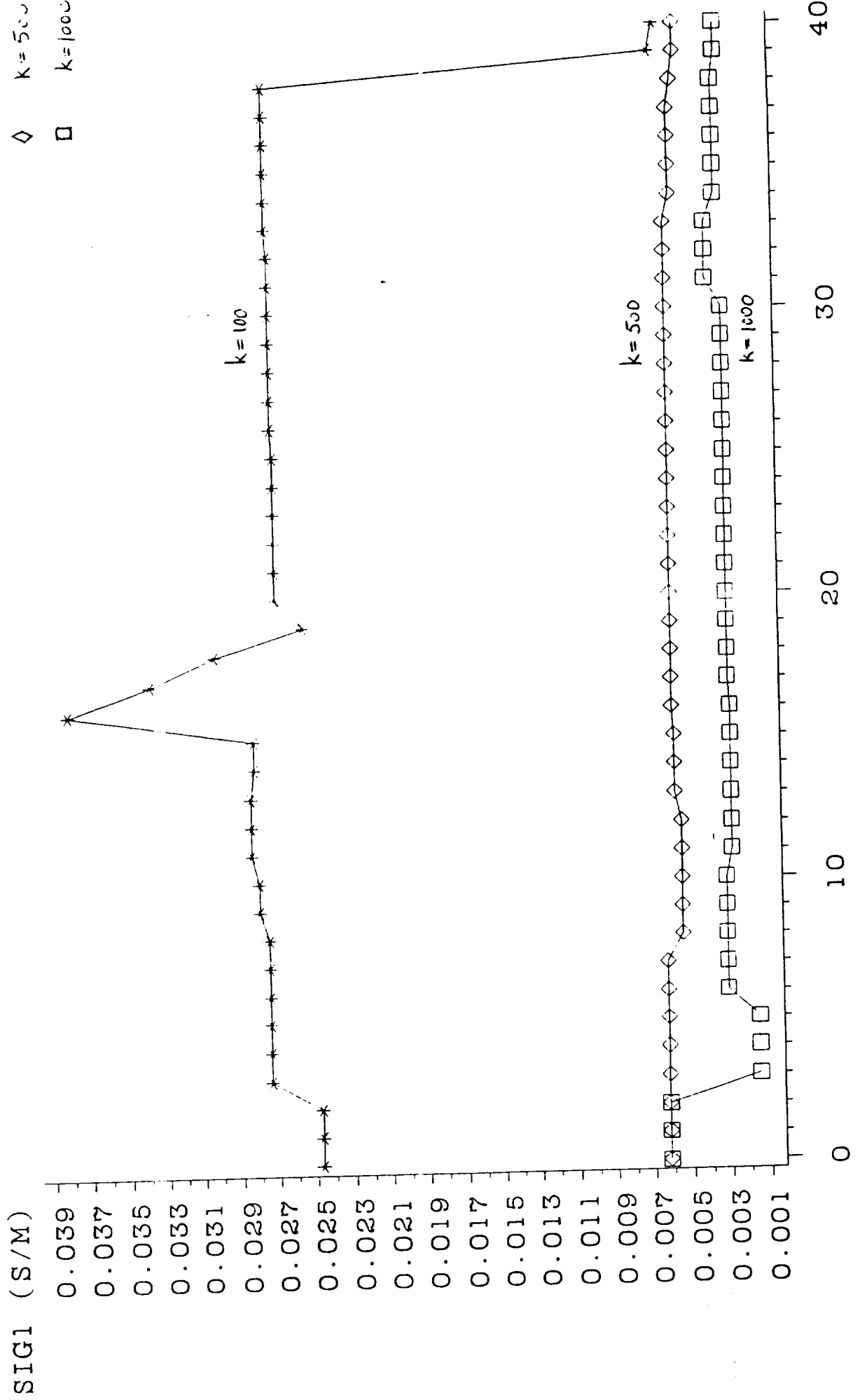


Figure 2

SEA ICE: INVERT SOM ZZ(HI)

$K=100.500, 1000 H=25 SIG2=2.7 F=1KHZ, 250KHZ N0=3$

* $k=100$
 ◇ $k=500$
 □ $k=1000$



SEA ICE: INVERT SOM ZZ(HH)

Figure 3

K=100,500,1000 H=25 SIG2=2.7 F=1KHZ,250KHZ N0=3

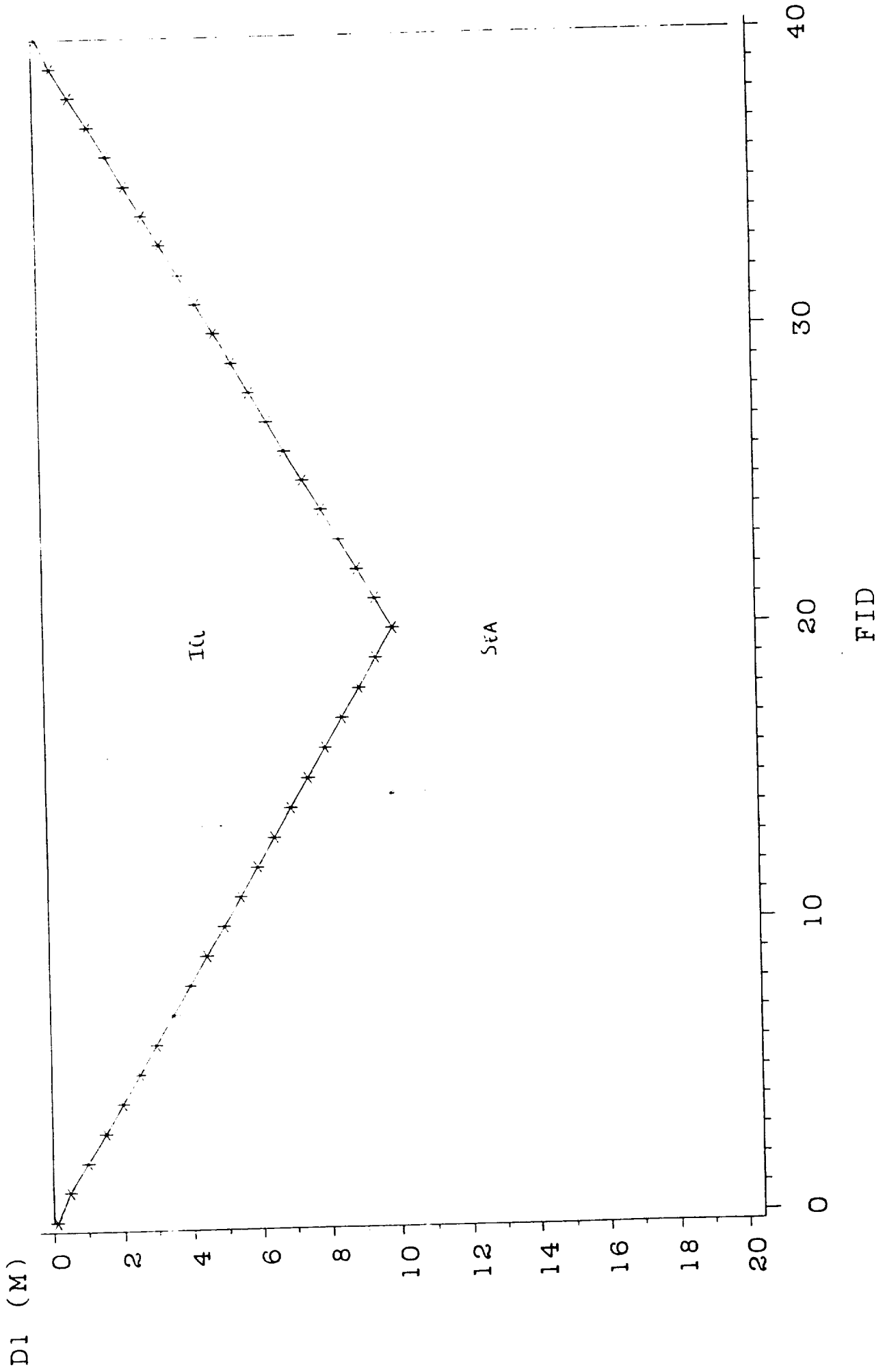
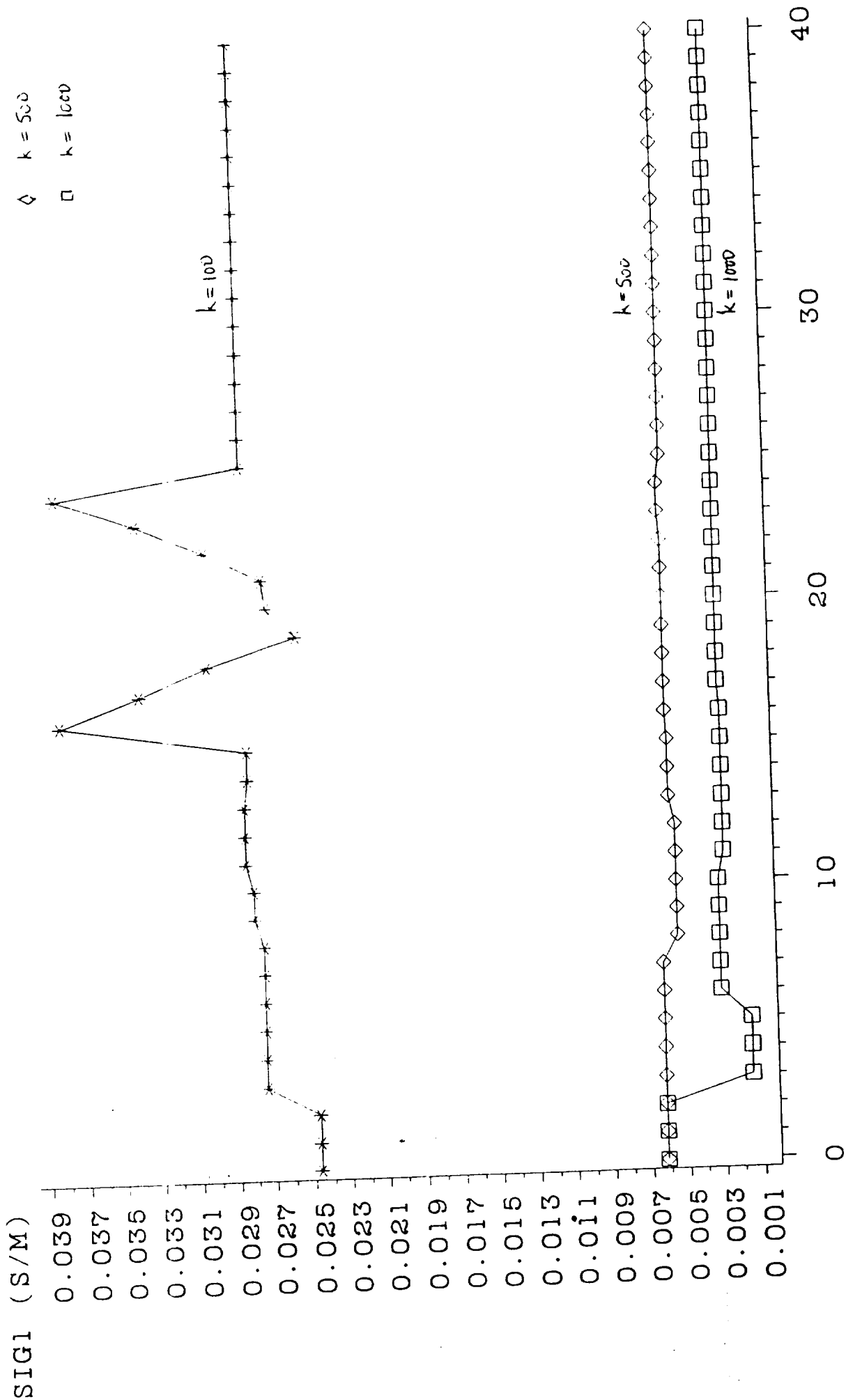


Figure 4

SEA ICE: INVERT NOM ZZ(HI)

K=100,500,1000 H=25 SIG2=2.7 F=1KHZ,250KHZ N0=3

* k=100
 ◊ k=500
 □ k=1000



FID

•

TABLE 1

=====

SIGMA1 (ACTUAL)=0.027 S/M

WORKING WITH

ZZMIM

XSTART= 0.5000000

KNOW D1 AND SIG2, SOLVE FOR X=D1/DELTA1 AND HENCE SIG1.

SIGeff IS THE HALF-SPACE EFFECTIVE CONDUCTIVITY,

AND IT IS COMPUTED ONLY WHEN INVERTING ZZSOM

FID	D1	X	SIG1	SIGeff
0.0	0.1	0.0156	0.0247	2.6960
1.0	0.5	0.0781	0.0247	2.5941
2.0	1.0	0.1563	0.0247	2.2813
3.0	1.5	0.2344	0.0247	1.7051
4.0	2.0	0.3250	0.0268	1.1303
5.0	2.5	0.4063	0.0268	0.7022
6.0	3.0	0.4875	0.0268	0.4009
7.0	3.5	0.5687	0.0268	0.2198
8.0	4.0	0.6500	0.0268	0.1332
9.0	4.5	0.7312	0.0268	0.0884
10.0	5.0	0.8125	0.0268	0.0613
11.0	5.5	0.9000	0.0271	0.0461
12.0	6.0	0.9818	0.0271	0.0373
13.0	6.5	1.0636	0.0271	0.0315
14.0	7.0	1.1455	0.0271	0.0277
15.0	7.5	1.2273	0.0271	0.0253
16.0	8.0	1.3091	0.0271	0.0238
17.0	8.5	1.3909	0.0271	0.0228
18.0	9.0	1.4727	0.0271	0.0224
19.0	9.5	1.5500	0.0270	0.0221
20.0	10.0	1.6355	0.0271	0.0222
21.0	10.5	1.7172	0.0271	0.0223
22.0	11.0	1.7990	0.0271	0.0226
23.0	11.5	1.8808	0.0271	0.0230
24.0	12.0	1.9626	0.0271	0.0234
25.0	12.5	2.0443	0.0271	0.0237
26.0	13.0	2.1218	0.0270	0.0241
27.0	13.5	2.2035	0.0270	0.0244
28.0	14.0	2.2851	0.0270	0.0247
29.0	14.5	2.3667	0.0270	0.0250
30.0	15.0	2.4483	0.0270	0.0252
31.0	15.5	2.5299	0.0270	0.0254
32.0	16.0	2.6115	0.0270	0.0255
33.0	16.5	2.6931	0.0270	0.0257
34.0	17.0	2.7747	0.0270	0.0258
35.0	17.5	2.8563	0.0270	0.0258
36.0	18.0	2.9379	0.0270	0.0259
37.0	18.5	3.0195	0.0270	0.0259
38.0	19.0	3.1012	0.0270	0.0259
39.0	19.5	3.1828	0.0270	0.0259
40.0	20.0	3.2644	0.0270	0.0259

TABLE 2

=====

SIGMAL (ACTUAL)=0.027 S/M

WORKING WITH

ZZSOM

XSTART= 0.5000000

KNOW D1 AND SIG2, SOLVE FOR X=D1/DELTA AND HENCE SIG1.

SIGeff IS THE HALF-SPACE EFFECTIVE CONDUCTIVITY,

AND IT IS COMPUTED ONLY WHEN INVERTING ZZSOM

FID	D1	X	SIG1	SIGeff
0.0	0.1	0.0156	0.0247	2.6973
1.0	0.5	0.0781	0.0247	2.5953
2.0	1.0	0.1563	0.0247	2.2816
3.0	1.5	0.2344	0.0247	1.7033
4.0	2.0	0.3375	0.0289	1.1265
5.0	2.5	0.4087	0.0271	0.6976
6.0	3.0	0.4904	0.0271	0.3973
7.0	3.5	0.5722	0.0271	0.2178
8.0	4.0	0.6664	0.0281	0.1324
9.0	4.5	0.7497	0.0281	0.0884
10.0	5.0	0.8330	0.0281	0.0619
11.0	5.5	0.9163	0.0281	0.0471
12.0	6.0	0.9996	0.0281	0.0386
13.0	6.5	1.0829	0.0281	0.0330
14.0	7.0	1.1662	0.0281	0.0294
15.0	7.5	1.2495	0.0281	0.0270
16.0	8.0	1.5500	0.0380	0.0256
17.0	8.5	1.5500	0.0337	0.0247
18.0	9.0	1.5500	0.0301	0.0242
19.0	9.5	1.4875	0.0248	0.0240
20.0	10.0	1.5500	0.0243	0.0240
21.0	10.5	1.7131	0.0270	0.0241
22.0	11.0	1.7947	0.0270	0.0244
23.0	11.5	1.8763	0.0270	0.0247
24.0	12.0	1.9579	0.0270	0.0250
25.0	12.5	2.0394	0.0270	0.0253
26.0	13.0	2.1210	0.0270	0.0256
27.0	13.5	2.2026	0.0270	0.0259
28.0	14.0	2.2842	0.0270	0.0261
29.0	14.5	2.3657	0.0270	0.0264
30.0	15.0	2.4473	0.0270	0.0265
31.0	15.5	2.5289	0.0270	0.0267
32.0	16.0	2.6105	0.0270	0.0268
33.0	16.5	2.6921	0.0270	0.0269
34.0	17.0	2.7736	0.0270	0.0270
35.0	17.5	2.8552	0.0270	0.0271
36.0	18.0	2.9383	0.0270	0.0271
37.0	18.5	3.0199	0.0270	0.0271
38.0	19.0	3.1024	0.0270	0.0271
39.0	19.5	1.5500	0.0064	0.0271
40.0	20.0	1.5500	0.0061	0.0271

ABLE 3

=====

SIGMA1 (ACTUAL)=0.0054 S/M

WORKING WITH

ZZSOM

XSTART= 0.5000000

KNOW D1 AND SIG2, SOLVE FOR X=D1/DELTA1 AND HENCE SIG1.

SIGeff IS THE HALF-SPACE EFFECTIVE CONDUCTIVITY,
AND IT IS COMPUTED ONLY WHEN INVERTING ZZSOM

FID	D1	X	SIG1	SIGeff
0.0	0.1	0.0078	0.0062	2.6998
1.0	0.5	0.0391	0.0062	2.6784
2.0	1.0	0.0781	0.0062	2.6794
3.0	1.5	0.1172	0.0062	2.5616
4.0	2.0	0.1563	0.0062	2.3817
5.0	2.5	0.1953	0.0062	2.1671
6.0	3.0	0.2344	0.0062	1.7031
7.0	3.5	0.2734	0.0062	1.1052
8.0	4.0	0.2930	0.0054	0.7481
9.0	4.5	0.3296	0.0054	0.5329
10.0	5.0	0.3662	0.0054	0.3495
11.0	5.5	0.4028	0.0054	0.2399
12.0	6.0	0.4395	0.0054	0.1807
13.0	6.5	0.4886	0.0057	0.1303
14.0	7.0	0.5262	0.0057	0.0979
15.0	7.5	0.5637	0.0057	0.0723
16.0	8.0	0.6076	0.0058	0.0536
17.0	8.5	0.6455	0.0058	0.0414
18.0	9.0	0.6835	0.0058	0.0325
19.0	9.5	0.7215	0.0058	0.0264
20.0	10.0	0.7595	0.0058	0.0213
21.0	10.5	0.7974	0.0058	0.0178
22.0	11.0	0.8354	0.0058	0.0148
23.0	11.5	0.8734	0.0058	0.0126
24.0	12.0	0.9114	0.0058	0.0109
25.0	12.5	0.9493	0.0058	0.0097
26.0	13.0	0.9873	0.0058	0.0087
27.0	13.5	1.1253	0.0070	0.0082
28.0	14.0	1.1670	0.0070	0.0075
29.0	14.5	1.2086	0.0070	0.0070
30.0	15.0	1.2503	0.0070	0.0066
31.0	15.5	1.2112	0.0062	0.0063
32.0	16.0	1.2503	0.0062	0.0060
33.0	16.5	1.2894	0.0062	0.0058
34.0	17.0	1.3285	0.0062	0.0056
35.0	17.5	1.3675	0.0062	0.0055
36.0	18.0	1.4066	0.0062	0.0054
37.0	18.5	1.5500	0.0071	0.0053
38.0	19.0	1.5500	0.0067	0.0052
39.0	19.5	1.5500	0.0064	0.0052
40.0	20.0	1.5500	0.0061	0.0051

TABLE 4

=====

SIGMAL (ACTUAL)=0.0027 S/M

WORKING WITH

ZZSOM

XSTART= 0.5000000

KNOW D1 AND SIG2, SOLVE FOR X=D1/DELTA AND HENCE SIG1.

SIGeff IS THE HALF-SPACE EFFECTIVE CONDUCTIVITY,

AND IT IS COMPUTED ONLY WHEN INVERTING ZZSOM

FID	D1	X	SIG1	SIGeff
0.0	0.1	0.0078	0.0062	2.7001
1.0	0.5	0.0391	0.0062	2.6894
2.0	1.0	0.0781	0.0062	2.7387
3.0	1.5	0.0586	0.0015	2.7221
4.0	2.0	0.0781	0.0015	2.7030
5.0	2.5	0.0977	0.0015	2.7093
6.0	3.0	0.1672	0.0031	2.3818
7.0	3.5	0.1951	0.0031	1.6995
8.0	4.0	0.2229	0.0031	1.2689
9.0	4.5	0.2508	0.0031	1.0030
10.0	5.0	0.2786	0.0031	0.7038
11.0	5.5	0.2874	0.0028	0.5150
12.0	6.0	0.3135	0.0028	0.4217
13.0	6.5	0.3396	0.0028	0.3189
14.0	7.0	0.3657	0.0028	0.2518
15.0	7.5	0.3918	0.0028	0.1897
16.0	8.0	0.4180	0.0028	0.1405
17.0	8.5	0.4566	0.0029	0.1086
18.0	9.0	0.4835	0.0029	0.0843
19.0	9.5	0.5103	0.0029	0.0680
20.0	10.0	0.5372	0.0029	0.0528
21.0	10.5	0.5640	0.0029	0.0426
22.0	11.0	0.5909	0.0029	0.0332
23.0	11.5	0.6177	0.0029	0.0265
24.0	12.0	0.6446	0.0029	0.0217
25.0	12.5	0.6715	0.0029	0.0180
26.0	13.0	0.6983	0.0029	0.0151
27.0	13.5	0.7252	0.0029	0.0128
28.0	14.0	0.7520	0.0029	0.0109
29.0	14.5	0.7789	0.0029	0.0095
30.0	15.0	0.8058	0.0029	0.0083
31.0	15.5	0.9326	0.0037	0.0073
32.0	16.0	0.9627	0.0037	0.0067
33.0	16.5	0.9928	0.0037	0.0061
34.0	17.0	1.0229	0.0037	0.0055
35.0	17.5	1.0529	0.0037	0.0051
36.0	18.0	1.0830	0.0037	0.0047
37.0	18.5	1.1131	0.0037	0.0044
38.0	19.0	1.1432	0.0037	0.0041
39.0	19.5	1.1733	0.0037	0.0038
40.0	20.0	1.2034	0.0037	0.0036



TABLE 5

=====

SIGMA1 (ACTUAL)=0.027 S/M

WORKING WITH

ZZSOM

XSTART= 0.5000000

KNOW D1 AND SIG2, SOLVE FOR X=D1/DELTA1 AND HENCE SIG1.

SIGeff IS THE HALF-SPACE EFFECTIVE CONDUCTIVITY,

AND IT IS COMPUTED ONLY WHEN INVERTING ZZSOM

FID	D1	X	SIG1	SIGeff
0.0	0.1	0.0156	0.0247	2.6973
1.0	0.5	0.0781	0.0247	2.5953
2.0	1.0	0.1563	0.0247	2.2046
3.0	1.5	0.2469	0.0274	1.6041
4.0	2.0	0.3292	0.0274	1.0232
5.0	2.5	0.4115	0.0274	0.6057
6.0	3.0	0.4938	0.0274	0.3527
7.0	3.5	0.5760	0.0274	0.2107
8.0	4.0	0.6583	0.0274	0.1324
9.0	4.5	0.7469	0.0279	0.0884
10.0	5.0	0.8299	0.0279	0.0631
11.0	5.5	0.9191	0.0283	0.0481
12.0	6.0	1.0027	0.0283	0.0388
13.0	6.5	1.0862	0.0283	0.0330
14.0	7.0	1.1652	0.0281	0.0294
15.0	7.5	1.2484	0.0281	0.0270
16.0	8.0	1.5500	0.0380	0.0256
17.0	8.5	1.5500	0.0337	0.0247
18.0	9.0	1.5500	0.0301	0.0242
19.0	9.5	1.5000	0.0253	0.0240
20.0	10.0	1.6274	0.0268	0.0241
21.0	9.5	1.5500	0.0270	0.0240
22.0	9.0	1.5500	0.0301	0.0242
23.0	8.5	1.5500	0.0337	0.0247
24.0	8.0	1.5500	0.0380	0.0256
25.0	7.5	1.2500	0.0281	0.0270
26.0	7.0	1.1667	0.0281	0.0294
27.0	6.5	1.0833	0.0281	0.0330
28.0	6.0	1.0000	0.0281	0.0388
29.0	5.5	0.9167	0.0281	0.0481
30.0	5.0	0.8333	0.0281	0.0631
31.0	4.5	0.7500	0.0281	0.0884
32.0	4.0	0.6667	0.0281	0.1324
33.0	3.5	0.5833	0.0281	0.2107
34.0	3.0	0.5000	0.0281	0.3527
35.0	2.5	0.4167	0.0281	0.6057
36.0	2.0	0.3333	0.0281	1.0232
37.0	1.5	0.2500	0.0281	1.6041
38.0	1.0	0.1667	0.0281	2.2046
39.0	0.5	0.0833	0.0281	2.5953
40.0	0.1	0.0167	0.0281	2.6973

TABLE 6

=====

SIGMA1 (ACTUAL)=0.0054 S/M

WORKING WITH

ZZSOM

XSTART= 0.5000000

KNOW D1 AND SIG2, SOLVE FOR X=D1/DELTA1 AND HENCE SIG1.

SIGeff IS THE HALF-SPACE EFFECTIVE CONDUCTIVITY,

AND IT IS COMPUTED ONLY WHEN INVERTING ZZSOM

FID	D1	X	SIG1	SIGeff
0.0	0.1	0.0078	0.0062	2.6998
1.0	0.5	0.0391	0.0062	2.6784
2.0	1.0	0.0781	0.0062	2.5848
3.0	1.5	0.1172	0.0062	2.3914
4.0	2.0	0.1563	0.0062	2.0990
5.0	2.5	0.1953	0.0062	1.7409
6.0	3.0	0.2344	0.0062	1.3686
7.0	3.5	0.2734	0.0062	1.0287
8.0	4.0	0.2930	0.0054	0.7481
9.0	4.5	0.3296	0.0054	0.5329
10.0	5.0	0.3662	0.0054	0.3759
11.0	5.5	0.4028	0.0054	0.2650
12.0	6.0	0.4395	0.0054	0.1879
13.0	6.5	0.4886	0.0057	0.1348
14.0	7.0	0.5262	0.0057	0.0979
15.0	7.5	0.5637	0.0057	0.0723
16.0	8.0	0.6076	0.0058	0.0544
17.0	8.5	0.6455	0.0058	0.0417
18.0	9.0	0.6835	0.0058	0.0325
19.0	9.5	0.7215	0.0058	0.0259
20.0	10.0	0.7595	0.0058	0.0210
21.0	9.5	0.7215	0.0058	0.0259
22.0	9.0	0.6835	0.0058	0.0325
23.0	8.5	0.6500	0.0059	0.0417
24.0	8.0	0.6118	0.0059	0.0544
25.0	7.5	0.5646	0.0057	0.0723
26.0	7.0	0.5269	0.0057	0.0979
27.0	6.5	0.4893	0.0057	0.1348
28.0	6.0	0.4517	0.0057	0.1879
29.0	5.5	0.4140	0.0057	0.2650
30.0	5.0	0.3764	0.0057	0.3759
31.0	4.5	0.3387	0.0057	0.5329
32.0	4.0	0.3011	0.0057	0.7481
33.0	3.5	0.2635	0.0057	1.0287
34.0	3.0	0.2258	0.0057	1.3686
35.0	2.5	0.1882	0.0057	1.7409
36.0	2.0	0.1506	0.0057	2.0990
37.0	1.5	0.1129	0.0057	2.3914
38.0	1.0	0.0753	0.0057	2.5848
39.0	0.5	0.0376	0.0057	2.6784
40.0	0.1	0.0075	0.0057	2.6998

TABLE 7

=====

SIGMA1 (ACTUAL)=0.0027 S/M

WORKING WITH

ZZSOM

XSTART= 0.5000000

KNOW D1 AND SIG2, SOLVE FOR X=D1/DELTA1 AND HENCE SIG1.

SIGeff IS THE HALF-SPACE EFFECTIVE CONDUCTIVITY,
AND IT IS COMPUTED ONLY WHEN INVERTING ZZSOM

FID	D1	X	SIG1	SIGeff
0.0	0.1	0.0078	0.0062	2.7001
1.0	0.5	0.0391	0.0062	2.6894
2.0	1.0	0.0781	0.0062	2.6414
3.0	1.5	0.0586	0.0015	2.5379
4.0	2.0	0.0781	0.0015	2.3690
5.0	2.5	0.0977	0.0015	2.1376
6.0	3.0	0.1672	0.0031	1.8600
7.0	3.5	0.1951	0.0031	1.5616
8.0	4.0	0.2229	0.0031	1.2689
9.0	4.5	0.2508	0.0031	1.0030
10.0	5.0	0.2786	0.0031	0.7760
11.0	5.5	0.2874	0.0028	0.5912
12.0	6.0	0.3135	0.0028	0.4462
13.0	6.5	0.3396	0.0028	0.3353
14.0	7.0	0.3657	0.0028	0.2518
15.0	7.5	0.3918	0.0028	0.1897
16.0	8.0	0.4180	0.0028	0.1437
17.0	8.5	0.4566	0.0029	0.1096
18.0	9.0	0.4835	0.0029	0.0843
19.0	9.5	0.5103	0.0029	0.0654
20.0	10.0	0.5372	0.0029	0.0513
21.0	9.5	0.5103	0.0029	0.0654
22.0	9.0	0.4835	0.0029	0.0843
23.0	8.5	0.4566	0.0029	0.1096
24.0	8.0	0.4297	0.0029	0.1437
25.0	7.5	0.4029	0.0029	0.1897
26.0	7.0	0.3760	0.0029	0.2518
27.0	6.5	0.3492	0.0029	0.3353
28.0	6.0	0.3223	0.0029	0.4462
29.0	5.5	0.2954	0.0029	0.5912
30.0	5.0	0.2686	0.0029	0.7760
31.0	4.5	0.2417	0.0029	1.0030
32.0	4.0	0.2149	0.0029	1.2689
33.0	3.5	0.1880	0.0029	1.5616
34.0	3.0	0.1612	0.0029	1.8600
35.0	2.5	0.1343	0.0029	2.1376
36.0	2.0	0.1074	0.0029	2.3690
37.0	1.5	0.0806	0.0029	2.5379
38.0	1.0	0.0537	0.0029	2.6414
39.0	0.5	0.0269	0.0029	2.6894
40.0	0.1	0.0054	0.0029	2.7001

FIGURE 1 - Appendix

